On The Turbulent Mixing in Horizontal Axis Wind Turbine Wakes

Lorenzo E.M. Lignarolo

On The Turbulent Mixing in Horizontal Axis Wind Turbine Wakes

Proefschrift

ter verkrijging van de graad van doctor
aan de Technische Universiteit Delft,
op gezag van de Rector Magnificus Prof. ir. K.C.A.M. Luyben,
voorzitter van het College voor Promoties,
in het openbaar te verdedigen op

vrijdag 1 april 2016 om 12:30 uur

door

Lorenzo Edoardo Maria LIGNAROLO

Master of Science in Energy and Nuclear Engineering

geboren te Turijn, Italië

This dissertation has been approved by the promotors:

Prof. dr. G. J. W. van Bussel

Copromotor: Dr. Ir. C. J. Simão Ferreira

Composition of the doctoral committee:

Rector Magnificus	chairperson	Delft University of Technology
Prof. dr. G.J.W. van Bussel	promotor	Delft University of Technology
Dr. C.J. Simão Ferreira	copromotor	Delft University of Technology

Independent members

Prof. dr. H. Alfredsson	Royal Institute of Technology
Prof. dr. R. Camussi	Università Roma Tre
Dr. J.G. Schepers	Energy research Centre of the Netherlands
Prof. dr. J.N. Sørensen	Technical University of Denmark
Prof. dr. L.L.M. Veldhuis	Delft University of Technology
Prof. dr. Georg Eitelberg	Delft University of Technology, reservelid

The work described in this thesis was carried out in the Faculty of Aerospace Engineering at the Delft University of Technology and was funded by the Dutch programme FLOW.

TU Delft FLOW

ISBN 978-94-028-0099-9

Cover design by Mihaela Radescu

Printed by Ipskamp Drukkers, Enschede, The Netherlands

An electronic version of this thesis is freely available at http://repository.tudelft.nl

A mio padre

To my father

PREFACE

It is when deep feelings are to express that an inexperienced and poor writer, as the author of these pages, understands the limitations of the written language. Indeed, it is for me nearly impossible to describe the immense gratitude I bear toward my great friend and colleague Dr Daniele Ragni. All the work described in this book is the result of our fruitful collaboration, and large part of what I have achieved in the last four years of scientific research would have been impossible without Daniele's constant guidance and teachings. Through a very spontaneous mixture of provocation and encouragement, fight and support (and very little patience), Daniele gave me the courage to dare going beyond my limitations. During my PhD, he has been for me not just a friend and a collaborator, but a true *magister*, who taught me what it means and what it takes to become a righteous man of science. Definitely, it is because of him if I never gave up.

I want to show my gratitude to Dr Carlos Simão Ferreira, who supervised my work for four years. Since the very beginning, he believed in me and always endeavoured to find opportunities to make me improve my skills and to show my capabilities. He gave me the necessary drive to start writing the first paper, which was a big source of self-confidence. I would like to thank Prof Gerard van Bussel, not only for being the promotor of my research, but also for his wise suggestions and directions, which especially at the beginning of my PhD have been a precious help for making important decisions.

I would also like to thank Prof Henrik Alfredsson, Prof Roberto Camussi, Dr Gerard Schepers, Prof Jens Nørkær Sørensen, Prof Leo Veldhuis and Prof Georg Eitelberg for serving as my committee members. In particular, Dr Gerard Schepers from ECN provided a considerable contribution to planning my research throughout the whole PhD process, taking into account the interests and needs of industry and to promoting my results.

I want to express my appreciation to Prof Gijs van Kuik from DUWIND, who has been a considerable source of inspiration in the last four years. I enjoyed our many conversations about art and I have always considered him as an example of a modern Renaissance man of exquisite scientific and artistic culture.

My sincere thanks also go to Prof Fulvio Scarano, from the Chair of Aerodynamics of the AWEP Department, who always showed interest in my research and willingness to help me with lots of technical issues, to listen to my concerns and to give me precious suggestions. He also gave a terrific contribution to raising the quality of my publications with careful reviews.

I would like to thank my first Master student, Mr Chidambaresan Krishnaswami, who did an amazing job during my second experimental campaign and the data analysis, and Dr Qiuhua Chen from Wuhan University, who collaborated with me throughout the second year of my PhD.

Without the great collaboration of other fellow PhD students, post-docs researchers and professors, my work would have certainly been of a lesser quality. For this reason, I want to say a big thank you to Dhruv Mehta from ECN, Dr Richard Stevens and Prof Charles

Meneveau from the Johns Hopkins University, Dr Ali Emre Yilmaz and Prof Johan Meyers from the Katholieke Universiteit Leuven and Dr Søren Andersen from the Technical University of Denmark, as well as Prof Gijs van Kuik, for contributing to my work with high-quality numerical simulations and for our great collaboration. I wish to thank Dr Norbert Warncke for his help in the POD analysis and Dr Marios Kotsonis, who helped me setting up my first experiment, Giuseppe Tescione for his critical comments that often led me to reconsider my positions, Busra Akay and Dr Daniel Micallef who let me assist to one of their PIV experiments, which was my first direct experience with this technique and allowed me learn a lot. I want to thank Dr Michiel Zaayer, Dr Wim Bierbooms, Rene Bos, Etana Ferede, Maarten Holtslag and Prof Gijs van Kuik who helped me with the Dutch translation of some parts of this book. Also, my thanks go to Giuseppe Correale for his directions during the last weeks before my PhD defence that helped me avoiding a lot of mistakes and optimising precious time, and to Dr Lars Bernhammer and Ricardo Pereira for their friendship and appreciation.

I want to give a very big thank to Ms Sylvia Willems, the amazing factotum and executive secretary of our group, who showed great endurance in withstanding my numerous requests for help and who contributed to rendering the more bureaucratic side of my PhD as easy (and funny) as possible. Also, I want to say thank you to all my other colleagues from the chair of Wind Energy and Aerodynamics.

I would like to thank Dr Roland Schmehl from the Kite Power group, who started helping me and giving me important suggestions already before the beginning of my PhD, and my colleagues and friends from the TUDelft Faculty of Architecture Dr Thaleia Konstantinou, who gave me great ideas for the structure of this thesis and Dr Michela Turrin and Prof Patrick Teuffel, who supervised me during my year as a guest researcher at the chair of Architectural Engineering and gave me the opportunity to learn a lot about that subject.

Obviously, special thanks go to the technicians of our laboratories and workshops: Ed Roessen, Nico van Beek, Frits Donker Duyvis, Peter Duyndam and Stefan Bernardy.

Several other people have been important to the success of this work, consciously or unconsciously. For this reason, I would like to give them my warmest thanks. Certainly, my good friend Dr Emanuela Negro was a very significant presence in these last years. I can say it is thanks to her if I made the decision to move to the Netherlands and start a PhD. This also made me realise that a simple evening spent with a friend and a bottle of wine can have considerable consequences. I want to say thank you to my friend Mihaela Radescu (Mika), who took care of the cover design and is always a source of inspiration and energy, and to Iván Brito, who was a comforting and encouraging presence in the most difficult part of my PhD. I want to express my gratitude to all my friends for their support and for making me become a better man. I have to thank my friends from Italy Giancarlo Maria Traina, Paola Barra, Stefania (Sveva) Borla and Vincenzo Anghelone for more than ten years of true friendship, for their caring support during my PhD and for visiting me several times, also in the day of my defence, and to the ones that accompanied me throughout the years I spent abroad, Aurora Rapalino, Alice Mela, Palma Fontana, Marco Alvarez, Alan Vargas, Francesco Apostoli and many others.

I want to thank Salvatore Ozzimo, Rev. Fr. Francesco Maj and Prof Emilio Cafaro, who has recently passed away, for supporting and inspiring my journey in science, from primary school to university, and Rev. Fr. Avin Kunnekkadan for giving me spiritual guidance in the hardest times of my PhD.

I want to thank my mother, who has always been of stable support, a source of strength and a confidant. I want to thank my brother, who accepted to serve as paranymph during my defence and who opened my way to TUDelft several years ago.

It is important to me to give special thanks to my grandfather, probably the greatest supporter of my PhD.

I dedicate this book to my father, the first man who introduced me to the mysterious beauty of science.

Lorenzo E.M. Lignarolo
Delft, February 2016

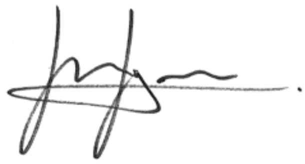

CONTENTS

SUMMARY

The wake flow of a horizontal axis wind turbine is characterised by lower wind speed and higher turbulence than the free-stream conditions. When clustered in large wind farms, wind turbines regularly operate inside the wake of one or more upstream machines. This is a major cause of energy production loss and a source of higher fatigue loads on the rotor's blades. In order to minimise the wake effects, a smart optimisation of the wind-turbine layout is essential and reliable method for modelling the wake behaviour is fundamental. The scientific community has broadly recognised the high level of uncertainty, which still affects the state-of-the-art numerical wake models and, in turn, leads to miscalculation of the wake effect. In order to develop more advanced models it is valuable to follow a back-to-basic approach and to investigate the physics of the transition from near-wake flow to far-wake flow. The near wake is characterised by the presence of organised structures as the tip- and root-vortex helices, which are trailed at the two extremities of each blade. In the far wake, the influence of the blade flow is no longer visible: this is the region where most of the turbulence mixing happens and the wake undergoes a re-energising process. Given the different physics governing the two regions, including in a single model a set of assumptions able to encompass both flow characteristics and to account for the influence of the near-wake features on the far-wake development is still problematic.

This research explores two aspects of the wake problem, adopting an experimental, numerical and theoretical approach. In the first place, the physics of the transition from near to far wake is explored. In particular, the main aim is to study how the near-wake turbulent flow structures affect the re-energising process of the far wake, by understanding the relationship between the near-wake vortex system and the resulting turbulence structures in the wake. In second instance, the *actuator disc* approach, which is at the basis of most rotor as well as wake models, is studied for shedding more light onto its limitations and potentials.

Stereo particle image velocimetry (SPIV) is adopted for mapping the three-component velocity field in a meridian plane encompassing a large portion of the near, transition and far wake of a two-blade wind turbine model. Measurements are carried out in the presence of an artificially-triggered tip-vortex pairing instability, the so-called *leapfrogging* instability, which determines the tip-vortex breakdown and the onset of a more efficient wake mixing. The analysis of the data revealed a major influence of the vortex instability on both the time-average velocity field and on the turbulence field. In particular, it was shown that the wake begins its re-energising process after the tip vortices have completed a 90 degree rotation around each other during the pairing mechanism. A second step in this analysis is the application of the triple decomposition of the flow in the shear layer at the border of the wake. With this approach, the role of the periodic and random flow motions in the turbulent mixing and wake re-energising process can be studied separately. Two components of the mean-flow kinetic-energy

transport are quantified for one single phase of the rotor rotation: the mean-flow kinetic-energy flux and the turbulence production. The analysis shows that only the random flow fluctuations are yielding considerable entrainment of kinetic energy, while the near-wake vortex structure seem to act as a shield preventing the wake mixing.

The study continues with the analysis of the wake of the wind turbine model compared with the one of an actuator disc. The latter is reproduced experimentally by means of a porous disc manufactured with metal mesh, having the same diameter and drag coefficient of the turbine model. Differences between the two wakes (velocity deficit, turbulence levels, mean-flow kinetic-energy transport, etc.) are quantified with SPIV measurements. The study shows that the actuator disc is in fact able to reproduce the time-average velocity field also in the very near wake with good accuracy, contrary to what is found in previous literature. Proper orthogonal decomposition (POD) of the flow field is adopted as an alternative method for separating periodic and random flow motions without the need of acquiring phase-locked measurements. This also allows estimating the mean-flow kinetic-energy flux and the turbulence production in the time-average field, rather than in one single rotation phase. The analysis confirms that major contribution to the momentum entrainment in the wind turbine wake is provided by the random flow fluctuations, while the periodic fluctuations have a zero or even negative contribution. In the actuator disc wake the kinetic energy transport is only positive and of a larger magnitude compared to the one in the wind turbine wake. The analysis of the turbulence production shows a distinct region characterised by large negative values in correspondence of the tip-vortex instability. This phenomenon constitutes a clear example of the failure of the gradient transport model in the time-mean field, which normally does not account for the possibility of reverse energy transfer from coherent structures to the mean flow.

Five state-of-the-art computational fluid dynamics (CFD) codes are validated against the experimental data in a benchmark workshop organised among several academic and industrial organisations. Four large eddy simulation (LES) codes and one vortex models are used for reproducing the near wake of the porous disk. The comparison shows that, despite the lack of viscosity and turbulence models, the vortex model is capable of reproducing the wake expansion and the centreline velocity with very high accuracy. Also all tested LES models are able to predict the velocity deficit in the very near wake well, contrary to what was expected from previous literature. However the resolved velocity fluctuations in the LES are below the experimentally measured values.

SAMENVATTING

Het zog van een horizontale-as windturbine wordt gekarakteriseerd door een lagere windsnelheid en een hogere turbulentie dan in de vrije stroming. Windturbines opereren regelmatig in het zog van één of meerdere stroomopwaartse machines wanneer ze geclusterd zijn in grote windparken. Dit is een belangrijke oorzaak van het verlies van energieproductie en een bron van hogere vermoeiingsbelastingen op de rotorbladen. Om deze zog effecten te minimaliseren is het essentieel om de lay-out van het park slim te optimaliseren. Hiervoor is een betrouwbare methode om het zog gedrag te modeleren fundamenteel. Het wordt algemeen erkent in de wetenschap dat de nieuwste numerieke zogmodellen nog steeds gepaard gaan met grote onzekerheid, wat leidt tot een misrekening van het zog effect. Om geavanceerdere modellen te ontwikkelen is het waardevol om terug naar de basis te gaan en de fysica te onderzoeken van de transitie van het nabije zog naar het verre zog. Het zog direct achter de rotor wordt gekenmerkt door de aanwezigheid van georganiseerde structuren, zoals de wervelspiralen van de blad tip en –wortel, die vanaf deze twee uiteinden van het blad de stroming in gaan. In het verderaf gelegen zog is de invloed van de stroming om het blad niet meer zichtbaar: dit is het gebied waar het grootste deel van de turbulente menging plaatsvindt en waar de energie in het zog wordt aangevuld. Omdat deze twee gebieden door verschillende fysische processen worden gedomineerd, is het nog steeds problematisch om met een set aannames in één model de kenmerken van beide stromen te beschrijven, en de invloed van de verschijnselen van het zog direct achter de rotor op de ontwikkeling van het verre zog te bepalen.

Dit onderzoek gaat over twee aspecten van het zog probleem, en volgt zowel een experimentele als een numerieke en theoretische aanpak. Als eerste worden de fysische aspecten van de overgang van het dichtbije zog naar het verre zog verkend. De belangrijkste vraag hierbij is hoe turbulente stromingsverschijnselen in het dichtbije zog invloed hebben op het aanvullen van de energie in het verre zog. Hiervoor is een goed begrip nodig van de relatie tussen het wervelsysteem in het dichtbije zog en de resulterende coherente turbulentie structuren in het zog. In tweede instantie wordt de actuator disc aanpak, welke aan de basis ligt van de meeste rotormodellen en zogmodellen, bestudeert om meer licht te werpen op de beperkingen en mogelijkheden van deze aanpak..

Stereo particle image velocimetry (SPIV) is toegepast voor het in kaart brengen van de drie componenten van het snelheidsveld in een meridiaan vlak dat een groot deel van het nabije, overgang en verre zog van een twee bladig windturbine model omvat. Metingen zijn uitgevoerd waarbij kunstmatig een instabiele tipwervel koppeling is geactiveerd, de zogenaamde leapfrogging instabiliteit, die het afbreken van de tipwervel en het begin van een efficiëntere menging van het zog bepaalt. De analyse van de data toonde dat de wervel instabiliteit een grote invloed heeft op het tijd-gemiddelde snelheidsveld en op de turbulentie. In het bijzonder werd aangetoond dat het aanvullen van de energie in het zog

begint nadat de tipwervels een 90 graden rotatie langs elkaar hebben afgerond tijdens het koppelingsproces. De tweede stap in deze analyse is de toepassing van de drievoudige decompositie van de stroming in de shear laag aan de rand van het zog. Met deze methode kan de rol van de periodieke en willekeurige fluctuaties in de turbulente menging en het proces van aanvullen van energie in het zog apart bestudeerd worden. Twee onderdelen van het transport van kinetische energie van de gemiddelde stroming worden gekwantificeerd voor een enkele fase van de rotor rotatie: de flux van kinetische energie van de gemiddelde stroming en de productie van turbulentie. De analyse toont dat alleen de willekeurige stromingsfluctuaties zorgen voor een aanzienlijk menging van kinetische energie, terwijl de wervelstructuur in het nabije zog lijkt op te treden als een schild dat menging van het zog verhindert.

Het onderzoek gaat verder met eeen vergelijking van het zog van het windturbinemodel met dat van een actuator disc. Laatstgenoemde is experimenteel gereproduceerd door middel van een poreuze schijf gemaakt van een gaas van metaal, met dezelfde diameter en weerstandscoëfficiënt als het turbinemodel. Verschillen tussen de twee zoggen (snelheidsvermindering, turbulentieniveaus, het transport van kinetische energie door de gemiddelde stroming, etc) worden gekwantificeerd met SPIV metingen. De studie laat zien dat de actuator disc erin slaagt om het tijdsgemiddelde snelheidsveld ook in het verre zog nauwkeurig te reproduceren, in tegenstelling tot wat er gevonden is in voorafgaande literatuur. Proper orthogonal decomposition (POD) van het stromingsveld is gebruikt als een alternatieve methode om de periodieke en willekeurige bewegingen in de stroming te scheiden zonder fasevergrendelde metingen nodig te hebben. Hierdoor kan ook de flux van kinetische energie door de gemiddelde stroming en de turbulentieproductie in het tijdsgemiddelde veld geschat worden, in plaats van in één enkele rotatiefase. De analyse bevestigt dat de willekeurige fluctuaties in de stroming voor een groot deel bijdragen aan het mengen van impuls in het zog van de windturbine, terwijl de periodieke fluctuaties geen of zelfs een negatieve bijdrage hebben. In het zog van de actuator disc is het transport van kinetische energie alleen positief en hoger dan in het zog van de windturbine. De analyse van de turbulentieproductie laat een duidelijk gebied zien dat gekarakteriseerd wordt door sterk negatieve waarden, overeenkomstig met de instabiliteit van de tipwervel. Dit fenomeen is een duidelijk voorbeeld van het falen van het gradiënt transport model in het tijdsgemiddelde veld, wat normaliter geen rekening houdt met de mogelijkheid van een omgekeerde energieoverdracht van coherente structuren naar de gemiddelde stroming.

In het kader van een vergelijkend onderzoek, georganiseerd door diverse academische en industriële partijen, zijn een vijftal actuele computerprogramma's voor simulatie van stromingen (computational fluid dynamics, CFD), getoetst met behulp van metingen. Het betreft vier "large eddy" simulatie (LES) programma's en een wervel model, die gebruikt zijn voor de beschrijving van het nabije zog van een poreuze schijf. De vergelijking laat zien dat het wervel model, ondanks het ontbreken van viscositeit en turbulentie modellering, in staat is om de zog uitbreiding en de snelheden op de middellijn met erg hoge nauwkeurigheid te bepalen. In tegenstelling tot bevindingen uit eerdere publicaties is gebleken dat ook de onderzochte LES modellen goed in staat zijn om de snelheidsafname in het nabije zog te voorspellen. De fluctuaties van het door het LES gefilterde snelheidsveld zijn echter lager dan de gemeten waarden.

1 INTRODUCTION

The chapter provides the necessary background about the physics of horizontal axis wind turbine wakes. The societal and economic implications of the wake effect in large wind farms is presented, as well as an overview of the main stability properties of the wake system and of the turbulent mixing. The state of the art of the numerical wake models is reviewed. The chapter includes also the description of the thesis outline and presents a series of research question that will be addressed and answered throughout the whole thesis.

1.1 SOCIETAL AND ECONOMIC IMPACT OF THE WAKE EFFECT

Windmills, together with the sailing boats, are among the oldest devices for exploiting the energy of the wind (Vermeer et al, 2003). In the last decades, a renewed interest in wind energy led to an increased exploitation of the wind resource, both onshore and offshore, with more and more turbines clustered in large wind farms. In this configuration, the wind turbines interact with each other when operating in the wake of one or more turbines. This is a region affected by lower wind speed and higher turbulence, which are both detrimental effects to the turbine's performance and structural integrity. For these reasons, the optimization of wind-turbine layout is an essential strategy for reducing wake losses: reliable wind-farm aerodynamic models are therefore of paramount importance.

The presence of the wake has two major negative consequences on the performance of the turbines within a wind farm. The lower wind speed behind a turbine causes a decreased energy production of the downstream turbines: the resulting energy loss of a wind farm is very much dependent on the conditions and the layout of the farm. Schepers (2012) showed that it can even be 20% for a farm of 140 turbines with a spacing of 5 rotor diameters. This in turn affects the cost of energy. The second effect is constituted by increased velocity fluctuations which lead to higher fatigue loads and shorted turbine life-time (Schepers, 2012). Wake effects increase in offshore wind farms, where the ambient turbulence intensity is lower than onshore and the wakes persist over a larger distance downstream due to the reduced atmospheric turbulence (Ivanell et al, 2010).

The wind farm wake effects are a considerable issue in different phases of the wind-farm lifespan. During the planning and design phase, it is important to optimise the wind-turbine layout in order to maximise the power production and minimise the fatigue loads. On this regard, wind-turbine wake models are used to assist the wind-farm planners in the layout-optimisation process, when also several other aspects such as wind farm lifetime, cables cost, type of soils and water depth are to take into account. Better wind farm wake models may therefore help decrease the cost of energy (Réthoré, 2009, Réthoré et al, 2010).

In the project development phase, investors require an accurate estimate of the wind farm Annual Energy production (AEP) and of the maintenance cost. Both items are significantly affected by the quality of the wind farm wake analysis, which nowadays is still hampered by a large level of uncertainty (Barthelmie et al, 2010), which in turn increases the investment risks. More accurate predictions of the total energy yield and loading of the individual wind turbines will substantially reduce the risks of an far offshore wind farm project. That would lead to a lower interest rate for the project, which might eventually make wind energy a more competitive solution.

In the operational phase, the wind farm operator needs a reliable forecast of the daily energy production of the wind farm in order to bid strategically on the short-term electricity market, with any variation from the initial forecast being translated into additional cost to the wind farm operator. The accuracy of the wake model affects the quality of the power production forecast significantly and in turn the cost of energy at energy exchange markets. As far as wind-farm control methods are concerned, it has been argued by Corten and Schaak (2004) that smarter wake-model based strategies could reduce the equivalent fatigue loads on the turbines and increase its power output.

1.2 WAKE STRUCTURE

The wake of a horizontal axis wind-turbine (HAWT) is a region of three-dimensional turbulent flow characterised by a deficit of kinetic energy and a complex vortical helical structure. The wake of a single rotor-blade consists of a continuous sheet of trailed vorticity due to the gradient in bound circulation along the blade span, which rolls up generating two concentrated vortices at the tip and the root region. The force field at the rotor accelerates the flow imposing a rotary motion to the wake, which is counter rotating with the rotor. The vorticity created at the blade boundary layer is also released into the wake, in a portion of the flow, which is co-rotating with the blade due to the presence of viscosity. The tip-vortex filaments define a helical structure, due to the combination of the rotational motion of the blade, the free-stream wind-flow and the velocity field induced by the vortex system itself.

Two regions can be identified: a *near-wake* and a *far-wake* region. In the *near wake*, in the proximity of the rotor, the flow is marked by the presence of organised structures as the tip- and root-vortex helices, which are trailed at the two extremities of each blade, and can show instable behaviour. In the *far-wake* region, the influence of the blade flow is no longer visible: this is the region where the wake-generated turbulence and the external atmospheric turbulence have contributed to the breakdown and diffusion of the tip-vortex spiral and most of the turbulence mixing happens, while the wake undergoes a re-energising process. This distinction is not well defined and there are several conventions in literature (Schepers, 2012, Vermeer et al, 2003). Between these two regions, a third zone can be distinguished, the *intermediate wake* (Figure 1-1). This is the region where the turbulent mixing begins to prevail on the organised vortical structures and, as it will be illustrated in the next section, where the tip-vortex spirals may start to mutually interact and become unstable.

1.3 WAKE STABILITY AND TURBULENT MIXING

The stability properties of the wake's system of vortex filaments have been investigated by several authors (see the review by Sørensen, 2011). The most evident forms of wake instability are the so-called *leapfrogging* and *meandering*. The latter is an unsteady behaviour of the wake, in which the whole wake is seen to oscillate randomly with a low-frequency motion (Bingöl et al, 2010, Medici, 2005). The former consists of a pairwise interaction among two or more consecutive tip-vortex filaments, which engage into a roll-up process around each other until their coherence is disrupted and they breakdown into small scale turbulent fluctuations (the topic will be thoroughly treated in Chapter 3 and Chapter 5).

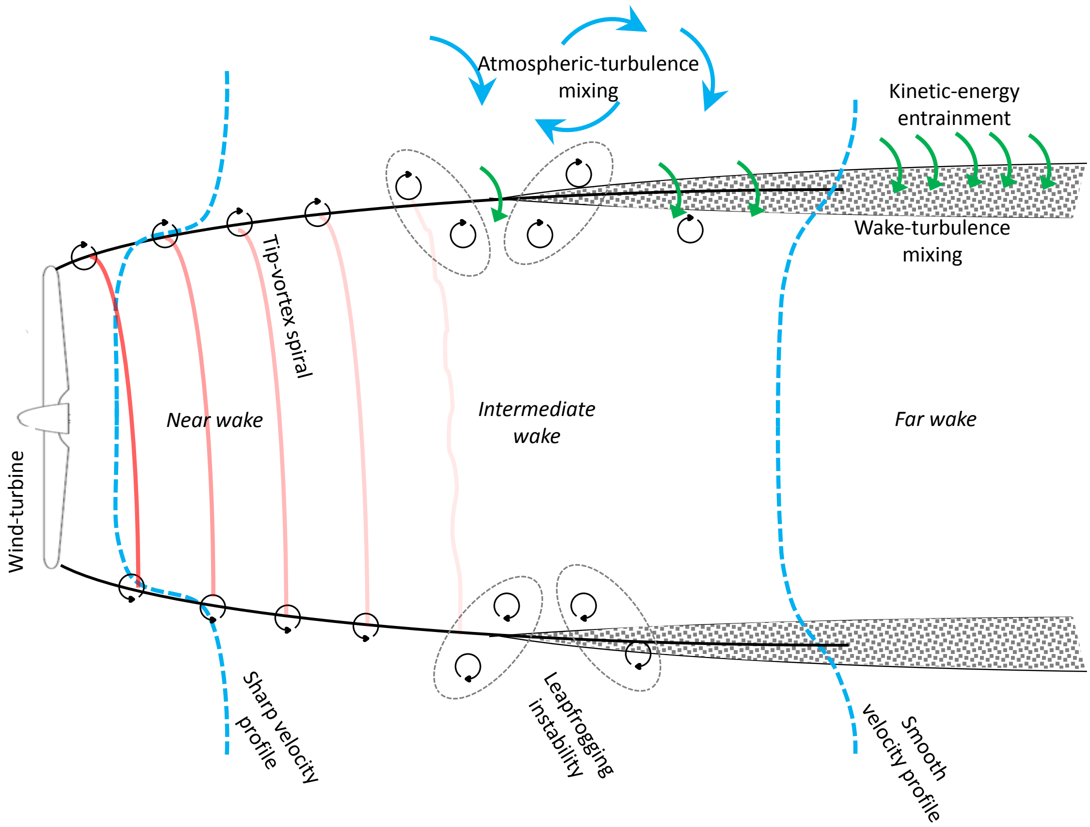

Figure 1-1. Schematic of a wind-turbine wake with tip-vortex leapfrogging instability.

In offshore wind, where the influence of the ambient turbulence is lower than in onshore conditions, knowledge about the basic mechanisms behind the breakdown of the tip-vortex spiral systems is needed in order to estimate the extension of the near-wake region, where the coherent fluctuations generated at the blade tip and root dominate. As it will be explained in Chapter 3, the instability and breakdown of the helical system of vortices in the near wake affects the development of the turbulence in the far wake, where the mixing process between the inner and the outer flow regions occurs. Cal et al (2010) and Hamilton et al (2012) showed how in large wind farms, the wake energy recovers via entrainment of kinetic energy from the flow surrounding the farm. This kinetic-energy entrainment occurs with two different mechanism (Réthoré, 2009). The large-scale flow fluctuations in the atmosphere causes the wind-farm flow to mix and re-energise; at wake level, the turbulence generated at the wake borders and by the tip-vortex instability and breakdown also plays an important role by enhancing the wake diffusion and the entrainment of kinetic energy (Figure 1-1). This second aspect is of particular interest because the wake stability properties are directly dependent on the turbine design and operation and as such can be controlled. Anticipating the mixing process and the recovery of the momentum losses by inducing earlier an instability can ultimately have a positive effect on the cost of energy by allowing a smaller spacing between turbines.

1.4 Wake Models

Wind-farm simulations are very demanding, not just due to their large size but also because the wake flow interacting with a turbine in a cluster is wind-direction dependant and differs for each turbine. This implies that for evaluating the performance of a wind farm for one given layout, all the wakes in the farm need to be simulated at very many different wind directions. As such, the performance of wind energy aerodynamic models is inextricably connected to their computational demand (Schepers, 2012).

The ultimate challenge in computer modelling of wind farm aerodynamics is to combine good physical accuracy of the model and an affordable computational cost, which is necessary for the implementation of the models in an industrial environment (Pierella et al, 2014).

Some of the most basic fluid-dynamics mechanisms governing the physics of a wind-turbine wake are not yet fully understood and often semi-empirical engineering methods have been developed. The use of the latter ones is currently well-established in common industrial applications, with all the disadvantages and uncertainties that their limited applicability brings along. Most of the codes used today continue to rely on assumptions and parameters, which still need to be calibrated against experimental data or fine-tuned according to the case (Ainslie, 1988, Crespo et al, 1988, Jensen, 1983, Schepers, 2012).

Barthelmie et al (2010) and Schepers (2012) state that the majority of the used approaches in the numerical simulation of a wind-turbine wake intrinsically misestimates the effects of flow turbulence, especially when based on eddy-viscosity turbulence models combined with the above-mentioned actuator disc assumption. The latter neglects the presence of the blade flow and of the tip-vortex development and breakdown. Consequently, the mixing process across the wake and ultimately the rate at which the wake recovers flow momentum is incorrectly modelled. This leads to a consequent not-optimum wind farm design and wrong energy yield prediction, which in turn has a repercussion on the cost of energy.

Nowadays, several models are available for simulating the wake flow in a wind farm. Each model is defined by different methods for representing the rotor and methods for simulating the flow. The former are strategies for modelling the induction of the rotor on the flow: with an increasing level of approximation, the range of possibilities spans from the unsteady three-dimensional modelling of the rotating blades to a static distribution of forces on a circular area, the so-called *actuator disc* model. The latter are approaches for solving different kind approximations of the flow equations, from simple algebraic engineering models to more advanced computational fluid dynamics (CFD) methods.

Section 1.4.1 and 1.4.2 include a partial review of the main wake models currently in use.

1.4.1 Flow Modelling

Numerical models used for wake simulation can be divided in algebraic, Computational Fluid dynamics (CFD) and hybrid models.

Most of the algebraic wake models use only the momentum equation to represent the evolution of the velocity deficit of the wake behind a turbine. Normally, the initial wake-expansion region is not considered, assuming a fully expanded wake at the rotor location and simulating only the viscous wake expansion. They also do not cover the change in turbulence intensity in the wake behind a turbine, so they have to be coupled with a turbulence model if values of the turbulence intensity in the wake and throughout the wind farm are desired. Some examples of these methods are the Larsen (Larsen et al, 1996), Frandsen (Frandsen et al, 2006) and Jensen (Jensen, 1983) models. The latter is implemented in some of the most used software, such as WAsP (Wind Atlas Analysis and Application Program), the Garrad Hassan's WindFarmer and in the first versions of WindPRO by the Danish company EMD.

CFD models calculate the complete flow field through a wind farm solving the Navier-Stokes equations. Depending on the turbulence treatment, several families of CFD models can be distinguished. The most diffused and used in wind energy applications are the steady RANS and LES models. Steady RANS codes solve the Reynolds-Average Navier-Stokes equations with a turbulence model for closure. The advantages of the model are a generally affordable computation cost and a relatively good representation of the flow physics. However, only the average quantities are directly calculated, losing any information on possible flow instability, wind gusts affects, etc. All flow fluctuations are represented through a turbulence model as the k-ε and the k-ω models. These are part of the linear eddy-viscosity turbulence models, in which the Reynolds stresses, as obtained from a Reynolds averaging of the Navier-Stokes equations, are modelled by a linear constitutive relationship with the mean flow straining field. As it will be discussed in Chapter 5, this methods fail to model correctly the turbulence generation in the proximity of the rotor, generating errors that can be propagated in the rest of the wake. In Large Eddy Simulation (LES) the large unsteady flow structures are directly solved, while the smaller scale fluctuations are accounted for by means of sub-grid-scale models. This is based on the implication of Kolmogorov's theory of self-similarity, that the large eddies of the flow are dependent on the geometry while the smaller scales more universal. LES methods have been receiving more attention in the wind energy wake community because of their ability to reproduce unsteady and anisotropic turbulent flows, characterised by large-scale structures and turbulent mixing, even though its computational cost is considerably higher than RANS (Sanderse et al, 2011).

Similarly to classical CFD, hybrid models solve the Navier-Stokes Equations, but adopt strong simplifications in order to reduce the number of equations to be solved simultaneously. Several of these models are based on the approach used by J.F. Ainslie [14] and referred to as the Ainslie model. The latter assumes axial symmetry in the wakes and solves the time-averaged Navier-Stokes equations for incompressible flow with an eddy-viscosity closure. A second simplifications of the model is to neglect streamwise pressure gradients in the wake. This assumption is not valid in the very near wake, just behind the rotor, and the model cannot be used in that region. For this reason the model has to be initialized after the near wake with an empirical wake profile. Since the Ainslie model leads to fewer equations to be solved, the simulation of the flow field is less time consuming. The method is implemented in commercial software such as WindPro, GH WindFarmer, The Farm Layout Program (FLaP).

A second example of a successful hybrid model is WakeFarm, developed by the Energy research Centre of the Netherlands (ECN), which is based on a modification of the UPMWAKE wake model by Universidad Polytecnica de Madrid. The latter is a three-dimensional parabolised Navier-Stokes code for the far wake coupled with a k-ε turbulence model. The parabolisation of the equations implies that the flow properties are determined only by the state of the upstream flow, while all influences from a downstream locations on an upstream location are neglected. In this way, the

Navier-Stokes equations can be solved with a fast space-marching scheme, considerably reducing the calculation time. However, the parabolisation is only justified in the far wake, where streamwise pressure gradients are low or null and the feedback flow influence can be neglected. For this reason, the near wake should be modelled in a separate way. In the later version of Wakefarm, this is achieved by prescribing the pressure gradient in the near wake. In order to calculate the pressure gradient a free vortex wake model is used.

1.4.2 Rotor Modelling

The rotor of a horizontal axis wind turbine can be modelled with a number of methods, which are characterised by different levels of fidelity to reality. The large majority of wake simulations are based on the actuator disc assumption, where the rotor is modelled as a discontinuous surface on which body forces act upon the surrounding flow, behaving as an infinite number of blades creating the needed pressure drop. The actuator disc constitutes the main assumption in the one-dimensional momentum theory formulated by Froude (1889) and in the classical BEM method by Glauert (1935). For horizontal axis wind turbines, the actuator disc is a permeable surface normal to the freestream wind direction, on which a constant or varying distribution of blade forces acts upon the flow. The advantage of using the actuator disc technique is that it is not necessary to resolve blade boundary layers. The disadvantage is that the method is a very simplified representation of the reality and the wake rotation and tip-vortices are not reproduced. In some cases, azimuthal induction is added to the actuator disc, allowing for the wake rotation representation.

In the actuator line method, the blades are represented by a line on which body forces representing the loading on each blade are introduced. Normally, the local body forces are computed by evaluating the local angles of attack and using tabulated aerofoil coefficients. Although the blade boundary layer is still not resolved, the actuator line method is one step more accurate than the actuator disc in the representation of the real wake flow. As a matter of fact, the method is fully unsteady and wake rotation as well as tip-vortices are always represented.

The rotor geometry can also be fully modelled with no assumption and simplification. This approach is extremely computational expensive and as such it is not viable for most of the industrial applications.

1.5 Objective, Research Questions And Approach

This research aims is to study **what are the key factors that influence the re-energising of the wake behind a wind turbine rotor.** The study shows and quantifies the influence of the near-wake phenomena, as the tip-vortex instability, on the far-wake development and re-energising process, which is one of the open questions in wind energy research. It analyses to what extent the actuator disc assumption is valid for the representation of the near-wake dynamics and investigates what is the level of accuracy of the state-of-the-art numerical models in reproducing the near wake features highlighted in the experiments. A database of measurements of wind-turbine and actuator-disc wakes is offered, to be used as validation (as well as source of inspiration for improvements) of wake models and CFD codes.

The work follows a *back to basics* approach, with two experimental campaigns where the wake of a horizontal axis wind turbine and a porous disc (physical emulation of the actuator disc numerical model) is studied with high-resolution stereo particle image velocimetry measurement in controlled conditions. The wake measurements are then used for validating a series of state-of-the-art numerical models, with a benchmark workshop involving researcher from several academic and industrial organisations. In particular, the following research questions (RQ) will be addressed:

1. **How does the tip-vortex instability influence the wake flow and its re-energising process?**
   - 1.1. What is the effect on the mean velocity field in the wake?
   - 1.2. What is the effect on the flow turbulence and on the wake re-energising process?
2. **What are the key turbulence phenomena in the wake of a wind turbine rotor?**
   - 2.1. What is the amount of kinetic energy transported and dissipated by the most relevant flow structures?
   - 2.2. What is the role of the tip-vortices, their instability and their breakdown in the turbulent mixing process?
3. **What are the main differences between the near wake of a wind turbine and an actuator disc?**
   - 3.1. What are the key differences in the wind turbine and actuator disc near wake and how do they affect the transport of mean-flow kinetic-energy?
   - 3.2. To what extent is the actuator disc assumption valid for the representation of the near wake?
4. **What is the level of accuracy of the state-of-the-art numerical models in reproducing the near wake features highlighted in the experiments?**

The research questions will be answered in a series of experimental and numerical analyses. The stereo particle image velocimetry (SPIV) is adopted for observing the near- and far-wake flow of a wind turbine model in the presence of the tip-vortex pairing instability (leapfrogging). The study includes the analysis of two load cases and it's aimed at exploring the macroscopic effects of the tip-vortex instability on the wake re-energising process (RQ1.1 and RQ1.2). The triple decomposition of the wake flow is then applied for quantifying two components of the mean-flow kinetic-energy transport equation (turbulence production and kinetic energy entrainment), distinguishing between the role of the periodic flow structures and the random turbulent fluctuations (RQ 2.1). After quantifying the role of the tip-vortex instability and breakdown in the process of wake re-energising (RQ2.2) and showing how the organised vortical motions in the near wake contribute to the wake mixing, the analysis will tackle the problem of the actuator disc approximation, which disregards the above-mentioned aspects. In a second experimental campaign, the wake of an actuator disc and a wind turbine are compared. The differences between the two wakes (velocity deficit, turbulence levels, mean-flow kinetic-energy transport, etc.) are quantified. The application of the proper orthogonal decomposition (POD) with a triple decomposition of the flow and the analysis of different components of the mean-flow kinetic-energy transport equation in the two wakes will help quantifying in details the different physics governing the mixing (RQ3.1 and RQ3.2). As last, a benchmark comparison between the experiments and numerical simulations from a series of state-of-the-art models is performed. Four LES codes from different institutions and a vortex model are part of the comparison. The purpose of this benchmark is to validate the numerical predictions of the flow field in the near wake of an actuator disc and a wind turbine (RQ3.2 and RQ 4).

1.6 THESIS OUTLINE

This dissertation reports the results of a project completed between 2011 and 2015 at the Faculty of Aerospace Engineering at the Delft University of Technology. The thesis is a collection of five publications, thus every chapter provides all the information, which is necessary for guaranteeing a full understanding, independently of the other chapters. The text and the nomenclature in each chapter is sometimes slightly modified, with respect to the published version, for sake of consistency in the thesis.

The thesis is divided in two parts. The first part addresses RQ1 and RQ2. It contains two chapters in which the turbulent mixing in a single wind turbine wake is studied. The second part addresses RQ3 and RQ4 and collects three chapters about the experimental and numerical comparison between the wake of a wind turbine and the one of an actuator disc.

Chapter 2 is focussed on the analysis of the wake of a small scale horizontal axis wind turbine in an open-jet wind tunnel. The aim is to observe all relevant flow phenomena involved in the complex dynamics of the near and transition wake and to understand their (macroscopic) relationship with the wake re-energising process. With this analysis, RQ1.1 and RQ1.2 will be addressed.

Chapter 3 is aimed at quantifying what is the amount of kinetic energy transported and the one dissipated by the different flow structures. The study will explain what is the level of turbulent mixing in the near wake and what is the role of the tip-vortices in the mean-flow kinetic-energy transport in the wake shear layer. With this analysis, RQ 2.1 and RQ2.2 will be addressed.

In **Chapter 4** it is analysed how the differences in the wind turbine and actuator disc near wake affect the physics of the wake flow and to what extend the actuator disc assumption is valid for the representation of the near wake dynamics (RQ3.1 and RQ3.2).

In **Chapter 5**, the application of the proper orthogonal decomposition (POD) with a triple decomposition and the analysis of different components of the mean-flow kinetic-energy transport equation in the two wakes will help quantifying in details the very different physics governing the mixing (RQ3.1 and RQ3.2).

As last, **Chapter 6** will explore what is the level of accuracy of some state-of-the-art numerical models in reproducing the near wake features highlighted in the experiments (RQ3.2 and RQ 4).

Figure 1-2 shows of a schematic of the thesis structure, highlighting what research questions are addressed in each publication.

Part 1

Turbulent mixing in a wind turbine wake

RQ 1

How does the tip-vortex instability influence the wake flow and its re-energising?

- What is the effect on the mean velocity field in the wake?
- What is the effect on the flow turbulence and on the wake re-energising?

RQ 2

What are the key turbulence phenomena in the wake of a wind turbine rotor?

- What is the amount of kinetic energy transported and the one dissipated by the most relevant flow structures?
- What is the role of the tip-vortices, their instability and their breakdown in the turbulent mixing process?

Chapter 2

Experimental analysis of the wake of a horizontal-axis wind-turbine model

Chapter 3

Tip vortex instability and turbulent mixing in wind turbine wakes

Part 2

Wind turbine and actuator disc wakes

RQ 3

What are the main differences between the near wake of a wind turbine and an actuator disc?

- 3.1.What are the key differences in the wind turbine and actuator disc near wake and how do they affect the transport of mean flow kinetic energy?

- To what extent is the actuator disc assumption valid for the representation of the near wake?

RQ 4

What is the level of accuracy of the state-of-the-art numerical models in reproducing the near wake features highlighted in the experiments?

Chapter 4

Experimental comparison of a wind turbine and of an actuator disc wake

Chapter 5

Turbulence production and kinetic energy transport in the wake of a wind turbine and of an actuator disc

Chapter 6

Validation of four LES and a vortex model against stereo-PIV measurements in the near wake of an actuator disc and a wind turbine

Figure 1-2. Graphic outline of the PhD thesis.

2 EXPERIMENTAL ANALYSIS OF THE WAKE OF A HORIZONTAL-AXIS WIND-TURBINE MODEL

The vortical structures of the wake of a horizontal-axis wind-turbine model are investigated in the Open Jet Facility wind-tunnel of the Delft University of Technology. Experiments are conducted with a wind turbine model with a diameter of 60 cm at a diameter-based Reynolds number range Re_D = 150,000 ÷ 230,000. The velocity fields in meridian planes encompassing a large portion of the wake past the rotor are measured both in the unconditioned and the phase-locked mode by means of stereoscopic particle image velocimetry, allowing for a statistical analysis of the mixing process of the wake. The evolution of the wake is measured up to five diameters downstream of the model. The streamwise development of the wake velocity, pressure and total enthalpy of the flow is determined. Results show that the wake instability, caused by the pairwise interaction of the tip vortices, has a strong impact on the momentum deficit recovery of the wake, by enhancement of the mixing process downstream of the tip-vortex helix instability, where the contribution of the random fluctuations becomes predominant over the one of the periodic vortical structures.

This chapter is published as:

Lignarolo, L.E.M., Ragni, D., Krishnaswami, C., Chen, Q., Simão Ferreira, C.J., van Bussel, G.J.W., 2014. Experimental analysis of the wake of a horizontal-axis wind-turbine model. *Renewable Energy* 70, 31-46.

2.1 INTRODUCTION

The wake of a horizontal axis wind-turbine (HAWT) is a region of three-dimensional turbulent flow characterised by a deficit of kinetic energy, higher turbulence and a complex vortical helical structure. When considering wind-farm applications, where multiple wakes are produced by clusters of turbine rotors, the accurate prediction of the wake characteristics such as the length of the re-energising region still is unfeasible. The large inaccuracies encountered in the numerical prediction of the kinetic energy recovery (wake re-energising) are typically associated with a poor modelling of the wake turbulence (see Barthelmie et al, 2007a). As shown by Schepers (2012), the actuator disc model in combination with the k-ε turbulence model produce a strong region of high turbulence close to the blade, quickly decaying in proximity of the turbine model. The presence of this region is primarily artificial and in disagreement with in-field experimental observations Medici (2005), showing that a consistent turbulent mixing persists up to the turbine far wake. The effect of the incorrect representation of the wake re-energising mechanisms is confirmed by the large dispersion of current CFD results in the prediction of wind-farm power by different turbulence models, as in Stevens et al (2013).

Cal et al (2010) and Hamilton et al (2012) showed how in large wind farms, the wake energy recovers via entrainment of kinetic energy from the flow surrounding the farm. The kinetic energy entrainment occurs at two different scales: the atmospheric turbulent flow level and the wake-induced flow level. The second one is of particular interest because it concerns the mixing process owing to the presence of the tip vortex helix, its instability and its breakdown, which are directly dependent on the turbine design and operation and on the interaction among multiple turbines and wakes. This is even more relevant for offshore wind farms, where atmospheric turbulence is lower than in onshore environments0.

Few studies focus on the self-induced mixing of the wake. Felli et al (2011), Ivanell et al (2010) and Sørensen (2011) showed the influence of different parameters (such as tip-speed ratio, inflow turbulence, tip-vortex core size) on the stability properties of the wake. Medici (2005), in contradiction with previous statements of Hütter (1977), hypothesized that the near wake tip-vortices inhibit the wake mixing and the outer air entrainment; however, this hypothesis is presented without a clear quantification of the effect of the vortices and their break-down on the mixing process. Hamilton et al (2012) demonstrates the importance of the vertical transport of kinetic energy to replenish the wake, analysing the mixing process due to the large scale atmospheric turbulence and its effect on the smaller scale flow structures within a wind farm. Sforza et al (1981) and Vermeulen (1979) experimentally studied the dynamics of the turbulent mixing in the wake of perforated discs as simulation of an actuator disk.

In this chapter, the results of an analysis of the vortical structures in the wake of a HAWT with high-resolution stereoscopic particle image velocimetry (SPIV) are reported. The analysis is performed for exploring the influence of the tip-vortex helix development on the wake re-energising process in the near and far wake of the turbine. The wake velocity field is mapped up to 5 diameters downstream. The different measurements are acquired with both phase-locked and unconditioned sampling techniques, respectively by triggering the acquisition system in phase with the rotor and randomly. The complete statistical representation of the phase-locked average and the unconditioned average flow allows for a first qualitative distinction of the random flow fluctuations in the phase-locked average field and the total flow fluctuations (compound effect of the random and periodic fluctuations) in the time average flow field. This study will be further developed in Chapter 3. A series of measurements with a six-component balance is performed for obtaining the thrust coefficient curve of the wind turbine model. The experiment is conducted in the presence of the an artificially generated instability of the tip-vortex helical structure, which causes the tip vortices to pair and roll around each other to form a single vortex structure. The instability is triggered by a an asymmetry in the blade pitch angle, as described in Section 2.2.1.

In Section 2.2, detailed information about the wind tunnel characteristics, the experimental set-up and wind turbine model is given. In Section 2.3 the results are presented and discussed. The last section contains the conclusions.

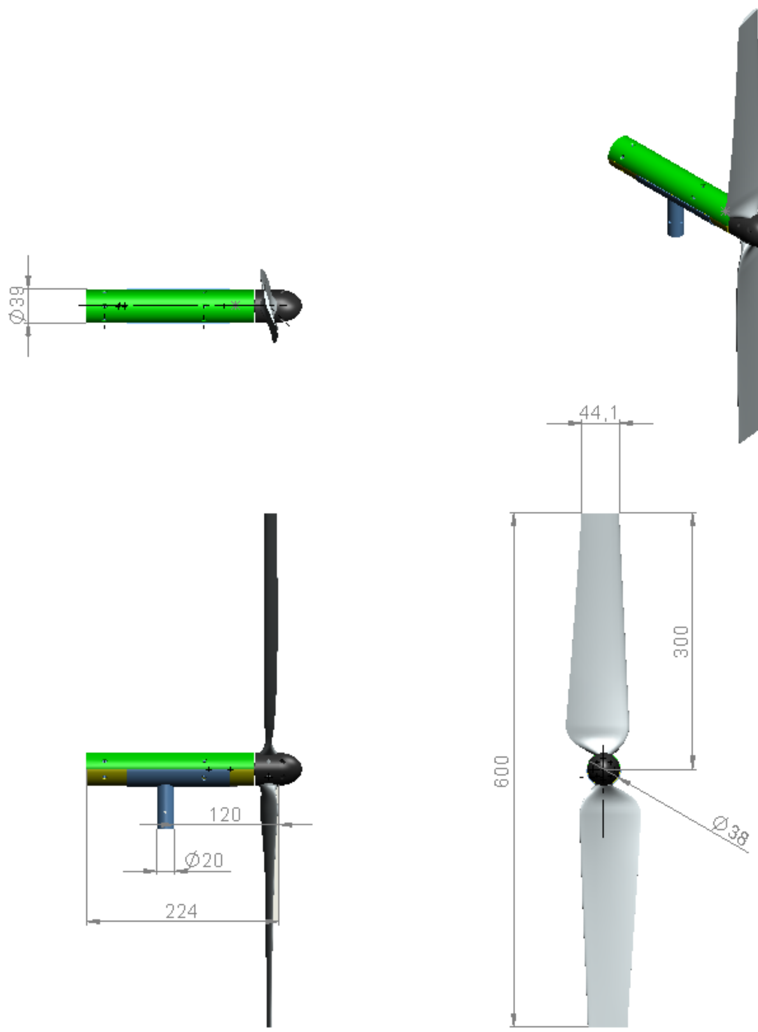

Figure 2-1. Wind turbine model. Dimensions are in millimetres

2.2 EXPERIMENTAL SET-UP

2.2.1 WIND-TUNNEL AND TURBINE MODEL

Experiments have been conducted in the Open-Jet Facility at the Aerospace Engineering Department of TU Delft. The wind tunnel has an octagonal test section with an equivalent diameter of 3 m and a contraction ratio of 3:1, delivering a uniform stream with approximately 0.5% turbulent intensity at 1 m from the jet exit and lower than 2% at 6 m from it. The uniform-flow region also reduces at 6 m from the jet exit from 3×3 m^2 to 2×2 m^2. A detailed characterization of the wind-tunnel flow can be found in Section 2.2.5. The wind tunnel is driven by a fan with an electrical engine of 500 kW and the temperature is kept constant by a heat exchanger which provides up to 350 kW of cooling power.

A two-bladed horizontal-axis wind turbine with a diameter D = 0.6 m has been designed for optimal conditions with a tip-speed ratio $\lambda = \upsilon R/U_\infty = 6$, where R is the rotor radius and υ the rotational speed (Figure 2-1). The induction factor is defined as:

$$a = 1 - \frac{U_r}{U_\infty} = \frac{1}{3} \tag{2-1}$$

where U_r is the wind speed at the rotor and U_∞ is the free-stream wind speed. For optimal conditions, the induction factor is a = 1/3. The blades are designed with a Blade Element Momentum (BEM) code based on the method proposed by Burton et al (2001). The induction factor and the tip-speed ratio are the main design parameters, while the BEM code calculates the chord and twist angle distribution. A root and tip correction is applied according to the method of Prandtl (Betz, 1919). The rotor blade is developed from an Eppler E387 airfoil with 9.06% thickness (Selig et al, 1995) with a twist distribution from 4.4° at the tip to 19.4° at the root (see Figure 2-2). The maximum blade chord is 0.074 m at r/R = 0.18 (with r being the radial coordinate). C_L-α curves of airfoil E387 are presented in Figure 2-3. The analysis is repeated for two different tip-speed ratios, namely λ = 6 and λ = 4.8, respectively, with free-stream velocities of U_∞ = 5.7 m/s and 3.8 m/s and rotational speeds of υ = 113.1 rad/s and 60.8 rad/s. The former value is the design tip-speed ratio and represents the optimum working condition of the machine. As shown in Figure 2-5, the turbine was installed at 1.17 rotor diameters (0.7 m) from the tunnel exit. The blockage ratio is small (A_{tunnel} / A_{rotor} = 4%) and no correction is needed, as suggested by Chen and Liou (2011) and Schreck et al (2007). According to Eitelberg (2016), the error on the measured thrust coefficient is between 2% and 4% for the present operating conditions. For both tip-speed ratios, wind speed and rotational speed are chosen in order to fulfil several requirements, such as avoiding tower vibration due to a possible resonances with the vortex shedding and with the blade rotation and achieving a high Reynolds number. As shown in Widnall (1972) and Felli et al (2011), the tip-speed ratio will modify the pitch of the tip-vortex helical filament, with higher λ values moving the tip-vortex pairing instability location upstream. There were three main drivers for the blade design: the first was constant circulation along the blade span at the design tip-speed ratio in order to have most of the vorticity trailing only at the tip and at the root, with no trailing vorticity at other blade locations. The second was to achieve attached-flow conditions over the entire span, which led to low angles of attack and low lift coefficients, and therefore to a large average chord. The third requirement was to achieve a relatively large Reynolds number, in turn leading to a large chord and high rotational speed. At the experimental conditions, the maximum chord-based Reynolds number achieved is $Re_c = 100\,000$ at the blade tip, as indicated in Table 2-1. In calculating the latter, the relative velocity of the wind on the blades has been used as reference. The blades have been manufactured in aluminium by CNC machinery. The blades are installed to the nacelle hub with a pitch-angle difference of 0.5°, which acts as a constant trigger for the wake instability, similarly to the studies of Bolnot et al (2014) and Odemark and Fransson (2013). The values of the thrust coefficients C_t for the two experimental conditions shown in Table 2-1 have been calculated with an external 6-components balance. The device is provided with six Wheatstone bridges which are able to measure three components of force, in the axial, spanwise and vertical directions, and three components of moments, for roll, pitch and yaw. For the present thrust measurements, only the axial force component is relevant and has been reported in Section 2.2.2. The nacelle is designed to reduce to minimum its impact on the flow while housing a DC brushless motor, a gearbox, a Hall encoder and an optical trigger (opto-coupler TCST 2103) which provides a one pulse per revolution signal allowing the PIV synchronization; the nacelle has a diameter of 0.038 m (6.3% of the rotor diameter). The DC brushless motor has a nominal voltage of 12V and a maximum power of 125W. It is a four-quadrant motor, able to act as a drive or a brake depending on the loading. In operation, the motor provides a torque to the hub which is equal and opposite to that exerted by the wind on the blades, thus maintaining a constant rotational speed. The extra energy is then dissipated by a large resistor at the base of the tower.

Table 2-1. Test conditions for the two investigated tip-speed ratios.

Parameters		***Units SI***	$\lambda = 4.8$	$\lambda = 6$
Free-stream velocity	U_∞	[m/s]	3.8	5.7
Rotational speed	υ	[rad/s]	60.8	113.1
Reynolds, blade root, $r/R = 0.20$	Re_{cr}	-	20,000	30,000
Reynolds, blade tip, $r/R = 1$	Re_{ct}	-	60,000	100,000
Reynolds (diameter based)	Re_D	-	150,000	230,000
Thrust coefficient	C_t	-	0.82	0.89
Induction factor	a	-	0.29	0.33
Tip speed ratio	λ	-	4.8	6
Turbine diameter	D	m	0.6	0.6

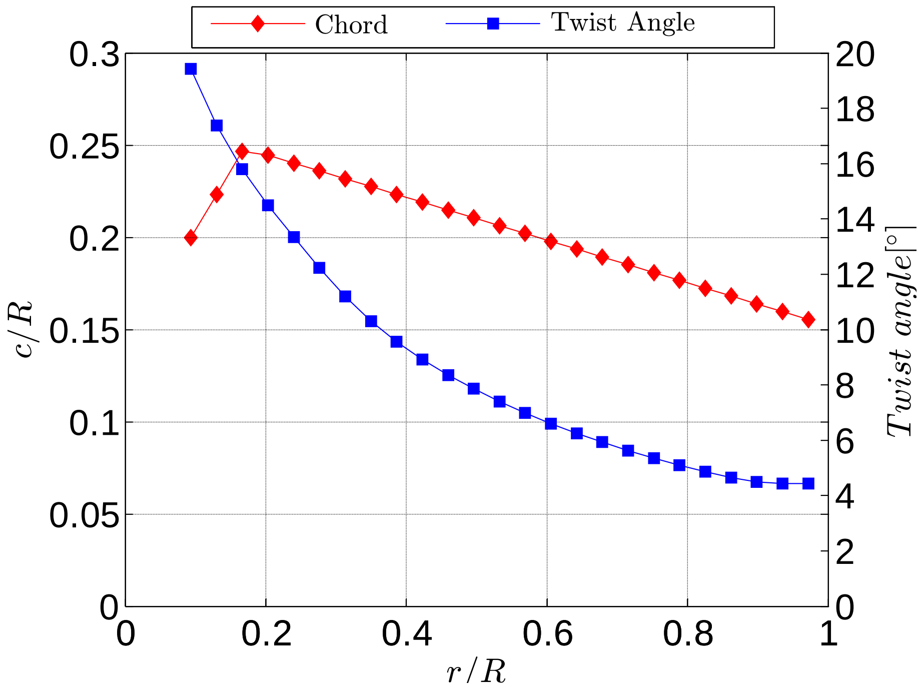

Figure 2-2. Chord-radius ratio and twist-angle distribution of the wind-turbine model blades.

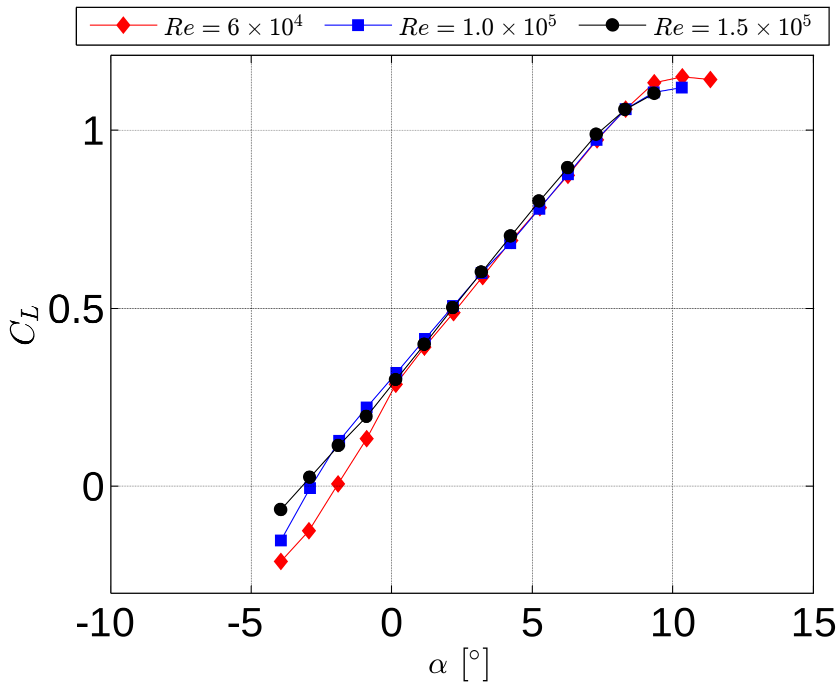

Figure 2-3. $C_{l\text{-}\alpha}$ curves of airfoil E387 from Re = 0.6 to Re = 1.5×10^5.

2.2.2 Thrust Force Measurements

The thrust curve of the wind turbine is obtained by measuring the thrust coefficient for different tip-speed ratios, placing the turbine on an external 6-components balance. The balance is 0.522 × 0.595 m^2 structure onto which the entire wind turbine tower can easily be mounted. The device is provided with six load cells (or Wheatstone bridges) which are able to measure three components of force, in the axial (F_x), radial (F_y) and vertical (F_z) directions, and three components of moment, in the rolling (M_x), pitching (M_y) and yawing (M_z) directions as indicated in Figure 2-4. For the present thrust measurements, only the axial force component has been recorded. The accuracy of the balance is ±0.23% of the measured load. To measure the thrust at different tip-speed ratios, the wind-tunnel speed and the turbine rotational frequency have been varied. The range of measured tip-speed ratios spans from $\lambda = 2$ to $\lambda = 8$. In order to correct the data for tower and nacelle effects, the axial force acting on the tower and the dummy clean nacelle with no blade has been recorded for the same range of wind speed and then subtracted from the results of the full turbine measurements. The C_t-λ characteristic of the turbine is shown in Section 3.1. The thrust coefficient is calculated with the formula

$$C_t = \frac{T}{0.5\rho A U_\infty^2} \tag{2-2}$$

where T is the thrust force applied by the wind on the turbine, ρ is the air density and A is the rotor.

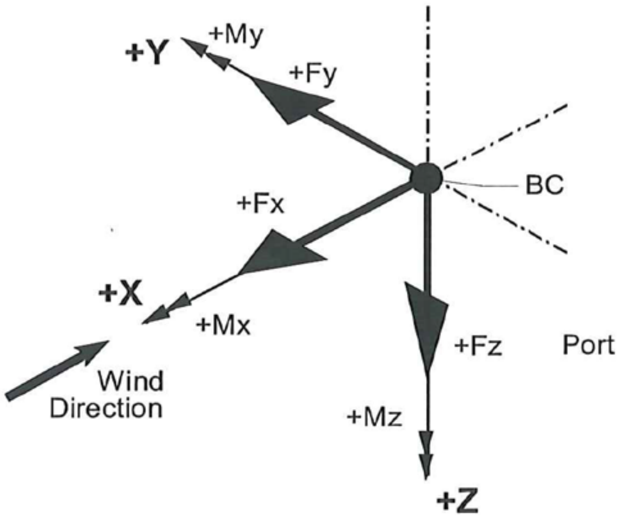

Figure 2-4. Reference system for the balance measurements. BC indicates the centre of the balance.

2.2.3 STEREOSCOPIC PIV EQUIPMENT

Stereoscopic PIV experiments are conducted, mapping the three-component velocity fields in the rotor wake; results are obtained via an average of the vector fields, as detailed in Table 2-2. A stereoscopic PIV setup has been installed on a traversing system able to scan the flow field in the wake of the horizontal-axis wind-turbine wake, as shown in Figure 2-5. Similar measurement setups have already proved to be suitable to obtain both the load distribution on the blade (Ragni et al, 2011) and the evolution of vorticity in the wake of a wind turbine (Akay et al, 2012). The required illumination is provided by a Quantel Evergreen Nd:YAG laser system with an average output of 200 mJ/pulse. The laser light is conveyed to form a 2 mm laser sheet of approximately 0.4 m width at the field of view. Two LaVision Imager Pro LX 16 Mpix (4870 × 3246 px, 12 bits) with pixel pitch of 7.4 μm/px are used to acquire images with a field of view of 0.357 × 0.253 m^2

(0.56D × 0.42D) with an overlap between two adjacent FOVs of 0.05 m in the axial and radial direction (darker shade between the FOV in Figure 2-5), obtained with two Nikon lenses of f = 180 mm and an aperture $f\#$ = 2.8 - 4, at a magnification factor M = 0.10. The focusing plane has been slightly offset with respect to the laser plane (defocusing), to obtain an image of the particle of approximately 2-3 px. Therefore no bias error arising from the peak-locking effect has been observed (Westerweel, 1997). Seeding was provided in the test section by a SAFEX smoke generator with SAFEX MIX, able to produce liquid droplets of less than 1 μm. The entire setup was mounted on a traversing system able to translate over a two-dimensional area of approximately 1.2 m × 0.9 m. An ensemble of 400 (phase-locked sampling), 720 (unconditioned sampling) double-frame recordings have been acquired and processed by LaVision Davis 8.1.4. In order to evaluate the digital range of the measurement system, estimation of the smallest and largest coherent structures within the wake flow can be performed. The smallest coherent structures in the flow, which are supposed to have a lifetime long enough to contribute to the statistics are typically generated within the blade boundary-layer and have a length scale of 20 times the wall units λ^+ (Ghaemi and Scarano, 2011, Stanislas et al, 2008). The latter one is calculated as $\lambda^+ = \nu/u_\tau$, where the friction velocity is estimated with a viscous simulation using the boundary-layer theory applied to the blade geometry (White, 1991). To the purpose, the TUDelft modification of the software XFoil has been used (van Rooij, 1996). At a tip-speed ratio of 6, the trailing-edge friction velocity at the tip location is 0.24 m/s and the wall unit is 62 μm: this corresponds to a length scale for the smallest coherent structures of 1.24 mm. The large-scale motion in the rotor wake has the length scale of the blade chord, which has a maximum extent of 0.074 m. Therefore the ratio between the large-scale motions and the smallest coherent structures is W_{str} = 60, which must be satisfied by the resolution of the measurement system (Herpin et al, 2008). Interrogation windows of 24 × 24 px with 50% overlap yields a resolution element of 1.76 mm and a vector spacing of 0.88 mm. In this configuration the final spatial dynamic range (SDR) in the stream-wise direction is 101 (as detailed in Table 2-2) and the smallest resolvable spatial variation is considered to be twice the size of the interrogation window. This does not allow one to capture till the smallest scale at the tip location, but is considered sufficient for the downstream developments, especially in the leapfrogging regime. By taking into consideration the combination of different fields of view (see Figure 2-5) the SDR becomes 4.5 times larger.

Table 2-2. System parameters for the stereoscopic PIV measurements.

Parameters		***Stereoscopic PIV setup***	
Measurement field of view	*FOV*	357 × 253 mm^2	4870 × 3246 px
Magnification	*M*	0.10	
Digital imaging resolution	*DR*	13.64 px/mm	
Interrogation window size	I_w	1.76 × 1.76 mm^2	24 × 24 px
Vector spacing	*S*	0.88 mm	12 px
Vectors	*NV*	404 × 270	
Spatial dynamic range	*SDR*	101	

2.2.4 Velocity Fields Configuration

The measurements were performed on the wake of the wind turbine model up to 5 rotor diameters downstream, in multiple fields of view (FOV) at hub height. The positions of the fields of view are represented in Figure 2-5, where each squared window represents a field of view (FOV) in the radial plane. The darker shade between the windows shows the overlap between two adjacent FOV, which varies from 0.097 m to 0.147 m (0.16 to 0.25 diameters) in the axial direction. Two different configurations were employed at two inboard positions with an overlap of 0.102 m to 0.098 m respectively (0.17 to 0.16 diameters). Table 2-3 summarises the parameters of the two considered test cases with $\lambda = 4.8$ and $\lambda = 6$. The schematics in Figure 6 show the different position of cameras and laser of the different sets of measurements.

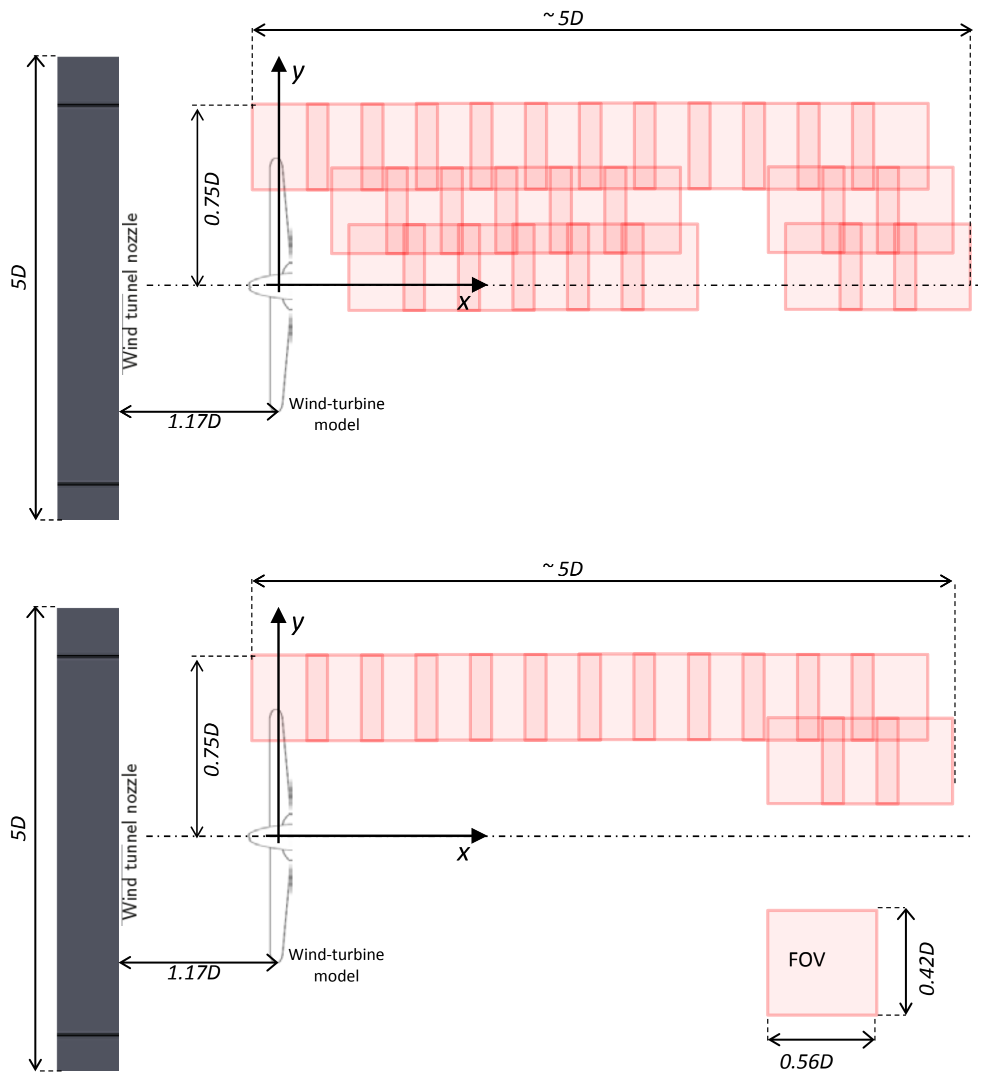

Figure 2-5. Schematics of the field of views employed for phase-locked analysis (upper image) and unconditioned sampling one (bottom image). The image is not in scale.

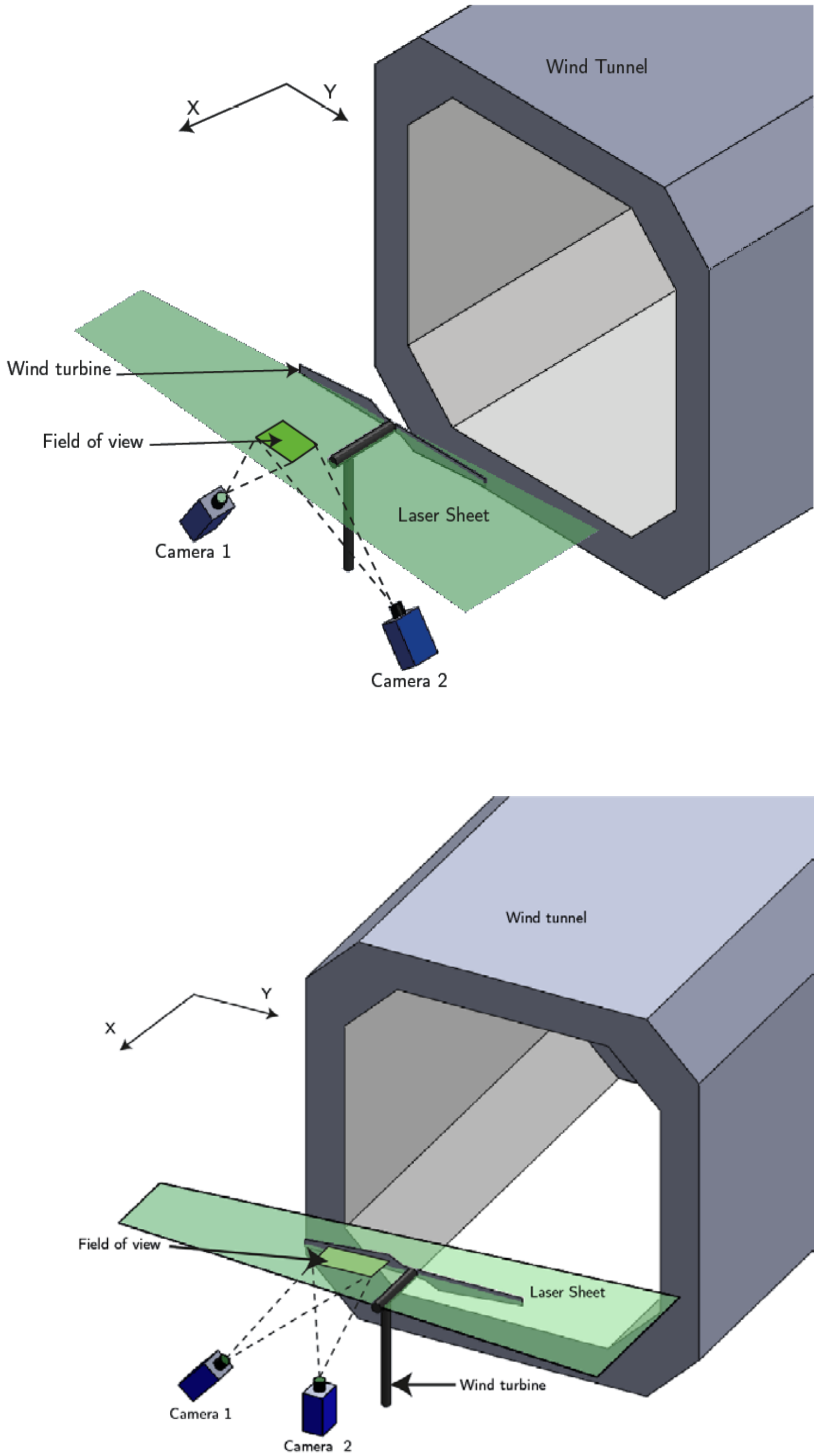

Figure 2-6. Schematic of the experimental set-up for wake measurements (top image) and measurements at rotor location (bottom image).

Table 2-3. Experimental operating conditions.

λ [-]	**Rotor rotational velocity [rad/s]**	**U_∞ [m/s]**	**C_t [-]**
4.8	60.8	3.8	0.82
6	113.1	5.7	0.89

2.2.5 Wind-Tunnel Flow Characterization

The flow quality of the empty OJF wind-tunnel is assessed prior to the acquisition of the wake measurements. A constant temperature hot-wire anemometer (HWA) and a static Pitot tube are employed to monitor the mean velocity and turbulence intensity along the jet, with as set wind speed $U_\infty = 6$ m/s. Results from the mean velocity profile in the radial direction at 1 m and 6 m from the tunnel nozzle (red squares in Figure 2-7) show relatively good uniform flow respectively within 1% and 3% at 1 m and 6 m from the jet. With a HWA sampling rate of 10 kHz and a sampling time of approximately 60 seconds the measured turbulence intensity is lower than 0.5% at 1 m from the nozzle and lower than 2% at 6 m from the nozzle. A second series of measurements with a sampling rate of 10 kHz and a sampling time of 10 seconds is used to calculate the shear layer thickness in the radial direction at 1.5, 2.1 and 3.6 m from the nozzle (black dots in Figure 2-7). Results show an angle aperture of 9.5° for the shear layer. The starting point of the shear layer is assumed at $u/U_\infty = 98\%$, giving a free-stream area reduction of 16.7 cm/m corresponding to a usable area (namely the area with uniform velocity $u = U_\infty$) of 2×2 m^2 at 6 m from the nozzle. Figure 2-8 (top image) and Figure 2-8 (bottom image) show the velocity and turbulence profile at three locations within the measurement region of the present experiments. A slight acceleration of the flow is still visible toward the inner region of the jet at $x/D = 2.5$. A last series of measurements is performed along the streamwise direction inside the jet shear layer (green triangles in Figure 2-7) with a sampling rate of 10 kHz and a sampling time of 10 seconds for checking the stability of the jet. Results from Fast Fourier Transform analysis of the velocity time series show highly energetic fluctuations at low frequency. The frequency of these oscillations is clearly dependent on the flow Reynolds number. At a velocity $U_\infty = 6$ m/s, the energy spectrum shows peaks at 1.1 ± 0.1 Hz and at 1.9 ± 0.1 Hz at 8 m/s in each streamwise location. The amplitude of the oscillations after 4 m downstream the wind tunnel nozzle is 1.6% of the mean velocity and becomes higher than 2.8% at after 6 m. The present experiments are performed within a region extending up to 3 m downstream the jet and, radially, up to 0.5 m from the jet centreline, zone with an assessed turbulence intensity of 0.5% and a flow inhomogeneity of less than 1% and free stream velocity fluctuations lower than 1.0%.

2.2.6 Reynolds Number Independency

Within the present measurement volume and available equipment the achievable Reynolds number based on the turbine diameter is of the order of ~ $10^4 \div 10^5$, two orders of magnitude lower than in full-scale operating conditions. Previous studies have demonstrated that the wake exhibits a low dependency on the Reynolds number. Whale et al (2000) compared experimental measurements in the wake of a small wind-turbine with a chord-based Reynolds number ranging from 6400 to 16000 with results from an inviscid vortex code. Results from the comparison show that the fundamental behaviour of the helical vortex wake is weakly sensitive to Reynolds number, being the numerical results fully comparable with the experimental ones. Further results from the Chamorro et al (2012) suggest that main flow statistics (mean velocity, turbulence intensity, kinematic shear stress and velocity skewness) become independent of Reynolds number from $Re = 9.3 \times 10^4$. In the present study the Reynolds number based on the rotor diameter ranges from $Re = 1.5 \times 10^5$ to 2.3×10^5 for $\lambda = 4.8$ and $\lambda = 6$ respectively, sufficiently higher than the critical value estimated by Chamorro et al (2012).

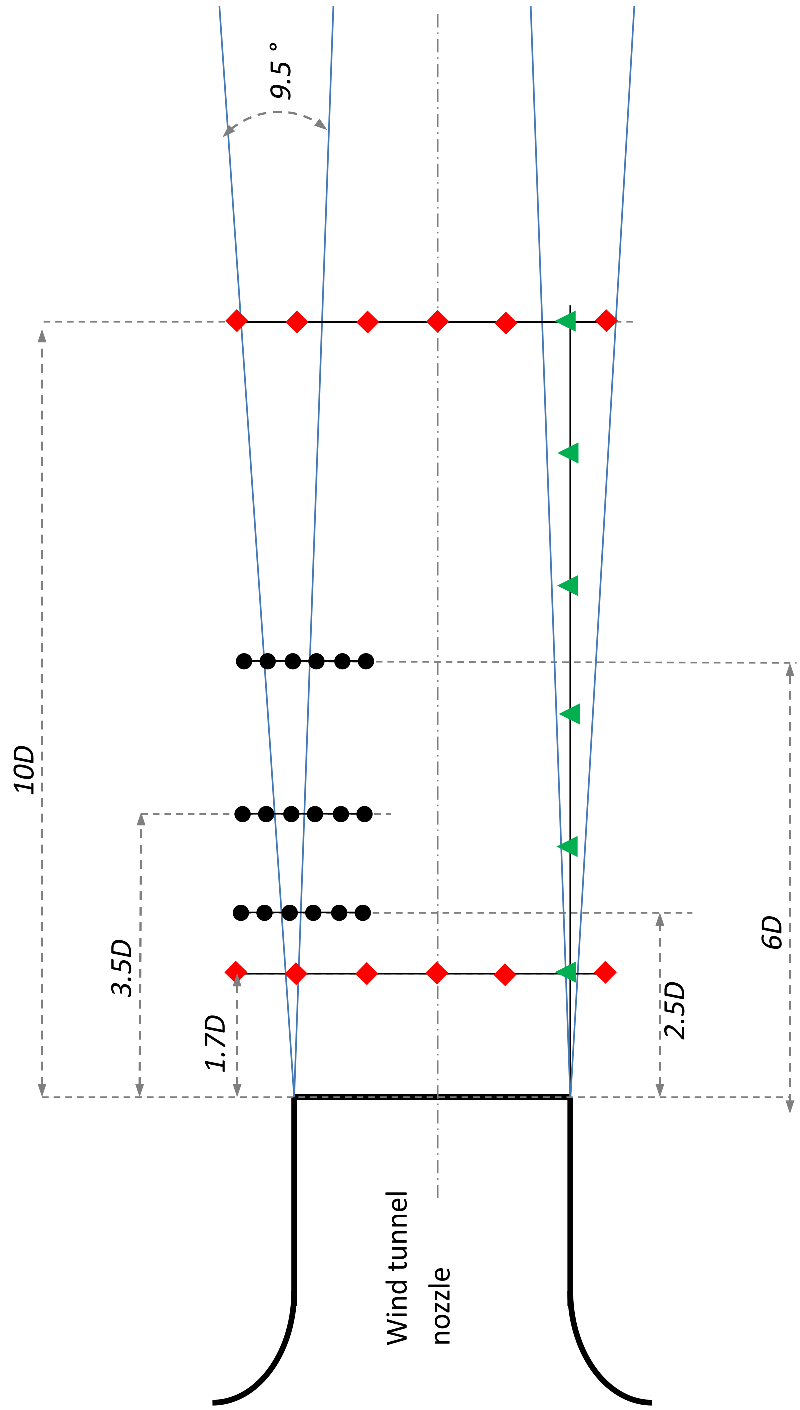

Figure 2-7. Wind tunnel jet schematics with measurement points (a).

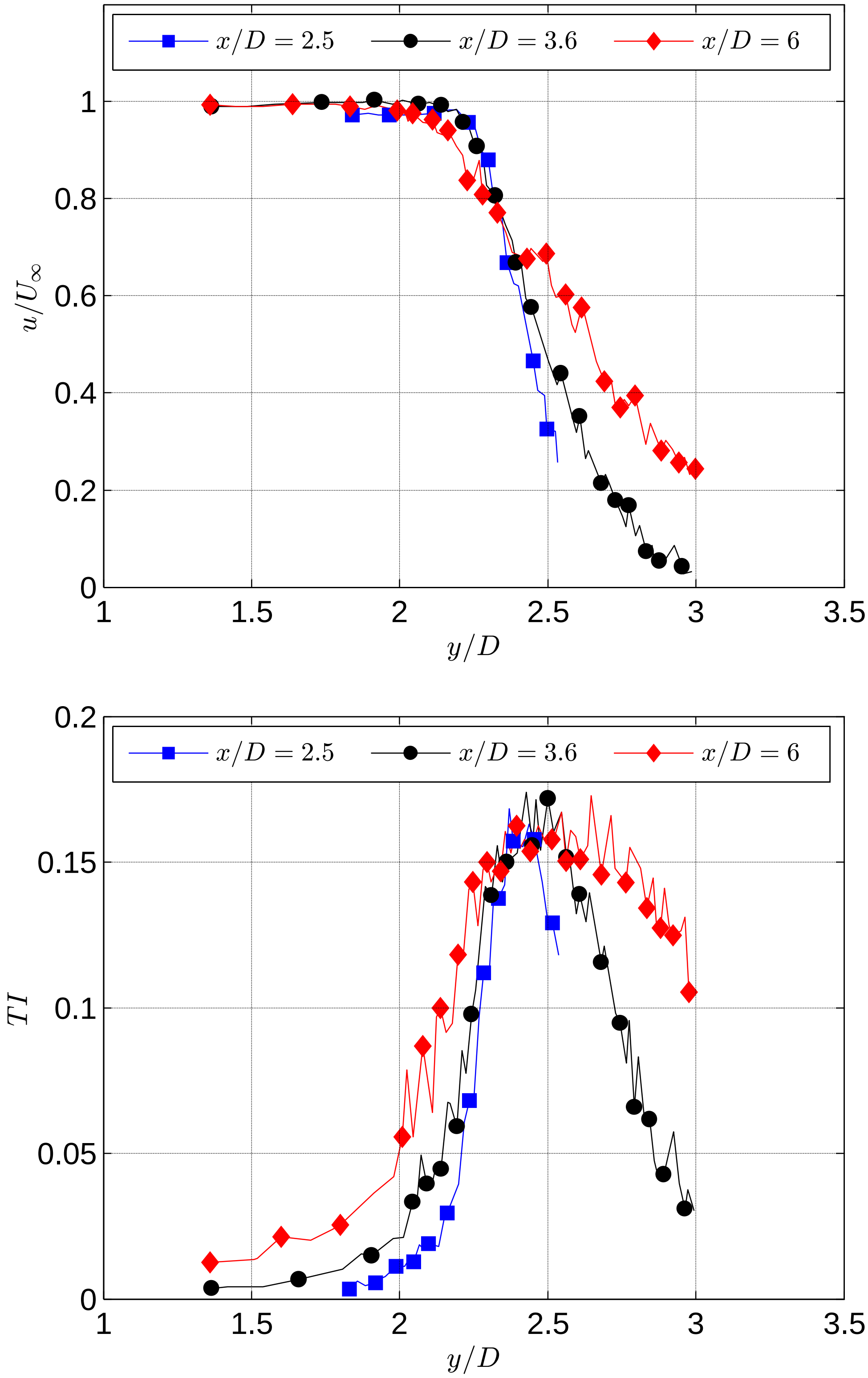

Figure 2-8. Velocity profiles (top image) and turbulence intensity profiles (bottom image) in the redial direction (black points in Figure 2-7) at three different streamwise locations.

2.3 Measurement results

2.3.1 Thrust Measurements

The results of the thrust measurement are reported in Figure 2-9, where blue dots indicate experimental data and the red dots the set conditions for the chosen case studies. For the design tip-speed ratio $\lambda = 6$ the thrust coefficient is $C_t = 0.89$ as predicted by momentum theory for the design induction factor $a = 1/3$.

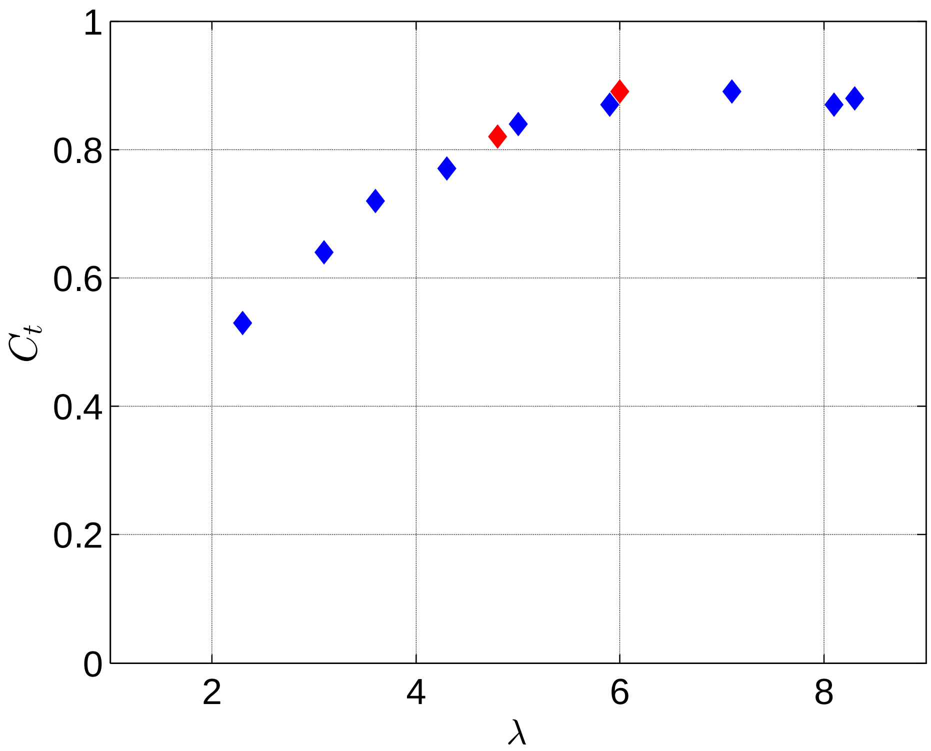

Figure 2-9. C_t-λ curve of the wind-turbine model.

2.3.2 Convergence Analysis

Study of the kinetic energy in the wake requires having a converged statistical dataset of the velocity components and their fluctuations. Hence, prior to start the acquisition, a convergence analysis is performed by acquiring a very large amount of images in a selected location in the wake and by testing the convergence of the statistics. Figure 2-10 and Figure 2-11 show the unconditioned average plot versus then number of samples acquired of the three mean velocity components and the Reynolds stresses tensor components. Approximately 400 acquisitions guarantee convergence of the phase-locked mean components, while 700 acquisitions are needed for the unconditioned averages. The values shown in the graphs are relative to a measurement point at $x/D = 2$ and $y/D = 0.5$ within the leapfrogging zone, where the flow fluctuations are very strong, for the $\lambda = 4.8$ case.

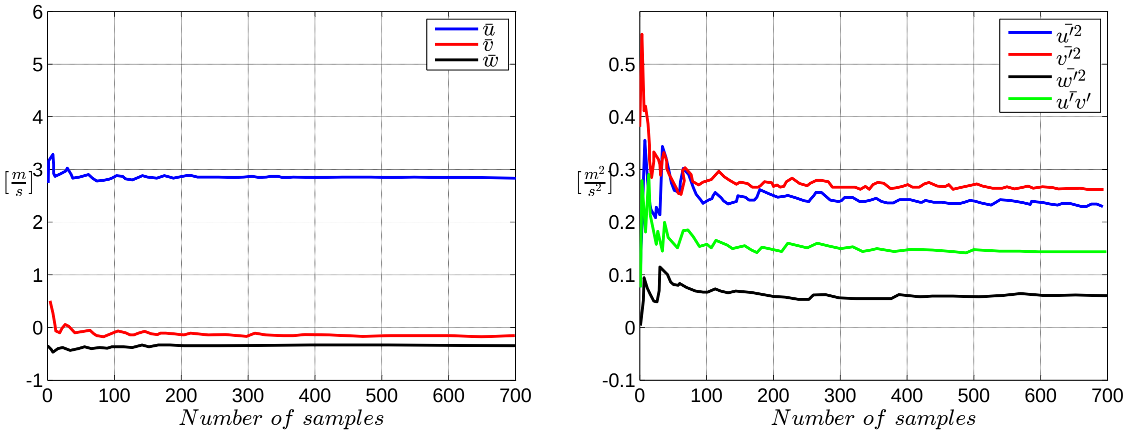

Figure 2-10. Evolution of the time average velocity (left image) and Reynolds stresses (right image) for a varying number of samples. Unconditioned sampling at *x/D* = 2 and *y/D* = 0.5 for λ = 4.8.

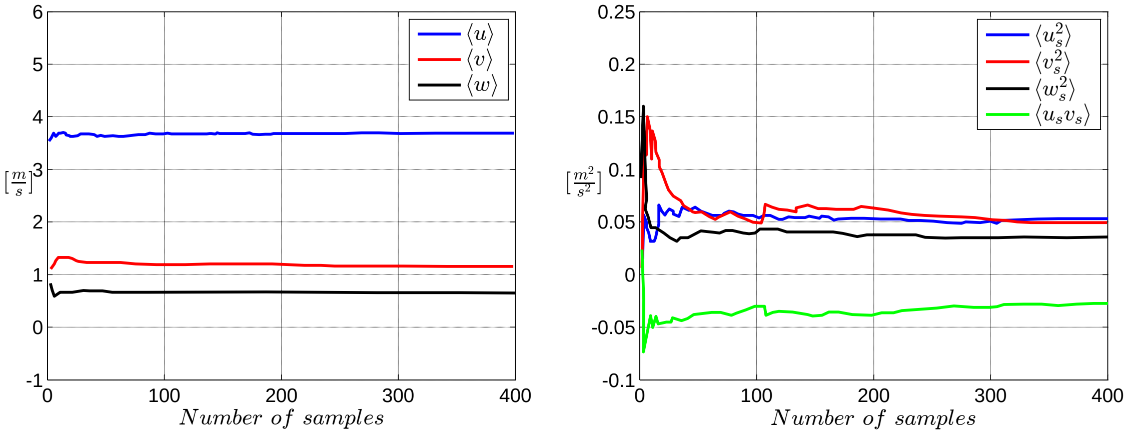

Figure 2-11. Evolution of the phase-locked average velocity (left image) and Reynolds stresses (right image). Phase-locked sampling at *x/D* = 2 and *y/D* = 0.5 for λ = 4.8.

2.3.3 Global Velocity Field And Wake Re-Energising Process

The near- and transition-wake velocity fields until approximately 5 diameters downstream are shown for two different tip-speed ratios. Results are presented for phase-lock and unconditioned average fields, respectively representing the average of the flow field corresponding to a prescribed phase of the blade rotation and the time-average flow field. Figure 2-12 to Figure 2-14 depict the normalized unconditioned average velocity field in the shear layer between the wake and the outer flow. In the contours of Figure 2-12, the location of the tip-vortex pairing instability is indicated by a sudden enlargement of the shear layer between the inner-wake and free-stream region, starting at *x/D* ~ 1 for λ = 6 and *x/D* ~ 1.3 for λ = 4.8 and reaching its maximum at *x/D* ~ 1.5 for λ = 6 and at *x/D* ~ 1.7 for λ = 4.8. The onset of the wake instability is therefore clearly depending on the λ as shown in Felli et al (2011). In Figure 2-13, showing the unconditioned average radial velocity field, the effect of the leapfrogging and the dependence on the tip-speed ratio are less evident. The most evident feature is an abrupt change of sign of the velocity direction, which becomes negative (namely toward in the inner region of the wake) after approximately one diameter for both tip-speed ratios, already before the onset of the tip-vortex instability. Figure 2-15 to Figure 2-17 show the phase-locked average velocity field of the shear layer and the inboard region until the hub centreline. In Figure 2-15 and Figure 2-16, showing respectively the axial and radial velocity, the presence of the tip vortices is recognisable by the periodic pattern of positive and negative velocity peaks (Naumov et al, 2012) that develops downstream in the region around $y/D = 0.5$. The intensity of these peaks is suddenly reduced after the locations $x/D \sim 1.5$ for $\lambda = 6$ and at $x/D \sim 1.7$ for $\lambda = 4.8$, identified above, which coincide with the locations where the tip vortices have completed a 90° revolution. This phenomenon suggests a predominant tip-vortex diffusion during and after the leapfrogging event, which eventually leads to the breakdown of the tip vortex. This suggests a strong influence of the large scale wake instability on the tip-vortex diffusive properties. This is also very evident in Figure 2-17 which depicts the azimuthal velocity field. Regions of positive velocity mean flow rotating in the same direction of the blades due to the viscous drag (e.g. the tip-vortex cores and the wakes of the blades), whereas negative regions represent counter rotating flow. After the leapfrogging, there is a clear change of sign of the velocity direction inside the tip-vortex. The analysis of such a phenomenon, also observed by Naumov et al (2012) is reserved for future studies. Figure 2-18 depicts the span-wise profile of axial velocity at different downstream locations. Data are taken from phase-locked measurements. The red dashed lines represent the value of maximum wake expansion predicted by momentum theory (horizontal line) and the value of minimum wake velocity (vertical line). Theoretical predictions are in rather good agreement with the experimental results. Another phenomenon is observed: the most downstream profiles exhibit an inversion of the wake expansion. At $\lambda = 4.8$ this is evident at 2.7D, but at $\lambda = 6$ this already evident at 1.6D. The hypothesis is that tip-vortex instability has also a sensible effect on the wake expansion process. The strong fluctuations of phase-locked velocity in the near hub region are mainly due to experimental error caused by possible shadowing and reflection from the nacelle and by the presence of the nacelle vortex shedding, which is not in phase with the turbine rotation. Figure 2-19, presenting the streamwise profiles of axial velocity at different radial locations, shows that the re-energising process starts right after the instability around locations ~ 1.5 diameters for $\lambda = 6$ and at ~ 1.7 diameters for $\lambda = 4.8$. Comparing Figure 2-19 and Figure 2-18, it is clear that the onset of the re-energising process coincides with the location of the leap-frogging event (in the graphs, the red dot represent the locations where the vortices have completed a 90° revolution and is defined as the "maximum leapfrogging" location). After reaching a minimum at the location of the maximum wake expansion, the axial velocity intakes a process of re-energising, starting from the outer regions where the turbulent mixing with the external flows happens as evident in Figure 2-18.

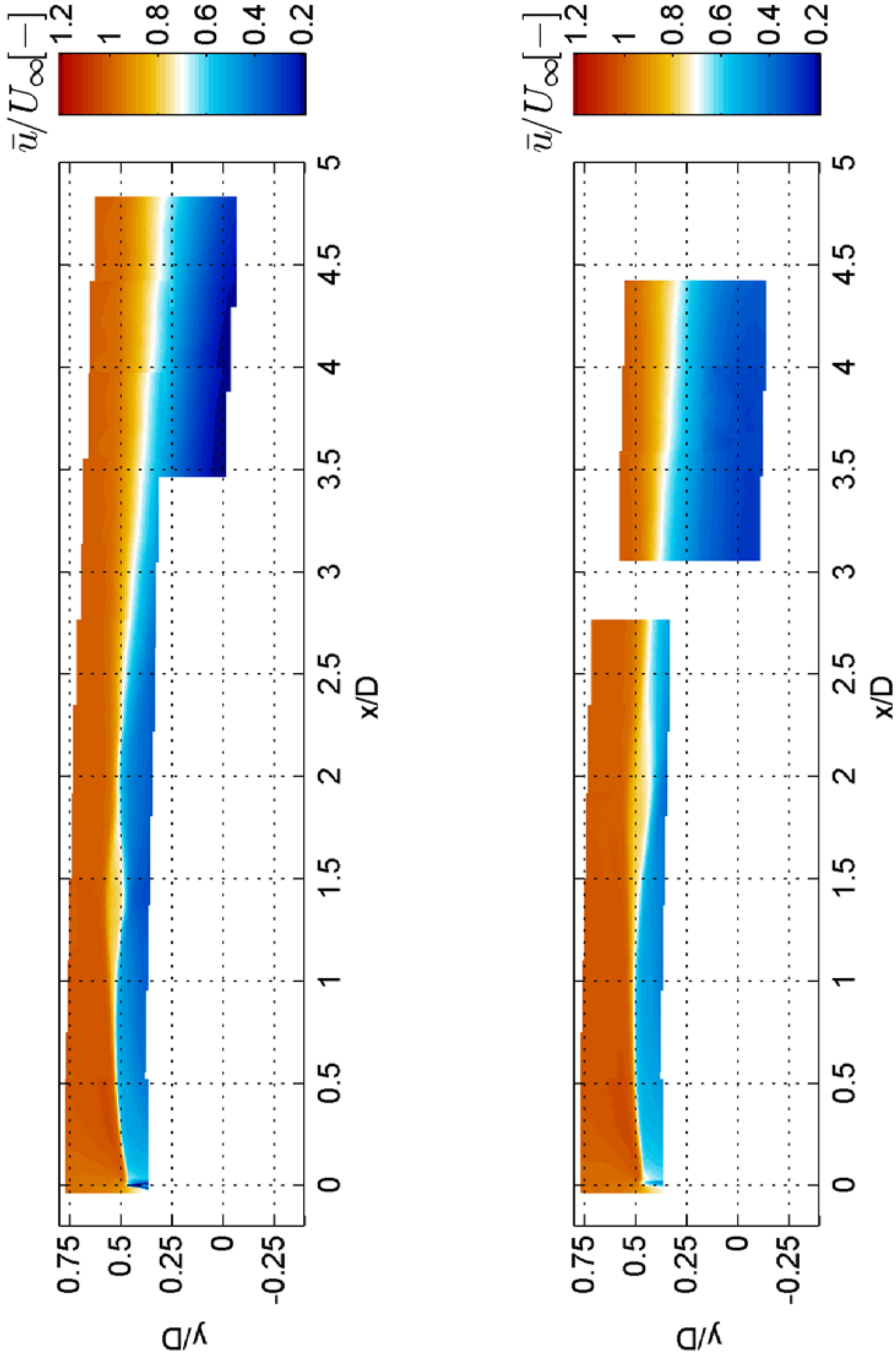

Figure 2-12. Unconditioned average axial velocity field $\overline{w}/U_\infty$ in the wake shear layer at $\lambda = 6$ (left image) and $\lambda = 4.8$ (right image).

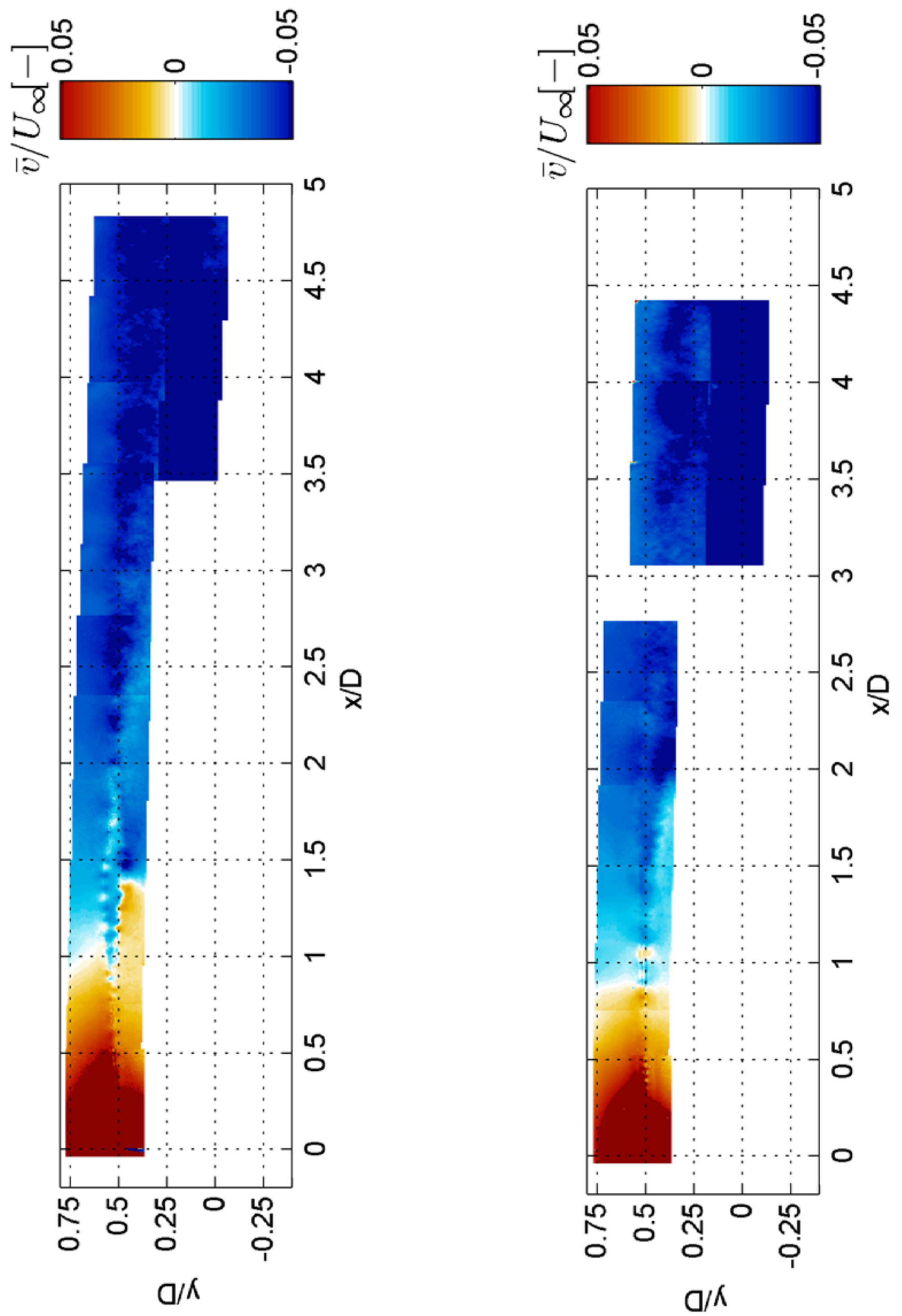

Figure 2-13. Unconditioned average radial velocity field $\bar{v}/U_\infty$ in the wake shear layer at $\lambda = 6$ (left image) and $\lambda = 4.8$ (right image).

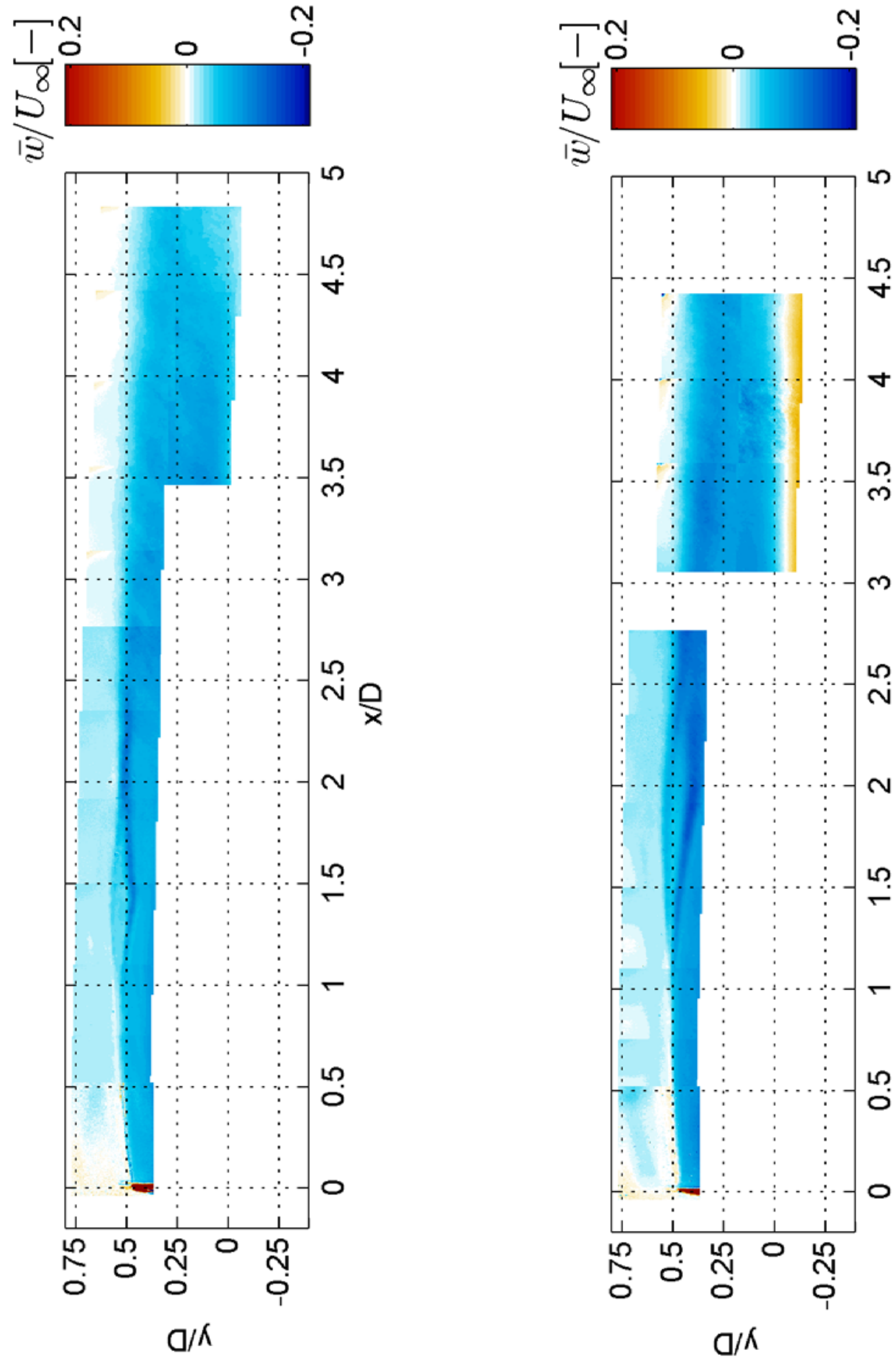

Figure 2-14. Unconditioned average azimuthal velocity field $\overline{w}/U_\infty$ in the wake shear layer at λ = *6* (left image) and λ = 4.8 (right image).

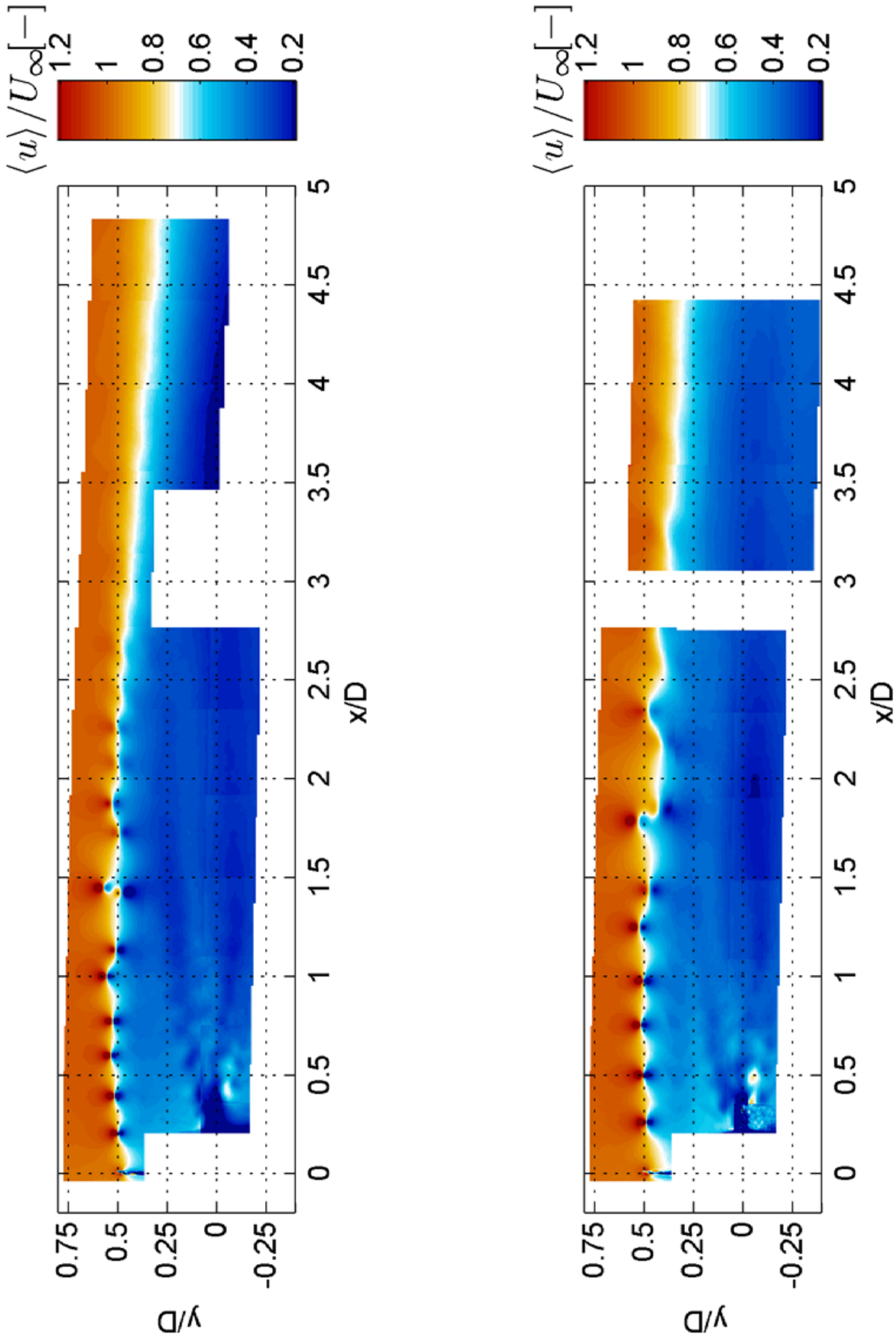

Figure 2-15. Phase-locked average axial velocity field $\langle u \rangle / U_\infty$ in the wake shear layer at λ = 6 (left image) and λ = 4.8 (right image).

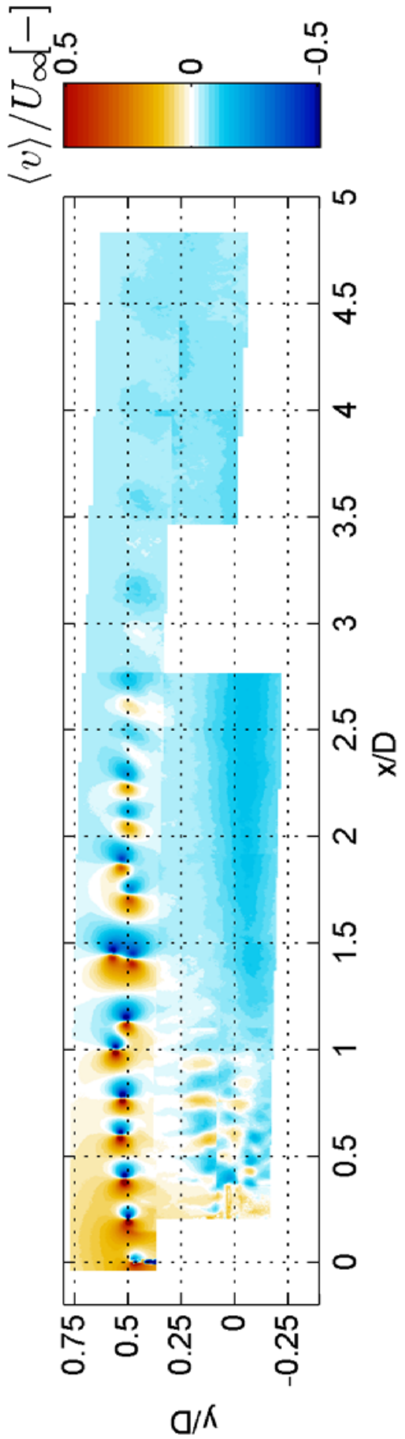

Figure 2-16. Phase-locked average radial velocity field $\langle v \rangle / U_\infty$ in the wake shear layer at $\lambda = 6$ (left image) and $\lambda = 4.8$ (right image).

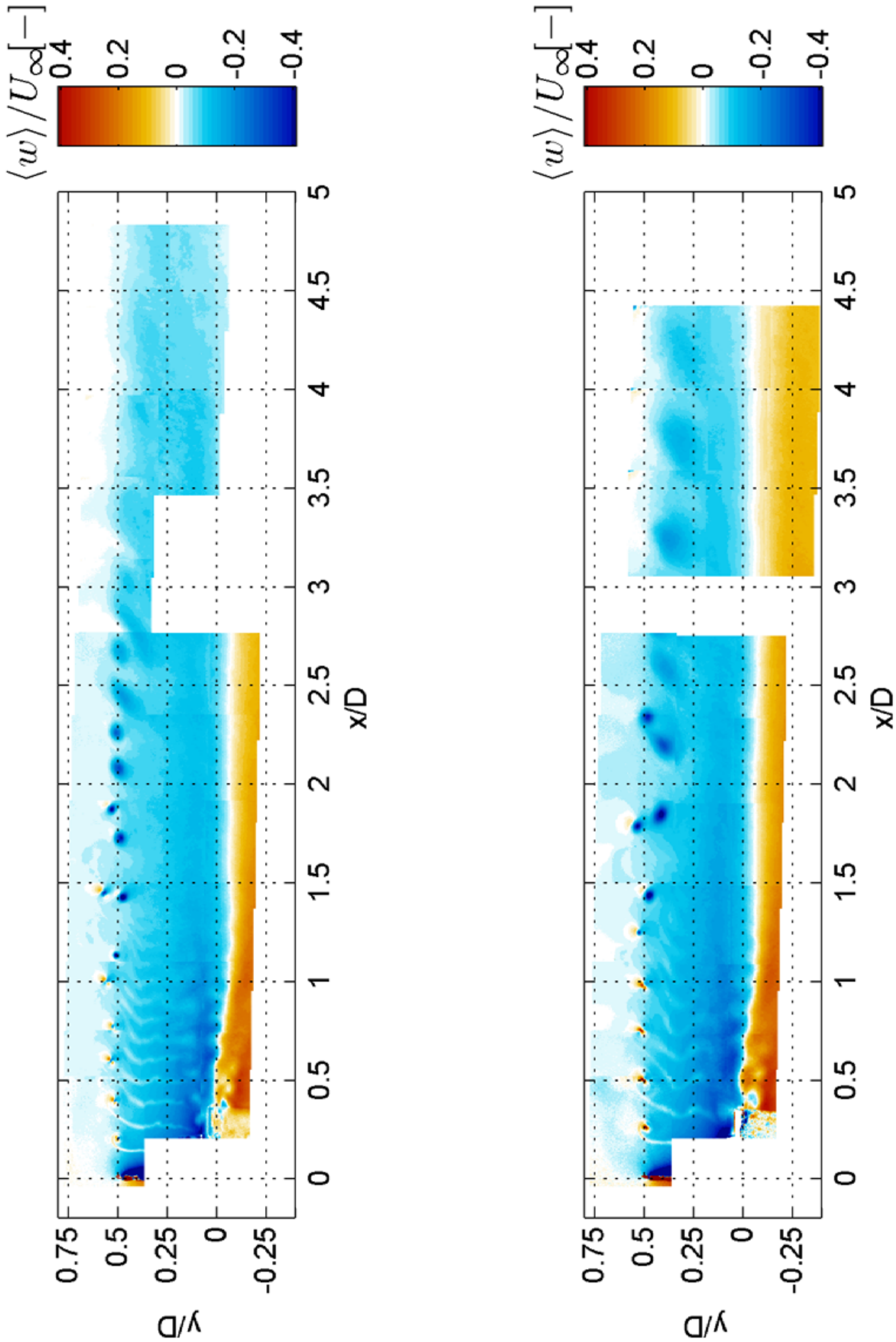

Figure 2-17. Phase-locked average azimuthal velocity field $\langle w \rangle / U_\infty$ in the wake shear layer at λ = 6 (left image) and λ = 4.8 (right image).

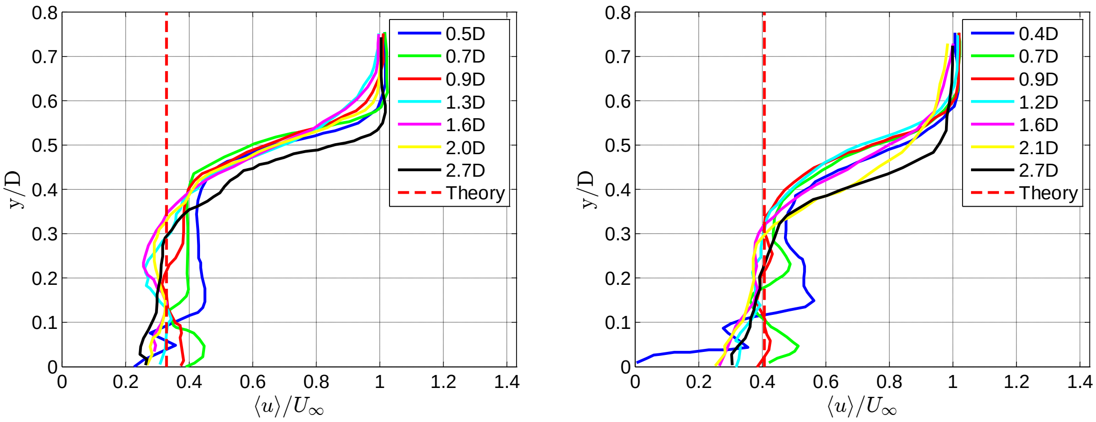

Figure 2-18. Vertical profiles of normalized phase locked axial velocity field $\langle u\rangle/U_\infty$ at 7 different downstream locations compared with the momentum theory profile at λ = 6 (left image) and λ = 4.8 (right image).

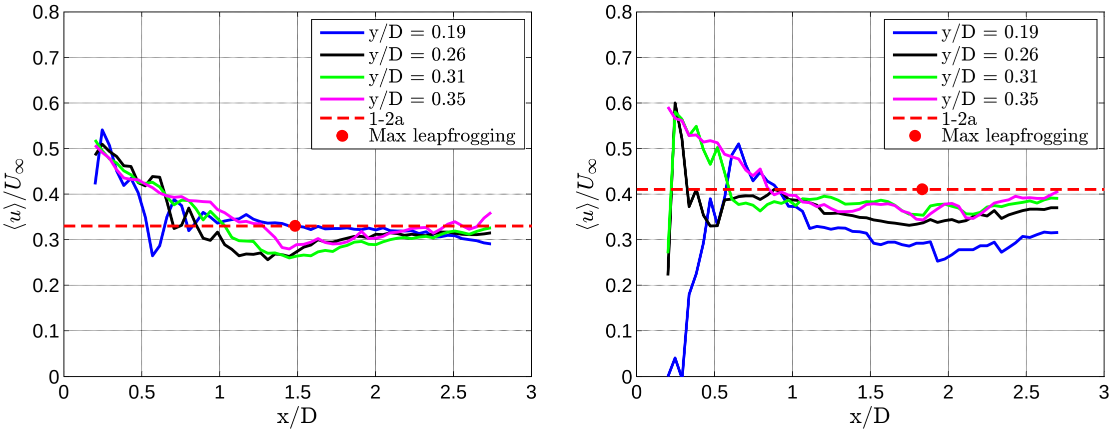

Figure 2-19. Streamwise evolution of normalized phase-locked axial velocity $\langle u\rangle/U_\infty$ at 4 different radial locations compared with the value calculated with the momentum theory at the maximum wake expansion $u_{wake} = U_\infty(1\text{-}a)$ at λ = 6 (left image) and λ = 4.8 (right image). The red dot indicates the location of the "maximum leapfrogging" in that phase, when the tip-vortices have completed a 90°rotation.

2.3.4 Vorticity Field and Tip Vortex Evolution

In this section, the evolution of the tip vortex is analysed in terms of vorticity. Figure 2-21 shows the value of out-of-plane phase-locked average vorticity obtained from the phase-locked average velocity fields. This is obtained with Equation (2-3):

$$\langle\omega_z\rangle = \frac{\partial\langle v\rangle}{\partial x} - \frac{\partial\langle u\rangle}{\partial y} \tag{2-3}$$

where $\langle u\rangle$ and $\langle v\rangle$ are the phase-locked average velocity components in the x- and y-directions, parallel to the measurement plane (see Figure 2-5). Results show the strong, concentrated vorticity at the tip-vortices location together with its disruption after the wake instability. Figure 2-20 depicts the evolution of circulation and vorticity as function of the vortex age. In the two graphs, the vortices from both blades have been considered. The flow circulation has been calculated integrating the velocity along a closed line C encompassing the vortex. From Figure 2-20 it is possible to notice that the vortex released by blade 1 is slightly stronger that the one released by blade 2 in both test cases. The difference is estimated around 10%, same magnitude of the difference in pitch angle of the two blades (0.5° difference over a pitch angle 4° at the tip). Figure 2-22 shows the time-average value of vorticity perpendicular to the field of view obtained from the unconditioned average velocity fields.

$$\overline{\omega_z} = \frac{\partial \overline{v}}{\partial x} - \frac{\partial \overline{u}}{\partial y} \tag{2-4}$$

where $\overline{u}$ and $\overline{v}$ are the unconditioned average velocity fields in the x- and y-directions. Results show that the vorticity is organised as a concentrated sheet which bifurcates at the location where the vortex leap-frogging occur, after which breaks down and diffuses quite rapidly.

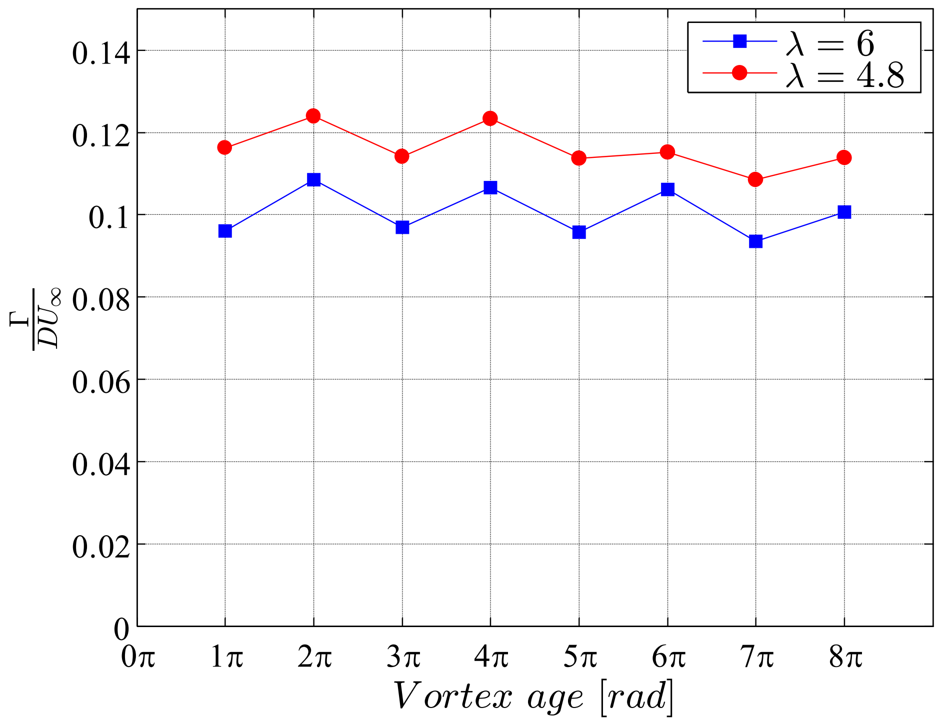

Figure 2-20. Evolution of tip vortex circulation Γ as function of vortex age.

2.3.5 Wake Turbulence

In this section the wake is analysed in terms of turbulence and Reynolds stresses. Figure 2-23 shows the phase-lock average x-y component of the shearing stresses $\langle u_s v_s \rangle$. This is an important quantity because, as demonstrated by Antonia et al (1986), Cal et al (2010), Cantwell and Coles (1983), Hamilton et al (2012) and Reynolds and Hussain (1972), is related to the vertical transport of momentum, with negative values of shearing

Reynolds stress meaning entrainment into the wake of the free-stream flow momentum and as such directly related to the re-energising process (see Section 3.2.1). The phase-lock shearing stresses are calculated with Equation (2-5):

$$\langle u_{s,i} u_{s,j} \rangle = \frac{\sum_{k=1}^{N} \left[u_i\left(t_{k,\varphi}\right) - \langle u_i \rangle \right] \left[u_j\left(t_{k,\varphi}\right) - \langle u_j \rangle \right]}{N} \tag{2-5}$$

where $t_{k,\varphi}$ is the sampling time at phase φ, N is the total number of samples and, for the case of the *x*-*y* component, $i = 1$ and $j = 2$. The phase-lock shearing stresses are associated with the random flow fluctuations, because the effect of the periodic fluctuations (namely the tip vortices, which are in phase with the rotor rotation) is filtered out by the phase-locked averaging process. The latter concept with the explained in Chapter 3. Two regions can be distinguished. In the near-wake region, the distribution of shearing stresses is strongly influenced by the evolution of the tip-vortex structure, with a concentration of the shearing stresses in the saddle points between two consecutive vortices (see Chapter 3). This is in good agreement with the findings of Cantwell and Coles (1983), who demonstrated experimentally how the shearing stresses due to the random turbulence have a negative peak near the saddle points between the vortices. This concentrated shear is associated with deep incursions of free-stream fluid into the regions between the vortices. In the region after the instability, the physics of the phenomenon changes radically: after the tip-vortex breakdown, the shearing stresses become suddenly larger, keeping their negative value, suggesting a more violent mixing, characterised by a strong entrainment of free-stream momentum. In the near-wake region it is also evident the presence of the nacelle's wake and the root vortex as a region with high positive and negative values of $\langle u_s v_s \rangle$, quickly disappearing within less than 2 diameters downstream.

Figure 2-24 shows the unconditioned average *x*-*y* component of the Reynolds stresses $\overline{u'v'}$ calculated with (2-6):

$$\overline{u'_i u'_j} = \frac{\sum_{k=1}^{N} \left[u_i(t_k) - \overline{u_i} \right] \left[u_j(t_k) - \overline{u_j} \right]}{N} \tag{2-6}$$

where t_k is the unconditioned sampling time. The unconditioned average shearing Reynolds stresses are inclusive of all flow fluctuations, both the random and periodic ones. Different regions can be distinguished. In the near-wake region, the shearing stresses are concentrated in a thin sheet at the border of the wake in locus of the vortex cores. In this region, the shearing stresses are characterised by a negative value. In the region where the wake instability occurs, the layer where the shearing stresses are concentrated becomes thicker and, after the location where the tip-vortices completed a 90° orbit around each other, an abrupt change of the shearing stresses sign occurs. After the breakdown of the tip-vortex, the very same behaviour observed in the phase-lock case can be observed.

Figure 2-25 shows the turbulence intensity in the shear layer between the inner wake and outer flow relative to the unconditioned average field obtained as:

$$TI = \frac{\overline{u_{RMS}}}{U_\infty} \tag{2-7}$$

where:

$$\overline{u_{RMS}} = \left(\frac{1}{3}\sum_{i=1}^{3}\overline{u'_i u'_i}\right)^{0.5} \tag{2-8}$$

and:

$$\overline{u'_i u'_i} = \frac{\sum_{k=1}^{N}[u_i(t_k) - \overline{u_i}]^2}{N} \tag{2-9}$$

The high values of *TI* close to the blades are due to the presence of strong concentrated vortices which are released at the blade tip. In Equation (2-9), this is accounted for as a flow fluctuation and as such contributes to the total *TI*. Figure 2-26 shows the phase-locked average turbulent intensity in the wake shear layer. This is calculated as:

$$TI = \frac{\langle u_{RMS}\rangle}{U_\infty} \tag{2-10}$$

where:

$$\langle u_{RMS}\rangle = \left(\frac{1}{3}\sum_{i=1}^{3}\langle u_{s,i}u_{s,i}\rangle\right)^{0.5} \tag{2-11}$$

and:

$$\langle u_{s,i}u_{s,i}\rangle = \frac{\sum_{k=1}^{N}\left[u_i\left(t_{k,\varphi}\right) - \langle u_i\rangle\right]^2}{N} \tag{2-12}$$

It is evident how the contribution of the organised periodic structures vanishes while travelling downstream: Figure 2-25 and Figure 2-26 in fact report the same values of *TI* after the maximum leapfrogging location, where the tip vortices lose their coherency. Results show how the contribution of the random structures become more important and extended in space while travelling downstream, with an opposite behaviour to the contribution of the periodic structures. As last, Figure 2-27 and Figure 2-28 show respectively the unconditioned and phase-locked average turbulence intensity of the *x*-, *y*- and *z*-component (results are presented only for λ = 6). The turbulence intensity in the three directions is calculated for the unconditioned measurements as:

$$TI = \frac{\overline{u_{i,RMS}}}{U_\infty} \tag{2-13}$$

where $\overline{u_{i,RMS}}$ is equal to $\sqrt{\overline{u'u'}}$, $\sqrt{\overline{v'v'}}$ and $\sqrt{\overline{w'w'}}$ for i = *1,2,3* respectively, and for the phase-locked field as:

$$TI = \frac{\langle u_{i,RMS} \rangle}{U_\infty} \tag{2-14}$$

where $\langle u_{i,RMS} \rangle$ is equal to $\sqrt{\langle u'u' \rangle}$, $\sqrt{\langle v'v' \rangle}$ and $\sqrt{\langle w'w' \rangle}$ for i = *1,2,3* respectively. From Figure 2-27 it is possible to appreciate the evident anisotropy of the wake turbulence, where the radial fluctuations are the most important ones, in accordance to previous literature about rotor wake aerodynamics (Cotroni et al, 2000, El Kasmi and Masson, 2008). On the contrary, the turbulence anisotropy is not visible in the phase-locked fields shown in Figure 2-28.

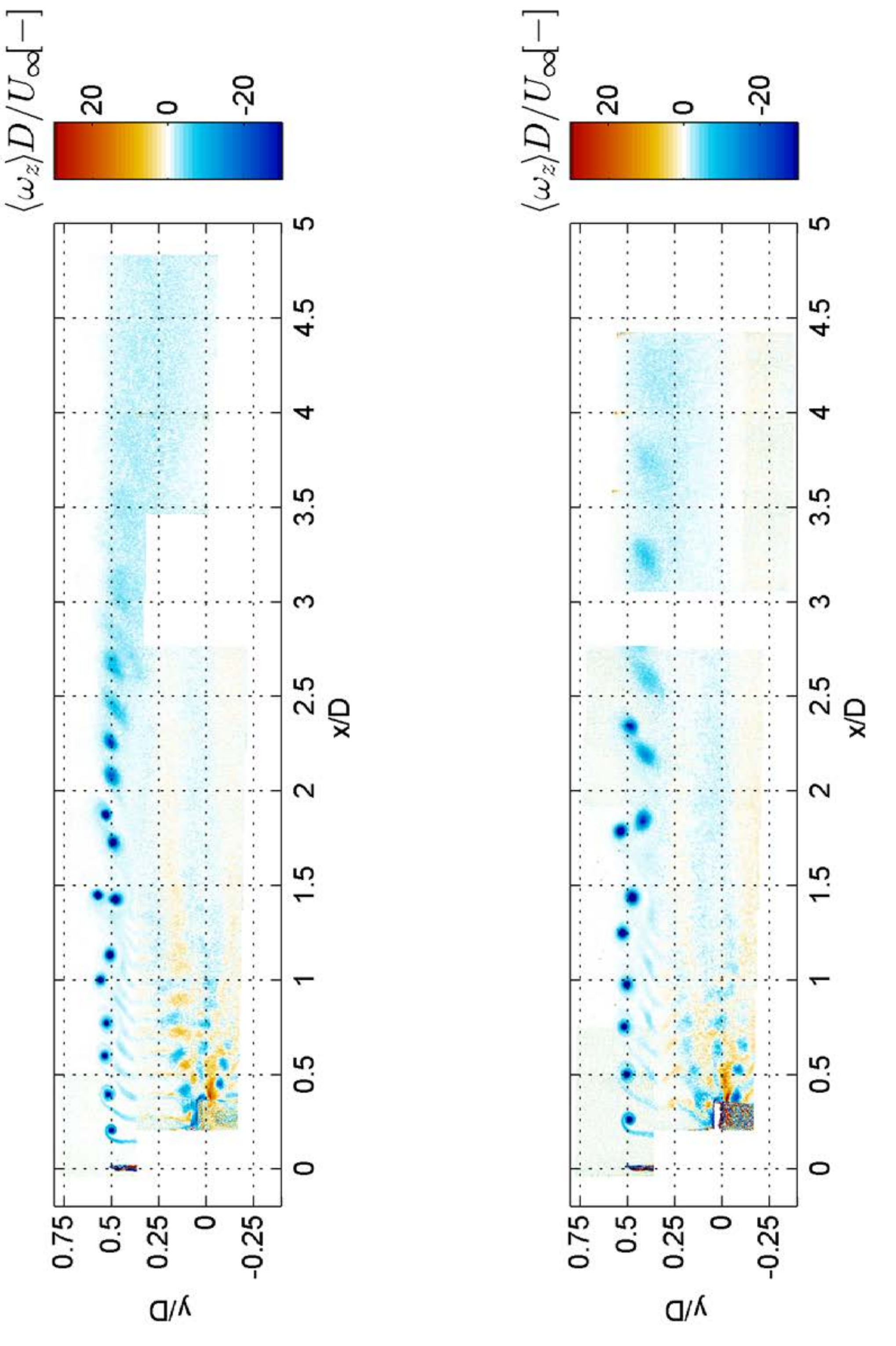

Figure 2-21. Phase-locked average out-of-plane vorticity field $\langle\omega_z\rangle D/U_\infty$ at λ = 6 (left figure) and λ = 4.8 (right figure).

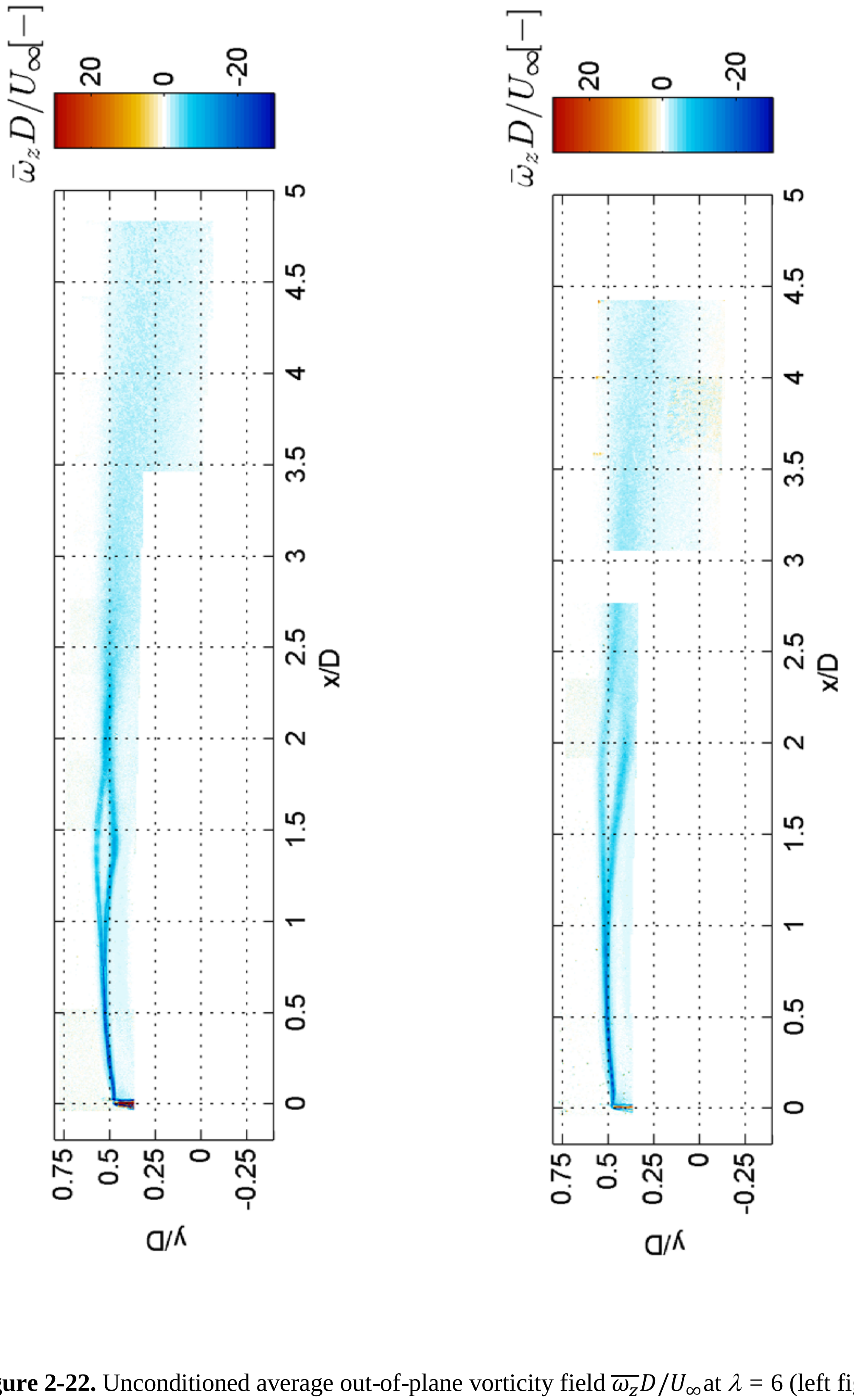

Figure 2-22. Unconditioned average out-of-plane vorticity field $\overline{\omega_z}D/U_\infty$ at λ = 6 (left figure) and λ = 4.8 (right figure).

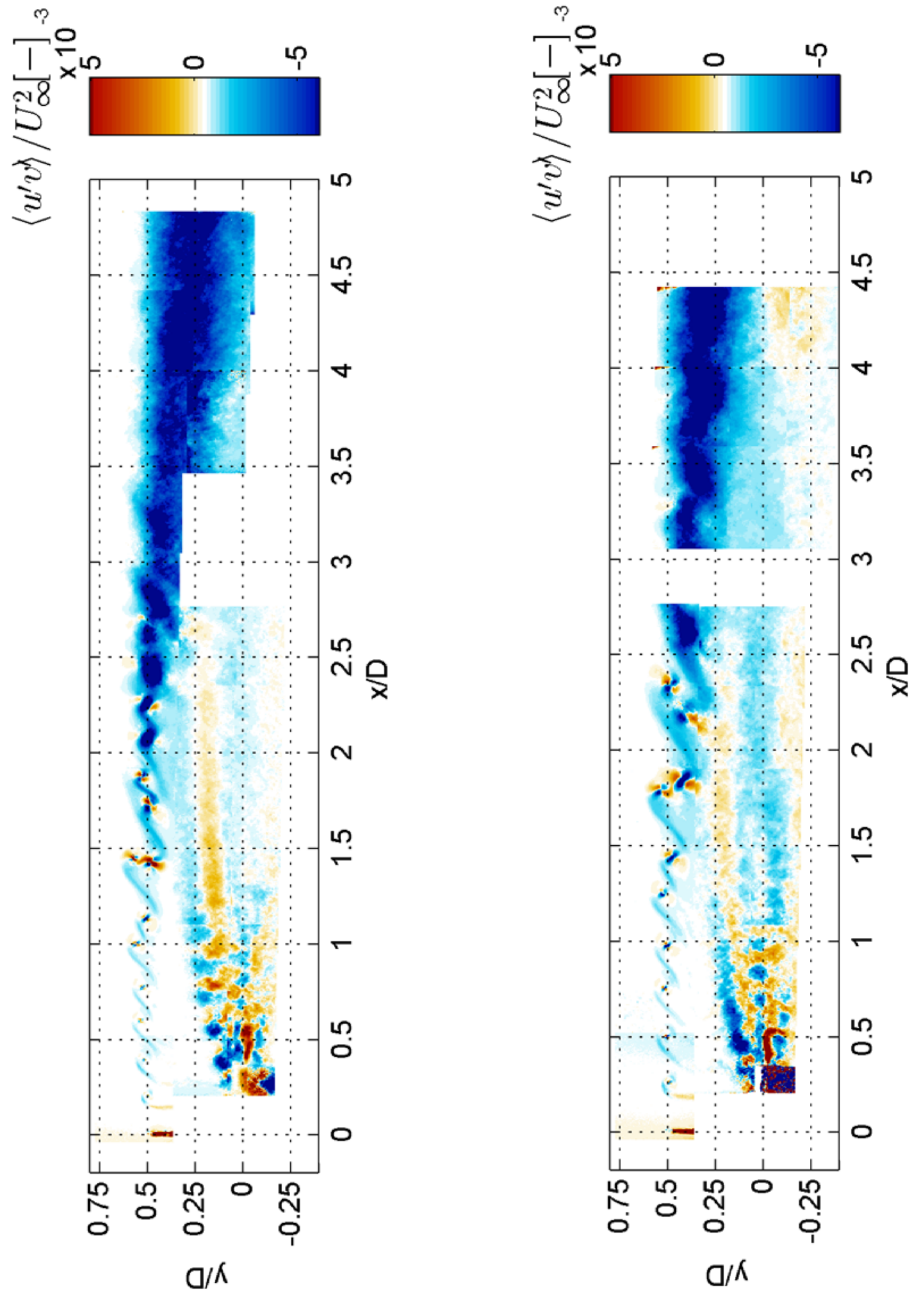

Figure 2-23. Phase-locked average x-y component of Reynolds stresses $\langle u'v' \rangle / U_\infty^2$ at λ = 6 (left figure) and λ = 4.8 (right figure).

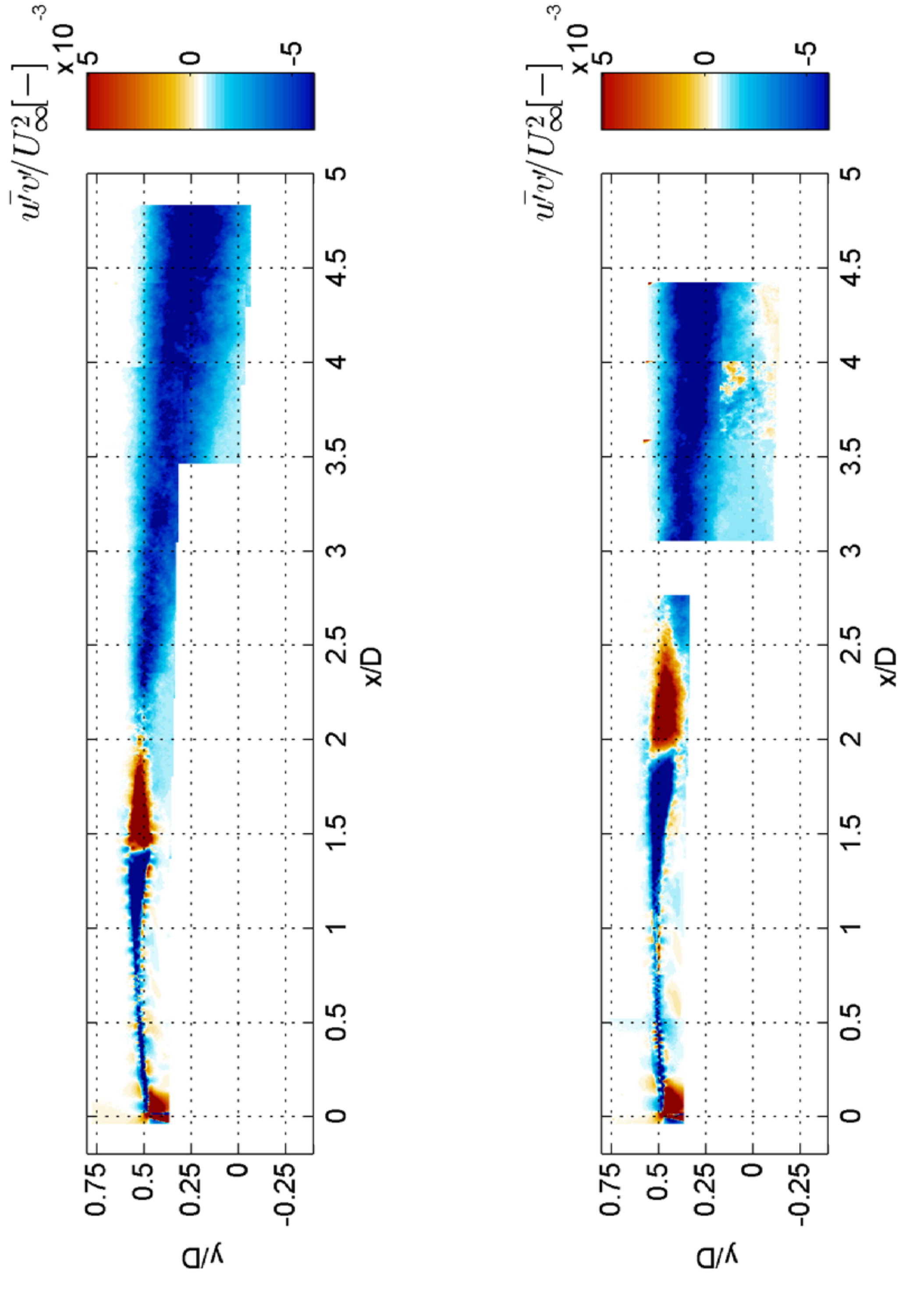

Figure 2-24. Unconditioned average x-y component of Reynolds stresses $\overline{u'v'}/U_\infty^2$ at λ = 6 (left figure) and λ = 4.8 (right figure).

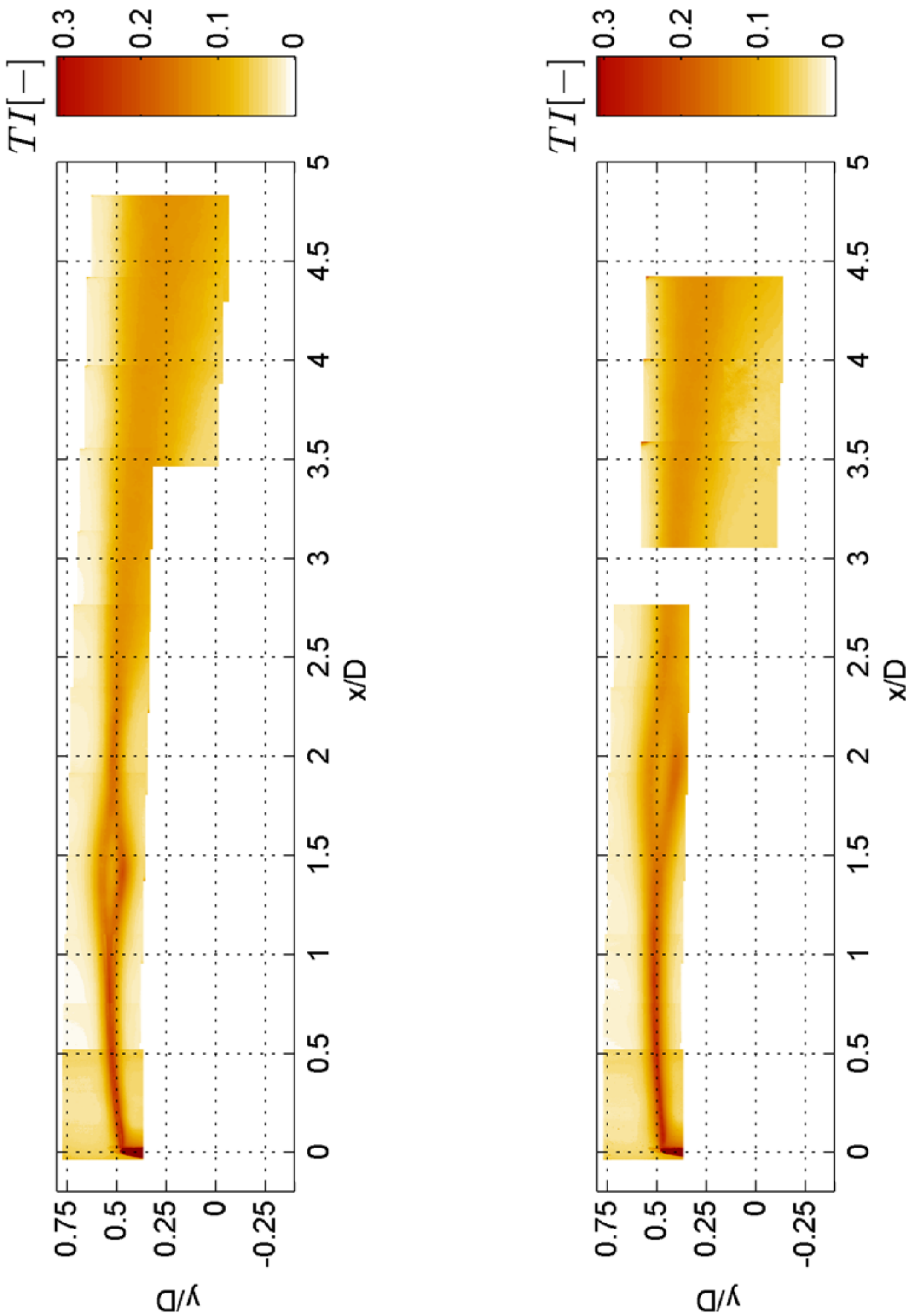

Figure 2-25. Unconditioned average turbulence intensity field at λ = 6 (left figure) and λ = 4.8 (right figure).

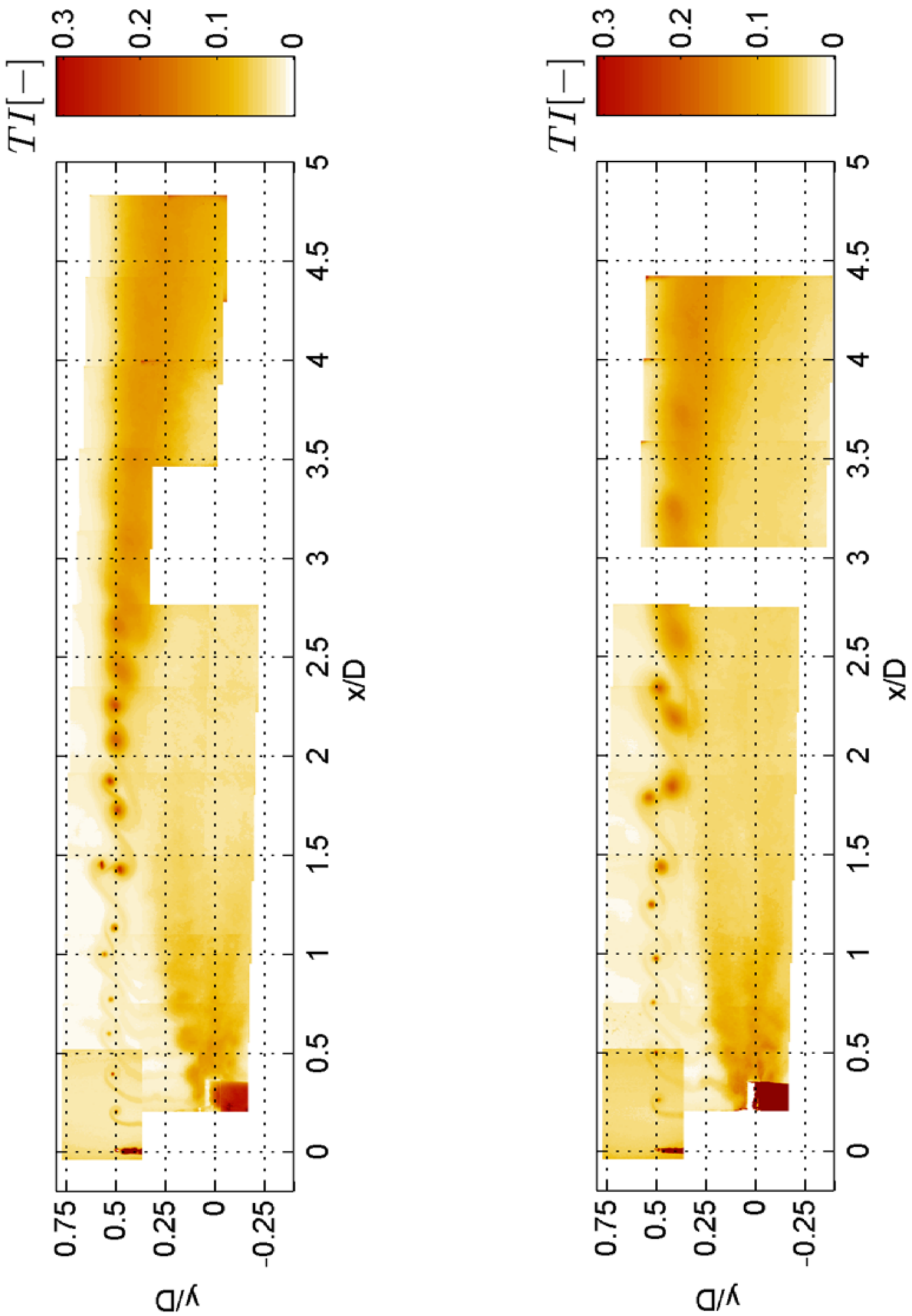

Figure 2-26. Phase-locked average turbulence intensity field at λ = 6 (left figure) and λ = 4.8 (right figure).

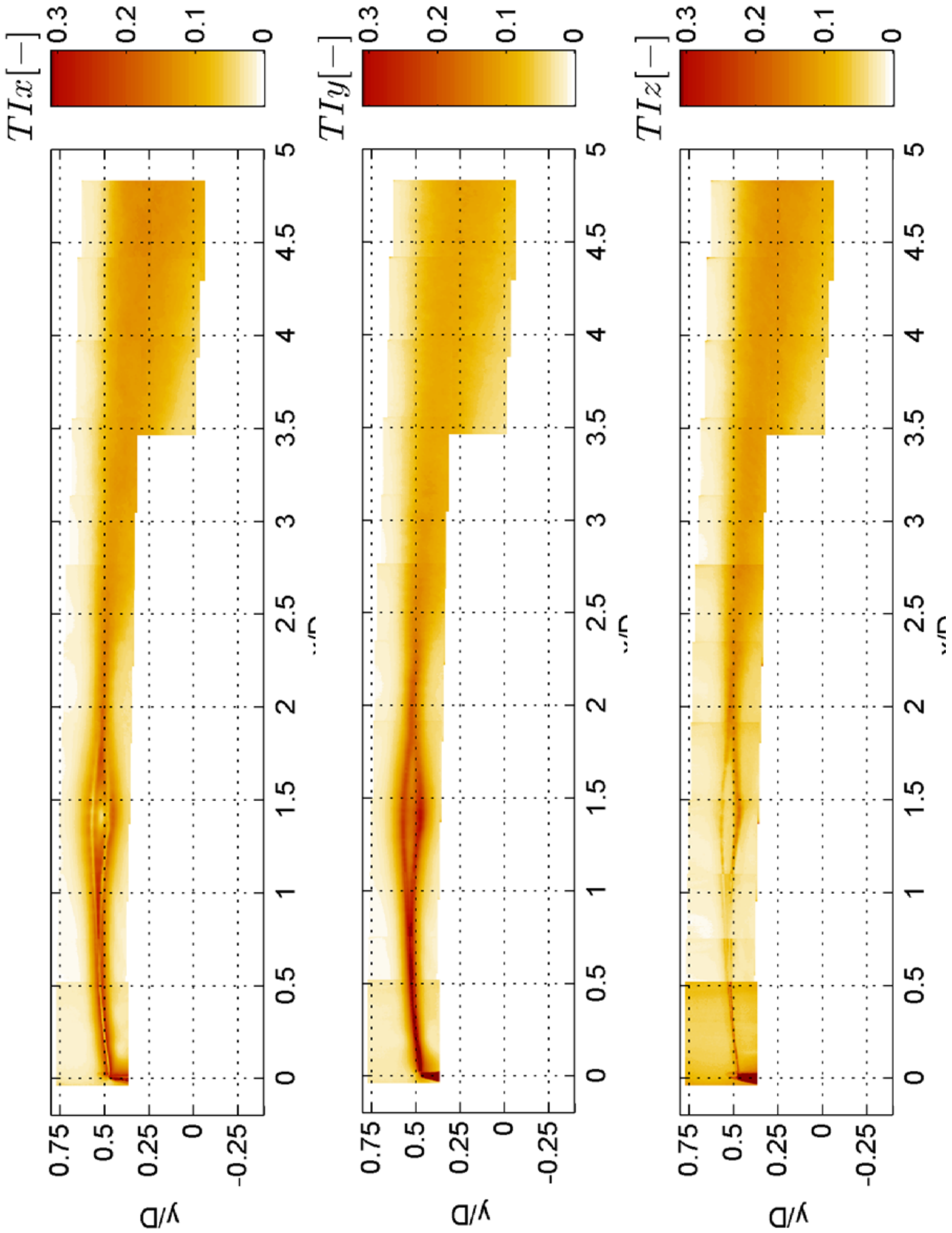

Figure 2-27. Unconditioned average average turbulence intensity field at λ = 6 in the three directions: TI_x (left), TI_y (centre) and TI_z (right).

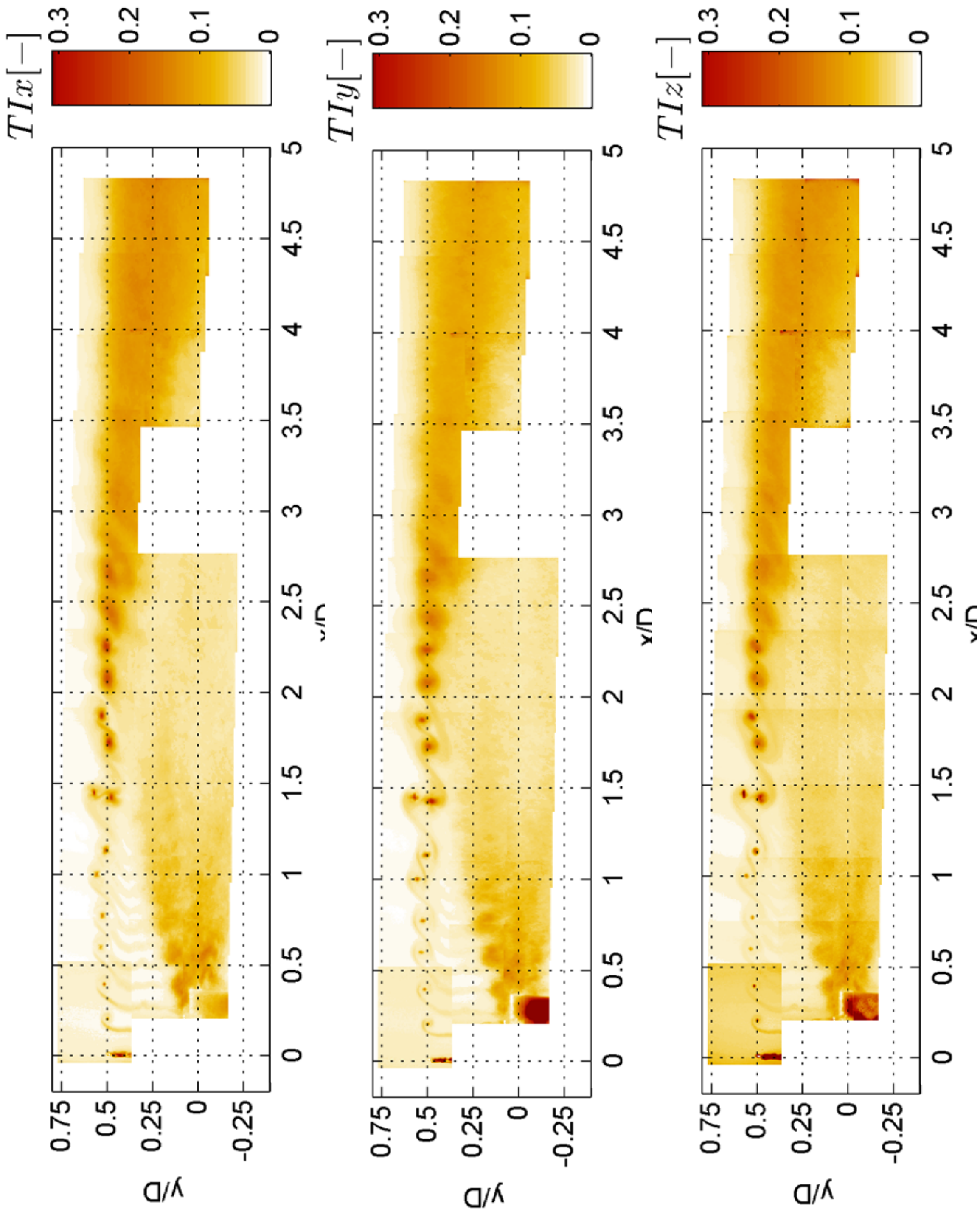

Figure 2-28. Phase-locked average average turbulence intensity field at λ = 6 in the three directions: TI_x (left), TI_y (centre) and TI_z (right).

2.4 CONCLUSIONS

Stereoscopic PIV experiments on a 0.6 m diameter horizontal-axis wind-turbine model have been conducted to study the flow region in the near- and transition-wake. The evolution of the wake flow structures with respect to the tip-speed ratio have been investigated together with the mixing properties of the wake. Analysis of the vortex structure revealed a clear dependency of the wake instability on the rotor tip-speed ratio. The study of the unconditioned average and phase-lock average velocity fields demonstrated how the wake instability affects all of the flow properties. The time-average velocity field show a localised enlargement of the wake shear layer in proximity of the tip-vortex instability location. The phase-lock velocity field shows a predominant diffusion of the tip-vortex after the instability, suggesting a direct influence of the large-scale wake behaviour on the tip-vortex diffusive properties. This finding is corroborated by the observation of the azimuthal velocity field, which shows a clear change of sign of the velocity direction in the vortex region after the leapfrogging location. Analysis of turbulence statistics demonstrated how the leap-frogging phenomenon has a strong influence on the development of the wake turbulence, leading to a more effective mixing after the location where the instability occurs and the vortex coherence is disrupted. This is also demonstrated by the analysis of the wake axial velocity, showing an evident re-energising process after the tip-vortex breakdown. The general comparison between the phase-lock and the unconditioned measurements shows that the mixing process after the wake instability is solely dominated by the random motions. The work in the next chapter is meant to analyse the different terms in the governing equations of the mean-flow kinetic-energy transport, quantifying the contributions of the periodic and random fluctuations.

3 TIP VORTEX INSTABILITY AND TURBULENT MIXING IN WIND TURBINE WAKES

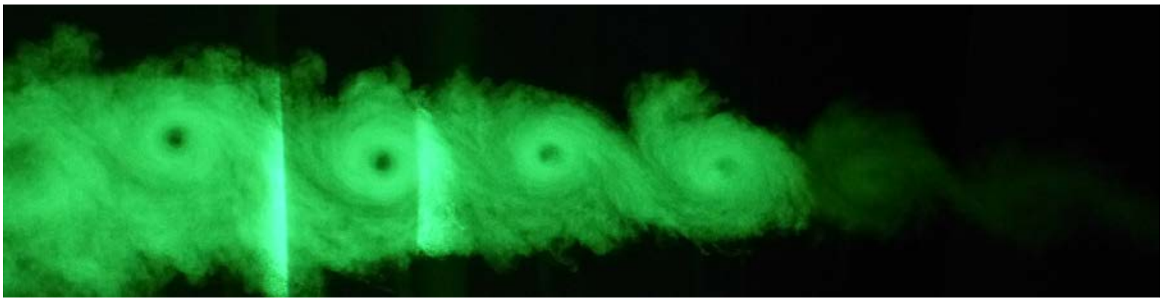

Kinetic energy transport and the turbulence production within the shear layer of a horizontal axis wind turbine wake are investigated with respect to their influence on the leapfrogging instability. The study quantifies the effect of near-wake instability and tip-vortex breakdown on the process of mean-flow kinetic-energy transport within the far-wake of the wind-turbine, in turn affecting the wake re-energising process. The detailed topology and development of the tip-vortex interactions are discussed prior to a statistical analysis based on the triple decomposition of the turbulent flow fields. The study emphasizes the role of the pairing instability as precursor to the onset of three-dimensional vortex distortion and breakdown, leading to increased turbulent mixing and kinetic energy transport across the shear layer. Quadrant analysis further elucidates the role of sweep and ejection events within the two identified mixing regimes. Prior to the onset of the instability, vortices shed from the blade appear to inhibit turbulent mixing of the expanding wake. The second region is dominated by the leapfrogging instability, with a sudden increase of the net entrainment of kinetic energy. Downstream of the latter, random turbulent motion characterises the flow, with a significant increase of turbulent kinetic energy production. In this scenario, the leapfrogging mechanism is recognized as the triggering event that accelerates the onset of efficient turbulent mixing followed by the beginning of the wake re-energising process.

This chapter is published as:

Lignarolo, L.E.M., Ragni, D., Scarano, F., Simão Ferreira, C.J., van Bussel, G.J.W., 2015. Tip vortex instability and turbulent mixing in wind turbine wakes. *Journal of Fluid Mechanics* 781, 467-493.

3.1 INTRODUCTION

The turbulent flow in the wake of a rotor is relevant for many engineering applications, ranging from wind turbines to marine propellers and helicopters. When considering clusters or arrays of rotors as in wind farms, the persistence of the wake over a significant distance from the rotor limits the energy performance of the entire farm (Schreck et al, 2008), and induces unsteady loads, noise and fatigue on the downwind turbines (Schepers, 2012, Vermeer et al, 2003). Wake effects become comparatively more important in offshore wind farms, where the atmospheric turbulence is lower than onshore, such that the wake persists for a longer distance behind the rotor (Ivanell et al, 2010).

The wake of a single rotor-blade consists of a continuous sheet of trailing vorticity due to the change in bound circulation along the blade span, which rolls up forming two concentrated tip and root vortices. In a wind turbine, the induction field created by the root vortex imposes a rotary motion on the whole wake, which is counter rotating with the rotor. The vorticity created by the blade boundary layer is also released into the wake, in a portion of the flow, which is co-rotating with the blade due to the viscosity. These vortical structures determine a helical system, due to the combination of the rotational motion of the blade, the free-stream wind-flow and the velocity field induced by the vortex system itself. The stability properties of such a system of vortex filaments have been investigated by several authors (see the review by Sørensen, 2011). Knowledge about the basic mechanisms behind the breakdown of the tip-vortex spiral systems is particularly relevant for offshore wind farms to correctly estimate the extent of the near-wake region, which is dominated by strong and coherent flow fluctuations. Moreover, the instability and breakdown of the helical system of vortices in the near wake is reported to affect the development of the turbulence in the far wake, where the mixing process between the inner and the outer flow regions occurs (Lignarolo et al, 2014). Any design modification able to accelerate or intensify the momentum-mixing process will result in a more rapid recovery of the wake deficit, with direct benefits on the energy efficiency of the above-mentioned systems (Sørensen, 2011).

Previous research in wake stability analysis has shown that the vortical structures released by the blade tip and root mutually interact in the near wake (Okulov and Sorensen, 2007); this interaction maintains the tip vortices in their stable helical pattern, which is otherwise unstable regardless of the characteristics of the vorticity distribution as already analytically demonstrated by Joukowsky (1912) (and Felli et al, 2011 for experimental analysis, Ivanell, 2009 for numerical, see Okulov and Sorensen, 2004 for theoretical). Most of the research on the stability of vortical structures is valid for a wide range of applications, from helicopters (Leishman, 1998) to wind-turbines (Okulov, 2004) and propeller rotors (Felli et al, 2011). Previous analytical research in Widnall (1972) indicated the existence of three different instability modes: short- and long-wave instability modes and a mutual-inductance instability mode. The first two instability modes are recognizable as smooth, sinuous-wave-type modes and are similar to the wave instability of a vortex ring (Saffman, 1970). The mutual-inductance instability mode appears when adjacent helical filaments are close enough to experience reciprocal influences, starting to roll-up around each other. This results in the well-known *leapfrogging* phenomenon, normally seen with parallel vortex rings (Lugt, 1996, Pentek et al, 1995, Riley and Stevens, 1993, Tophøj and Aref, 2013). Felli et al (2011) experimentally showed the simultaneous presence of all three modes, widening the range of possible interactions predicted by theory. Bolnot et al (2011) numerically simulated the helical wake using an array of axisymmetric vortex rings, for studying the onset of pair-wise instabilities in helicopter and wind-turbine rotor wakes. Leweke et al (2013) experimentally measured the growth rate of pair-wise instability in a water channel with different triggering modulations. Notwithstanding the number of studies associated with the stability of the wake in the near field, two problems still remain open:

- the identification of the triggering mechanism for the instability (Felli et al, 2011), especially in the presence of a significant level of free-stream turbulence. In fact, the inclusion of viscosity and turbulence challenges the simplified vortex models, which are often inaccurate for the prediction of the flow field.
- the quantification of the effect of the near-wake instability and the tip-vortex breakdown on the mixing process of the wind-turbine far wake and, subsequently, on the wake re-energising process (Sørensen, 2011).

The present study focuses on the second problem. In particular, the mutual-inductance instability, leading to the pairing of the tip-vortex filaments, is analysed in its effects on wake mixing and the production of turbulence. The issue of the tip-vortex effect on wake mixing has triggered a debate in the scientific literature, with Medici (2005) ascribing the missing energy recovery in the near wake to the *shielding* effect of the strongly concentrated tip vortices; in contrast, previous studies tend to consider tip vortices as structures that enhance the mixing by entraining high-momentum fluid from the outer stream (Hütter, 1977). In particular, the study examines details of the mean-flow kinetic-energy transport and turbulence production in the different stages of the rotor wake development. When this mechanism is unambiguously identified, further open questions in the area of aerodynamic modelling of wind turbine can be answered:

- what are the most relevant turbulent structures for correctly modelling the kinetic energy transport in the wake and what are the amounts of kinetic energy transported and dissipated by different flow structures?
- How does the development of these structures depend on the tip-speed ratio?
- How does the pairing instability of the tip-vortex helices in the near wake affect the evolution of turbulence and turbulent mixing in the far wake region?
- What is the role of the tip-vortices in the near wake, i.e. do they inhibit or enhance the transport of kinetic energy?

Abundant literature is available dealing with kinetic energy transport associated with coherent flow structures in several shear flows: bluff-body wakes, jets, boundary layers and mixing layers. Antonia et al (1987) analysed the momentum and heat transfer in jets and in the far wake of circular cylinders, also identifying the role of large coherent structures. Cantwell and Coles (1983) studied the entrainment process in the turbulent wake of a circular cylinder. Winant and Browand (1974) demonstrated, that most of the entrainment in mixing layers can be ascribed to the successive merging of vortices. Browand and Weidman (1976) also showed that the vortex pairing promotes the transport of transverse momentum in the shear layer of the wake. The wake of a wind turbine is characterized by the presence of helical vortices with similar behaviour to those encountered in free shear layers. However, a detailed analysis of their dynamical behaviour is currently not available, that would further explain the relationship between the vortex dynamics and the energy and momentum transfer in the wake re-energising process. Works dealing with the kinetic-energy transport in flow characterised by the presence of concentrated vortical structures have often made use of the triple decomposition (Reynolds and Hussain, 1972). This is due to the fact that the classical Reynolds decomposition is inadequate, in that the fluctuating term would result from strongly inhomogeneous contributions (discrete vortices and random turbulent fluctuations).

The present analysis is based on the experimental results documented in Chapter 2. The present study is focussed on the shear-layer region at the border of the wake until 3.5 diameters downstream, the area where the pairing instability takes place and the tip-vortices break down into smaller-scale turbulent structures, losing their coherence and periodicity. In this region, the mean-flow kinetic-energy flux and the turbulence production will be quantified in studying the effect of the pairing instability on wake turbulent mixing. The ability to measure both unconditioned-averaged flow-field properties as well as phase-locked snapshots allows one to explore details of wake turbulent mixing by making use of the triple decomposition of the velocity field into mean, periodic and random fluctuating components.

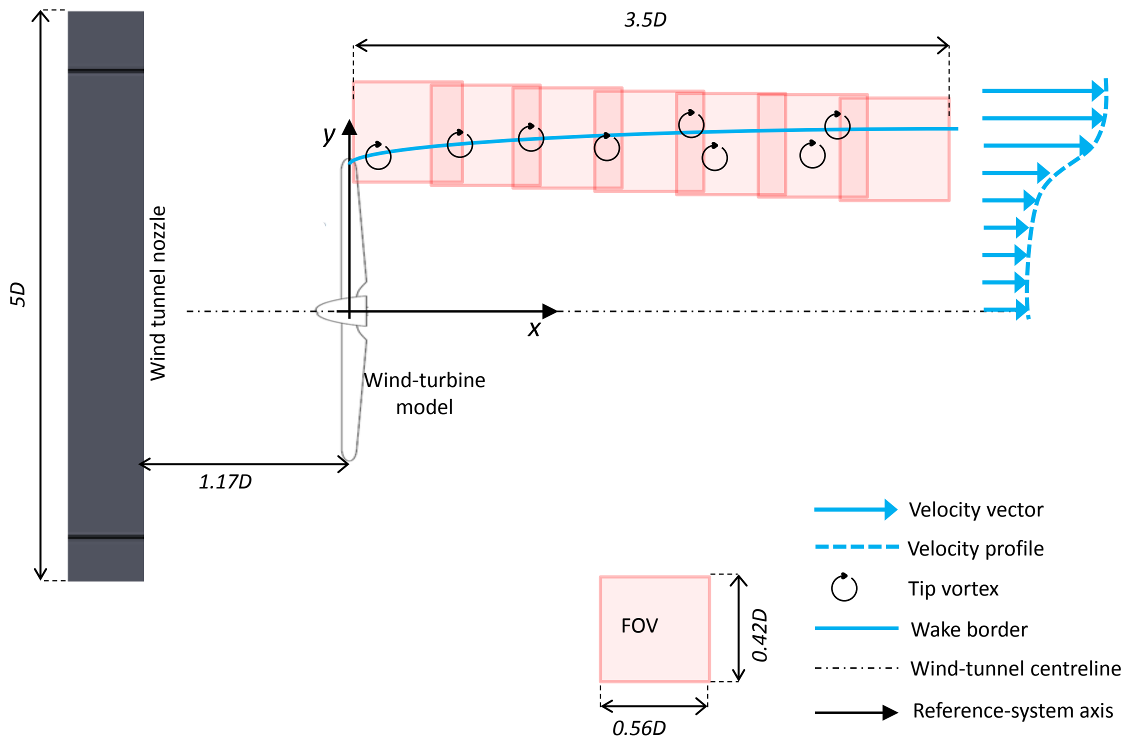

Figure 3-1. Schematic top-view of the experimental layout (not in scale): wind tunnel exit, wind turbine model and measurement domain obtained by superposition of multiple and partly overlapping fields of view (FOV). Each squared window represents a FOV in the horizontal (*x*-*y*) plane. The schematic shows also a qualitative impression of the wake border, of the unstable tip vortices and of the wake axial velocity profile.

The study has been conducted at low turbulence intensity in order to separate the problems of the flow mixing caused by the external turbulence from that caused by the turbulence induced directly by the presence of the wind turbine, as well as to give full control over the tip-vortex instability. This is in contrast to most of the studies on similar subjects, which have been performed in the presence of high wind tunnel turbulence or simulated atmospheric boundary layers (and atmospheric turbulence). The study as such focuses solely on the wake-induced turbulent flow, minimising the number of parameters affecting wake mixing. Similarly to the studies of Bolnot et al (2014) and Odemark and Fransson (2013), a systematic trigger for the wake instability has been introduced by installing the blades at two slighly different pitch angles. The analysis is repeated for two different tip-speed ratios, in order to investigate the effect of this parameter on the development of the pairing instability and wake mixing.

3.2 METHOD

The present analysis is based on the results of the experiments discussed in Chapter 2. Only a specific region of the flow encompassing the shear layer at the border of the wake has been taken into consideration, as shown in Figure 3-1.

3.2.1 TRIPLE DECOMPOSITION, MEAN-FLOW KINETIC-ENERGY TRANSPORT AND TURBULENCE PRODUCTION

The kinetic energy transport of the periodic structures is studied via a triple decomposition of the flow into mean, periodic and random velocity contributions (Antonia and Browne, 1987b, Antonia et al, 1986, Reynolds and Hussain, 1972). The procedure is typically applied in mixing flows (Escudié and Liné, 2003) when the unsteady boundary conditions are of periodic type (rotors, flapping aerofoils, etc.) to separate the contribution of the periodic fluctuations from the random turbulence. The triple decomposition defines the velocity field u_i as:

$$u_i(t) = \bar{u}_i + \tilde{u}_i(t + nT) + u_{s,i}(t) \qquad (3\text{-}1)$$

where $u_i(t)$ is the instantaneous velocity field, $\bar{u}_i$ denotes the time averaged value, $\tilde{u}_i$ the periodic fluctuations and $u_{s,i}$ indicates the random fluctuations. The period of $\tilde{u}_i$ is given by T. n is the number of periods, t is the time and the subscripts i indicate the coordinate directions, with i = 1, 2, 3 corresponding to x-, y- and z-directions respectively, or axial, radial and azimuthal (out-of-plane). In the classical Reynolds decomposition, the velocity field is defined as $u_i = \bar{u}_i + u'_i$, where $u'_i = \tilde{u}_i + u_{s,i}$. Typically, the time-average flow field $\bar{u}_i$ is obtained as the time average of a series of unconditioned samples, while the phase-average field $\langle u_i \rangle$ is obtained by phase-locking of the measurement acquisition with the periodic motion. The fluctuating component pertaining to one phase of the turbine rotation φ can be obtained from the phase-locked average field as

$$\tilde{u}_i = \langle u_i \rangle - \bar{u}_i \qquad (3\text{-}2)$$

for a given value of the phase. This entails a clear distinction between the time- and phase-averaged Reynolds stresses $\overline{u'_i u'_j}$ and $\langle u_{s,i}u_{s,j}\rangle\big|_{\varphi}$, respectively calculated with Equation (2-6) and Equation (2-5). The mathematical relationship between the above two quantities is:

$$\overline{u'_i u'_j} = \overline{\tilde{u}_i\tilde{u}_j} + \overline{u_{s,i}u_{s,j}} \tag{3-3}$$

where

$$\overline{\tilde{u}_i\tilde{u}_j} = \sum_{\varphi=1}^{N_f}\frac{\langle\tilde{u}_i\tilde{u}_j\rangle\big|_{\varphi}}{N_f}; \qquad \overline{u_{s,i}u_{s,j}} = \sum_{\varphi=1}^{N_f}\frac{\langle u_{s,i}u_{s,j}\rangle\big|_{\varphi}}{N_f}; \tag{3-4}$$

are the averages over all N_f phases of the Reynolds stresses relative to the random fluctuations and periodic motion, respectively. As denoted by Reynolds and Hussain (1972) the average kinetic energy associated with a fluid having velocity u_i is, using the Einstein's summation convention.

$$\frac{1}{2}\overline{u_i u_i} = \frac{1}{2}\bar{u}_i\bar{u}_i + \frac{1}{2}\overline{\tilde{u}_i\tilde{u}_i} + \frac{1}{2}\overline{u_{s,i}u_{s,i}} = \overline{K_E} + \overline{K_P} + \overline{K_T} \tag{3-5}$$

where $\overline{K_E}$ is the kinetic energy of the mean flow, $\overline{K_P}$ is the kinetic energy of the periodic structures and $\overline{K_T}$ is the kinetic energy contribution of the random turbulent fluctuations. It should be noted that the components $\overline{K_P}$ and $\overline{K_T}$ are the sum of the contributions corresponding to all phases, while typically phase-locked measurements are singularly acquired at a prescribed time delay from a reference position of the blade. Neglecting the viscous effects, the transport equation of the kinetic energy, as derived from Reynolds and Hussain (1972), can be written for one phase φ in the phase-locked form, by multiplying the Navier-Stokes equation by $\bar{u}_i$, and phase averaging with no time averaging:

$$\begin{aligned}(\bar{u}_j + \tilde{u}_j)\frac{\partial K_E}{\partial x_j} = {} & -\frac{1}{\rho}\left(\frac{\partial\bar{p}\bar{u}_i}{\partial x_i} + \frac{\partial\tilde{p}\bar{u}_i}{\partial x_i}\right) - \bar{u}_i\left(\frac{\partial\tilde{u}_i}{\partial t} + \bar{u}_j\frac{\partial\tilde{u}_i}{\partial x_j}\right) \\ & - \left(-\langle u_{s,i}u_{s,j}\rangle - \tilde{u}_i\tilde{u}_j\right)\frac{\partial\bar{u}_i}{\partial x_j} - \frac{\partial}{\partial x_j}\left[\bar{u}_i\langle u_{s,i}u_{s,j}\rangle + \bar{u}_i\left(\tilde{u}_i\tilde{u}_j\right)\right]\end{aligned} \tag{3-6}$$

The term on the left-hand side denotes the net rate of increase of the energy component, while the right-hand side describes the mechanisms governing it. The first and fourth terms on the right represent the transport of mean flow kinetic energy within the flow by means of the pressure gradient, random and periodic flow fluctuations; the third term represents the mean flow kinetic energy which is absorbed by the random and periodic flow fluctuations (the former is the production of turbulent kinetic energy presented in 0). The second term derives from the fact that the obtained averaged field is convected with the mean flow. This allows restricting the study to one single phase, with evident advantages in data post-processing and experimental time. In the present study the third and fourth terms of the right-hand side of Equation (3-6) are of relevance, since they represent the mean-flow kinetic-energy loss into turbulence and coherent vortices and the kinetic-energy transport due to the turbulence and the periodic vortices at a phase φ. Consideration of such energy fluxes for wind energy data analysis has been proposed and introduced in previous literature by Cal et al (2010) and Calaf et al (2010a). The behaviour of the periodic vortical structures and the random turbulent-fluctuations is studied by calculating the fluxes of the mean-flow kinetic energy. This can be done by estimating the terms contained in the gradient of the last element of (3-6), namely

$$\langle\widetilde{\Phi}\rangle = -\bar{u}_i\big(\tilde{u}_i\tilde{u}_j\big); \qquad \langle\Phi_s\rangle = -\bar{u}_i\langle u_{s,i}u_{s,j}\rangle \tag{3-7}$$

The spatial gradients of these terms represent a net transport of kinetic energy in the volume of flow. In (3-7) the only terms which contribute to the wind-turbine wake recovery process are the fluxes of kinetic energy relative to the mean axial-velocity directed toward the wake centreline, namely $\langle\widetilde{\Phi}\rangle = -\bar{u}\langle\tilde{u}\tilde{v}\rangle$ and $\langle\Phi_s\rangle = -\bar{u}\langle u_s v_s\rangle$ in the *x-y* plane of the measurements, which represent the fluxes of the mean-flow kinetic energy in a selected phase caused by the action of the periodic and random fluctuations, respectively.

The quantification of the turbulence production rate can be carried out by expanding the random part of the third term in (3-6), leading to

$$\langle Pe_{m-t}\rangle = -\langle {u_s}^2\rangle\frac{\partial\bar{u}}{\partial x} - \langle {v_s}^2\rangle\frac{\partial\bar{v}}{\partial y} - \langle u_s v_s\rangle\left(\frac{\partial\bar{u}}{\partial y}+\frac{\partial\bar{v}}{\partial x}\right) - \langle u_s w_s\rangle\frac{\partial\bar{w}}{\partial x} - \langle v_s w_s\rangle\frac{\partial\bar{w}}{\partial y} \tag{3-8}$$

which describes the decay into turbulence of the mean-flow kinetic energy. However, at each phase angle, turbulence is also produced by decay of the kinetic energy of the rotating tip-vortex. For this reason, the equation presented in Cantwell and Coles (1983) is used to obtain the phase-locked average total production $\langle Pe\rangle$ of turbulent kinetic energy associated to random fluctuations, shown in (3-9):

$$\langle Pe\rangle = -\langle {u_s}^2\rangle\frac{\partial\langle u\rangle}{\partial x} - \langle {v_s}^2\rangle\frac{\partial\langle v\rangle}{\partial y} - \langle u_s v_s\rangle\left(\frac{\partial\langle u\rangle}{\partial y}+\frac{\partial\langle v\rangle}{\partial x}\right) - \langle u_s w_s\rangle\frac{\partial\langle w\rangle}{\partial x} - \langle v_s w_s\rangle\frac{\partial\langle w\rangle}{\partial y} \tag{3-9}$$

which is the summation of (3-8) and the term relative to the turbulence production due to the vortex decay $\langle Pe_{p-t}\rangle$, shown in (3-10):

$$\langle Pe_{p-t}\rangle = -\langle {u_s}^2\rangle\frac{\partial\tilde{u}}{\partial x} - \langle {v_s}^2\rangle\frac{\partial\tilde{v}}{\partial y} - \langle u_s v_s\rangle\left(\frac{\partial\tilde{u}}{\partial y}+\frac{\partial\tilde{v}}{\partial x}\right) - \langle u_s w_s\rangle\frac{\partial\widetilde{w}}{\partial x} - \langle v_s w_s\rangle\frac{\partial\widetilde{w}}{\partial y} \tag{3-10}$$

In (3-8), (3-9) and (3-10), the components of the gradient along the *z*-direction are assumed to be negligible with respect to the other quantities.

3.2.2 Quadrant Analysis

Quadrant analysis (Wallace et al, 1972, Willmarth and Lu, 1972) allows the identification of four types of events in the flow, through the analysis of the fluctuating velocity components. The events are represented by quadrants defined by the four possible combinations of sign of the instantaneous value of the fluctuating velocity components (see Antonia and Browne, 1987b). Hattori et al (2010), Poggi and Katul (2008) give an example of the application of quadrant analysis in studying the generation of coherent structures in turbulent flows. Previous applications can be found in Raupach (1981) using the analysis for turbulent boundary layers over rough and smooth walls; atmospheric boundary layers have been explored in such a manner by Katul et al (1997), and Katul et al (2006), while (Antonia and Browne, 1987a, Fabris, 1979) characterized the wake behind a cylinder. Recently, Hamilton et al (2012) applied quadrant analysis in studying turbulent mixing in the atmospheric boundary layer of a large wind farm. In the present study, quadrant analysis is particularly useful for analysing $\langle\Phi_s\rangle$, the mean-flow kinetic-energy transport caused by the action of random flow fluctuations, in order to identify the regions where most of the positive kinetic-energy flux takes place. Only the regions where u_s and v_s are anti-correlated contribute to a net kinetic energy entrainment. In the periodic field, the direction of $\tilde{u}$ and $\tilde{v}$ are more easily identifiable and quadrant analysis is not necessary (see 3.3.2 and 3.4). In the shear layer of a wind turbine wake, ejections represent turbulent bursts of low-momentum fluid directed away from the wake centreline, as indicated by a negative value of the fluctuating stream-wise velocity and a positive fluctuating normal velocity (quadrant 2). Sweeps represent turbulent bursts of high speed fluid directed toward the inner part of the wake, as indicated by a positive value of the fluctuating stream-wise velocity and a negative fluctuating normal velocity (quadrant 4). However, this is not always the case and outward (or inward) interaction may also occur, where $u_s > 0$ and $v_s > 0$ (or $u_s < 0$ and $v_s < 0$), respectively in quadrants 1 and 3. As in Hamilton et al (2012), quadrant analysis applied to the mean-flow kinetic-energy flux implies the definition of the four quadrants in the $u_s\sqrt{\bar{u}} - v_s\sqrt{\bar{u}}$ plane. No quadrant-hole analysis has been applied, namely fluctuations of all magnitudes have been included. The flux $\langle\Phi_s\rangle|_q$ in the quadrant q is calculated as in Equation (3-11)

$$\langle\Phi_s\rangle|_q = -\bar{u}\langle u_s v_s\rangle|_q \tag{3-11}$$

where

$$\langle u_s v_s\rangle|_q = \frac{1}{N}\sum_{k=1}^{N} u_s(t_{k,\varphi})v_s(t_{k,\varphi})\, J_q\left[u_s(t_{k,\varphi})v_s(t_{k,\varphi})\right] \tag{3-12}$$

with

$$J_q(u_s, v_s) = \begin{cases} 1, & if\ (u_s, v_s)\ is\ the\ quadrant\ q \\ 0, & \geq otherwise \end{cases} \tag{3-13}$$

3.3 Analysis Of The Tip-Vortex Instability

In section 3.3.1, the topology of the flow in the regime of leapfrogging vortices is shown, highlighting the vortex core locations, divergent and convergent separatrices and saddle points. The latter is of particular interest in the analysis of fluxes and turbulence production rate. Section 3.3.2 and 3.3.3. comment on the distribution of the mean-flow kinetic-energy flux and turbulence production.

3.3.1 Vortex Flow, Cores And Saddle Points

The vortex cores can be identified after calculating the phase-locked vorticity field as in Equation (2-3) where the *z*-direction corresponds to the out-of-plane direction in the rotor frame of reference (Figure 3-1) and applying Equation (3-14):

$$x_{core} = \frac{\sum_{n,m} x_{n,m} \langle \omega_z \rangle_{n,m} dA}{\sum_{n,m} \langle \omega_z \rangle_{n,m}\, dA} \qquad y_{core} = \frac{\sum_{n,m} y_{n,m} \langle \omega_z \rangle_{n,m} dA}{\sum_{n,m} \langle \omega_z \rangle_{n,m}\, dA} \tag{3-14}$$

where dA is the discrete portion of an area A encompassing the vortex and n and m are column and row indices of the two-dimensional matrices x, y, and ω. The equation is the average of the position vector weighted over a distribution of vorticity (Ferreira, 2009). The convection velocity U_c at the vortex cores can be calculated by estimating the time-average velocities $\bar{u}$ and $\bar{v}$ (see Figure 2-12 and Figure 2-13) at the locations of the vortex cores for several vortices at both tip speed ratios. The axial convection velocity U_c is estimated as $U_c / U_\infty = 0.67 \pm 0.002$ for $\lambda = 4.8$ and $U_c / U_\infty = 0.65 \pm 0.005$ for $\lambda = 6$ (with 95% confidence interval) and can be considered constant in the region of interest. The vertical convection velocity is found to be almost two orders of magnitude smaller than U_c in the region swept by the vortex passage, and as such is neglected. The same assumption has been adopted by Antonia et al (1986). Consequently, the velocity fields in Figure 3-2 are representative of the two-dimensional velocity field $[\bar{u} + \tilde{u} - U_c]$, $[\bar{v} + \tilde{v}]$ as seen by an observer travelling with the vortex convective velocity U_c. The stream-line pattern identifies the location of the saddle points between the vortex pairs and slopes of the convergence and divergent separatrices. The close-ups of Figure 3-2 show the pairwise organization of the vortices, separated by stream-line saddle points A1, B1, A2, B2. The two arrowed lines indicate the convergent and divergent separatrices connecting two consecutive vortices. The absolute inclination of the divergent separatrices with respect to the wake centre-line varies during the wake evolution due to the wake expansion (which deflects the shear layer in the very near wake) and to the leapfrogging. The relative value of the separatrix inclination with respect to the vortex-pair middle plane was estimated to be approximately 40°, in good agreement with the findings of Antonia et al (1987). This value is constant at all locations, also during the leapfrogging.

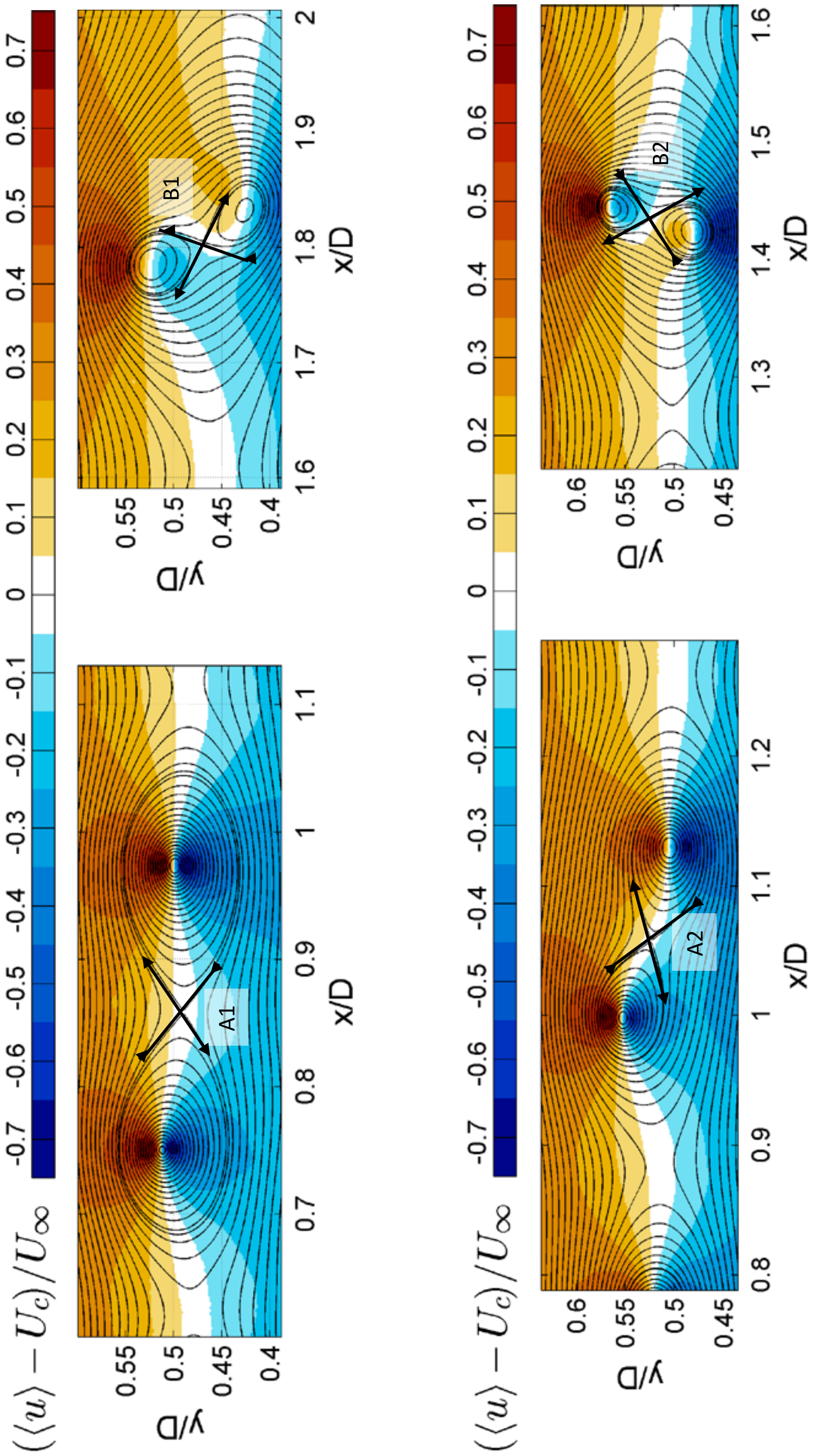

Figure 3-2. Normalised phase-locked average axial velocity field at λ = 4.8 (left figure) and λ = 6 (right figure). Close-ups on the tip-vortices before and during leapfrogging

3.3.2 Mean-Flow Kinetic-Energy Flux

The rapid increase in the kinetic energy content of the wake has been observed to begin after the tip-vortices have paired and completed an approximately 90° rotation around their saddle points (Lignarolo et al, 2014). This location coincides with the onset of a three-dimensional breakdown of the helical vortices inducing a more efficient mixing, dominated by random fluctuations. Previous studies have shown that this phenomenon induces a reorientation of the azimuthal vorticity towards the streamwise direction, in turn enhancing the mixing (Violato and Scarano, 2011, Widnall and Sullivan, 1973, Yule, 1978). However, the relative importance of the coherent vortical structures and the random flow fluctuations is in the transport of the mean flow kinetic energy remains to be quantified in order to draw a conclusive statement on the process dominating wake re-energising. For this purpose, it is useful to consider the spatial distribution of the mean-flow kinetic-energy flux. Prior to proceeding with the analysis, two spurious contributions affecting the phase-locked-average u_{RMS} are quantified that arise from PIV measurement uncertainty. A typical value of 0.1 pixel standard-error is associated with a three-point fit of the correlation peak (see Ragni et al, 2009). For the 400 samples used in the phase-averaging, the relative error on the turbulent velocity fluctuations $\langle u_{RMS}\rangle$ is estimated as 0.1%, 0.3% and 0.6%, where $\langle u_{RMS}\rangle$ is 30% , 10% and 4% of the free-stream velocity respectively, which is a negligible contribution (see Benedict and Gould, 1996, and Humble, 2008). The second spurious effect is due to the so-called *vortex wandering* effect, namely the random fluctuation of the location of the vortex core in time (Dobrev et al, 2008). An *a posteriori* evaluation of the importance of this aspect has been carried out by re-aligning all the images of each PIV dataset with the location of a chosen vortex core, respectively, in the near wake and in the leapfrogging region (see Vandernoot et al, 2008) at $x/D = 0.69$ and $x/D = 1.45$. The wandering of the vortex contributes to the $\langle u_{RMS}\rangle$ peaks at the vortex core locations with an additional 3% in the near wake and an additional 8% in the leapfrogging region, but no effect of re-centering has been observed outside the vortex core, in the region where most of the analysis is carried out.

Figure 3-3 depicts the radial profiles of mean-flow kinetic energy at five different locations in the wake shear layer, whose transport in space for one phase is described by Equation(3-6). The location at $x/D = 1.4$ is within the leapfrogging region and shows the characteristic splitting of the shear layer, also noted in Chapter 2. The terms $\langle\widetilde{\Phi}\rangle = -\bar{u}\langle\tilde{u}\tilde{v}\rangle$ and $\langle\Phi_s\rangle = -\bar{u}\langle u_s v_s\rangle$ in (3-7) represent the fluxes in the *x*-*y* plane of the mean-flow kinetic energy at a selected phase by the respective actions of the periodic (Figure 3-4) and random fluctuations (Figure 3-5). Positive values represent downward fluxes of kinetic energy and, therefore, energy entrained in the inner part of the wake. By looking at both tip-speed ratios, two zones can be identified in Figure 3-4 and Figure 3-5. The first one is located before the vortex leapfrogging where the wake expansion occurs. In this region the tip-vortices are the only ones determining a mean flow kinetic energy transport across the wake layer, both positive and negative contributions of similar magnitude are present in this area. The second zone is located after the wake instability and the tip-vortex breakdown. This area is characterised by solely positive flux corresponding to a downward net entrainment of kinetic energy. Here the random turbulent motions have a dominant role in the recovery process entraining flow towards the inner region of the wake. The beginning of the second zone can be identified in proximity of the position where the vortex pairs are about to complete a 90 degree rotation around their saddle points. This locates at $x/D \sim 1.5$ for $\lambda = 6$ and at $x/D \sim 1.7$ for $\lambda = 4.8$. It must be noted that at both tip-speed ratios the phenomenon happens after the same number of evolutions of the tip-vortex helix.

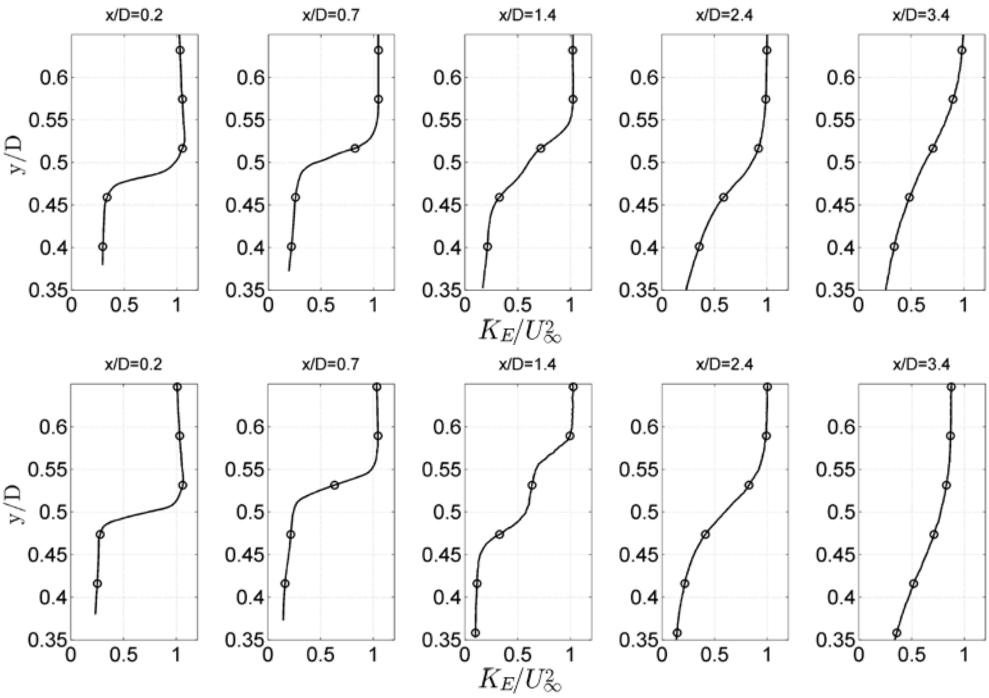

Figure 3-3. Radial profiles of mean-flow kinetic energy at five different locations in the wake shear layer at λ = 4.8 (top image) and λ = 6 (bottom image).

In order to evaluate the net transport of kinetic energy, $\langle\widetilde{\Phi}\rangle$ and $\langle\Phi_s\rangle$ are integrated and averaged in space. Figure 3-6 and Figure 3-7 (respectively for λ = 4.8 and λ = 6) show two different spatial integrals of the mean-flow kinetic-energy flux. The quantities IF_{per} and IF_{rdm} are the area average of $\langle\widetilde{\Phi}\rangle$ and $\langle\Phi_s\rangle$ respectively, calculated in different sections of the wake shear layer as in Equation (3-15):

$$IF_{per} = \frac{1}{AU_\infty^3}\int_A \langle\widetilde{\Phi}\rangle dxdy \qquad IF_{rdm} = \frac{1}{AU_\infty^3}\int_A \langle\Phi_s\rangle dxdy \tag{3-15}$$

where A is the area of each section. The streamwise extension of a section corresponds to the distance travelled by a vortex during a complete blade rotation. The limits of each section are indicated by the black arrows in Figure 3-5 and reported in the x-axes of Figure 3-6 and Figure 3-7 (graphs on the left). The quantities CSF_{per} and CSF_{rdm} are the cumulative sums of the area integral of $\langle\widetilde{\Phi}\rangle$ and $\langle\Phi_s\rangle$ respectively, calculated as in Equation (3-16):

$$CSF_{per} = \frac{1}{dA\cdot U_\infty^3}\int_0^x\int_{in}^{out}\langle\widetilde{\Phi}\rangle dxdy \quad CSF_{rdm} = \frac{1}{dA\cdot U_\infty^3}\int_0^x\int_{in}^{out}\langle\Phi_s\rangle dx\,dy \tag{3-16}$$

The infinitesimal area integrals $\int_{in}^{out}\langle\widetilde{\Phi}\rangle dxdy/dA$ and $\int_{in}^{out}\langle\Phi_s\rangle dxdy$ are calculated across the wake shear layer, from innermost to the outermost radial locations available in the section dA with streamwise extension dx. This quantity allows one to observe the streamwise evolution of the total energy entrained in the wake.

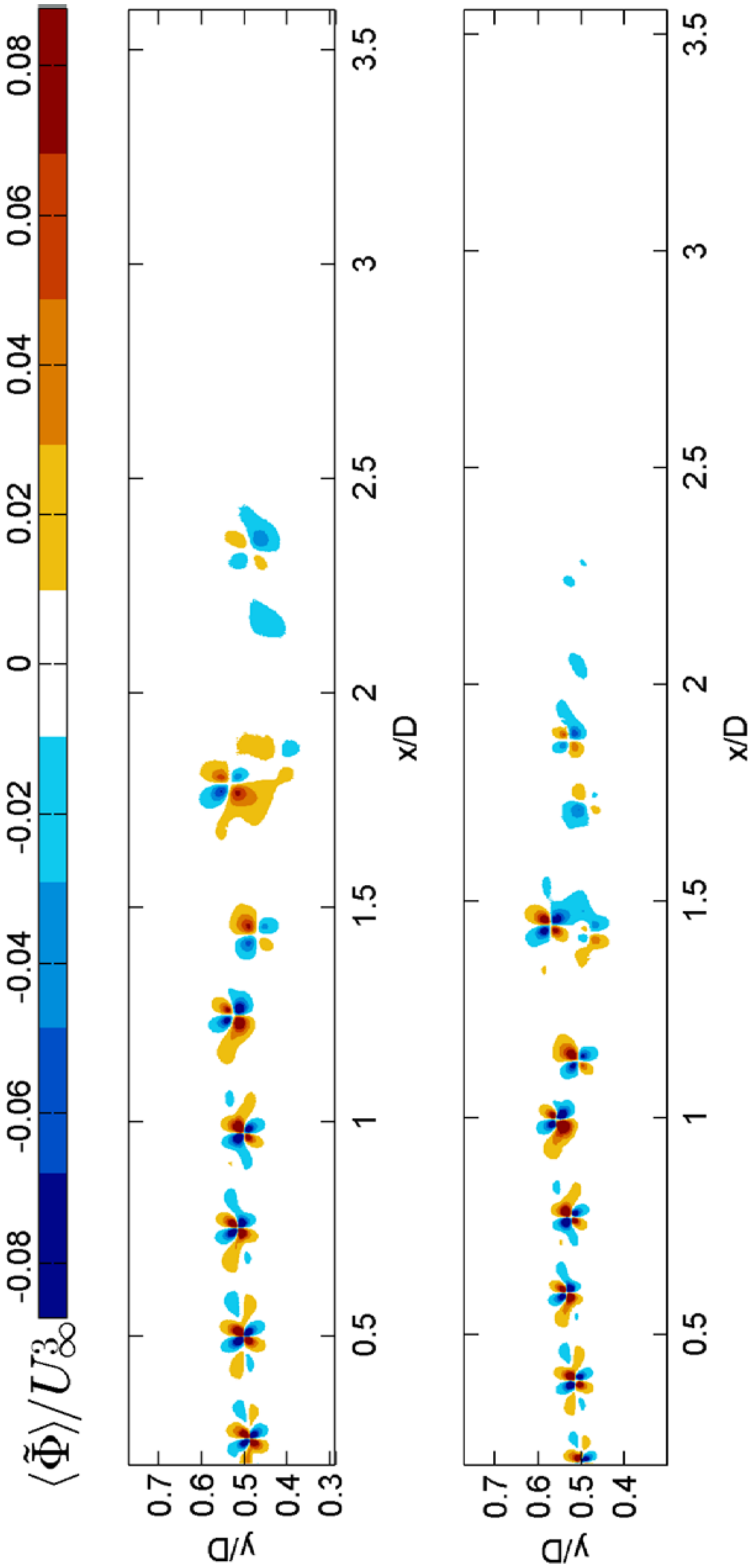

Figure 3-4. Mean flow kinetic energy transport due to the periodic fluctuation at λ = 4.8 (left image), and λ = 6 (right image).

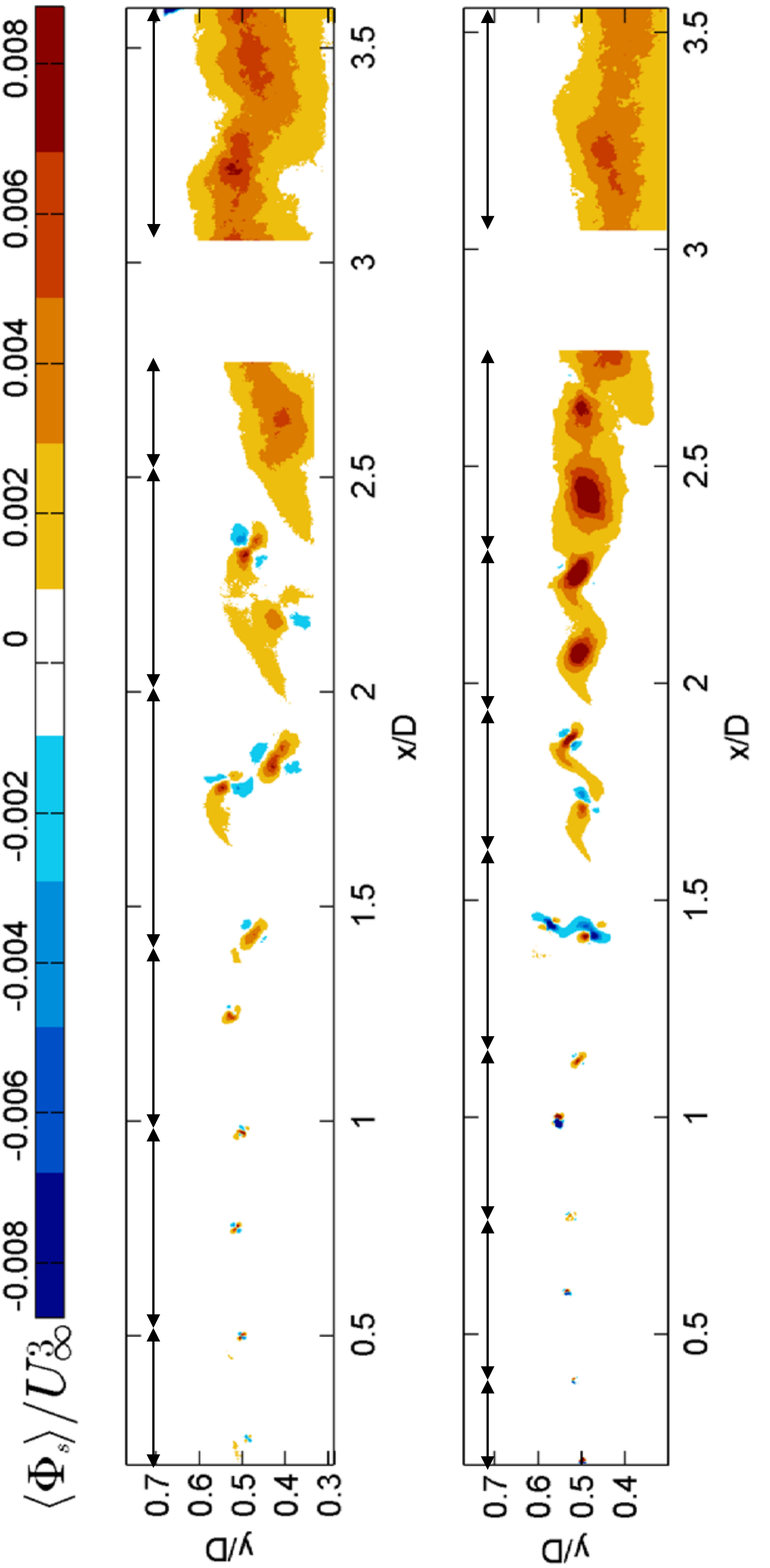

Figure 3-5. Mean flow kinetic energy transport due to the random fluctuations, at $\lambda = 4.8$ (left image), and $\lambda = 6$ (right image).

At $\lambda = 6$ the values of IF_{per} in Figure 3-7 (top image) are generally close to zero, also in the proximity of the rotor, where the periodic fluctuations are stronger. This shows that in fact the positive and negative flux areas depicted in Figure 3-4 are compensating for each other. A peak of positive flux in the area between 0.8 *D* and 1.1 *D* is visible immediately before the beginning of the leapfrogging region. After this location, the value of the flux is generally negative, and quickly returns to zero after 2.4 *D*.

The CSF_{per} curve in Figure 3-7 (bottom iamge) shows that there is a net positive kinetic energy transport until 1.5 *D* (the location where the tip-vortices have paired and completed a 90 degrees rotation around their saddle points), which then turns into a decreasing trend due to the beginning of an overall negative transport. The total balance of the transported energy by the action of the periodic motion is nearly zero as indicated by the value of CSF_{per} after 2 *D*.

The values of IF_{rdm} in Figure 3-7 (top image) are positive everywhere, characterised by a very low magnitude in the near wake and a sudden rapid increase in the region between 1.1 *D* and 1.7 *D*, as also evident in the cumulative sum in Figure 3-7 (bottom image).

In Figure 3-6 (top image), the values of IF_{per} at $\lambda = 4.8$ have a behaviour similar to the exhibited at $\lambda = 6$, with value everywhere very close to zero, with the exception of the leapfrogging region, where the positive flux is much higher and followed by a negative peak of comparable intensity. This inversion of the direction of $\langle\tilde{\Phi}\rangle$ present in both tip-speed ratios is strictly related to the orientation of the vortex pairs and will be discussed in section 3.4.

The cumulative sum CSF_{per} in Figure 3-6 (bottom) again shows a peak at the location where the tip-vortices are about to complete a 90° rotation and the $\langle\tilde{\Phi}\rangle$ inversion takes place, but then it does not fall to zero, meaning that for this tip-speed ratio the total kinetic energy transported by periodic motion is still positive (although very low) in the wake region considered. CSF_{per} and IF_{per} at $\lambda = 4.8$ have a general behaviour similar to that at $\lambda = 6$.

The analysis of the mean-flow kinetic-energy flux has shown the absence of considerable mixing and entrainment of kinetic energy in the very near wake under the action of both periodic and random flow fluctuations. Also, the analysis of the total balance (CSF_{per} curves) has shown how the tip-vortices have a zero or negligible contribution to the mixing, confirming the hypothesis of Medici (2005) about the tip-vortex *shielding* effect.

Figure 3-8 shows the results of the quadrant analysis of the mean-flow kinetic-energy flux due to the random fluctuations (four close-ups in selected shear layer sections). Only the results for $\lambda = 6$ have been shown, since $\lambda = 4.8$ leads to the same conclusions. Positive fluxes due to sweep and ejection events have been summed together (Figure 3-8 top), as the negative contributions due to outward and inward interactions (Figure 3-8 bottom). In the near wake region, the location of the tip vortices has been visualized with streamlines forming convergent and divergent separatrices. The contours in the first and second regions show that most of the random fluctuations in the wake shear layer are due to sweep and ejection events, causing a positive flux of mean-flow kinetic-energy. These positive contributions are located in the regions along divergent separatrices. Some peaks of the flux are also observed at the very centre of the vortex cores. The latter, however are ascribed to a locally higher experimental error, as discussed in section 3.3.2. This means that in the random fluctuations along the divergent separatrices the terms u_s and v_s are anti-correlated. In the second region, the divergent separatrices shows a peak of inward and outward interactions causing a negative flux: the process of leapfrogging induces a re-orientation of the turbulent fluctuations, leading to the u_s - v_s correlation to locally switch sign. The concept is further developed in section 3.4. In the far wake (fourth location), after the tip-vortex breakdown, sweep and ejection events induce a positive flux encompassing the whole shear-layer. Negative contributions, caused by outward and inward interactions are much less frequent and concentrated in proximity of the vortex cores only.

Figure 3-9 shows the cumulative sum CSF_{per} (dashed lines with triangles) of the spatially-integrated contribution of the periodic motion to the total mean-flow kinetic-energy flux decomposed into four quadrant contributions (both tip-speed ratios). As expected, positive contributions (sweep and ejection events) and negative contributions (outward and inward interactions) are of the same magnitude, leading to a quasi zero net flux, with the exception of the region preceding the leapfrogging. Figure 3-9 (bold lines with circles) shows the results of the quadrant analysis applied to the cumulative sum CSF_{rdm} of the spatially-integrated flux. The total of the sweep and ejection events contribute equally to the total positive flux and so do the inward and outward interaction to the total negative flux, with the former ones having a magnitude approximately four times larger than the latter ones. It must be noted that the sum of the four quadrants contributions (in both random and periodic motions) results in the same curves plotted in Figure 3-6 and Figure 3-7.

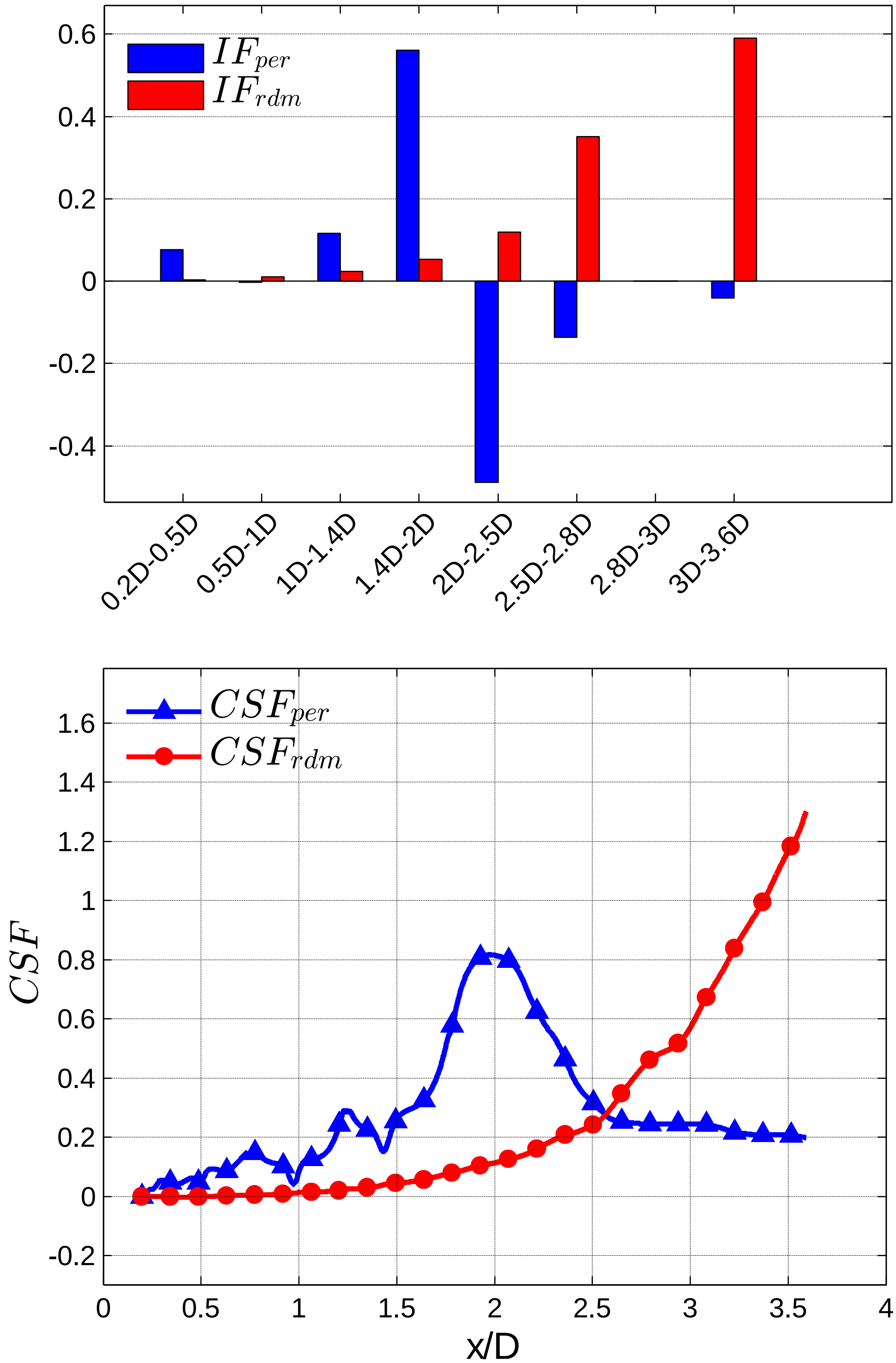

Figure 3-6. Spatial integrals IF_{per} and IF_{rdm} in different sections of the wake shear layer (top image) and the cumulative sums CSF_{per} and CSF_{rdm} of the periodic and random flux respectively (bottom image) at λ = 4.8.

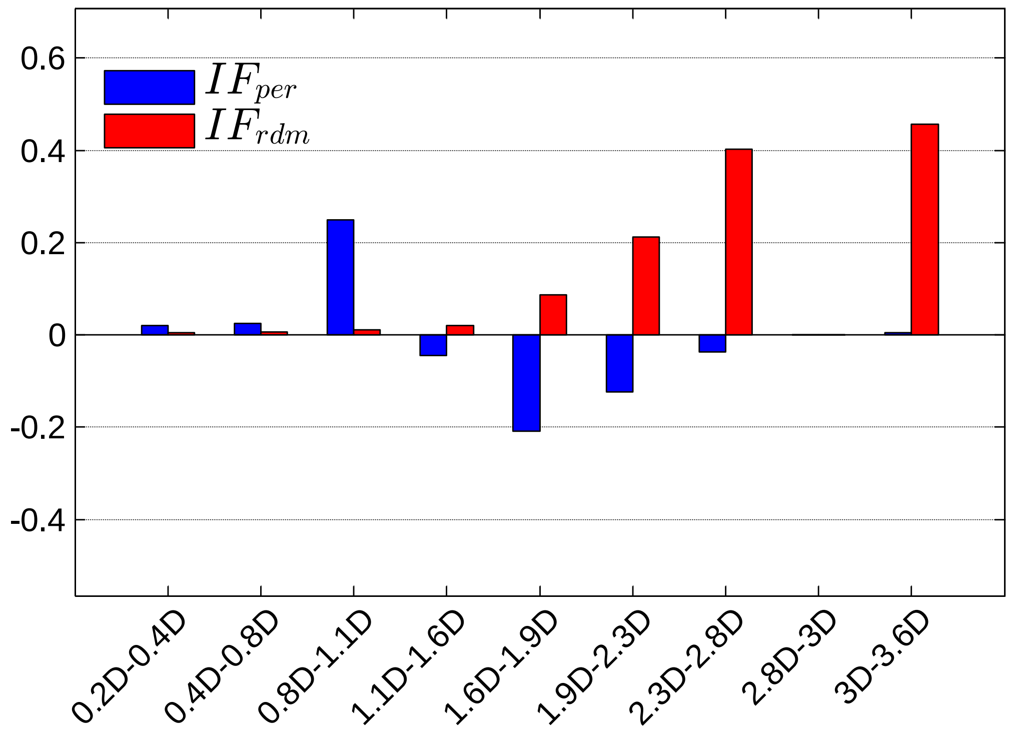

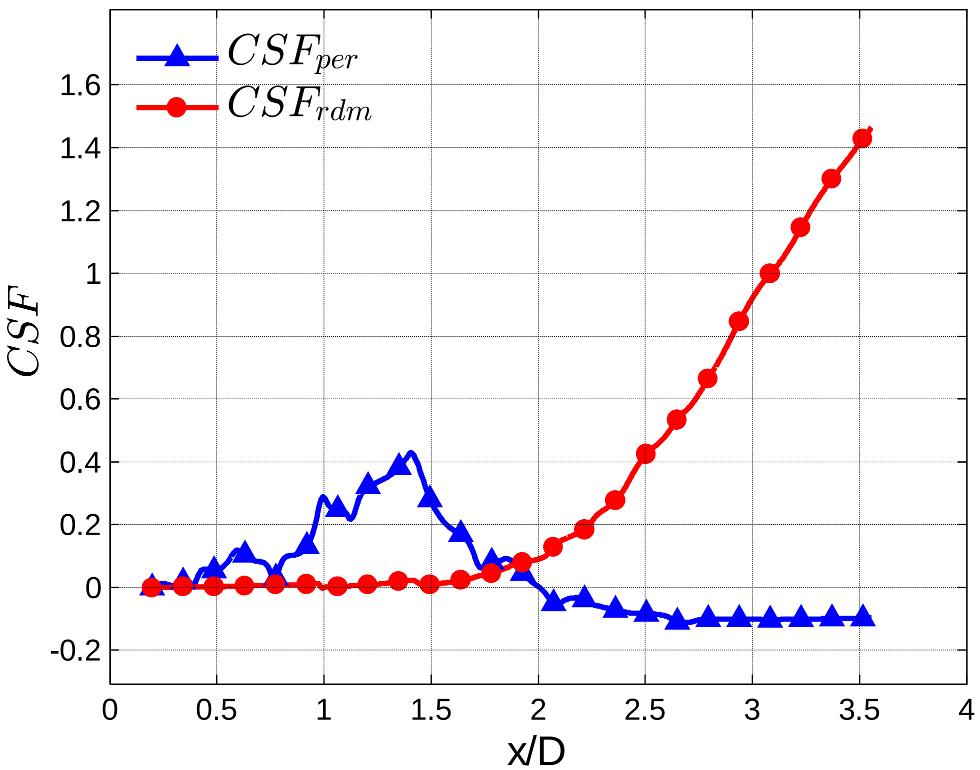

Figure 3-7. Spatial integrals IF_{per} and IF_{rdm} in different sections of the wake shear layer (top image) and the cumulative sums CSF_{per} and CSF_{rdm} of the periodic and random flux respectively (bottom image) at $\lambda = 6$.

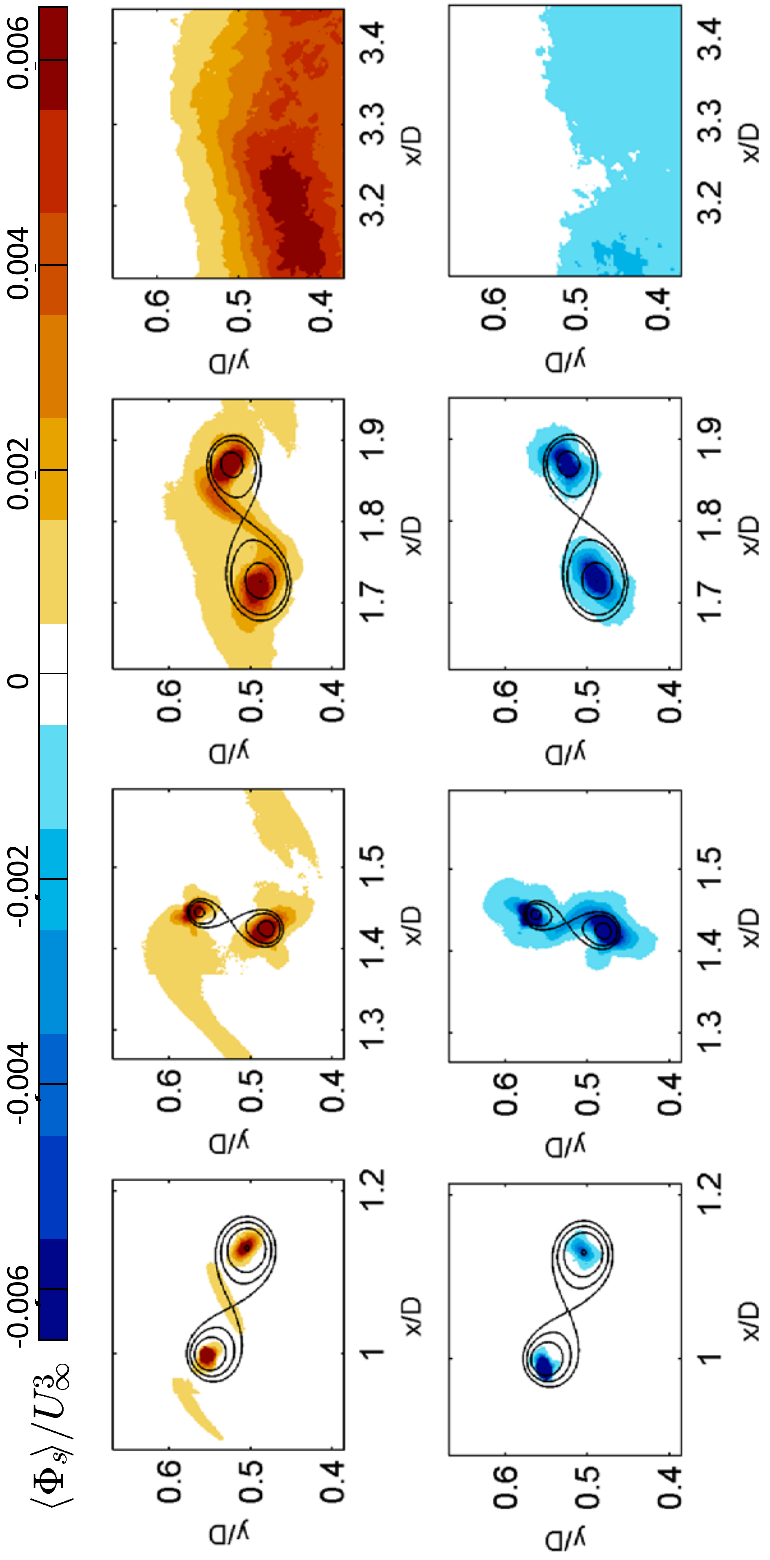

Figure 3-8. Quadrant analysis applied to ⟨Φ_s⟩ at λ = 6. The first row shows the sum of the sweeps and ejections causing a positive flux. The second row shoes the sum of inward and outward interactions, causing a negative flux. In the first three locations, the vortex pair is followed during the leapfrogging process. The last location is taken in the far wake.

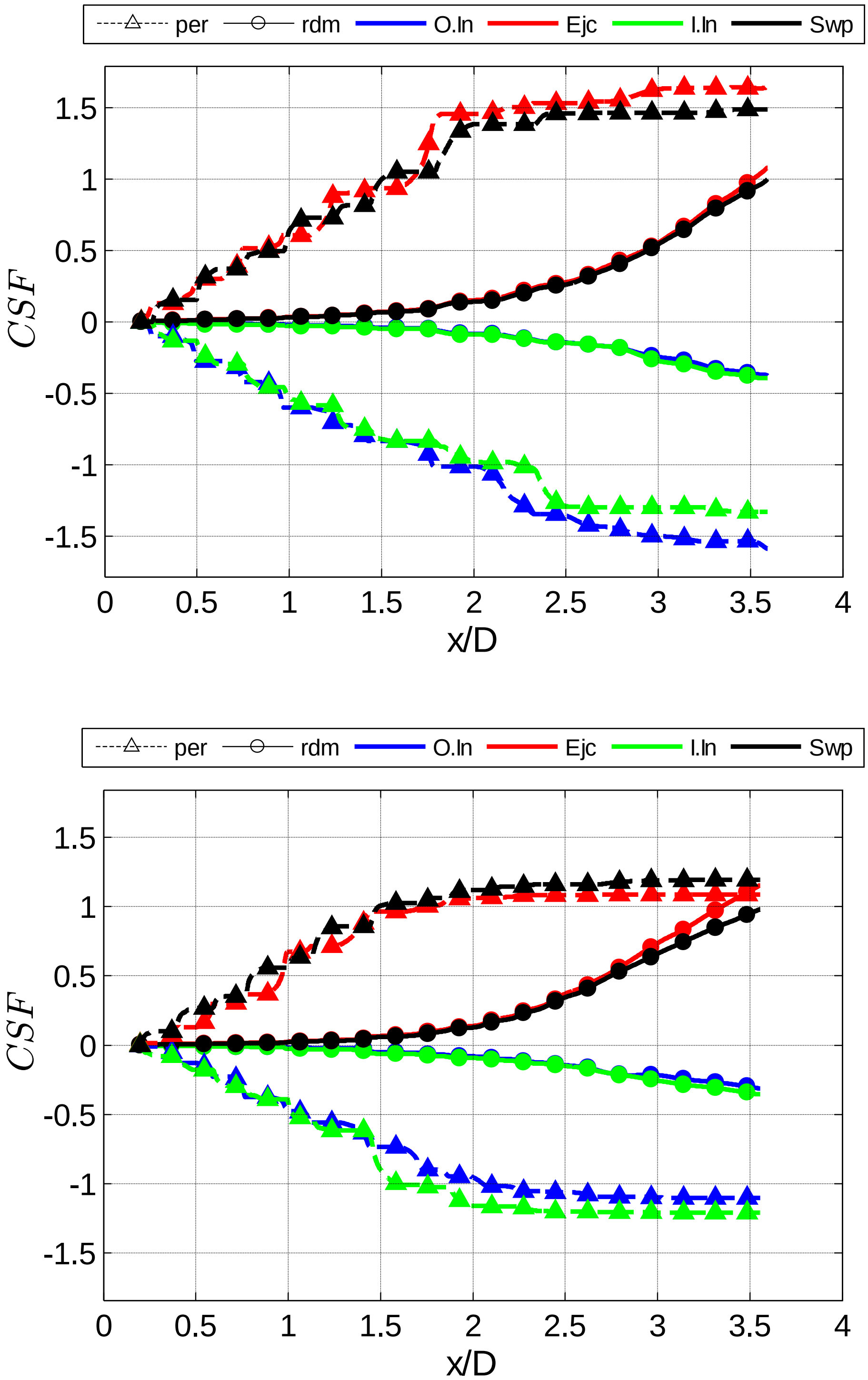

Figure 3-9. Quadrant analysis applied to $\langle \Phi_S \rangle$ at $\lambda = 4.8$ (left) and at $\lambda = 6$ (right). The images show the cumulative sum CSF_{per} and CSF_{rdm} decomposed into four quadrant contributions. The dashed lines with triangles and the bold lines with circles represent the contributions of the periodic and random motions respectively. The abbreviations *O.in*, *Ejc*, *I.In* and *Swp* refer to outward interactions, ejections, inward interactions and sweeps respectively.

3.3.3 PRODUCTION OF TURBULENT KINETIC ENERGY

Figure 3-3 depicts the radial profiles of the turbulence intensity at five different locations in the wake shear layer. This represents the turbulence relative to the unconditioned-averaged field, as such including contributions from both contributions from periodic and random fluctuations with no distinction. The production of turbulence for one phase is described by Equation (3-9).

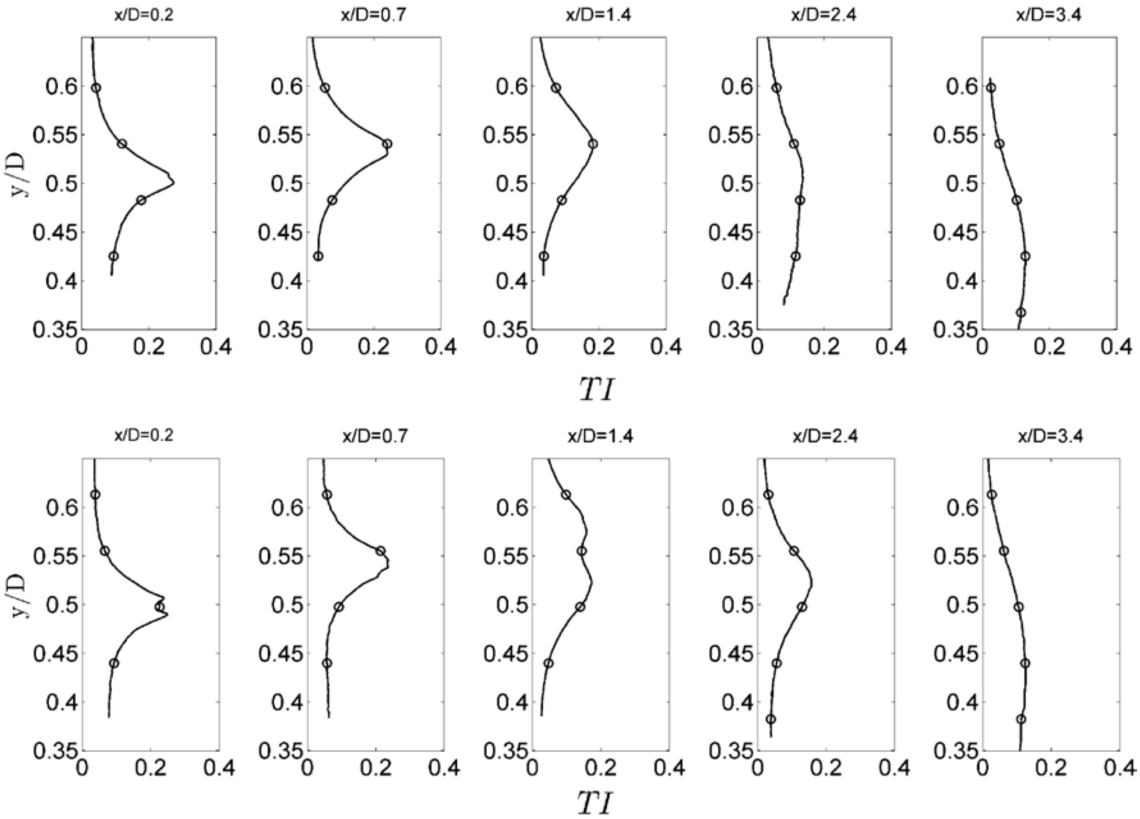

Figure 3-10. Radial profiles of turbulence intensity relative to the unconditioned-averaged field at five different locations in the wake shear layer at λ = 4.8 (top image) and λ = 6 (bottom image).

Figure 3-11 shows the contour level of the normalised phase-locked production of turbulent kinetic energy $\langle Pe \rangle$ calculated as in (3-9). This quantity represents the decay into turbulence of the kinetic energy of the mean flow and of the periodic flow structures. In Figure 3-11, the contours of $\langle Pe \rangle$ are stronger in the region along the divergent separatrices, as well as the proximity of the vortex core. The production of turbulence values along the divergent separatrix for both tip-speed ratios reach their maxima in the leapfrogging location. This finding shows similarities between the behaviour of the vortical structures in the cylindrical shear layer of a wind turbine wake and in bluff body wakes or planar mixing layers. These findings confirm previous observations of Hussain (1981), who noted that the turbulence is produced mainly in the braids between the large vortices along the divergent separatrix and then transported to and accumulated in the vortices, as well as those of Cantwell and Coles (1983) and Antonia et al (1987), who showed that the saddle points between two consecutive vortices are zones of large production of turbulent kinetic energy.

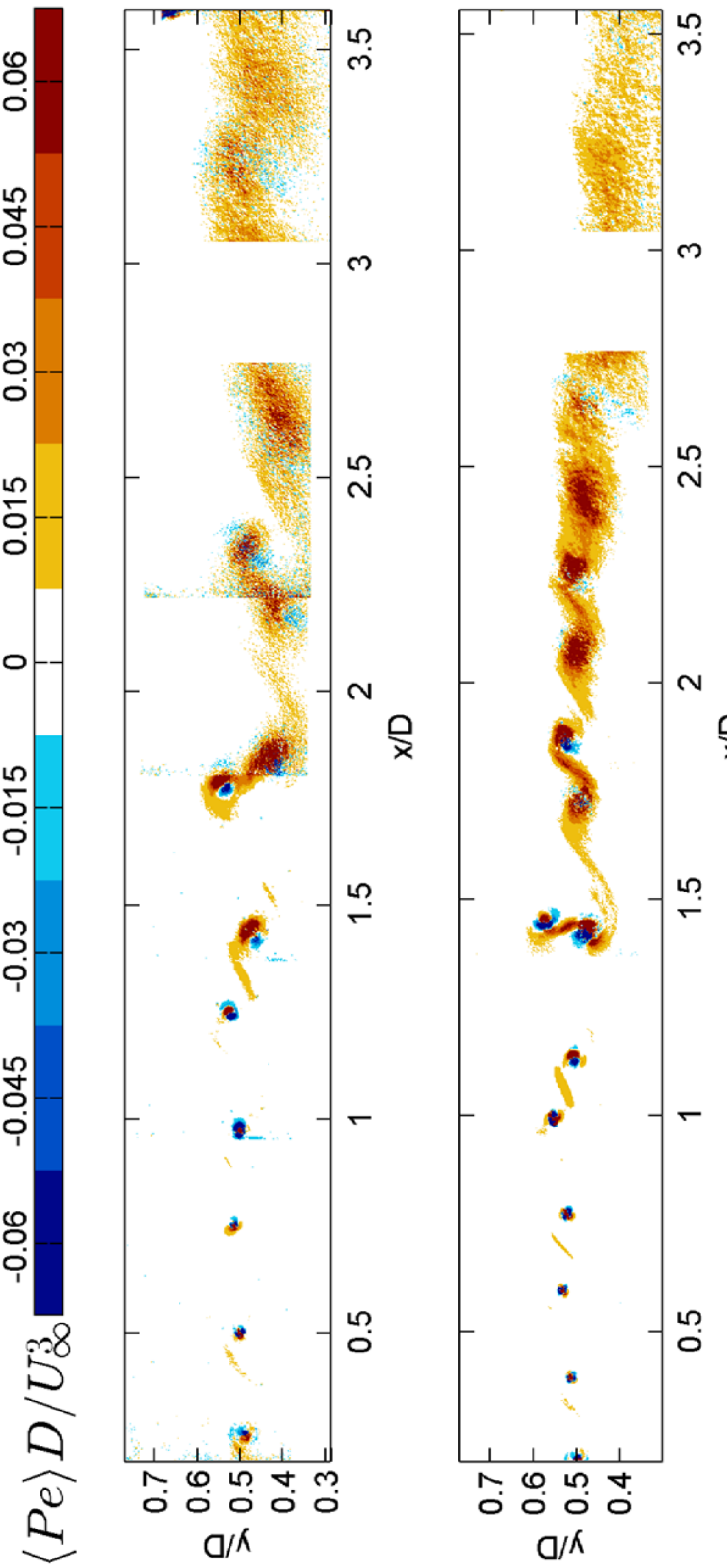

Figure 3-11. Total turbulent kinetic energy production $\langle Pe \rangle = \langle Pe_{p-t} \rangle + \langle Pe_{m-t} \rangle$ at λ = 4.8 (left image), and λ = 6 (right image).

Figure 3-12 and Figure 3-13 (respectively for $\lambda = 4.8$ and $\lambda = 6$) show the spatial integrals of the turbulence production, similarly to what presented in section 3.3.2. The quantities $IP_{m\text{-}t}$ and $IP_{p\text{-}t}$ are the area average of $\langle Pe_{m-t}\rangle$ and $\langle Pe_{p-t}\rangle$ respectively, calculated in different sections of the wake shear layer as in Equation (3-17):

$$IP_{m-t} = \frac{D}{AU_\infty^3}\int_A \langle Pe_{m-t}\rangle dxdy \qquad IP_{p-t} = \frac{D}{AU_\infty^3}\int_A \langle Pe_{p-t}\rangle dxdy \tag{3-17}$$

where $\langle Pe_{m-t}\rangle$ is the phase locked turbulence production due to the decay of the mean-flow kinetic energy and $\langle Pe_{p-t}\rangle$ the phase locked turbulence production due to the decay of the organised periodic structures. The sections (indicated by A) are the same as in Equation (3-15). The quantities $CSF_{m\text{-}t}$ and $CSF_{p\text{-}t}$ are the cumulative sums of the area integral of $\langle Pe_{m-t}\rangle$ and $\langle Pe_{p-t}\rangle$ respectively, calculated as in Equation (3-18):

$$\begin{aligned} CSF_{m-t} &= \frac{D}{dA\cdot U_\infty^3}\int_0^x\int_{in}^{out}\langle Pe_{m-t}\rangle dxdy \\ CSF_{p-t} &= \frac{D}{dA\cdot U_\infty^3}\int_0^x\int_{in}^{out}\langle Pe_{p-t}\rangle dx\,dy \end{aligned} \tag{3-18}$$

As in Equation (3-16), the infinitesimal area integrals are calculated across the wake shear layer, from innermost to the outermost radial locations available in the section dA with streamwise extension dx. Although minor regions characterised by a negative production were visible in Figure 3-11, the balance is positive in total and in each wake section: this is valid for both contributions $\langle Pe_{m-t}\rangle$ and $\langle Pe_{p-t}\rangle$.At both tip-speed ratios, it is evident how the very near wake is characterised by a negligible rate of production. The production due to the decay of the periodic structures is maximum in the instability region where the tip-vortices break down, after which it decreases to negligible values. This is evident in the steep increase of the $CSP_{p\text{-}t}$ in figure Figure 3-12(bottom) at $\lambda =$ 4.8 between 1.5D and 2D and by the more gradual increase in Figure 3-13(bottom) at $\lambda =$ 6 between 1.5D and 2.5D. Past these location, the $CSP_{p\text{-}t}$ curves tend to flatten, indicating no more turbulence production by decay of the periodic structures, because tip vortices have completed their breakdown process. The production due to the mean flow kinetic energy decay $\langle Pe_{m-t}\rangle$ also starts increasing in the instability region together with $\langle Pe_{p-t}\rangle$, for both values of λ, from a quasi-zero value in the near wake, but after the vortex breakdown it maintains large values.

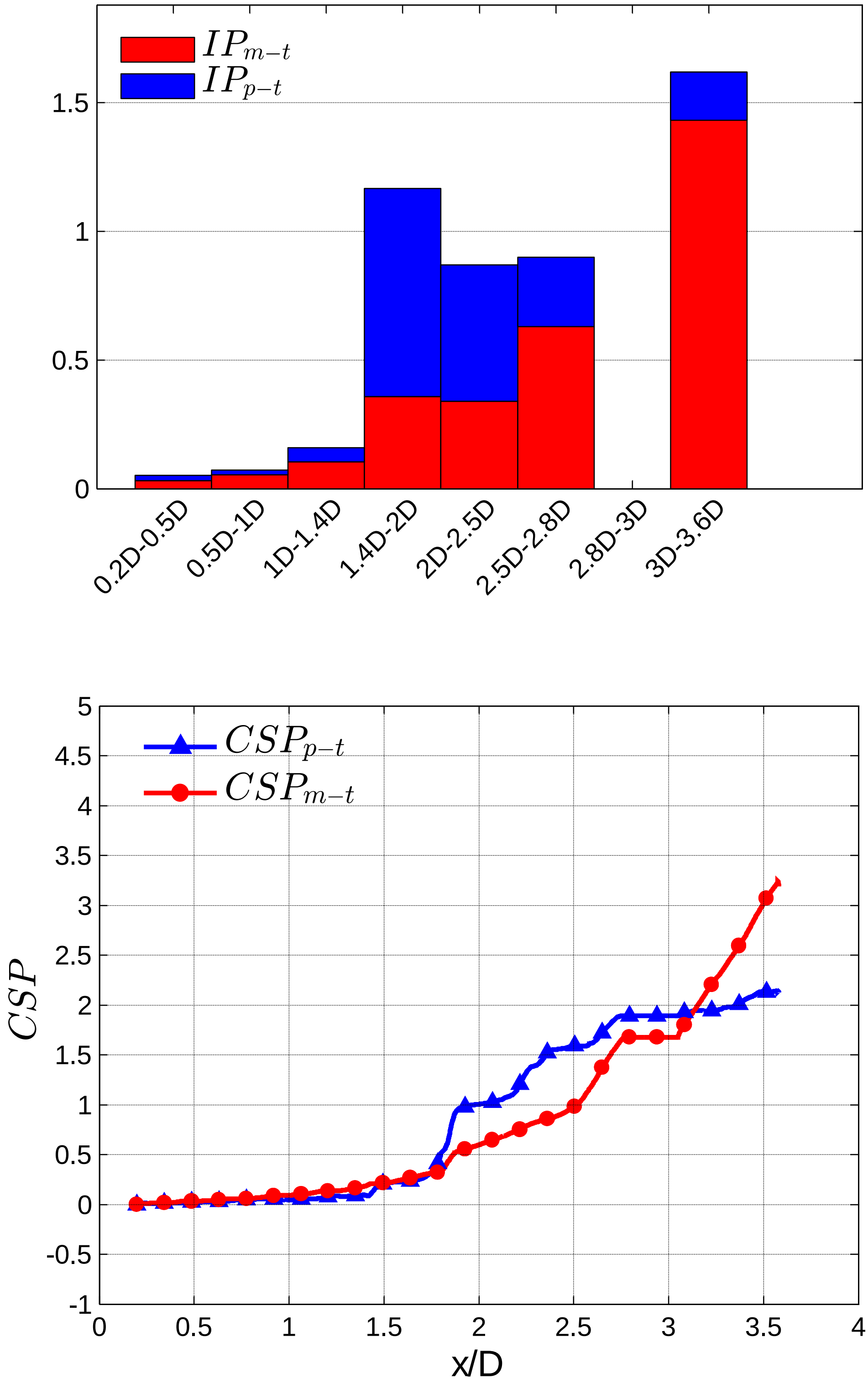

Figure 3-12. Spatial integrals of the production IP_{m-t} and IP_{p-t} for different sections of the wake shear layer (top) and the cumulative sum of the production CSP_{p-t} and CSP_{m-t} (bottom) at λ = 4.8.

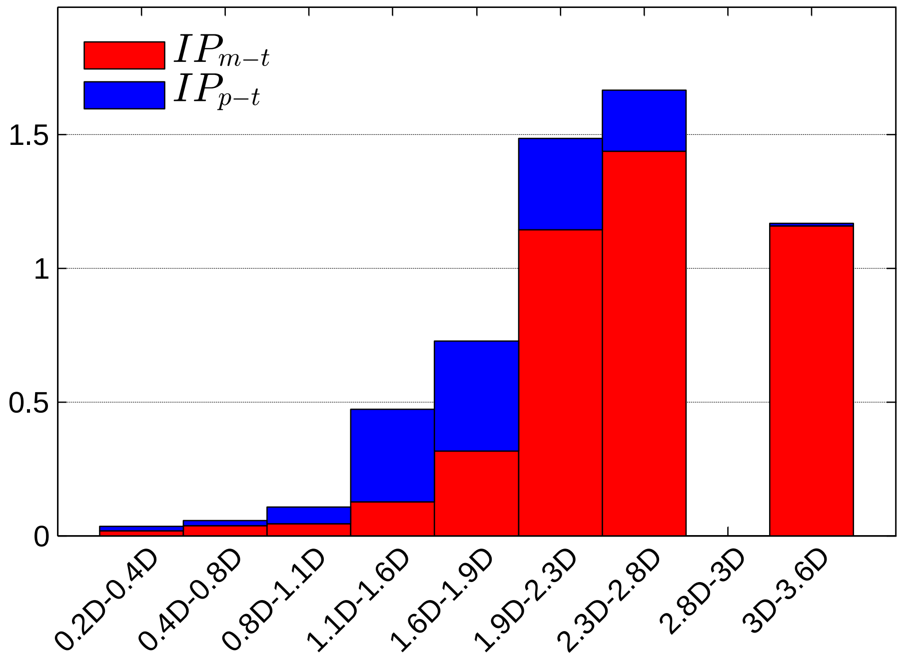

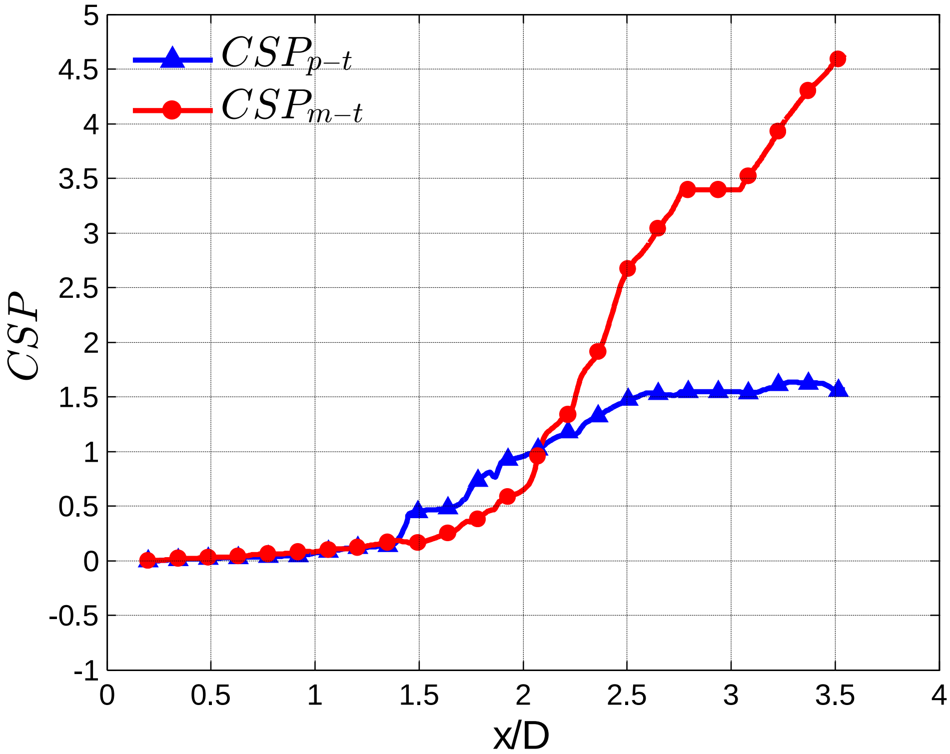

Figure 3-13. Spatial integrals of the production IP_{m-t} and IP_{p-t} for different sections of the wake shear layer (top) and the cumulative sum of the production CSP_{p-t} and CSP_{m-t} (bottom) at $\lambda = 6$.

3.4 Effect of Orientation of the Flow Fluctuations

The analysis of Figure 3-6(left) and Figure 3-7(left) indicated an inversion of the flux $\langle\widetilde{\Phi}\rangle$ direction, present in both tip-speed ratios, although at a different magnitude (at $\lambda = 4.8$ the passage from positive to negative flux is more pronounced). This inversion is caused by the different orientation of the tip-vortex pairs during the leapfrogging process. In particular, in the initial stage of leapfrogging the vortex pairs have a negative inclination (see between 1.4D and 2D at $\lambda = 4.8$ and between 0.8D and 1.1D at $\lambda = 6$ in Figure 3-11) which leads to a strong anti-correlation of $\tilde{u}$ and $\tilde{v}$ and to a positive peaks of $\langle\widetilde{\Phi}\rangle$. In the later stage of leapfrogging, the vortex pairs show a positive inclination (see between 2D and 2.5D at $\lambda = 4.8$ and between 1.6D and 1.9D at $\lambda = 6$ in Figure 3-11), with $\tilde{u}$ and $\tilde{v}$ being oriented so to produce a negative peak of $\langle\widetilde{\Phi}\rangle$. This behaviour is depicted schematically in Figure 3-14. The results suggest that the magnitude of the inversion (which is different for the two tip-speed ratios) depends on the angle of the vortex pair with respect to the wake centreline, namely on the phase of the pairing process. As a matter of fact, despite measurements being taken at the same phase of rotation of the turbine, vortex pairing and leapfrogging happen at different locations at different tip-speed ratios. In the selected phase, the vortex pairs at $\lambda = 6$ have a smaller inclination compared to $\lambda = 4.8$, which causes the smaller magnitude of the inversion visible in Figure 3-6(left).

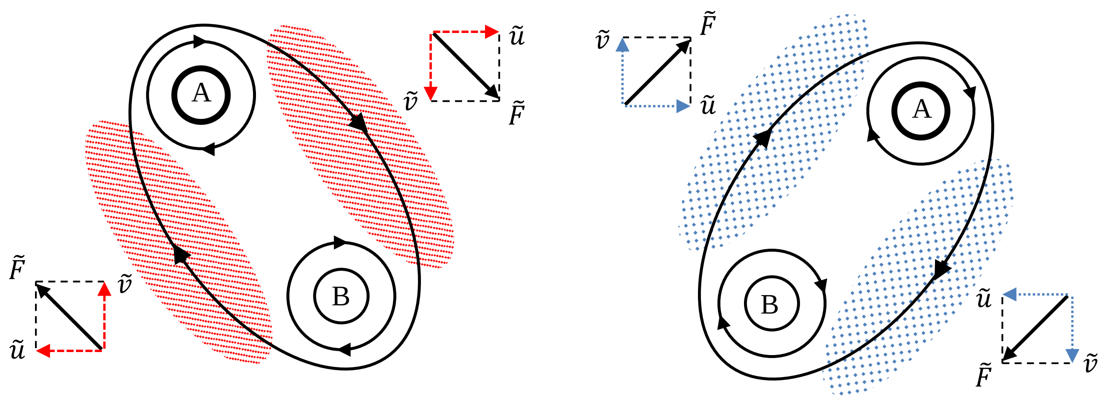

Figure 3-14. Change of orientation of the vortex pairs. On the left, the initial stage of leapfrogging (vortex A leaps over vortex B) causes a negative inclnation of the vortex pair. The red and blue areas indicate the regions where the highest flux is (red and blu indicate respectively positive and negative flux). The bolde lines depicts schematically the streamlines and the black arrows indicate the direction of the flow fluctuation $\tilde{F}$. The coloured arrows indicate the direction of the components $\tilde{u}$ and $\tilde{v}$ (red indicates anti-correlation and blue indicates correlation)

In Figure 3-4, the flux $\langle\widetilde{\Phi}\rangle$ exhibits a peculiar four-lobed structure, which is known from previous literature, such as in the study of (Hussain, 1983). Figure 3-15 schematises this behaviour, showing the different orientations of $\tilde{u}$ and $\tilde{v}$ around each vortex and the origin of the alternating negative and positive flux regions.

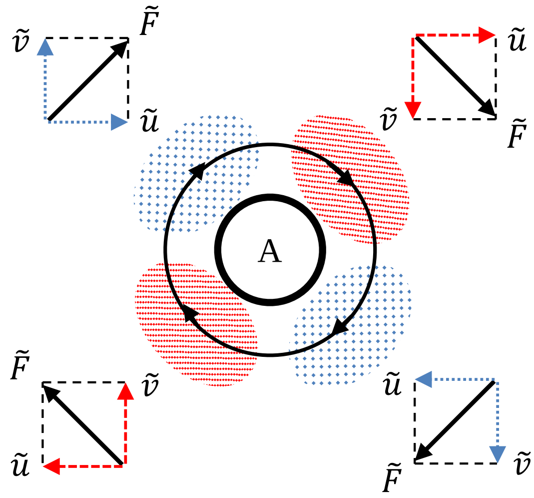

Figure 3-15. Schematic representation of the mean-flow kinetic-energy transport induced by a single vortex. The red and blue areas indicate the regions where the highest flux occurs (red and blue indicate positive and negative flux respectively). The black arrows indicate the direction of the induced velocity fluctuation $\tilde{F}$. The coloured arrows indicate the direction of the components $\tilde{u}$ and $\tilde{v}$ (red indicates anti-correlation and blue indicates positive correlation)

As far as the random motions are concerned, the quadrant analysis in Figure 3-8 indicates a local change of flux orientation, which, from a positive value in the braid region along the divergent separatrix, switches to negative values, during the pairing and leapfrogging phase, and eventually reacquires positive values. This is explained in Figure 3-16, which shows the different orientations of the random fluctuations u_s and v_s in the braid regions between two pairing vortices. Considering the orientation of the separatrices and the results of the quadrant analysis, it can be deduced that random fluctuations are always at an opposite inclination with respect to the divergent separatrices, keeping this relative orientation during the leapfrogging process. In particular, it was calculated that the angle between the random fluctuations and the divergent separatrices is roughly 80°±15° at any location. The contour in Figure 3-11(bottom) shows that, despite the changing absolute orientation of the u_s and v_s, the turbulence production stays positive, showing that while the mean-flow kinetic-energy flux depends on the inclination of the vortex pairs, the turbulence production depends only on the modulus of the random fluctuations. This behaviour is synthesised at the bottom of Figure 3-16.

3.1 Conclusions

An experimental investigation has been performed using SPIV in order to study the evolution of the vortex structure in the wake of a 0.6 m diameter horizontal-axis wind turbine and the influence of the pairing instability of the tip-vortex filaments (leapfrogging) on the evolution of the far-wake turbulence production and mean-flow kinetic-energy transport, which in turn affects the wake re-energising process. The analysis of the interacting vortex pairs shows a general structure in agreement with previous studies on bluff-body wakes and planar jets. In Chapter 2, the qualitative analysis of the flow statistics revealed a major difference between the unconditioned-average and the phase-locked average turbulence-intensity. In the present investigation, transport of the mean-flow kinetic energy and the production of turbulence have been quantified to distinguish the role of periodic structures and of random flow fluctuations in turbulence mixing and in turn to the wake re-energising.

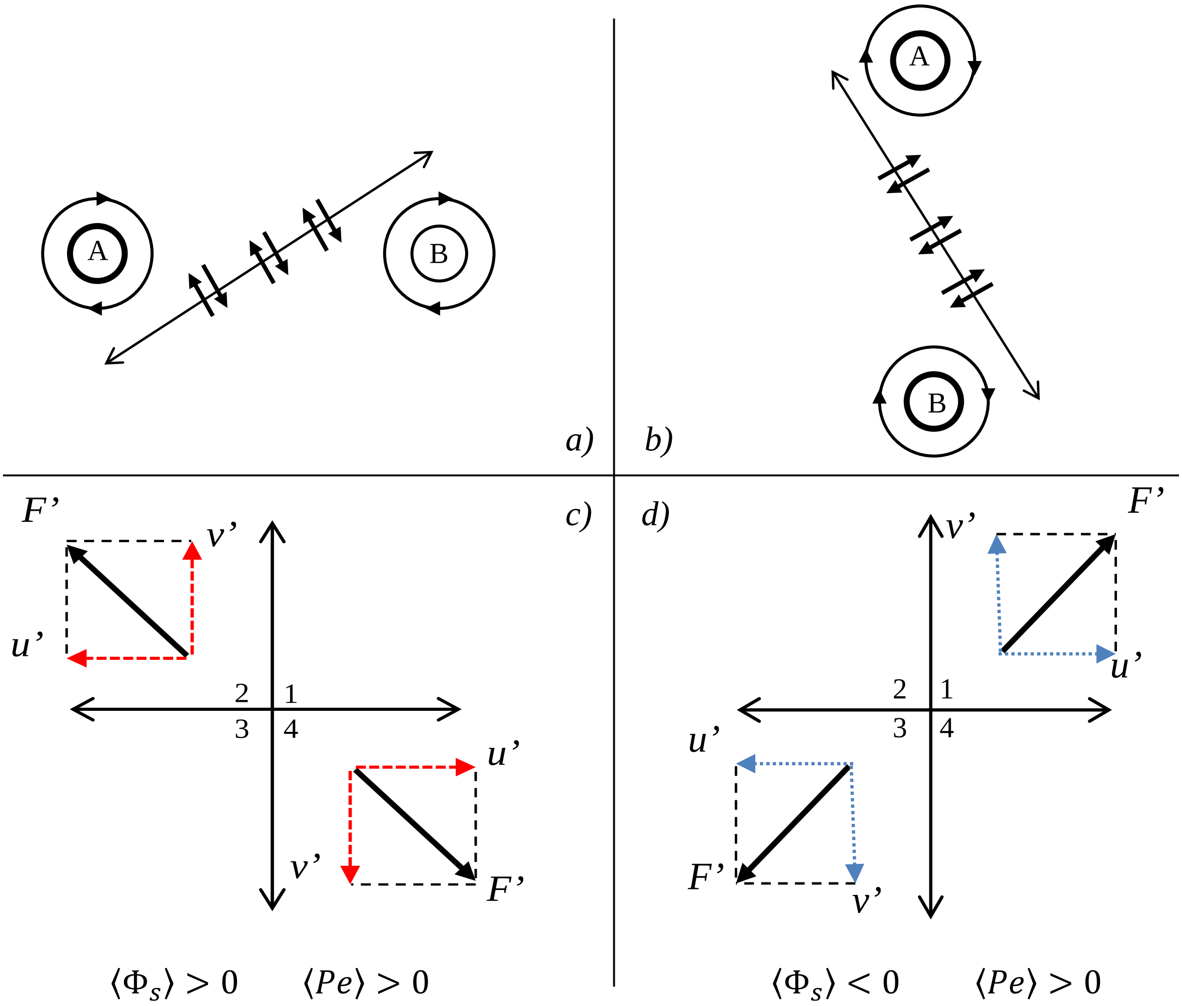

Figure 3-16. Change of orientation of the random fluctuations u_s and v_s during leapfrogging. *a)* and *c)*: before leapfrogging, u_s and v_s are an opposite inclination respect to the divergent separatrix and anticorrelated, leading to a positive flux $\langle \Phi_s \rangle$ and positive turbulence production $\langle Pe \rangle$. *b)* and *d)*: during the leapfrogging u_s and v_s keeps their orientation relative to the divergent separatrix but show positive correlation, leading to a negative flux $\langle \Phi_s \rangle$ and positive turbulence production $\langle Pe \rangle$.

The study demonstrates the fundamentally different roles of the vortex structures and the turbulent fluctuations in the dynamics of the wake turbulence. Both kinds of flow structures are normally accounted for in the estimation of what in wind-energy jargon is called *added turbulence*. The latter represents the flow turbulence caused by the presence of the turbine, which is added to the ambient turbulence (Crespo et al, 1999). This includes both periodic and random velocity fluctuations, which are not separated in a classical double Reynolds decomposition. This leads to the well-known peaks of turbulence intensity close to the rotor at the blade-tip location. However, this is not theoretically correct. In fact, as pointed out by Yule (1978), a vortex is “the flow field accompanying a concentrated, continuous, coherent distribution of vorticity which is uniform in the direction of the vorticity vector and which grows in scale by viscous diffusion alone”, whereas “an eddy may be described as a vorticity-containing region of fluid which can be identified as moving as a coherent structure in a flow”. Also, as demonstrated in this analysis, the concentrated tip-vortices in the near wake provide a strong contribution to the added turbulence, but do not take part in the mixing and the mean-flow kinetic-energy entrainment. Fluctuations due to the passage of tip vortices cannot as such be treated as turbulence, although they obey the same laws of vorticity transport as they are determined by the Navier-Stokes equations. The distinction between the two flow structures is not sharp, but it is their predictability (namely periodicity, in this case) that can be used as distinction. The analysis of the mean-flow kinetic-energy flux suggests the presence of two zones characterised by a different mixing. In the first zone the tip vortices inhibit the mixing of the wake during its expansion; in the second zone the leapfrogging causes a sudden increase of the net entrainment of the mean flow kinetic energy and generates a more efficient mixing by the action of random flow motions, contributing to the wake re-energising. The result is in accordance with the hypothesis of Medici (2005), who stated that the near-wake tip-vortices are acting as a shield, preventing the wake from mixing with the outer flow. Quadrant analysis of the random flow fluctuations showed that the total of sweep and ejection events contribute equally to the total positive flux. Also inward and outward interactions have equal contributions to the total negative flux. The process of leapfrogging causes a re-orientation of the turbulent fluctuations leading to the u_s - v_s correlation switching sign locally along the divergent separatrix. Following the tip-vortex breakdown, sweep and ejection events occupy the whole shear-layer thickness, having total values about four times larger than the inward and outward interactions, concentrated in proximity of the vortex cores only. The analysis of the production of turbulence shows very low values in first region, with an abrupt increase of production rate in the leapfrogging zone. This confirms that the vortex system of the near-wake plays an important role in the production of turbulence and that eddy-viscosity models (only based on mean velocity gradients) fail to represent turbulence production in the near wake of a wind turbine.

4 EXPERIMENTAL COMPARISON OF A WIND TURBINE AND OF AN ACTUATOR DISC WAKE

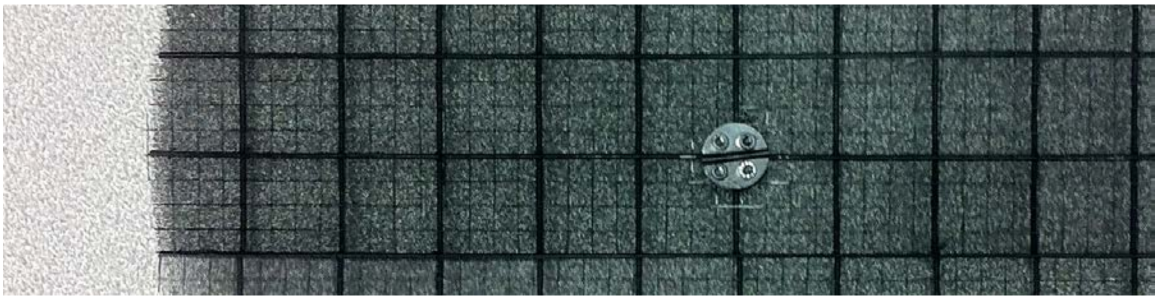

The study in this chapter is aimed at providing an experimental analysis of the near-wake turbulent flow of a wind turbine and a porous disc, emulating the actuator disc numerical model. The general purpose is to highlight the similarities and to quantify the differences of the two models in the near-wake region, characterised by the largest discrepancies. The velocity fields in the wake of a wind turbine model (in the presence of the leapfrogging instability) and a porous disc (emulation of the actuator disc numerical model) have been measured in a wind tunnel using stereo particle image velocimetry using an unconditioned sampling method at a diameter-based Reynolds number of $Re_D = 1.8 \times 10^5$. The data analysis provided the time-average three-component velocity and turbulence intensity fields, pressure fields, rotor and disc loading, vorticity fields, stagnation enthalpy distribution and mean-flow kinetic-energy fluxes in the shear layer at the border of the wake. The properties have been compared in the wakes of the two models. Even in absence of turbulence, the results show a good match in the thrust and energy coefficient, velocity, pressure and enthalpy fields between wind turbine and actuator disc. However, the results show a different turbulence intensity and turbulent mixing. The results suggest the possibility to extend the use of the actuator disc model in numerical simulation until the very near wake, provided that the turbulent mixing is correctly represented.

This chapter is published as:

Lignarolo, L.E.M., Ragni, D., Ferreira, C.J., van Bussel, G.J.W., 2016. Experimental comparison of a wind-turbine and of an actuator-disc near wake. *Journal of Renewable and Sustainable Energy* 8

4.1 INTRODUCTION

Currently in-use wind farm numerical models often struggle to accurately reproduce the flow within a wind farm, in particular at the second row of wind turbines as the incoming flow develops from an atmospheric boundary layer to a wind farm canopy boundary layer. For this reason, the wind energy community is working toward full-wake models, including a better representation of the near-wake flow induced by a more realistic modelling of rotor aerodynamics (Sanz Rodrigo and Moriarty, 2014). The actuator disc is a thin circular region where body forces extract momentum from the flow: it is commonly used for modelling the rotor of an horizontal axis wind turbine for simplifying the numerical simulation of the flow development in a wind farm. This simplification is obtained at the expenses of accuracy in the near wake, which is strongly affected by the presence of the rotating blades, whereas in the far wake this simplification is generally more acceptable (see the numerical analysis by Wu and Porté-Agel (2011) on the far-wake discrepancies in the flow prediction between a wind turbine and an actuator disc). Schepers (2012) notes that the actuator disc approach, in combination with the k-ε turbulence model, leads to strong velocity gradients at the wake edges, causing unphysical turbulence production peaks, which enhance the near-wake mixing. In his review study, he suggests that the actuator disc approach often fails in reproducing the effects of flow turbulence, due to the absence of the blade tip-vortex development and breakdown and writes about the importance of investigating how to reduce the inaccuracy of the actuator disc (AD) model in the wake region within 5 diameters from the rotor. In fact, the incorrect estimation of the near wake turbulence has repercussions on the mixing process across the wake and ultimately on the rate at which the wake recovers flow momentum is incorrectly modelled (Schepers, 2012). With the increased utilization of the wind-farm space, this limitation is no longer acceptable for current engineering applications. For example, in the Lillgrud offshore wind farm rotors are dislocated in grid with spacing between 3.3 and 4.3 diameters (Gaumond et al, 2012), and in the Horns Rev offshore wind farm around 7 diameters (Barthelmie et al, 2007b).

Recent extensive application of the actuator disc model in the numerical simulation of wind farms can be found in the works of Meyers and Meneveau (2012) and Calaf et al (2010b). El Kasmi and Masson (2008) developed a modified k-ε model for actuator disc accounting for energy exchange between large and small scale turbulence structures in the region close to the disc. Nishino and Willden (2012) studied numerically the effect of the near wake mixing on the energy extraction performance of a wind turbine simulated with the actuator disc model. Other examples of actuator disc application in numerical simulations can be found in the thesis of Mikkelsen (2003) and in the reviews from Sanderse et al (2011), Schepers (2012) and Vermeer et al (2003). Despite the popularity of this simplified numerical model, too seldom this has been taken into consideration for wind tunnel studies. The actuator disc can be emulated in a wind tunnel by a porous disc. The device, which can be realised with different techniques, does not extract directly energy from the flow, but has the function to dissipate the kinetic energy of the incoming wind into turbulence and, eventually, into heat. Few studies are available, which analyse the flow field in the near wake of a porous disc with the purpose of emulating a wind turbine wake and examples of various techniques for realising the model can be found.

For instance, Aubrun et al (2013) and Aubrun et al (2007) manufactured a small-scale porous discs using fine metal meshes, while perforated metal plates have been adopted by Medici (2005) and Sforza et al (1981). Pierella and Sætran (2010) realised a porous disc with wooden grids. Nevertheless, a direct experimental comparison of the turbulent flow in the near wake a porous disc with the one of a rotating turbine of the same dimension and axial force, with high-resolution two-dimensional measurements, is currently not available.

The present study is aimed at providing an experimental analysis of the near-wake turbulent flow of a wind turbine (WT) and a porous disc emulating the actuator disc (AD) numerical model. The underlying question is how much the near wake of a WT differs from the one of an AD given similarity of dimension, axial force and extracted energy. The wake velocity field is measured in the low-speed Open Jet Facility (OJF) wind tunnel of Delft University of Technology (TUDelft) with the stereoscopic particle image velocimetry (SPIV) technique. The porous disc is assembled in order to have the same diameter and drag coefficient of the WT model. The latter is the same two-bladed 60 cm diameter rotor used Chapter 2. The comparison of the two wakes is conducted in the presence of the leapfrogging instability of the tip-vortex helical structure. The tip-vortex instability is in fact a critical near-wake feature, whose main effect is to start a more efficient mixing process which anticipates the far wake features. This phenomenon cannot be reproduced with the AD model and as such constitute a major difference between the two wakes. A comparison between a WT wake and an AD wake in the presence of leapfrogging is for this reason of particular interest. Following the experimental studies of Dobrev et al (2008), Felli et al (2011) and Sherry et al (2010), in Chapter 3 it has been shown how the instability of the tip-vortex helix has a major effect on the wake mixing and re-energising mechanism. Lignarolo et al (2015) have conducted a detailed analysis of the effect on the turbulence field and wake mixing due to the presence of the leapfrogging instability. Bolnot et al (2011) simulated numerically the helical wake using an array of axisymmetric vortex-rings for studying the onset of pair-wise instability in helicopter and wind-turbine rotor wakes. Leweke et al (2013) measured experimentally the growth rate of pair-wise instability in a water channel with different triggering modulations. Ivanell (2009) and Ivanell et al (2010) reproduced with large eddy simulation the tip-vortex helix development and instability and measured the near wake length as function of the inflow turbulence. In this study, the wake instability was triggered by an artificial disturbance introduced at the blade tip during the simulation. In experimental studies by Bolnot et al (2014) and Odemark and Fransson (2013) artificial disturbances were also used for triggering the tip-vortex instability, as asymmetries in the rotor geometry and pulsed air jets. In the present study, the leapfrogging is triggered by an asymmetry of the blade pitch angle, as in the study presented in Chapter 2. The use of an adapted formulation of the momentum equation in differential form allowed to compute the pressure field and stagnation enthalpy around the rotor and the porous disc directly from the velocity data in the incompressible regime (Ragni et al, 2011, 2012, van Oudheusden, 2013). The out-of-plane vorticity field is calculated by differentiation of the time-average velocity field with a central difference scheme. The three-component turbulence intensity is calculated and compared in the wakes of both models. A double decomposition of the flow velocity field is employed to extend the analysis performed Chapter 3 and to quantify the mean-flow kinetic-energy transport across the wake shear layer. On this regard, two wake locations are chosen before the leapfrogging and results are compared with the ones obtained in the wake of the actuator disc at the same locations.

Most of the studies mentioned above have been performed in the presence of high wind tunnel turbulence or simulated atmospheric boundary layers (and atmospheric turbulence). The present study has been conducted at very low turbulence intensity (0.5%) in order to focus the analysis solely on the wake-induced flow, with no influence of external flow fluctuation, minimising the number of parameters affecting the wake mixing. The objective is in fact to study the intrinsic differences and similarities between the flow in the wake of an AD and a WT, separating the problems of the mixing caused by the external turbulence and the one caused by the turbulence induced directly by the AD or the WT. The scope is not to represent a real situation, but to analyse the core nature of an AD and a WT wake in its essence.

4.2 EXPERIMENTAL METHOD

The present section contains information on the wind-tunnel and experimental models used in this project. The experiments are performed in the OJF wind tunnel at the Delft University of Technology. A detailed description and characterization of the wind-tunnel feature can be found in Section 2.2.1 and 2.2.5. The wind turbine model and the porous disc design are presented in section 4.2.1 and 4.2.2 respectively. Section 4.2.3 and 4.2.4 summarise the experimental conditions and the SPIV setup parameters. In section 4.2.5 the Reynolds-average mean-flow kinetic energy transport equation is derived.

4.2.1 WIND-TURBINE MODEL

In the present experiments, the turbine described in Chapter 2 was operated at an above-optimal tip-speed ratio λ =6.97 at a free-stream wind speed of U_∞ = 4.7 m/s. The rotational speed was υ = 109.3 rad/s (see Table 4-1). The maximum chord-based Reynolds number achieved at these conditions is Re_{ct} = 96,000 at the blade tip. The diameter-based Reynolds number is Re_D = 188,000, which is approximately one order of magnitude lower than in full-scale operating conditions and higher than the critical value for Reynolds independency discussed in Section 2.2.6 and in Chamorro et al (2012). The model was installed at 1.17 rotor diameters (0.7 m) from the tunnel exit. As discussed in Section 2.2.1, no blockage correction is applied. The turbine blades and nacelle are coated with a black paint for dimming the reflection of the laser beam. A six-component balance is used for measuring the drag force on the turbine (and on the disc, see Section 4.2.2). The device is described in Section 2.2.1 and 2.2.2. The results of the thrust measurements are reported in Figure 4-4. The thrust coefficient was calculated with Equation (2-2). The calculated value is C_t = 0.93. For triggering the *leapfrogging* instability an asymmetry of the blade pitch angle is introduced. The blades are installed to the nacelle hub with a pitch-angle difference of 0.5°: this acts as a constant trigger for the wake instability, similarly to the studies of Bolnot et al (2014) and the experiments described in Chapter 2.

4.2.2 DESIGN OF AN ACTUATOR DISC MODEL

Several solutions for reproducing a “physical” actuator disc can be found in the literature, as discussed in Section 4.1. The main design drivers are porosity, structural stiffness and wake-flow uniformity. The porosity is a measure of the permeable area of the disc and it is defined as the ratio between the open area and the total area of the disc. In Figure 4-1 ,the results of five experiments found in wind energy literature are compared, showing a consistent decreasing drag coefficient with increasing porosity. Structural stiffness is important in order to avoid oscillations at the free edge of the disc, which would strongly compromise the quality of the flow in the wake. In Section 4.1 examples have been given about stiff structure obtained by modelling the actuator disc with perforated metal plates or by employing a mesh composed by wooden sticks. However, for the present study the metal-mesh solution adopted by Aubrun et al (2013) and Aubrun et al (2007) was chosen. A 0.6 m diameter porous disc is manufactured by stacking three layers of fine metal mesh with uniform porosity ξ = 60% and spacing δ = 1mm with two additional larger meshes for structural stiffness (δ = 10mm and δ = 50mm respectively) as shown in Figure 4-2. Mesh A has the double function of fine-tuning the drag coefficient and of flattening the underlying layers of fine mesh, whereas mesh B has the only function of supporting and stiffening the entire structure. A disc with total porosity ξ = 32% and drag coefficient C_D = 0.93 (equal to the turbine C_t = 0.93) is obtained. This is consistent with the results of previous experiments in Figure 4-1. The total thickness of the disc is 4mm, which is 0.6% of the disc diameter. A uniform porosity disc has been adopted, disregarding the distribution of loads on the WT blades. The uniform disc of porosity ξ = 32% matches the thrust coefficient of the WT at tip-speed ratio λ =6.97. Also the disc is coated with a black paint for dimming the reflection of the laser beam. Section 4.3.3 presents a comparison between two different methods for calculating the thrust coefficient. The disc structure was connected to the same nacelle of the turbine: in this way, both wakes show the same nacelle flow and all differences are only due to the presence or absence of the blades.

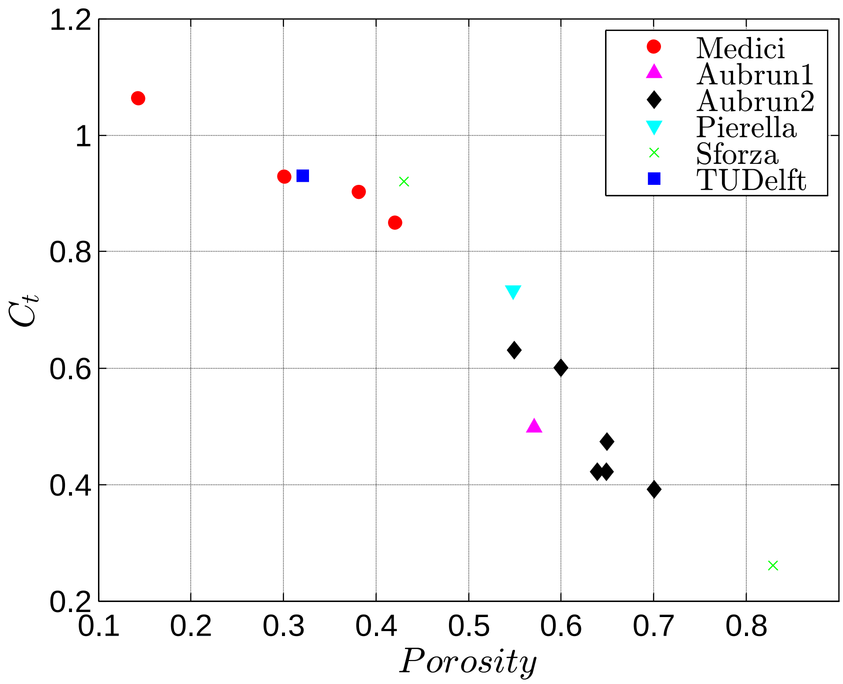

Figure 4-1. Porous-disc drag coefficient as function of porosity for several cases in literature.

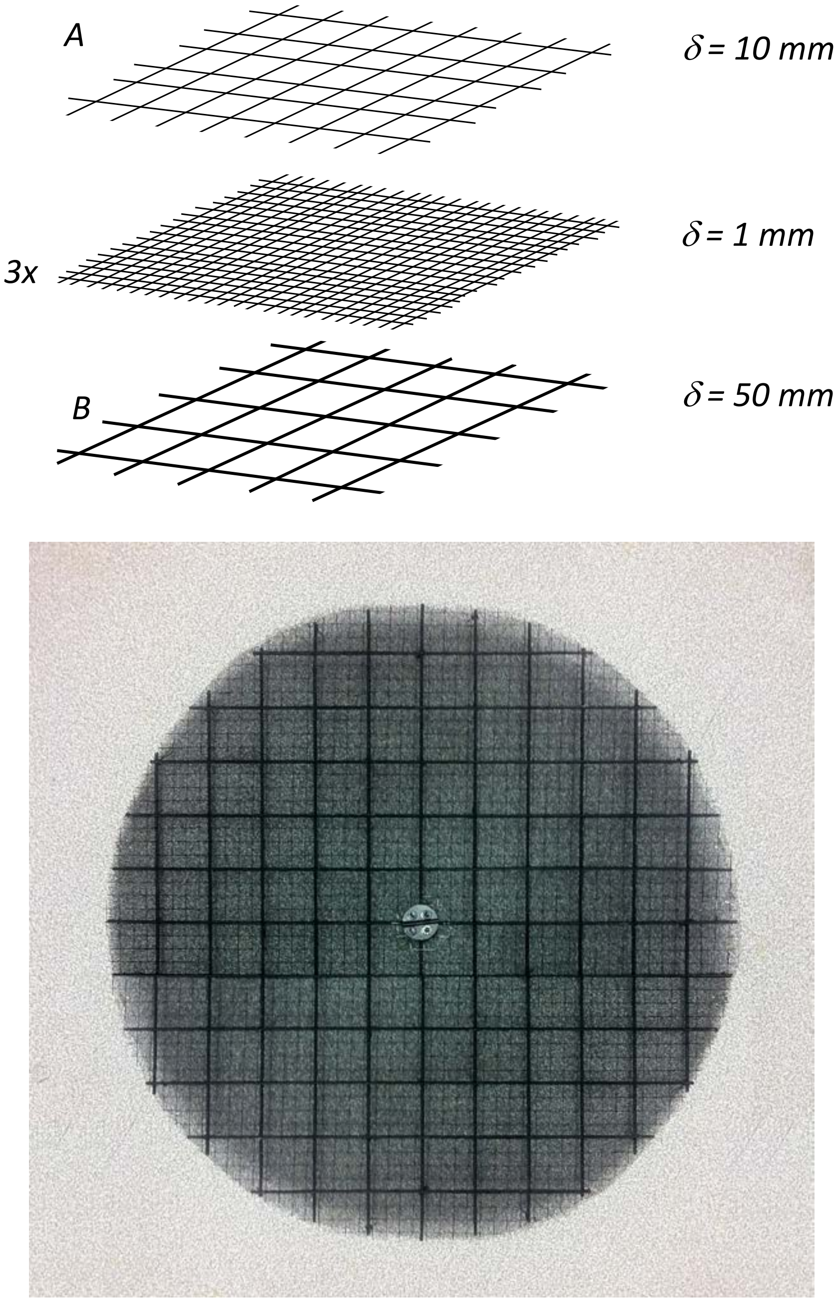

Figure 4-2. Porous disc structure, not in scale (top image) and picture of the porous disc model (bottom image).

4.2.3 Experimental Conditions

The measurements were performed in the wakes of the two models up to 2.2 diameters downstream, with multiple fields of view (FOV) in a horizontal plane at the hub height. The positions of the fields of view are represented in Figure 4-3, where each squared window represents a field of view (FOV) in the horizontal plane. The darker shade between the windows shows the overlap between two adjacent FOV, which is 0.05 m in the axial and radial direction. The size of each field of view is 0.297 × 0.227 m^2 (0.50 × 0.39 diameters). The measurement plane is parallel to the ground and perpendicular to the tower, therefore the wake measurements do not exhibit any tower effect and the wake can be considered symmetric. For this reason, only one the flow in half of the wake is captured. The distance between the turbine and the wind tunnel exit is approximately 1 rotor diameter. Table 4-1 summarises all relevant parameters about the experimental conditions. For each FOV, 200 unconditionally-sampled three-component SPIV vector fields are averaged in order to obtain the mean velocity fields and second order turbulence statistics. In Chapter 2 it was shown that such number of samples in very similar experimental conditions is sufficient for having a well-converged flow statistics. In four particular FOV (near and far wake of the AD and near and far wake the WT, see Figure 4-24 in 4.3.7) a much larger number of samples have been taken (1000 for the AD and 5000 for the WT). The velocity fields in each FOV are combined with a simple stitching algorithm, selecting only one field in the overlapping region. No smoothing nor averaging is applied to the data.

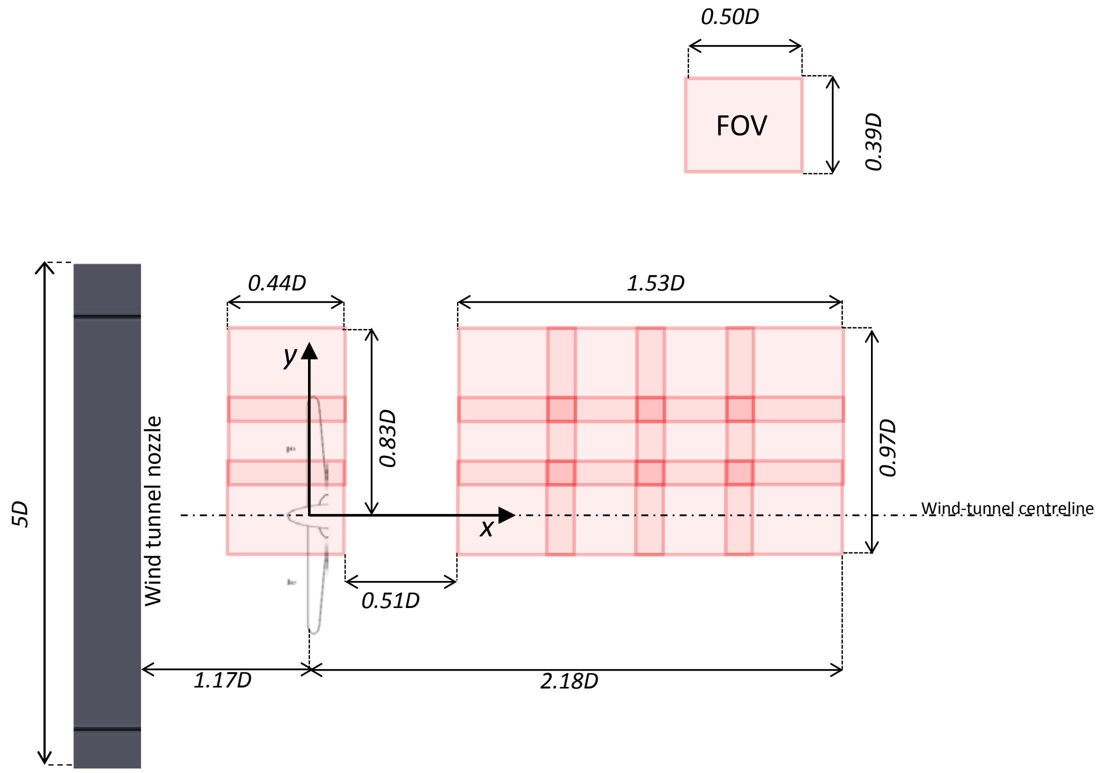

Figure 4-3. Flow-field measurement configuration.

4.2.4 STEREOSCOPIC PARTICLE IMAGE VELOCIMETRY

The three-component velocity fields in the rotor wake is obtained with Stereoscopic PIV experiments; the total vector field is obtained by stitching the results from different fields of view, as detailed in Figure 4-3. A traversing system, supporting the whole set up, enables to scan the flow field in the wake of the horizontal-axis wind-turbine wake, translating in two dimensions of approximately 1.2 m × 0.9 m. A Quantel Evergreen Nd:YAG laser system, with an average output of 200 mJ/pulse, provides the required illumination. The laser light is conveyed to form a 2 mm laser sheet of approximately 0.4 m width at the field of view. Images with a field of view of 0.297×0.227 m^2 (0.50×0.39 diameters) are acquired with two LaVision Imager Pro LX 16 Mpix (4870 × 3246 px^2, 12 bits) with pixel pitch of 7.4 µm/px. Two Nikon lenses of f = 180 mm and an aperture *f#* = 2.8 – 4 has been used. The obtained magnification factor is M = 0.10. The focusing plane has been slightly offset with respect to the laser plane (defocusing), to obtain an image of the particle of approximately 2-3 px. Therefore no bias error due to peak-locking is expected (Westerweel, 1997). Seeding was provided in the test section by a SAFEX smoke generator with SAFEX MIX, able to produce liquid droplets of less than 1 µm. Double-frame recordings have been acquired and processed with LaVision Davis 8.1.4; the final interrogation window size is 24 × 24 px^2 with 50% overlap, with a resolution of 1.46 mm and a vector spacing of 0.732 mm. Table 2-3 summarises the main parameters of the stereo PIV setup.

Table 4-1. Experimental parameters.

Parameters		**WT**	**AD**
Free-stream velocity	U_∞	4.7 m/s	4.7 m/s
Free-stream turbulence intensity	TI_∞	0.5%	0.5%
Rotational frequency	υ	109.3 rad/s (17.4 Hz)	
Reynolds (chord based) at root, r/*R* = 0.20	Re_{cr}	32,000	
Reynolds (chord based) at tip, *r/R* = 1	Re_{ct}	96,000	
Reynolds (diameter based)	Re_D	188,000	188,000
Thrust coefficient (from balance)	C_t	0.93	0.93
Tip speed ratio	λ	6.97	

Table 4-2. System parameters of the SPIV setup.

Parameters		**SPIV setup**	
Measurement field of view	*FOV*	297 × 227 mm^2	4870 × 3246 px^2
Interrogation window size	I_w	1.46 × 1.46 mm^2	24 × 24 px^2
Vector spacing (50% overlap 50%)	*S*	0.732 mm	12 px
Digital resolution	*DR*	16.40 px/mm	
Vectors	*N#*	404 × 270	

4.2.5 THEORY

The mean-flow kinetic-energy transport in the wake shear layer is evaluated in two selected locations, before and after the leapfrogging phenomenon. Results are compared in the wake of the WT and of the AD. The transport equation of the mean-flow kinetic-energy Equation (4-1) is obtained as in Hamilton et al (2012), with a Reynolds double decomposition of the flow where $\overline{u}_i$ is the time average velocity in the *i*-direction and $\overline{K}_E$ is the mean-flow average kinetic energy, p is the pressure and $\overline{u'_i u'_j}$ are the Reynolds stresses. The third term of the right-hand-side of Equation (4-1) represents the spatial gradient of the mean-flow kinetic-energy fluxes.

$$\overline{u}_j \frac{\partial \overline{K_E}}{\partial x_j} = -\frac{1}{\rho}\frac{\partial \overline{p}\overline{u}_i}{\partial x_i} - \left(-\overline{u'_i u'_j}\right)\frac{\partial \overline{u}_i}{\partial x_j} - \frac{\partial}{\partial x_j}\left[\overline{u}_i\left(\overline{u'_i u'_j}\right)\right] \tag{4-1}$$

When the equation is applied to a control volume including the wake shear layer but not encompassing the AD/WT, as shown in Section 3.2.1 for i = 1 and j = 2, the term $\overline{\Phi} = -\overline{u}\left(\overline{u'v'}\right)$ represents the flux in the radial direction of the streamwise mean-flow kinetic-energy. In other words, the term represents the entrainment of free-stream kinetic energy across the wake shear layer. It must be noted that a positive flux, meaning positive entrainment of kinetic energy toward the inner part of the wake, can happen only in case of a negative correlation between u' and v' ($\overline{u'v'} < 0$). This condition is satisfied in case of a turbulent bursts of slow speed fluid directed away from the wake centreline (u'<0 and v'>0) or in case of turbulent bursts of high speed fluid directed downward toward the inner part of the wake (u'>0 and v'<0).

4.3 RESULTS

In this section reports the results of the experiments. Time-average velocity fields, wake turbulence intensity and vorticity in the AD and WT wake are be compared. The pressure field and the stagnation enthalpy at the rotor/disc location is calculated and compared. In the last paragraph the differences in the mixing processes in the wake of the turbine and of the actuator disc will be explained.

4.3.1 DIRECT THRUST MEASUREMENTS RESULTS

The results of the thrust measurement are reported in Figure 4-4: the blue dots are results of the measurements reported in Figure 2-9. For the design tip-speed ratio $\lambda = 6$ the thrust coefficient was $C_t = 0.89$. The red dot is the results of the present measurements: for tip-speed ratio $\lambda = 6.97$ the thrust coefficient was $C_t = 0.93$.

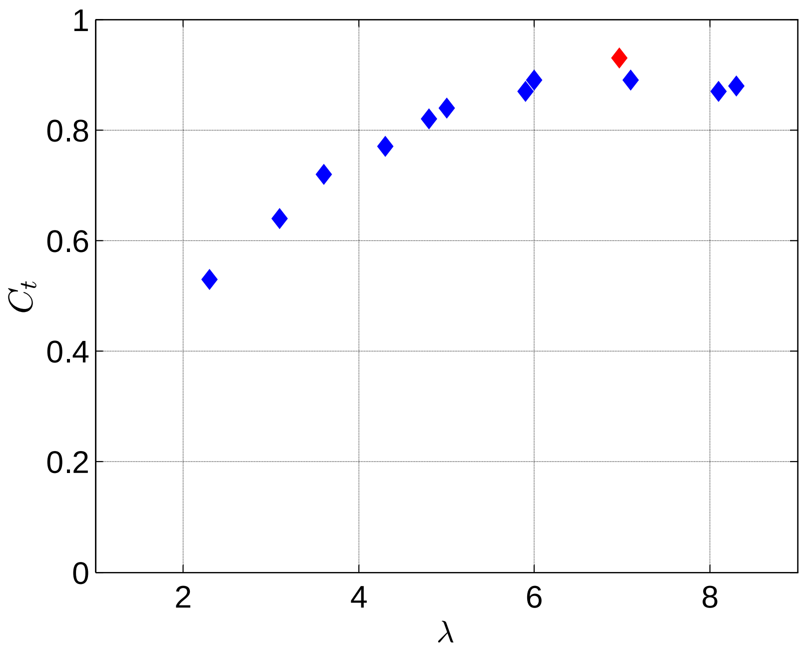

Figure 4-4. Thrust coefficient curve of the 2-bladed wind turbine model: comparison between old (blue dots) and present measurements (red dot).

4.3.2 GLOBAL VELOCITY FIELD AND INDIRECT THRUST CALCULATION WITH MOMENTUM DEFICIT

In Figure 4-5 to Figure 4-6 the time-averaged wake normalised velocities fields *(u,v,w)/U∞* are shown up to *x/D= 2.2* downstream the rotor/disc location. A mask has been applied to the areas encompassing the disc and the rotor. However, the thickness of this mask is not representative of the physical thickness of the disc and the rotor themselves, but also accounts of the regions affected by laser reflections and shadowing. As noted in Figure 2-12, in Figure 4-5 a localized increase of the wake shear layer thickness is visible starting from *x/D* =1.5 downstream the turbine wake and with maximum at *x/D* =1.75, corresponding to the leapfrogging region. For a tip-speed ratio $\lambda = 6$, in Chapter 2 the onset of the pairing instability was found at *x/D*=1 and it was shown that the phenomenon has a strong dependency on the tip-speed ratio and on the mounting conditions, with higher tip-speed ratios leading to earlier instability. On the contrary, in the present experiments, when the system tower-nacelle-rotor was rebuilt, for a higher tip-speed ratio ($\lambda = 6.97$) the onset of the pairing instability was moved downstream at *x/D* =1.5. This shows how sensitive the wake vortex system is to any variation of the boundary condition (Bolnot et al, 2014) and to the possibility that the tower-nacelle-rotor system of the present experiments may have differed slightly from the one of the previous campaign, introducing less perturbing vibrations. Figure 4-6 shows a localised region of strong positive radial velocity in both the AD and the WT wake due to the sudden wake expansion. The contours show that this phenomenon is mainly concentrated at the tip location. The rest of the AD wake (Figure 4-6, top) is characterised by a generally positive and close to zero radial velocity. On the contrary, the WT wake (Figure 4-6, bottom) shows also a large region of negative radial velocity at the root region. This could be ascribed to an interaction between the wake rotational motion and the tower's wake (not present in the measurements) that causes a wake asymmetry. The same phenomenon is also visible in Schümann et al (2013) and in Medici (2005): although the latter reported negative values of radial velocity only after 2 diameters, the form recorded negative values also in the very near wake and a visible wake asymmetry due to the tower effect. A second region of negative radial velocity appears at approximately *x/D* =1.5 in Figure 4-6 (bottom) after the tip-vortex instability location. Figure 4-7 contains the contours of normalised azimuthal velocity $\overline{w}/U_\infty$, which as expected is nearly null in the AD wake. In the WT wake the out-of-plane contribution is instead counter rotating with respect to turbine rotation (negative for $y/D > 0$ and positive for $y/D < 0$). An interesting feature of Figure 4-7 (top) is the region of positive $\overline{w}/U_\infty$ at the upper edge of the WT wake, which then develops into a region of negative $\overline{w}/U_\infty$ with absolute value larger than the surrounding field from *x/D*=1.5. This is consistent with the findings Chapter 2, where a clear change of sign in the azimuthal velocity direction close to the vortex core after the leapfrogging location was shown. Figure 4-8 to Figure 4-10 show the normalised velocity profiles $\overline{u}/U_\infty$, $\overline{v}/U_\infty$ and $\overline{w}/U_\infty$ at five different downstream locations. The first location is very close to the rotor/disc (0.1D); the second at an undisturbed location before the instability (0.7D); the third location is right at the beginning of the leapfrogging region (1.1D); the fourth is in the middle of the leapfrogging region (1.8D) and the last location is at the end of the measurement area (2.2D). The plots confirm the analysis of Figure 4-5 and Figure 4-6. At *x/D*= 0.1 the mean axial velocity profile in the AD wake shows dishomogeneity compared to the WT wake velocity profile with $\Delta\overline{u}/U_\infty = \pm 0.1$. This is due to the different process of wake generation. The metal mesh of the AD does not extract mechanical energy from the flow as the WT, but it dissipates the kinetic energy of the incoming wind into turbulence, which quickly decays (Batchelor and Townsend, 1947, 1948a, b). At *x/D*= 0.8 and *x/D*=

1.1 upfront the leapfrogging region, the presence of the tip vortices at the border of the WT wake induces a sharp velocity gradient. On the contrary, the AD wake shows a smoother velocity variation. After the instability location, the WT and the AD wakes become more similar: as a matter of fact, the tip vortices break down and the velocity gradient in the shear layer is less strong. The largest differences between the two velocity profiles are in the region between y/D = -0.1 and y/D = 0.2, with $\Delta\bar{u}/U_\infty = \pm 0.25$. The expansion of the two wakes is calculated, with the wake border being the locus of the points where the velocity is 99% of U_∞. Matching diameter and thrust coefficient of the two models should ensure the same wake expansion. As a matter of fact, Figure 4-11 demonstrates that the wake expansion is very similar in the AD and WT wakes, with the relative difference, calculated as $(expansion_{AD} - expansion_{WT}) / expansion_{WT}$, everywhere lower than 4%.

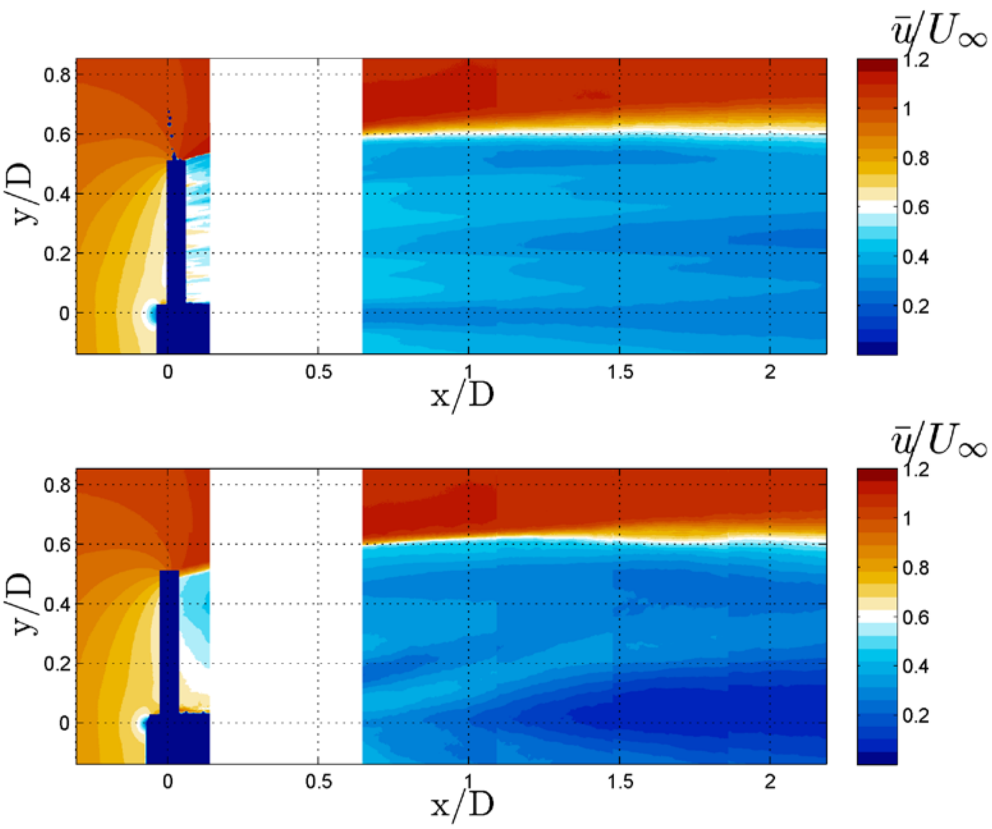

Figure 4-5. Axial (x-direction) velocity field in the wake of the AD (top) and of the WT (bottom).

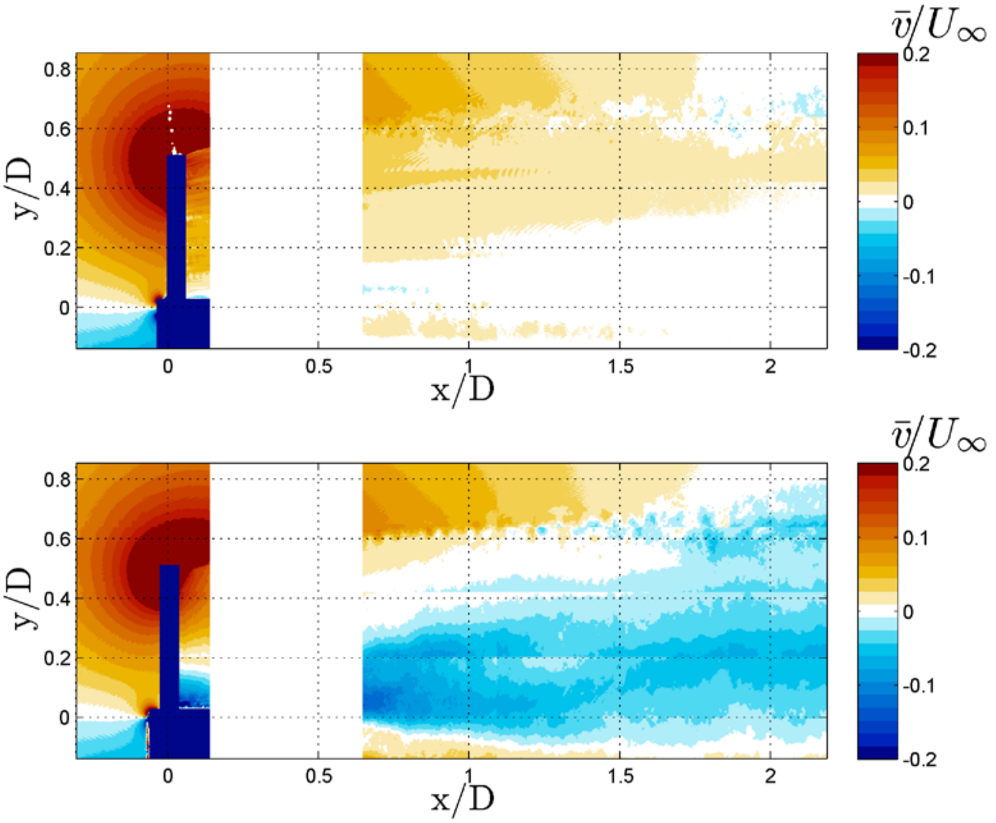

Figure 4-6. Radial (y-direction) velocity field in the wake of the AD (top) and of the WT (bottom).

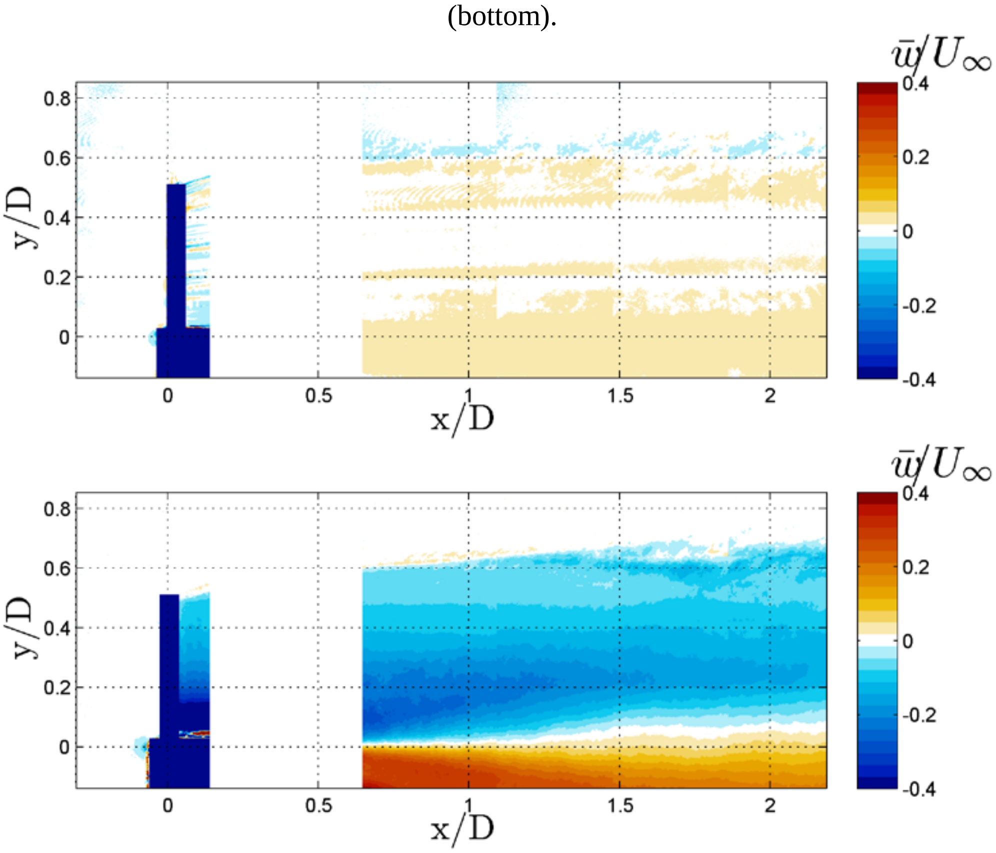

Figure 4-7. Azimuthal (z-direction) velocity field in the wake of the AD (top) and of the WT (bottom).

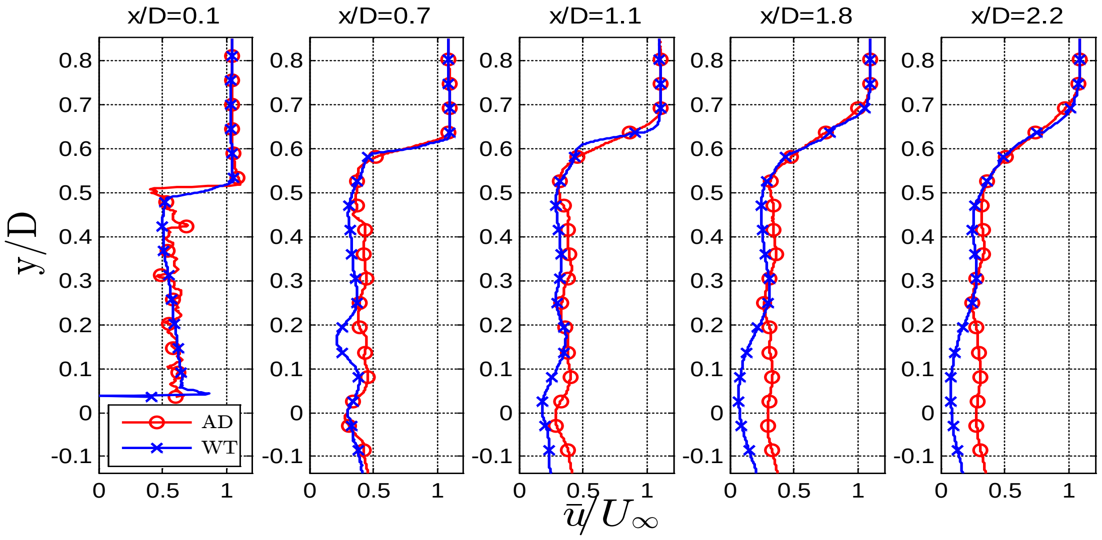

Figure 4-8. Axial (x-direction) velocity profiles at five different locations in the wake of the AD and of the WT.

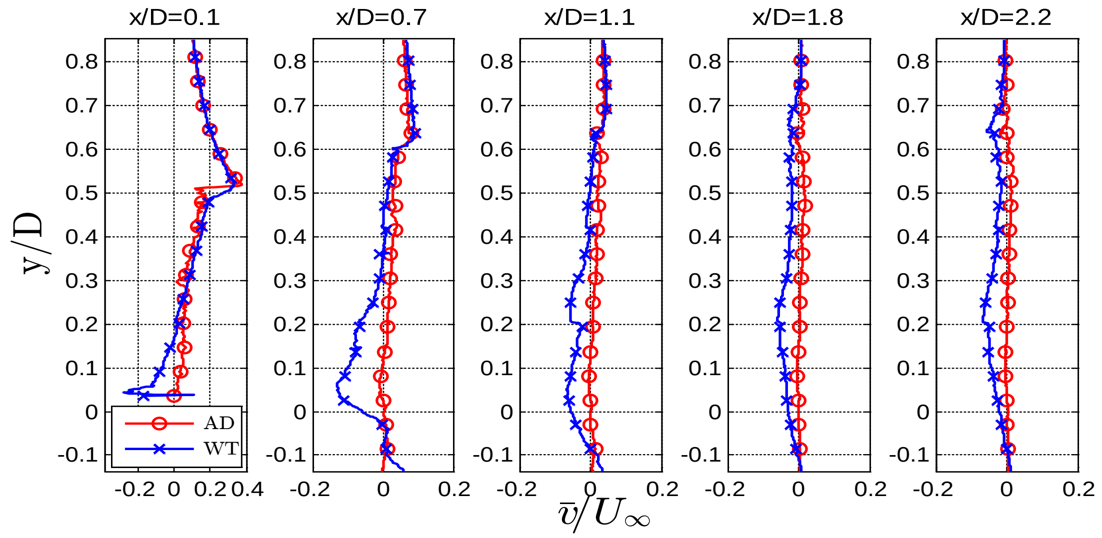

Figure 4-9. Radial (y-direction) velocity profiles at five different locations in the wake of the AD and of the WT.

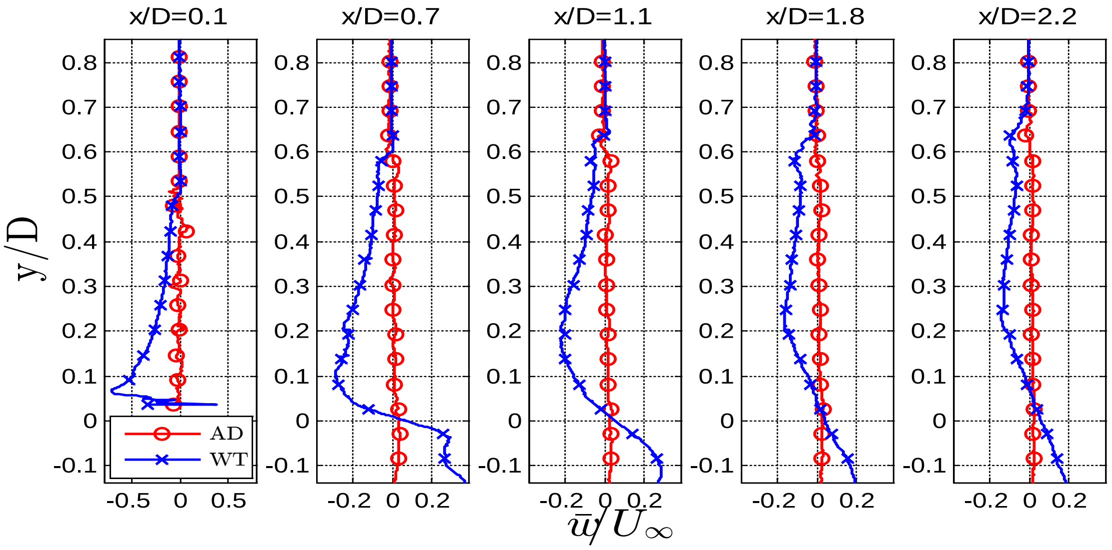

Figure 4-10. Azimuthal (z-direction) velocity profiles at five different locations in the wake of the AD and of the WT.

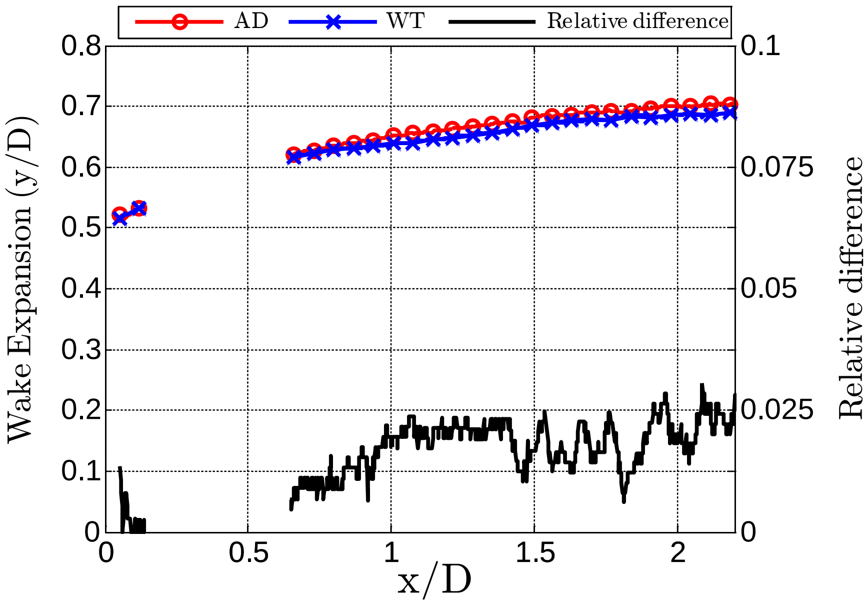

Figure 4-11. AD and WT wake expansion and relative difference. The curves represent the loci of the points where the axial velocity is 99% of the free stream value.

A second method for calculating the thrust coefficient is by indirect calculation from the velocity field, by integrating the momentum deficit in the wake. This is compared to the value obtained with direct measurement via the 6-component balance. In this case, the thrust coefficient has been calculated using Equation (4-2) from Burton et al (2001), with the strong assumption of Bernoulli equation being applicable separately to the upstream and downstream sections of the stream-tube:

$$C_t = 4a(1-a) \quad (4\text{-}2)$$

$$a = 2\pi \int_{R_{root}}^{R_{tip}} \left[1-\overline{u}(r,x=0)/U_\infty\right] r dr \cdot \frac{1}{A} \quad (4\text{-}3)$$

$$A = \pi\left(R_{tip}^2 - R_{root}^2\right) \quad (4\text{-}4)$$

The term $\overline{u}(r, x = 0)/U_\infty$ is the radial distribution of normalized velocity at the rotor or disc location $x=0$. The induction factor is calculated with and it is equal to a = 0.388 for the WT and a = 0.376 for the AD. The thrust coefficient is C_t = 0.949 for the WT and C_t = 0.938 for the AD, respectively 2.0% and 0.86% higher than the balance measurement.

4.3.3 Static Pressure and Indirect Thrust Calculation with Pressure Jump

The static pressure field at the rotor/disc location can be calculated directly from the SPIV data. The derivation of the pressure from SPIV data has been extensively addressed in many fields of research, as in Liu and Katz (2006), Raffel et al (1998), Ragni et al

(2011) and van Oudheusden (2013). Applications in phase-locked environments for propeller and wind-turbines have allowed reconstructing the three-dimensional periodic pressure fields and subsequently non-intrusively obtaining loads on the rotor blade Ragni et al (2011). The method allows reconstruction of the pressure field from its own gradient obtained from the Navier-Stokes momentum equation:

$$\frac{\partial p}{\partial x_i} = -\rho\left(\frac{\partial u_i}{\partial t} + u_j \frac{\partial u_i}{\partial x_j}\right) + \mu \frac{\partial^2 u_i}{\partial x_j \partial x_j} \tag{4-5}$$

where ρ and μ are respectively the flow density and the dynamic viscosity assumed constant. In the present analysis, due to the high Reynolds number, the viscous terms have been neglected compared to the inertial contribution. The time derivative of the velocity is null, because data are time averaged (axisymmetric wake). Also gradients along the *z*-direction have been neglected, because much smaller than the other quantities. The equation is as such reduced to its two-dimensional steady-state version. The pressure integration is performed by rewriting the Poisson equation into a two-dimensional Poisson scheme. The pressure integrator used in the present chapter is based on the version in use by Ragni et al (2011). The algorithm solves the Poisson Equation (4-6), where the pressure gradient is calculated as in Equation (4-5), inverting a linear system of equations obtained through a second order finite difference scheme in two dimensions. Dirichlet (Bernoulli pressure) and Neumann boundary conditions are applied to solve the Poisson equation:

$$\nabla^2 p = \frac{\partial}{\partial x_i}\frac{\partial p}{\partial x_i} \tag{4-6}$$

The pressure integration is performed in an area spanning from 0.3D upstream until 0.15D downstream the rotor/disc location on the axial direction and from the turbine axis up to 0.85D distance along the radial direction. The results are shown in Figure 4-12, where the c_p is calculated as:

$$c_p = \frac{2p}{\rho U_\infty^2} \tag{4-7}$$

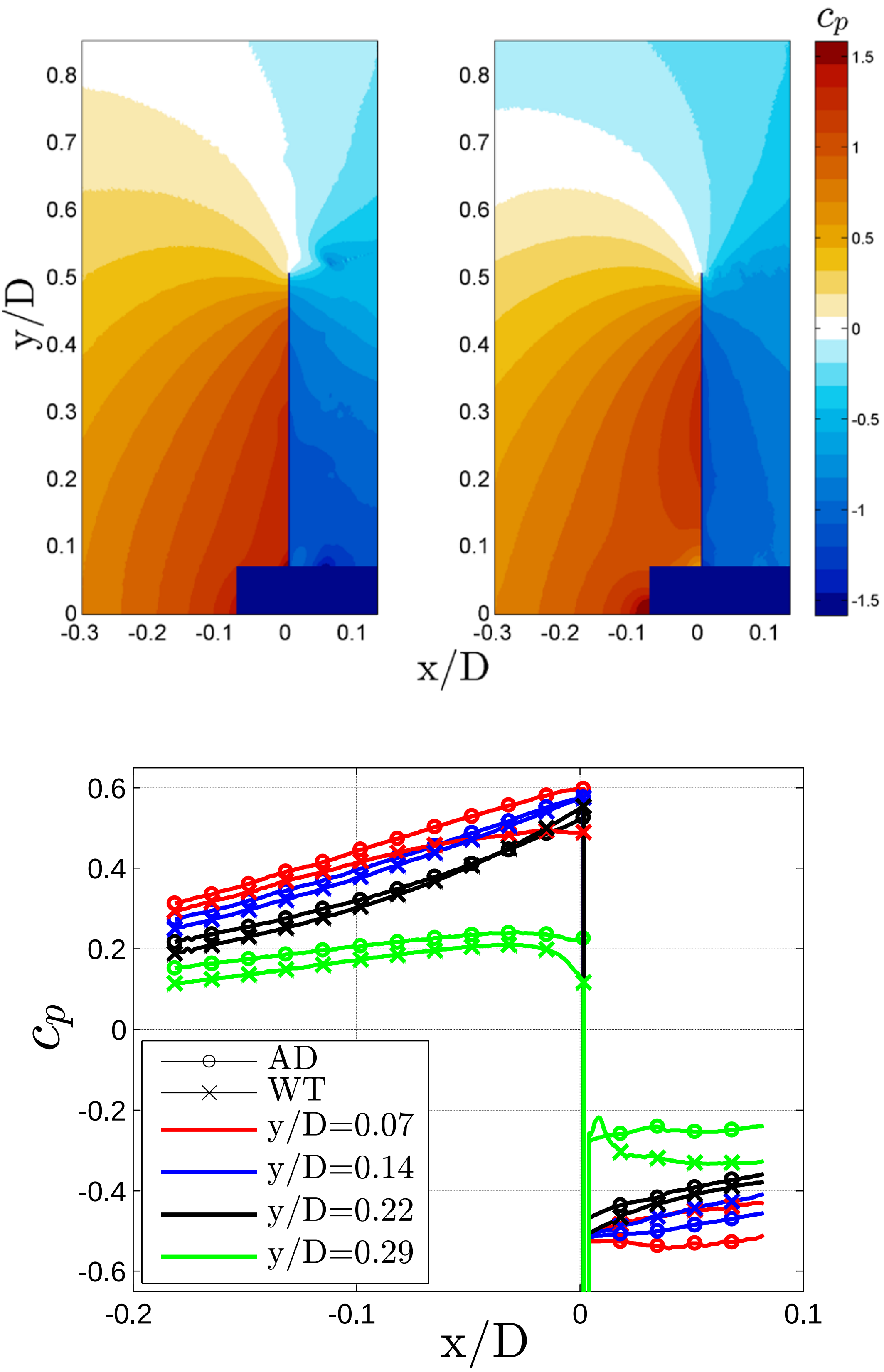

Figure 4-12. Pressure distribution at the disc (top left image) and rotor (top right image) location. Streamwise development of pressure at different radial locations across the AD and WT (bottom image).

For allowing a smooth calculation of the velocity gradients, the velocity fields have been interpolated in proximity of the rotor/disc using a least squares approach, where data are compromised due to the presence of shadowing and reflection from the model itself (see masks applied in velocity, vorticity and turbulence fields throughout the whole chapter). This also explains the much thinner mask applied to the field in Figure 4-12 compared to the one used in Figure 4-5 to Figure 4-7. Figure 4-12 (top image) compares the streamwise development of pressure at 4 radial locations in the AD and WT wake. A strong pressure jump is evident at $x/D = 0$ consistently with the presence of the model. Results from the AD and the WT agree within a difference lower than 8% everywhere, with larger differences up to 20% in the tip and root location at $y/D = 0.07$ and $y/D = 0.29$. Figure 4-13 (top image) depicts the pressure profiles along the upwind and downwind surfaces (respectively c_p^+ and c_p^-) of the disc and rotor, showing the strong root effect from $y/D = 0.08$ and $y/D = 0.2$, visible in the c_p^+ curves. The pressure jump across the disc/rotor is shown in Figure 4-13 (bottom image). This value can be integrated on the disc/rotor surface as shown in (4-8) for calculating the thrust coefficient, yielding a thrust coefficient of $C_t = 0.934$ for the AD and $C_t = 0.927$ for the WT, respectively 0.43% higher and 0.32% lower than the balance measurement.

$$C_t = \frac{4\pi}{A} \int_{R_{root}}^{R_{tip}} \left(c_p^+ - c_p^-\right) r dr \tag{4-8}$$

Table 4-3 summarises the AD and WT thrust coefficients calculated with the three methods (with the six-component balance, from velocity field, from pressure field) and shows the relative difference between them.

Table 4-3. Values of AD and WT thrust coefficient C_t obtained with direct balance measurements and by indirect calculations (from velocity and pressure).

Method	***AD***	***WT***	***Relative difference***
Direct (balance)	0.930	0.930	0%
From velocity field	0.938	0.949	-1.17%
From pressure field	0.934	0.927	0.75%

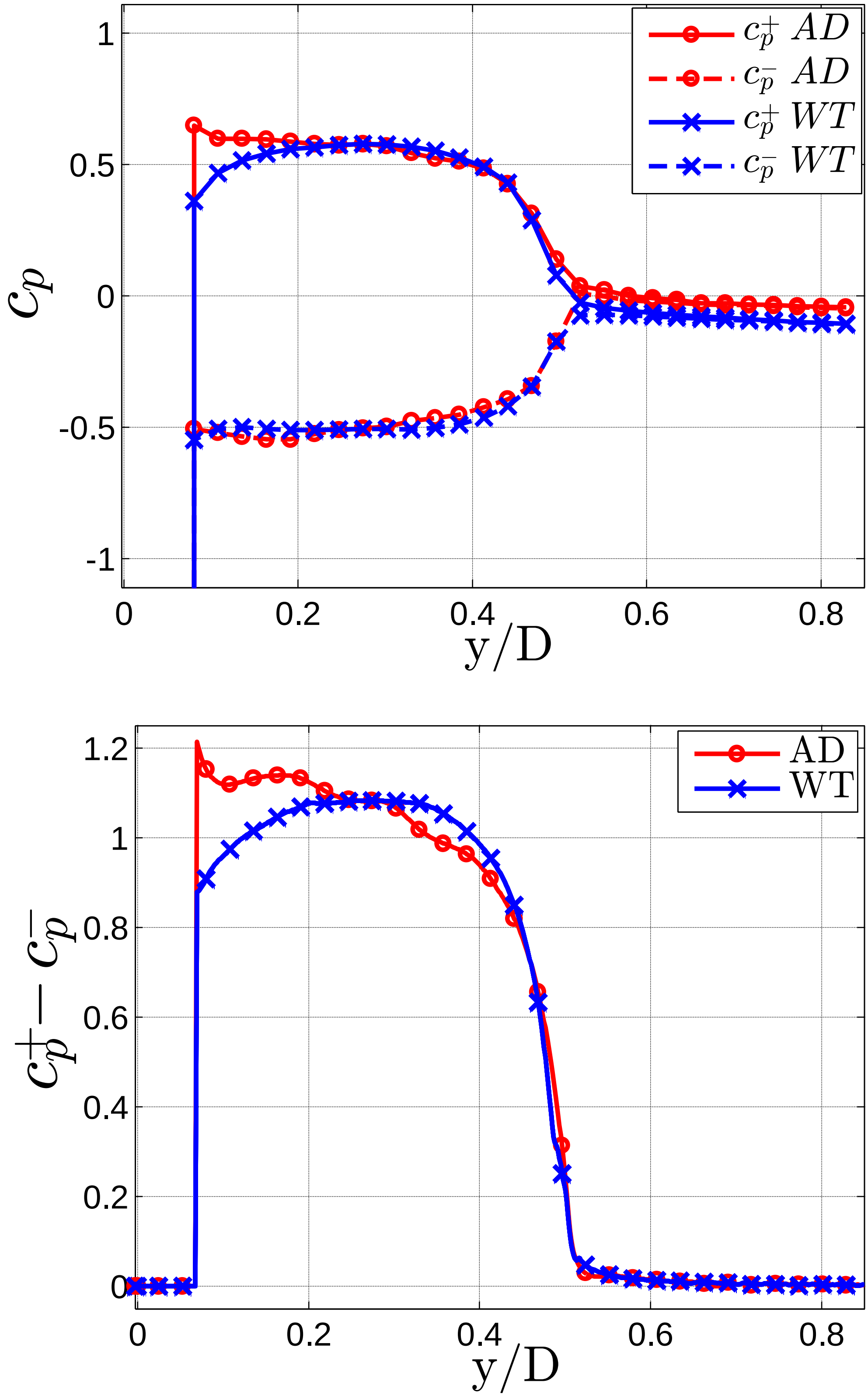

Figure 4-13. Pressure distribution along upwind and downwind surface of the AD and the WT (top image). Pressure jump across the AD and WT along the radial direction (bottom image).

4.3.4 Stagnation Enthalpy

With no net shaft work and heat transfer, the stagnation enthalpy is constant along each streamline for a frictionless non-conducting fluid in motion with a steady pressure distribution (Batchelor, 2000). A wind turbine extracts power from the flow in form of shaft work, therefore in this case the flow experiences a drop of enthalpy. For this reason, the variation of stagnation enthalpy is the best indicator of the amount of power $\dot{W}$ extracted from the flow by the rotor, which can be calculated as $\dot{W} = -\dot{m}\Delta h$, where $\dot{m}$ is the mass flow rate across the rotor area A, and Δh is the difference between the stagnation enthalpy in the wake region and the one of the free-stream flow H_∞. The variation of stagnation enthalpy per unit mass is calculated as:

$$\Delta h = \Delta e + \frac{\Delta p}{\rho} + \Delta q + \Delta \Psi \tag{4-9}$$

where Δe is the variation of internal energy of the flow per unit mass, Δp is the static pressure variation estimated from the SPIV velocity field as in 4.3.3, $\Delta q = 0.5(\Delta u^2 + \Delta v^2 + \Delta w^2)$ is the variation of the flow kinetic energy per unit mass and $\Delta\Psi$ represents the variation of body forces. The latter one can be neglected in absence of substantial variation of potential energy as in this case. Also, in absence of heat transfer, the flow temperature across the wind turbine can be considered constant and the variation of internal energy null, with an acceptable approximation. Therefore the power extracted by the wind turbine can be calculated as:

$$\dot{W}_{WT} = -\dot{m}\left(\frac{\Delta p}{\rho} + \Delta q\right)_{WT} \tag{4-10}$$

The flow across the disc does not experience a power extraction through shaft work nor external heat transfer (Δh = 0), but rather a degradation of the inflow kinetic and pressure energy into heat through turbulence dissipation. The pressure energy and the kinetic energy variations are therefore balanced by a variation of internal energy, which is calculated as:

$$\dot{E}_{AD} = -\dot{m}\left(\frac{\Delta p}{\rho} + \Delta q\right)_{AD} \tag{4-11}$$

with Δh = 0. The contours in Figure 4-14 (left) show the value of $-\Delta e/H_\infty$ in the AD wake flow. The contours in Figure 4-14 (centre) show the value of $\Delta h/H_\infty$ in the WT wake flow. Figure 4-14 (right) shows the profiles of $-\Delta e/H_\infty$ and $\Delta h/H_\infty$ at x/D=0.1. It is evident how the internal energy variation in the AD wake corresponds very well to the stagnation enthalpy variation in the WT wake. The normalised power dissipated by the AD and the one extracted by the WT are calculated respectively in (4-12) and (4-13).

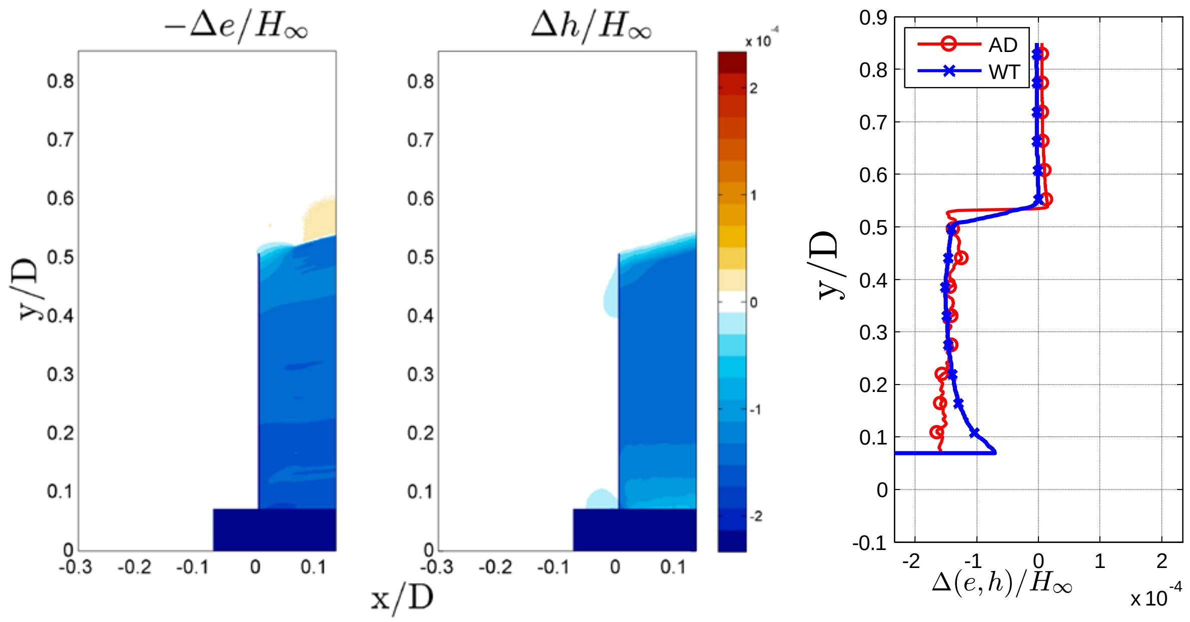

Figure 4-14. Stagnation enthalpy distribution at the disc (left) and rotor (centre) location. On the right: radial profile of stagnation enthalpy at *x/D* = 0.1 for the AD and the WT.

$$C_{p,AD} = \frac{4\pi}{U_\infty^3 A} \int_{R_{root}}^{R_{tip}} \bar{u}(r, x=0)\Delta e(r) r dr \tag{4-12}$$

$$C_{p,WT} = -\frac{4\pi}{U_\infty^3 A} \int_{R_{root}}^{R_{tip}} \bar{u}(r, x=0)\Delta h(r) r dr \tag{4-13}$$

The calculation leads to a normalised power $C_{p,AD}$ *=0.593* for the disc and $C_{p,WT}$ *=0.578* for the wind turbine. The relative difference between them is equal to *2.53%*, of the same order of magnitude of the wake expansion relative difference. Knowing C_t from the balance measurements, the expected induction factor *a* is calculated with Equation (4-2) and used for calculating the expected power coefficient with Equation (4-14) from Burton et al (2001):

$$C_p = 4a(1-a)^2 \tag{4-14}$$

Table 4-4 summarises the AD and WT power coefficients calculated with the two methods (expected from balance measurements and from enthalpy field) and shows the relative difference between them.

Table 4-4. Values of AD and WT power coefficient C_p as expected from direct balance measurements and by indirect calculation

Method	*AD*	*WT*	*Relative difference*
Expected (from balance measurements)	0.588	0.588	0%
From enthalpy field	0.593	0.578	2.53%

For the actuator disc, the C_p calculated with this method is very close to the Betz limit. As a matter of fact, the disc was designed for having an induction factor close to the optimum value. However, the device does not involve an actual extraction of energy from the flow, but the kinetic energy of the incoming flow is converted into turbulence and eventually heat. In fact, a physical emulation of the actuator disc (the latter is only a theoretical model) does not obey to the Betz theory. The C_p of the wind turbine is also very close to the Betz limit because also the WT was designed for quasi-optimal operation. However, the C_p is not calculated with the power available at the shaft, but with the energy extracted from the flow. For this reason, the efficiency is quite high, but a considerable part of it is still wasted in heat for viscous effects and in friction inside the nacelle.

4.3.5 Vorticity Field

Figure 4-15 shows the value of the out-of-plane time-average vorticity, calculated as in Equation (2-4). The derivatives are estimated with a second-order finite-difference scheme. Results in Figure 4-15 (top) show that the AD vorticity is organised as a very concentrated sheet of negative vorticity close to the disc at the tip region which diffuses very quickly. As a matter of fact, at $x/D = 0.6$ the vortex sheet has already diffused in a broader region. Figure 4-15 (bottom) shows that, on the contrary, the WT wake shows a less concentrated vortex sheet that nonetheless diffuses more slowly, preserving its strength for longer distance. As also shown in Chapter 2, the WT vortex sheet bifurcates at the location where the vortex leapfrogging occurs, after which it eventually breaks down and diffuses quite rapidly. The vorticity in the AD and WT wake are comparable only after the tip-vortex instability. In the very near wake, the flow vorticity is higher in the AD wake shear layer; in the second and third locations, while the tip-vortices are still stable, the vorticity in the WT shear-layer exceeds the one in the AD wake, while after the tip-vortex breakdown the values of vorticity are comparable in the two wakes. The inner part of the wake also shows some region of positive vorticity. In the AD wake, these regions constitute the smaller wakes of the wires of mesh B (see Figure 4-2). In the WT wake, regions of positive vorticity are due to the presence of the root vortex. Figure 4-16 depicts the development in the axial direction of the maximum value of vorticity in the AD and WT vortex sheet. The AD initial value of vorticity is three times as large as the WT one and decreases exponentially until $\omega_{z,max}D/U_\infty < 10$ within 2D. For the development of the WT vorticity, three regions can be identified. The first region, in the very near wake before $x/D = 0.5$, is characterised by an increase of the maximum vorticity of approximately 20%. Since a considerable portion of the flow field is not available in this region, the results from the experimental campaign presented in Chapter 2 have been included in the graph of Figure 4-16. It is evident how also in this case the near wake vorticity is subjected to an increase which might be due to the tip-vortex stretching, caused by the fast wake expansion.

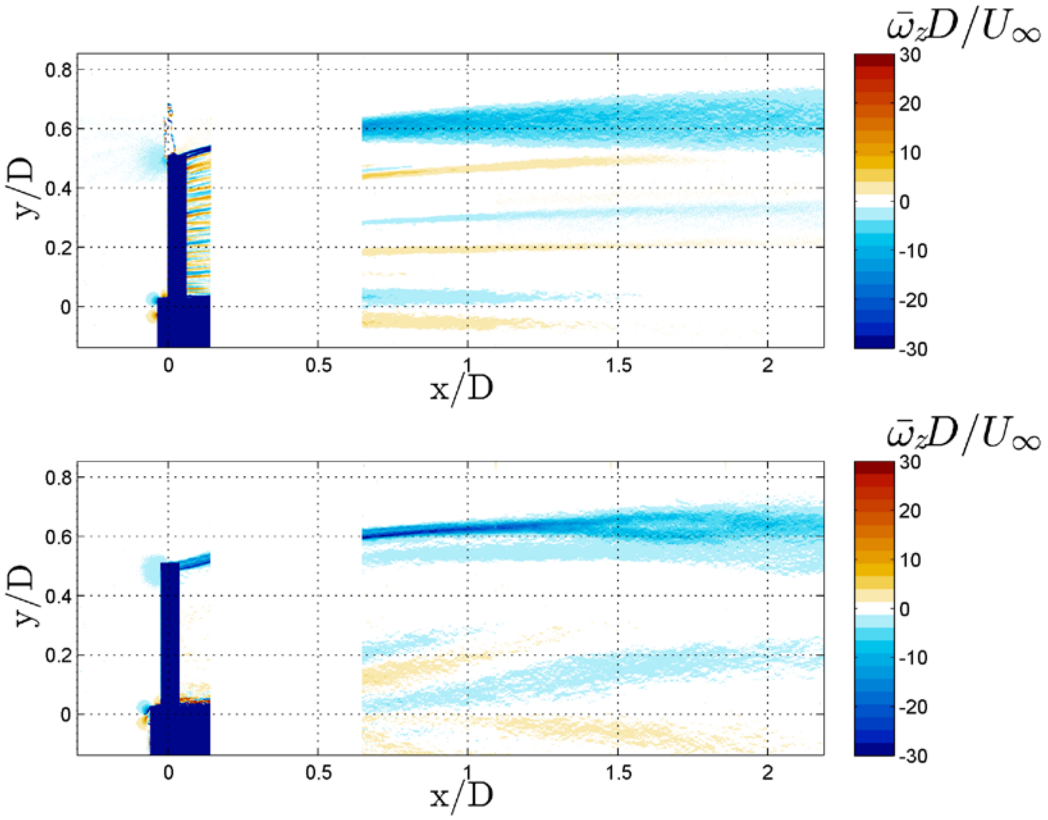

Figure 4-15. Out-of-plane vorticity field in the wake of the AD (top) and of the WT (bottom).

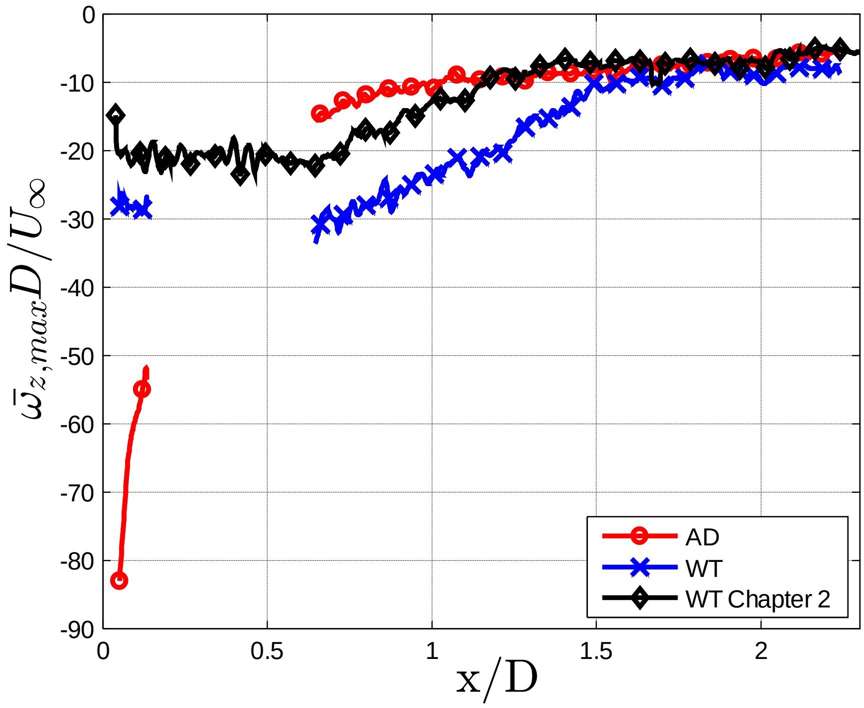

Figure 4-16. Streamwise evolution of the maximum normalized vorticity in the vortex sheet at the edge of the wake. The three curves depicts the values in the AD and WT turbine wake from the present experiments and from the experiments of Chapter 2

As a matter of fact, in the region between $x/D = 0$ and $x/D = 0.5$ 50% of the wake expansion takes place, as shown in Figure 4-11. The second region is characterised by a linear decrease of the peak value of vorticity until the location of the tip-vortex breakdown at $x/D = 1.5$. From this location, the third region starts, where the peak vorticity decreases at a slower rate, comparable to the one of the AD wake.

4.3.6 Wake Turbulence

In Figure 4-17 to Figure 4-19 the three components of the time-average wake turbulence intensity is shown until 2.2D downstream: these figures show a general perspective on the whole wake turbulence field. In Figure 4-20 to Figure 4-22, the same quantities, shown as profiles at selected locations, allow a more precise reading of the values of *TI*. The WT and AD wake turbulence profiles exhibit more evident differences, compared to the velocity profiles in Figure 4-5 to Figure 4-7. The turbulence intensity in the three directions is calculated as Equation (2-13). In this regard, it is very important to stress that the fluctuating terms of velocity *u'*, *v'* and *w'* include any deviation from the mean value of velocity, either if this is caused by a turbulent fluctuation or by a coherent vortex. At a first general observation, both wakes show evident anisotropic turbulent fluctuations, demonstrated by the visible differences among the turbulence values in the three directions TI_x, TI_y and TI_z. Both the AD and the WT profiles show a strong peak in turbulence intensity in correspondence of the wake shear layer. The analysis of the profiles of turbulence in each location (Figure 4-20 to Figure 4-22) will help highlight the sensible differences in the two wakes. In the first location in Figure 4-20 to Figure 4-22, the WT wake exhibits a peak of radial fluctuations intensity TI_y which is 33% larger than the peak of fluctuations in the axial direction TI_x. Coherently with previous literature studies from (Cotroni et al, 2000) it has been found out that the radial fluctuations are the predominant ones. The out-of-plane fluctuations show a more uniform distribution in space, with a value which is roughly 50% of the TI_x peak. In the second location, the persistence of strong tip vortices keeps the peak of fluctuations in the *x*- and *y*-direction equal to their initial values. In the fourth and fifth location, after the tip-vortex breakdown, the fluctuations in the radial direction collapse and the wake turbulence assumes rather isotropic characteristics, with similar values in TI_x, TI_y and TI_z. In the out-of-plane direction, the fluctuation intensity keeps on increasing in the shear layer region from the first to the fifth location. In the shear layer of the AD wake, the peak of turbulence intensity remains constant from the second location to the fifth location, with a value of the out-of-plane fluctuations always two time larger than the one in the *x*- and *y*-direction. The largest differences between WT and AD wake turbulence appear within 1.8D from the model, where the peak of radial fluctuations in the WT wake is two to four times larger than the one in the AD wake. This behaviour is attributed to the convected tip-vortex in the WT wake. As a matter of fact, in the time-averaging process the tip vortex is considered as a turbulent fluctuation in the stream-wise and radial directions (Lignarolo et al, 2015), which dissipates and diffuses after the instability and is not present in the AD wake. In the inner region of the wake, the presence of the WT blades turbulence is prominent. As a matter of fact, the WT wake is characterised by a turbulence intensity which is always higher than the AD one. The fine metal mesh in the AD generates turbulence characterised by smaller-scales structures, that decay very quickly (Batchelor and Townsend, 1947, 1948a, b) and almost completely dissipate within one rotor radius, while the blade root generates vortex structures, which are more self-sustaining. Differences between WT and AD wake turbulence vanish downstream, after *x/D* = 1.8.

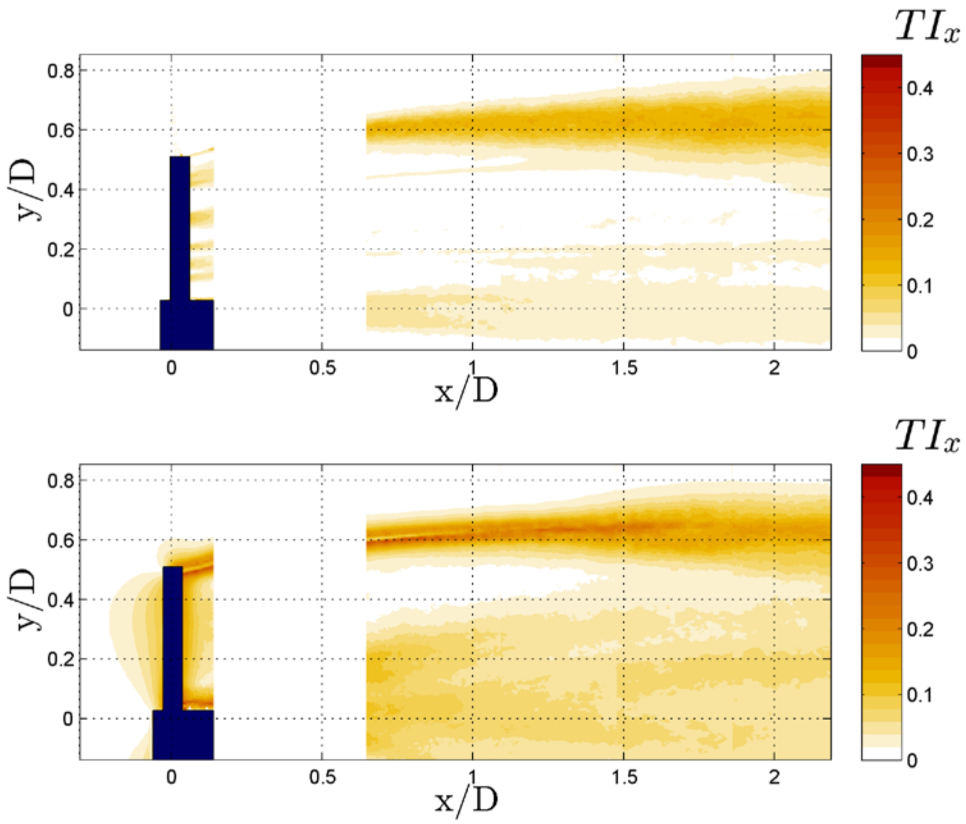

Figure 4-17. Turbulence intensity in the axial (x-direction) direction in the wake of the AD (top) and of the WT (bottom).

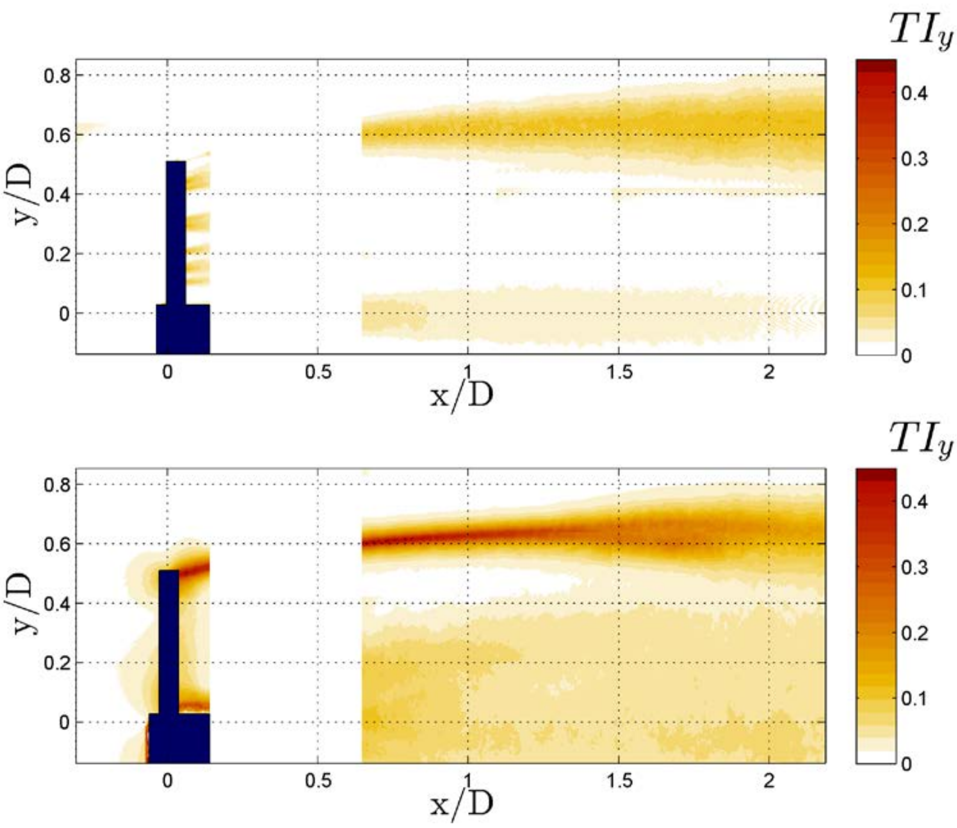

Figure 4-18. Turbulence intensity in the radial (y-direction) direction in the wake of the AD (top) and of the WT (bottom).

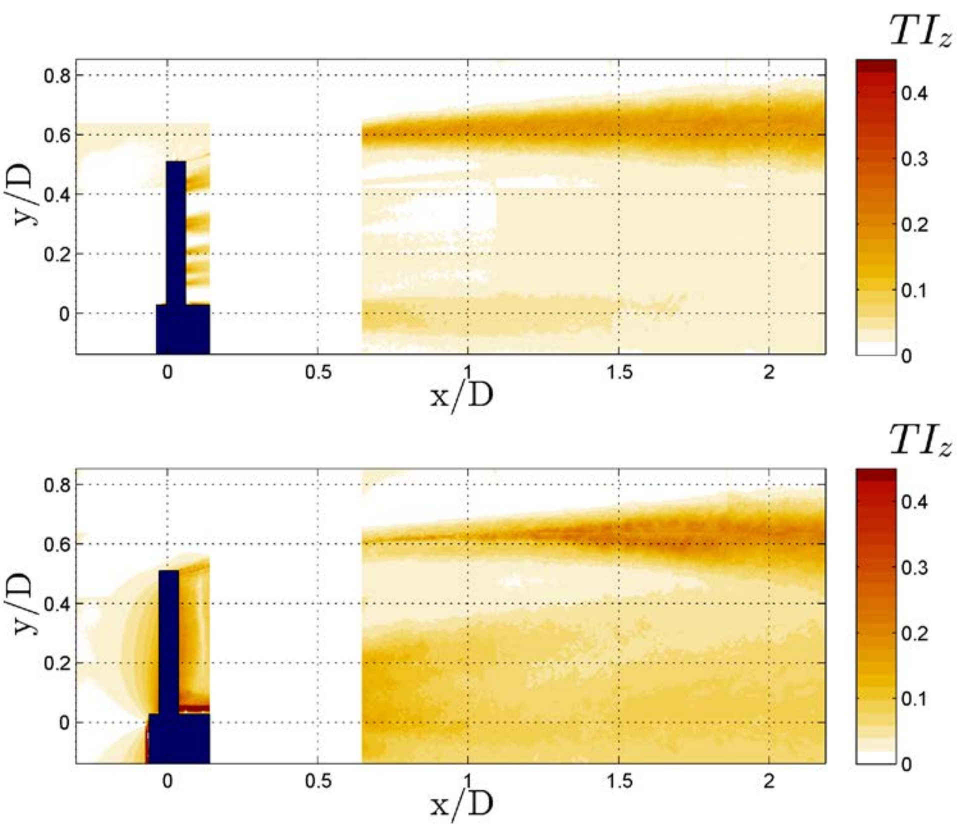

Figure 4-19. Turbulence intensity in the out-of plane (z-direction) direction in the wake of the AD (top) and of the WT (bottom).

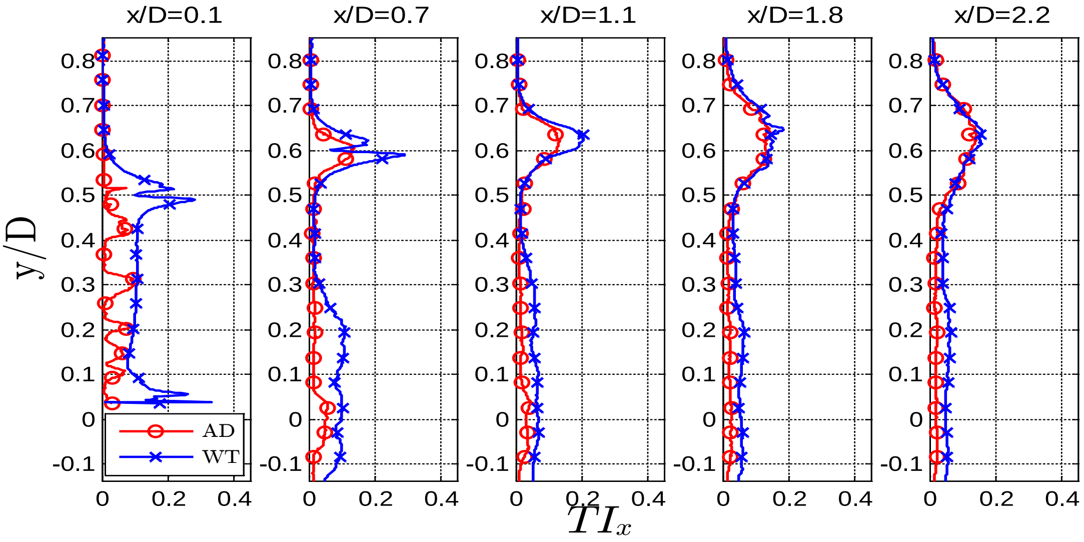

Figure 4-20. Profiles of turbulence intensity in the axial direction (x-direction) at five different locations in the wake of the AD and of the WT.

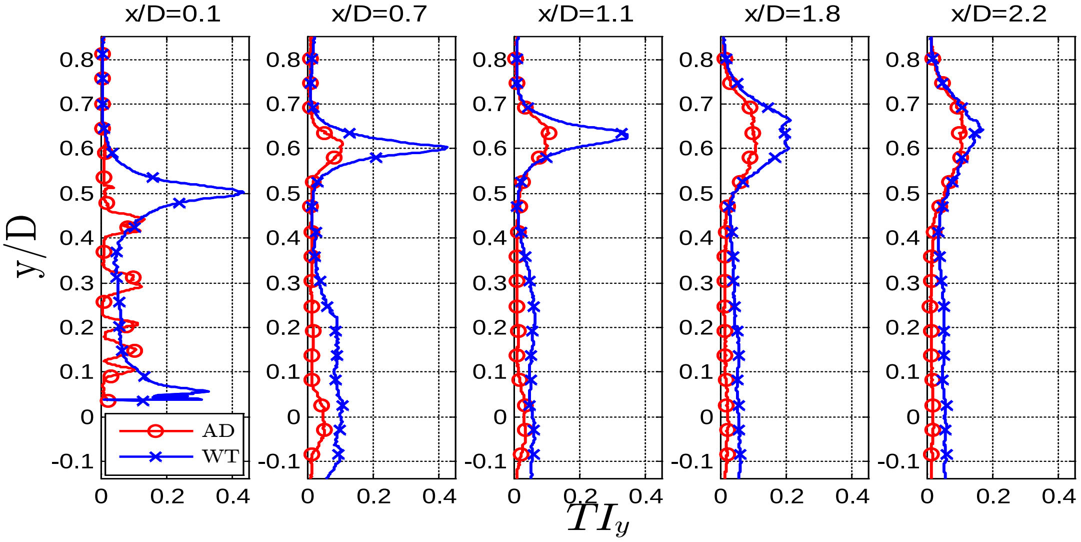

Figure 4-21. Profiles of turbulence intensity in the radial direction (y-direction) at five different locations in the wake of the AD and of the WT.

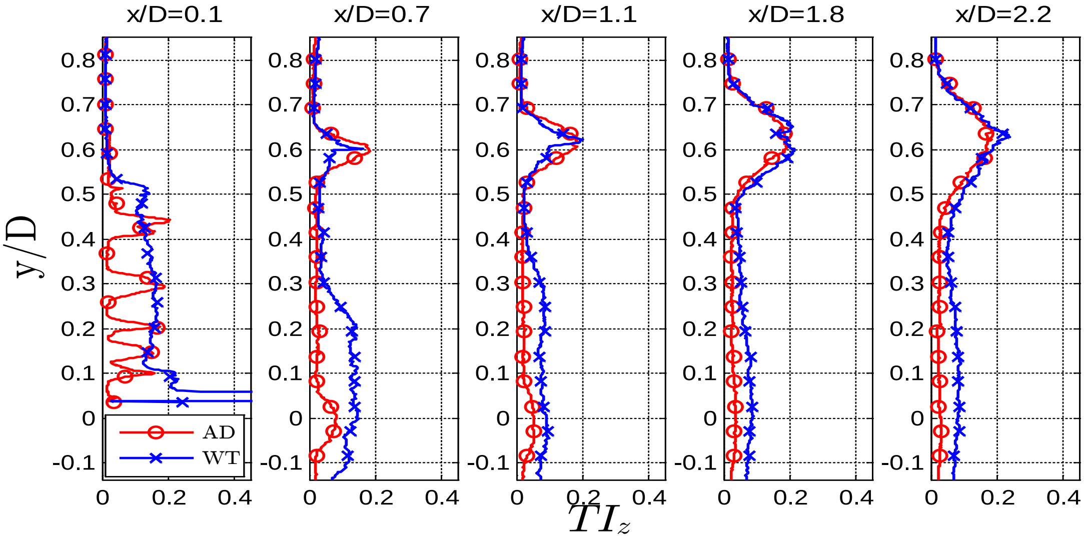

Figure 4-22. Profiles of turbulence intensity in the out-of-plane direction (z-direction) at five different locations in the wake of the AD and of the WT.

4.3.7 WAKE MIXING

Although the turbulence intensity could intuitively be associated with the flow mixing, it has been demonstrated that the Reynolds shear stresses *uv*, *uw* and *vw* are responsible of the flow kinetic energy transport (Antonia et al, 1986, Cal et al, 2010, Cantwell and Coles, 1983, Escudié and Liné, 2003, Hussain, 1983, Reynolds and Hussain, 1972) and that as such they must be taken into consideration for evaluating the turbulent mixing in a particular region of the flow. For this reason the last term of Equation (4-1), which represents the spatial gradients of the flux of mean-flow kinetic energy, has been evaluated in the *x*-*y* plane as $\overline{\Phi} = -\bar{u}\left(\overline{u'v'}\right)$ (streamwise mean-flow kinetic energy flux in the radial direction). As explained in Section 4.2.5, this term represents the entrainment of kinetic energy in the inner part of the wake. The schematic impression in Figure 4-23 shows the regions where the flux $\overline{\Phi}$ has been calculated, indicated by the green squares. The locations are in the near wake and in the transition wake, respectively centred at x/D = 0.95 and x/D = 1.83. The first location is before the tip-vortex instability and the second is right after the beginning of the instability. In these locations, a large number of samples has been used for obtaining a good convergence of the Reynolds stresses *u'v'* (1000 for the AD and 5000 for the WT). Figure 4-24 shows the radial profiles of the mean-flow kinetic energy fluxes towards the inner part of the wake as described in Section 4.2.5. The AD wake shear layer is characterised by a solely positive flux of mean-flow kinetic energy, whereas in the WT wake shear layer the more coherent flow fluctuations give rise to both positive and negative fluxes. In contrast with what expected after observing the strong peak of fluctuations intensity in Figure 4-20 to Figure 4-22, where the WT exhibits a *TI* peak two to four times larger than the AD one, the WT wake shear layer does not show the same peak in mean-flow kinetic energy entrainment in the near wake region ($0 < x/D < 1.8$). On the contrary, the value of the entrainment in the two wakes is comparable, with the AD one involving a larger portion of the flow. In the WT wake both random fluctuations and periodic vortices are accounted for as turbulence, as mentioned in Section 4.3.6. In Chapter 3 it was shown that the periodic vortical fluctuations do not lead to a net positive transport of mean-flow kinetic-energy (and therefore entrainment of energy in the WT wake). The entrainment in the AD wake shear layer is relatively stable, preserving the same intensity from the very near wake until the end of the measured field. On the contrary, the WT wake shear is characterised by pronounced variations of mean-flow kinetic energy flux. In particular in the transition wake, the magnitude of the entrainment collapses to a strong negative value within a distance smaller than 0.2D and reaches again positive values after 0.2D. This behaviour was also observed in Chapter 2 (Figure 2-24) in the analysis of the Reynolds shear stresses. The sudden collapse to negative values is caused by the tip-vortex pairs changing orientation during the leapfrogging process, passing from a negative to a positive *u'*-*v'* correlation (see Hussain, 1983). The subsequent low positive value of entrainment is caused by the vortex break-down, which leads to the disappearance of the strong coherent vortical fluctuations and gives start to a new mixing process only dominated by random turbulent fluctuations. At x/D = 2.04, the flux intensity is roughly just 50% of the one in the AD wake, despite the WT *TI* is equal or slightly larger than the AD one as seen in Figure 4-20 to Figure 4-22. This is the sign that turbulence intensity alone is not enough for analysing the mixing phenomenon.

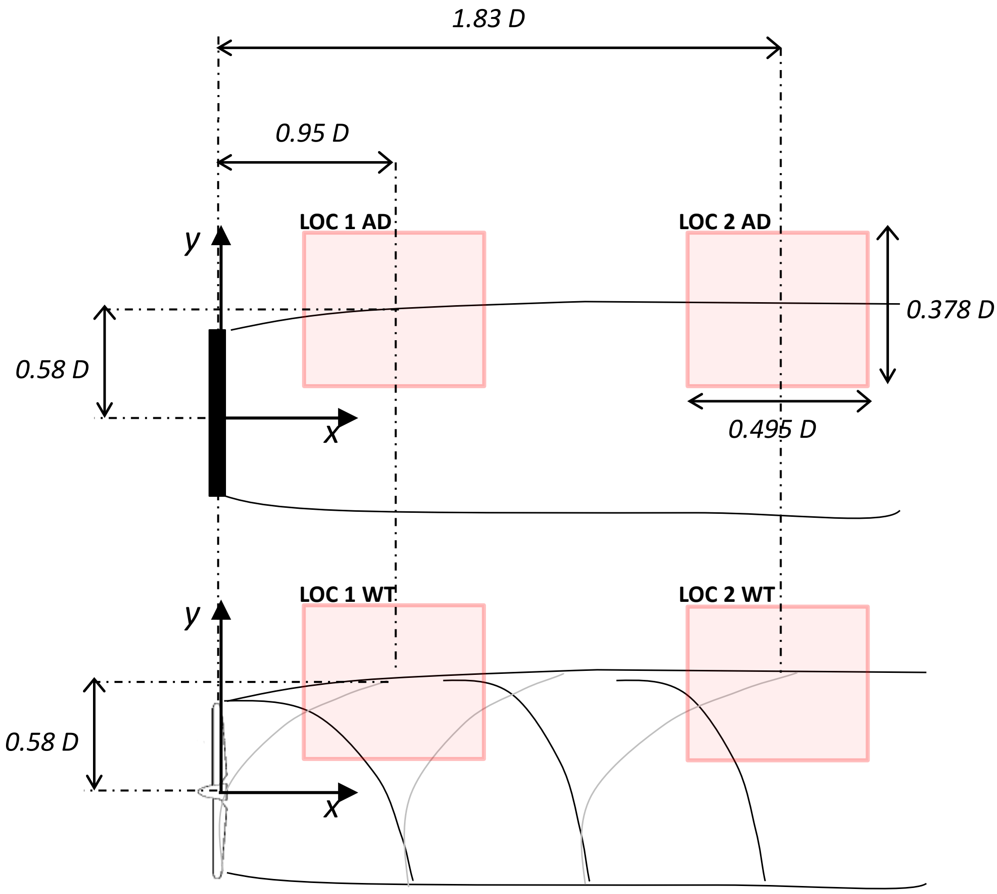

Figure 4-23. Schematic impression of the measurement locations of the mean flow kinetic energy transport. The green areas are represent the FOV (AD in the top image and WT in the lower image). Distances and dimensions are indicated by the blue lines.

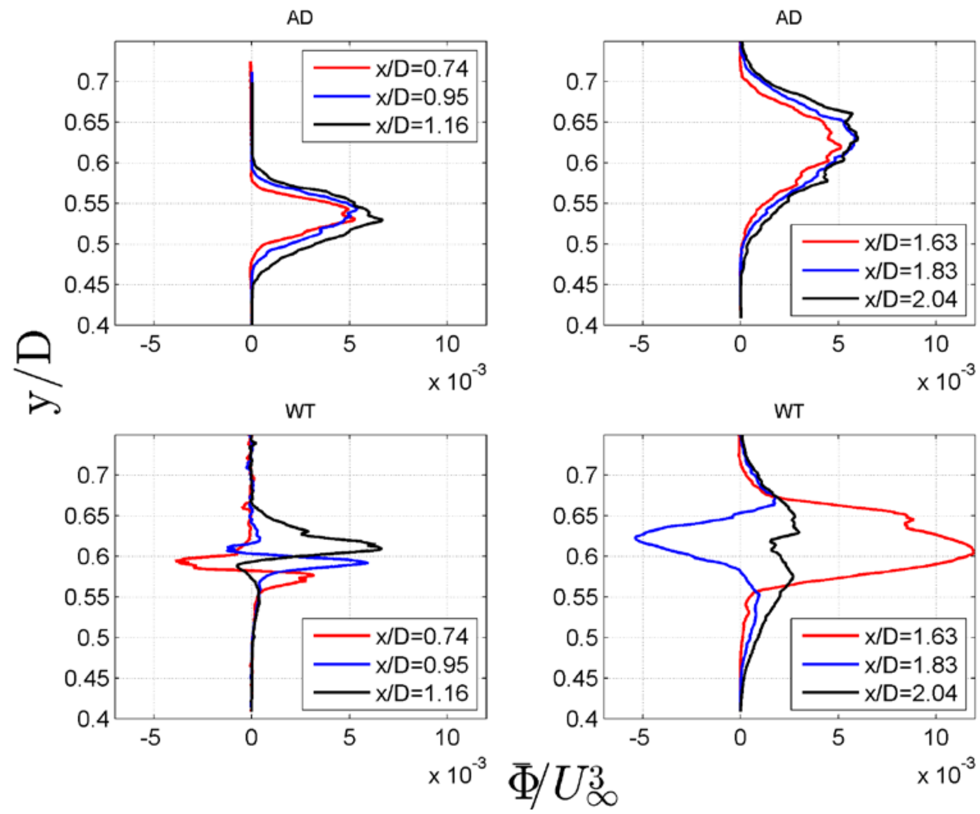

Figure 4-24. Mean flow kinetic energy flux at x/D = 0.95 and x/D = 1.83.

4.3.8 STEREO PIV UNCERTAINTY

Measurement uncertainties on the stereo PIV velocity data contain random components, primarily caused by random oscillation of the drive motor rotational frequency, random delays in the triggering systems of the stereo PIV set up, cross-correlation uncertainty and turbulent fluctuations. The first two sources of uncertainty are considered negligible compared to the others, due to the high-accuracy devices adopted in the present setup. Due to statistical convergence, the effect of the components due to cross-correlation and flow fluctuations scales with $1/\sqrt{N}$ (with N 200 in the present analysis). For the cross-correlation uncertainty on the vector fields, a typical value of 0.1 pixels on the axial and radial velocity components and 0.2 pixels on the out-of-plane component is expected (Elsinga et al, 2005, Westerweel, 1993). In this analysis, the method presented in Wieneke (2015) is used for calculating the cross-correlation uncertainty on each instantaneous velocity field and Equation (4-15) is used for calculating the uncertainty on the mean values:

$$\overline{\varepsilon_u} = \frac{\sqrt{\sum_{i=1}^{N}\left(\varepsilon_{u,i}\right)^2}}{N} \qquad \overline{\varepsilon_{u'u'}} = \frac{\sqrt{\sum_{i=1}^{N}\left(\varepsilon_{u'u',i}\right)^2}}{N} \tag{4-15}$$

respectively for the time-average velocity and the time-average Reynolds stresses, where ε_u and $\varepsilon_{u'u'}$ are the errors on the single instantaneous SPIV snapshot on the velocity and turbulent fluctuations respectively: $\varepsilon_{u'u'}$ is calculated with Equation (4-16):

$$\varepsilon_{u'u'} = 2(u - \bar{u})\sqrt{{\varepsilon_u}^2 - {\varepsilon_{\bar{u}}}^2} \tag{4-16}$$

which derives from applying the equation of the error propagation (Taylor, 1997) to the $\overline{u'_i u'_i}$ equation. The overall relative uncertainty on the mean velocity due to random components is presented in Table 4-5. A second source of uncertainty of the mean flow properties is related to the limited size of the averaging ensemble, namely the number of SPIV instantaneous fields. In order to estimate the magnitude of the uncertainty, the relative difference between the flow statistics calculated at 200 samples and the one obtained with 5000 samples has been evaluated. Results are presented in Table 4-5. Where the flow is characterized by a negligible vorticity (e.g. free stream and inner wake, excluding the shear layer region), the steady Bernoulli equation can be used to retrieve pressure and the pressure uncertainty is a function of the velocity uncertainty. The former can be estimated from a linear propagation analysis of the Bernoulli equation. The estimation for the pressure uncertainty are reported in Table 4-5. The pressure in the vortical regions is obtained by a second-order Poisson algorithm with potential boundary conditions as explained in section 4.3.3. Because of the relatively well-resolved velocity fields, it can be assumed that the pressure solver keeps the uncertainty on the pressure of the order of the Bernoulli values, as stated in Ragni et al (2014)

Table 4-5. Maximum cross-correlation and convergence uncertainty for the mean velocity, Reynolds stresses and pressure.

Quantity	*Cross-correlation uncertainty*	*Convergence uncertainty*
$\bar{u}$	0.15%	0.6% (2% in the shear layer)
$\bar{v}$	2%	2%
$\bar{w}$	1.5%	2.5%
$\overline{u'u'}$	3.5%	5.5%
$\overline{v'v'}$	0.9%	4%
$\overline{w'w'}$	10%	13%
$\bar{p}$	0.1%	1%

4.4 CONCLUSIONS

The stereo particle image velocimetry technique has been adopted for studying the turbulent velocity field in the wake of two-bladed wind-turbine model and of a porous disc. The analysis has shown that the two models produce remarkably similar wake expansion and energy extraction, within 4% difference, by matching the diameter and thrust coefficient. Larger differences (locally up to 20%) are observed in the pressure field at the blade-tip and root region, however the global pressure field produces the same total axial force on the disc and turbine. Observation of the second order flow statistics shows that both wakes are characterised by anisotropic fluctuations. More evident anisotropy in the WT wake fluctuations, with higher magnitude in the radial direction, confirms the findings of previous studies. The stronger fluctuations in the WT wake are due to the presence of concentrated tip vortices. These are normally accounted for in the calculation of the *added turbulence*. The latter one represents the flow turbulence caused by the presence of the turbine, which is added to the ambient turbulence as explained in

Crespo et al (1999) and includes both coherent periodic structures, as the tip-vortices, and random velocity fluctuations, which are not separated in the classical double Reynolds decomposition applied in this work. This leads to the well-known peaks of turbulence intensity close to the rotor at the blade-tip location. However, despite the so-calculated total turbulence intensity in the near wake of the WT is considerably larger than the one in the AD wake (two to four times), both wakes exhibit the same levels of mean-flow kinetic-energy transport in the shear layer, which then collapses to 50% of its original value after the breakdown of the WT tip-vortices after the leapfrogging. This demonstrates how the physics governing the turbulent mixing in the two wakes are intrinsically different and, as hypothesised by Medici (2005), that the presence of strong coherent fluctuations in the near wake does not enhance the wake mixing. The study has been conducted at low turbulence intensity in order to separate the problems of the flow mixing caused by the external flow fluctuations and the one caused by the turbulence induced directly by the AD or the WT presence. The analysis, as such, showed the intrinsic differences and similarities between the flow in the two wakes, solely due to the wake-induced flow, with no influence of external flow fluctuation, differently from most of the studies on similar subjects, which have been performed in the presence of high wind tunnel turbulence or simulated atmospheric boundary layers (and atmospheric turbulence). The study has shown that even in absence of inflow turbulence the velocity fields in the AD and WT wakes are very well comparable, despite the fact that the turbulent mixing is very different. This seems to contradict statements affirming that results from actuator disc simulations are valid only after 5 diameters downstream the disc (Schepers, 2012). The results suggest the possibility to extend the use of the actuator disc model in numerical simulation until the very near wake, provided that the turbulent mixing is correctly represented.

5 TURBULENCE PRODUCTION AND KINETIC ENERGY TRANSPORT IN THE WAKE OF A WIND TURBINE AND OF AN ACTUATOR DISC

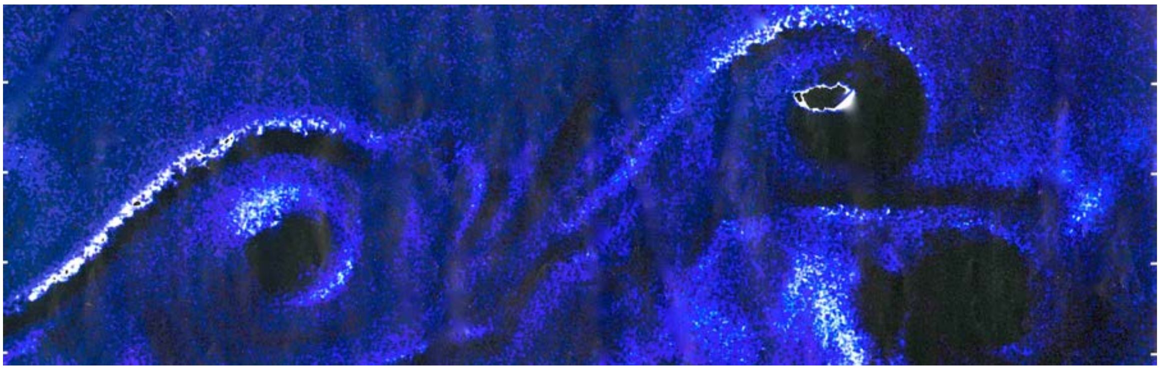

The time average spatial distributions of the axial, radial and out of plane velocity and the six component of the Reynolds stresses have been studied at two different locations within three diameters from the wind-turbine and actuator-disc model in the shear layer between the wake and the free stream. The spatial distribution of the Reynolds stresses allow to elucidate the vortex pairing dynamics and its effect on the mean flow kinetic energy transport and turbulence production. These quantities are further calculated separating the contribution of the periodic structures from the background random turbulence by mean of a POD based filter. The random turbulent motions are found to give the largest positive contribution to the mean flow kinetic energy entrainment in the wake. The periodic structures are yielding both positive and negative transport, depending on the location and on the orientation of the vortex pairs. Coherently to what found in previous literature, periodic flow motions are found to lead to a large zone of "negative production" of turbulence. The same analysis performed in the porous disc wake shows a considerably larger turbulent mixing and turbulence production.

This chapter is submitted as:

Lignarolo, L.E.M., Ragni, D., Simão Ferreira, C.J., van Bussel, G.J.W., 2015. Turbulence production and kinetic energy transport in the wake of a wind turbine and of an actuator disc. *Physics of Fluids* (in review).

5.1 INTRODUCTION

The challenge of numerically reproducing the turbulent flow in the near-wake region of a wind turbine is a topic of increasing interest in the wind-energy scientific community. Turbulence modelling is a key issue for correctly simulating the entire wake velocity field, especially from the near-wake region just behind the turbine to the far wake. Most of the numerical models currently used are based on the actuator disc assumption, which neglects the effect of blade rotation, tip-vortex development and decay. In the actuator disc assumption, the wake is treated as an ensemble average over many rotor revolutions, and it is approximated with a cylindrical shear-layer resembling the classical turbulent shear-layer region of mixing layers. In a previous study from Gómez-Elvira et al (2005), it has already been pointed out that the formation of the shear layer in a wind turbine wake results from the induction of concentrated vortices. One of the peculiar characteristic of such vortical system is their coherence, which does not allow to treat the near wake as globally turbulent. This has been reflected in the misunderstandings associated with the well-known concept of “added turbulence” (Chamorro and Porté-Agel, 2009, Crespo and Hernandez, 1996), as representative of both periodic and random velocity fluctuations on a mean flow field. In this framework, Gómez-Elvira et al (2005) propose an anisotropic turbulence model as a more accurate representation of the flow. Some other corrections to turbulence models for actuator disc have been proposed and validated: El Kasmi and Masson (2008) added an extra term to the transport equation for the turbulence energy dissipation rate in the k-ε model. This accounts for the energy transfer-rate from large-scale turbulence to small-scale turbulence in the turbine near-wake, improving considerably the agreement with experimental data.

In Chapter 2, the analysis of the flow statistics using stereo particle image velocimetry (SPIV) in the wake of a 0.6 m diameter horizontal-axis wind-turbine revealed a major difference between the unconditioned-and the phase-locked average turbulence-intensity. The former exhibits characteristic peaks close to the rotor at the blade tip region due to the presence of strong coherent vortices, while the latter shows a sudden increase after the tip-vortex breakdown. The analysis was conducted in presence of a tip-vortex pairing instability (leapfrogging). In order to distinguish between the role of the periodic structures and the one of random fluctuations in the turbulence mixing and in turn in the wake re-energising, the transport of the mean-flow kinetic energy was analysed with phase-locked and unconditioned average data with a triple decomposition of the flow in Chapter 3. The analysis of interacting vortex pairs quantified the different effects of the vortex structures and the pure turbulent fluctuations, both typically accounted for as turbulence (Crespo and Hernandez, 1996). In particular, the analysis presents two zones of totally different mixing. In the first zone, the tip vortices act as inhibitors of the wake mixing during its expansion; in the second zone, the leapfrogging causes a sudden increase of the net entrainment of the mean flow kinetic energy, generating a more efficient mixing by action of random flow motions, with benefit of the wake re-energising. The result is in accordance with the hypothesis of Medici (2005) who stated that the near-wake tip-vortices are acting as a *shield*, impeding the mixing with the outer flow. The production of turbulence is thus very low in the first region, with an abrupt increase after the leapfrogging zone.

In the framework of the abovementioned analyses, the present chapter is intended to tackle the problem of the transition from the organised vortex structures in the near wake and the turbulence flow in the post-instability region (Sørensen, 2011). The study focuses on two specific locations along the shear layer at the border of the wake of a wind turbine model (WT) and of a porous disc, physical emulation of the actuator disc (AD) numerical model. The analysis is based on the experimental data presented in Chapter 4. The proper orthogonal decomposition (POD) is used for decomposing the flow field fluctuations into a periodic and a random component in order to apply a triple decomposition of the flow (Reynolds and Hussain, 1972). The use of the POD technique as a flow filter is employed to avoid acquiring long phase-locked measurements at several phases of the rotor rotation (Perrin et al, 2007). The analysis is meant to provide with a more complete quantitative estimation of the re-energising of the wake shear layer.

5.2 THE EXPERIMENT

For the present analysis, the data from the experiment presented in Chapter 4 have been used. All necessary information about the design of the actuator disk (AD) and the wind turbine (WT) models are included in Chapter 4, as well as a detailed description of the stereo PIV setup. In this work, only four specific sets of data have been analysed, constituted by rectangular fields of view (FOV) with an extension of 0.495D × 0.378D. These are the same data presented in Section 4.3.7 in the previous Chapter. The first two FOV's are centred at 0.95D and 1.83D from the AD model (respectively LOC 1 AD and LOC 2 AD): 1000 SPIV images have been acquired and averaged. The other two FOV's are centred at 0.95D and 1.83D from the WT model (respectively LOC 1 WT and LOC 2 WT): 5000 SPIV images have been acquired and averaged. Figure 4-23 in Section 4.3.7 presents the location and the extension of the four sets. The tip-vortex pairing instability is triggered by a very small asymmetry of the blade pitch angle (0.5°) which acts as a constant perturbation, therefore ensuring a constant excitation of the leapfrogging mode and inducing the vortex pairing to happen always at the same location.

5.3 POD DECOMPOSITION AND SELECTIVE FLOW RECONSTRUCTION

A POD-based selective flow reconstruction is adopted for separating the flow fluctuations into their periodic and random components in the WT wake. The POD decomposition is based on an implementation of the discrete method of Chatterjee (2000), a singular value decomposition (SVD) of matrices applied to the three components of velocity. The POD decomposition is followed by a lower-rank reconstruction of the velocity field in each PIV snapshot using only a number i of selected modes for obtaining the periodic flow fluctuations and N-i for obtaining the random flow fluctuations. This distinction is based on the assumption that the strong periodic fluctuations contains a large part of the flow kinetic energy and, as such, will be best described by a low-rank reconstruction including only the most energetic modes. Figure 5-1 shows the eigenvalues associated to the POD modes, representative of the levels of energy associated to each mode in which the wake flow is decomposed (only the first 25 are shown). For ensuring the convergence of the decomposition, all 5000 PIV snapshots have been used. The analysis has been performed only on the flow fluctuations, namely the time-average velocity field has been subtracted to each snapshot. In the two locations of the WT wake, modes which are appearing in couples are associated to periodic fluctuations. Indeed, a periodically repeating signal with unknown phase can be represented in Fourier series as superposition of sines and cosines of the same frequency (Fourier, 1808), which will be therefore treated as coupled modes in the PDO decomposition. In comparison the energy distribution in the AD wake (Figure 5-1) is relatively more uniform, with no peaks nor coupled modes. This is due to the different nature of the flow, dominated by random fluctuations. The first 6 modes are used for reconstructing the periodic fluctuations in LOC 1 and the first 4 modes in LOC 2. Figure 5-2 shows an example of a snapshot decomposition into periodic and random flow fluctuations. The red markers show the last mode included in the reconstruction of the periodic fluctuations: the first 6 modes are used for reconstructing the periodic fluctuations in LOC 1 WT and the first 4 modes in LOC 2 WT, accounting for 8% and 3% of the total energy of the flow fluctuations respectively. For comparison, Table 6-1 reports the number of modes necessary for reconstructing different amounts of the total fluctuation energy. Figure 5-2 shows an example of a snapshot decomposition into periodic and random flow fluctuations.

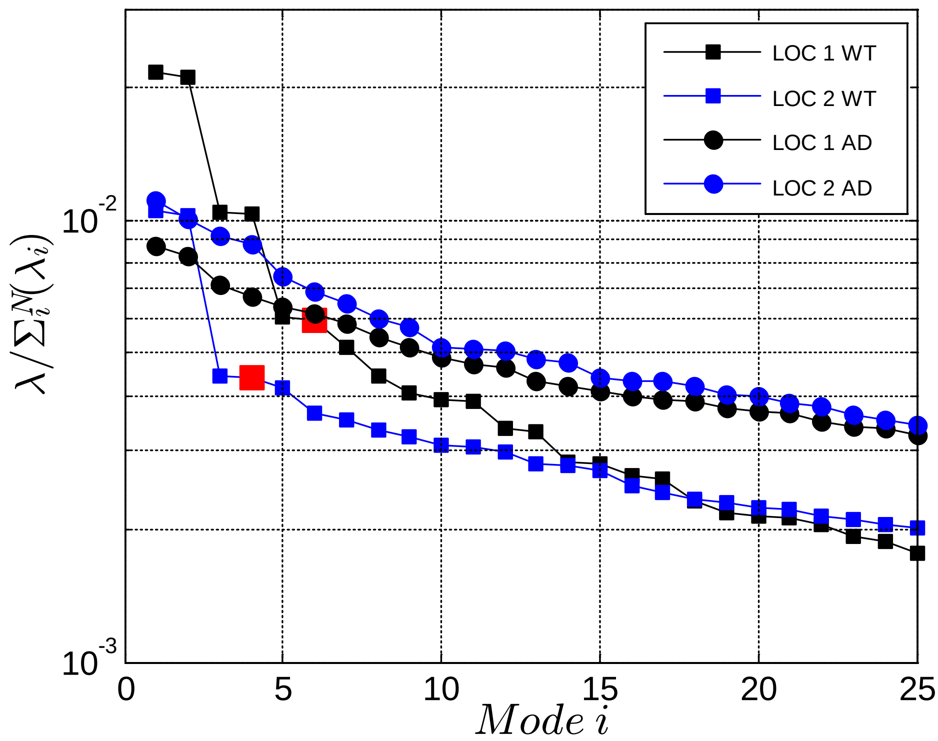

Figure 5-1. Normalised POD eigenvalues (only 25 of the total 5000 values are shown). The red markers show the last mode included in the reconstruction of the periodic fluctuations: in LOC 1 WT, the first 6 modes account for 8% of the energy of the flow fluctuations and in LOC 2 WT the first 4 modes account for 3% of the energy.

Table 5-1. Number of modes necessary for reconstructing different amounts of the total fluctuation energy. The figures in bold are relative to the decomposition adopted in this analysis.

Number of modes		Energy	
LOC 1 WT	LOC 2 WT	LOC 1 WT	LOC 2 WT
6	4	8%	3%
732	831	50%	50%
2047	2114	75%	75%
4098	3961	95%	95%

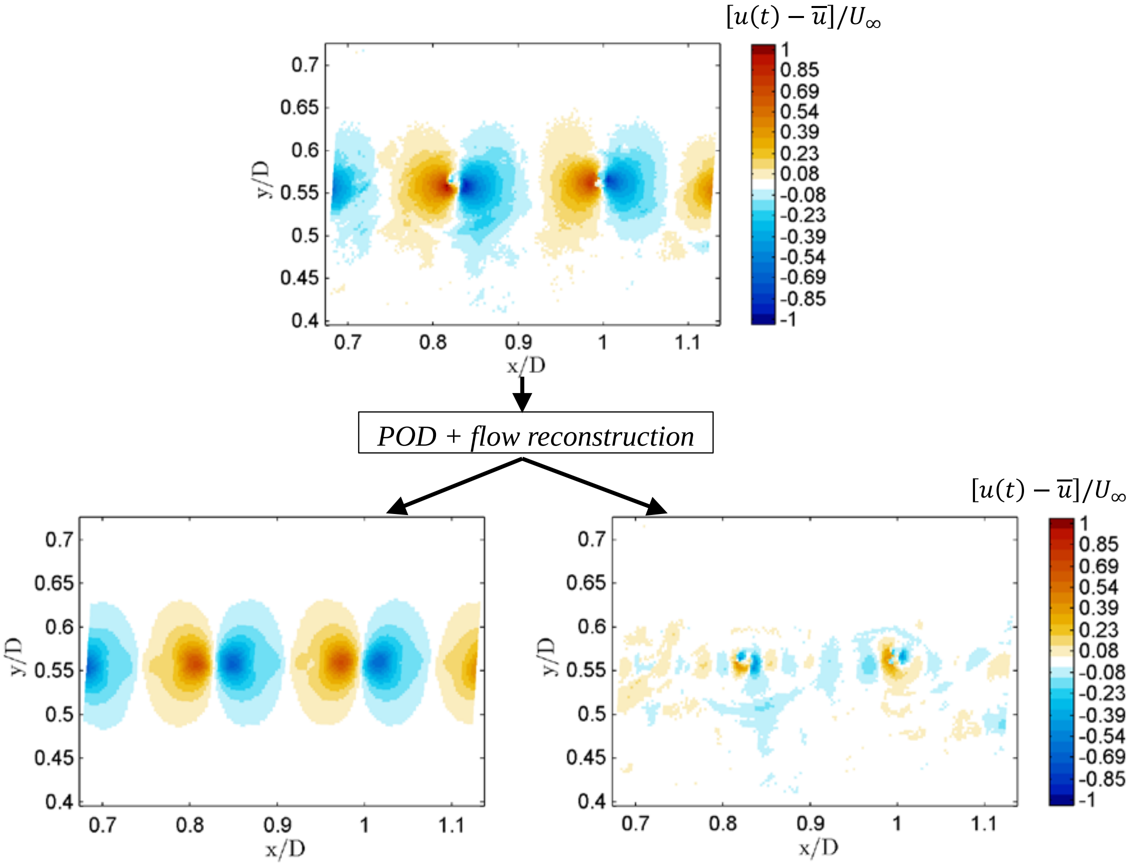

Figure 5-2. Example of instantaneous velocity-fluctuation snapshot (top graph). Instantaneous periodic motion $\tilde{u}_i^f(t)$ (bottom left) and random fluctuations $u_{s,i}^f(t)$ (bottom right) in the shear layer at the edge of the WT wake (LOC 1 WT), separate through the POD filter.

5.4 Analysis Of Turbulent Mixing

5.4.1 Mean-Flow Kinetic Energy Transport

In Chapter 3, a phase-locked analysis of the mean-flow kinetic-energy transport through the wind-turbine wake shear layer for one single phase of the rotor rotation was performed, showing how the leapfrogging and the consecutive vortex breakdown represent a discontinuity in the process. With the current volume of data, the analysis is extended to the time-average case, accounting for the contribution of all rotational phases. This allows to have a more complete quantitative estimation of the mean-flow kinetic energy which is entrained in the wake shear layer by the periodic and random flow fluctuations. Using the selective flow reconstruction presented in section 5.3, a triple decomposition of the flow is performed. The velocity field u_i is defined as:

$$u_i(t) = \bar{u}_i + \tilde{u}_i^f(t) + u_{s,i}^f(t); \tag{5-1}$$

where $u_i(t)$ is the instantaneous velocity field, $\bar{u}_i$ denotes the time averaged value, $\tilde{u}_i^f(t)$ indicates the periodic fluctuations, $u_{s,i}^f(t)$ the random fluctuations and t is the time: the superscript f indicates that the quantity has been obtained via a filtering operation with the selective flow reconstruction. The subscripts i indicates the direction, with $i = 1, 2, 3$ corresponding to x-, y- and z-directions (respectively the axial, radial and out-of-plane directions in the present set-up). With a classical Reynolds decomposition, the velocity field would be defined as:

$$u_i(t) = \bar{u}_i + u'_i(t) \tag{5-2}$$

where $u'_i = \tilde{u}_i^f(t) + u_{s,i}^f(t)$. The time-average Reynolds stresses related to the periodic motion and the random flow fluctuations are calculated respectively as:

$$\overline{\tilde{u}_i\tilde{u}_j} = \frac{\sum_{k=1}^{N} \tilde{u}_i^f(t_k) \cdot \tilde{u}_j^f(t_k)}{N}; \qquad \overline{u_{s,i}u_{s,j}} = \frac{\sum_{k=1}^{N} u_{s,i}^f(t_k) \cdot u_{s,j}^f(t_k)}{N}; \tag{5-3}$$

where k is the sample index, t_k is the time of the k^{th} sample and N the number of samples. In the wake of the AD, where no periodic fluctuations are detected, a standard double decomposition is applied as in Equation (5-2), with the Reynolds stresses calculated as in Eq. (5-4):

$$\overline{u'_i u'_j} = \frac{\sum_{k=1}^{N} [u_i(t_k) - \overline{u_i}] \cdot [u_j(t_k) - \overline{u_j}]}{N} \tag{5-4}$$

The analysis allows to calculate time-average mean-flow kinetic-energy flux due to the periodic fluctuations $\overline{\Phi_{p,WT}}$ and the random fluctuations $\overline{\Phi_{s,WT}}$ WT wake and the total flux due to all fluctuations $\overline{\Phi_{tot,AD}}$ in the AD wake as:

$$\overline{\Phi_{p,WT}} = -\bar{u}_i\left(\overline{\tilde{u}_i\tilde{u}_j}\right); \qquad \overline{\Phi_{s,WT}} = -\bar{u}_i\left(\overline{u_{s,i}u_{s,j}}\right) \qquad \overline{\Phi_{tot,AD}} = -\bar{u}_i\left(\overline{u'_i u'_i}\right) \tag{5-5}$$

Figure 5-3 shows the zone average of the quantities in Equation (5-5), respectively $IF_{per,WT}$, $IF_{rdm,WT}$ and $IF_{tot,AD}$, where IF stands for Integral Flux across the wake shear layer calculated in cylindrical coordinates as:

$$IF_{per,WT} = \frac{1}{dAU_\infty^3}\int_{in}^{out}\overline{\Phi_{p,WT}(x,y)}ydy \qquad IF_{rdm,WT} = \frac{1}{dAU_\infty^3}\int_{in}^{out}\overline{\Phi_{s,WT}(x,y)}ydy \qquad IF_{tot,AD} = \frac{1}{dAU_\infty^3}\int_{in}^{out}\overline{\Phi_{tot,AD}(x,y)}ydy \quad (5\text{-}6)$$

where dA is an area with height equal to the FOV height and width equal to dx (= dy) and $IF_{tot,WT} = IF_{per,WT} + IF_{rdm,WT}$. The notation $\int_{in}^{out}$ indicates an integral from the inner-wake region to the freestream, namely from $y/D = 0.40$ to $y/D = 0.73$. In LOC 1 WT (Figure 5-3, top figure), the mean-flow kinetic-energy transport due to periodic flow motions in the WT wake $IF_{per,WT}$ is mainly negative with some sparse positive regions. This means that the periodic motion, does not contribute to the wake mixing, on the contrary it introduces a negative flux which subtracts energy from the wake flow in the very near wake. The random fluctuation produces a solely positive flux $IF_{rdm,WT}$ which steadily increases throughout the whole area. After $x/D = 2$, $IF_{rdm,WT}$ exhibit a more rapid increase due to the vortex breakdown after the leapfrogging. In LOC 2 WT (Figure 5-3, bottom image) both positive and negative transport is observed, due to the periodic motion. In the area where $x/D < 1.75$, the transport term is positive, whereas the region $x/D > 1.73$ is characterised by a negative transport. The location $x/D < 1.73$ was described in Chapter 4 as the maximum of a localised increase of the shear layer thickness. In the experiments performed by Lignarolo et al (2014), this was the location where the pairing tip-vortices have completed a 90° rotation around their saddle points. This location was proved to coincide with a sign inversion of the phase-locked mean-flow kinetic-energy transport from positive to negative. This behaviour is in fact preserved in the time-average field. As discussed in Chapter 3, this is owed to a change of the vortex-pair orientation. After $x/D = 2$, $IF_{per,WT}$ exhibits a rapid decrease, which may be due to the vortex breakdown after the leapfrogging. The total flux $IF_{tot,WT}$ is strongly affected by the behaviour of $IF_{per,WT}$, quickly decaying along the first half of the area until it reaches a small region of total negative flux in $1.8 < x/D < 1.9$. After this location, the total flux is mainly dominated by the action of the random fluctuations and it steadily increases. In the AD wake, the total mean-flow kinetic-energy transport $IF_{tot,AD}$ is about two to three times larger than $IF_{tot,WT}$ in the WT wake, everywhere positive and steadily increasing with a trend similar to $IF_{tot,WT}$ in LOC 1 AD and more similar to $IF_{per,WT}$ in LOC 2 AD.

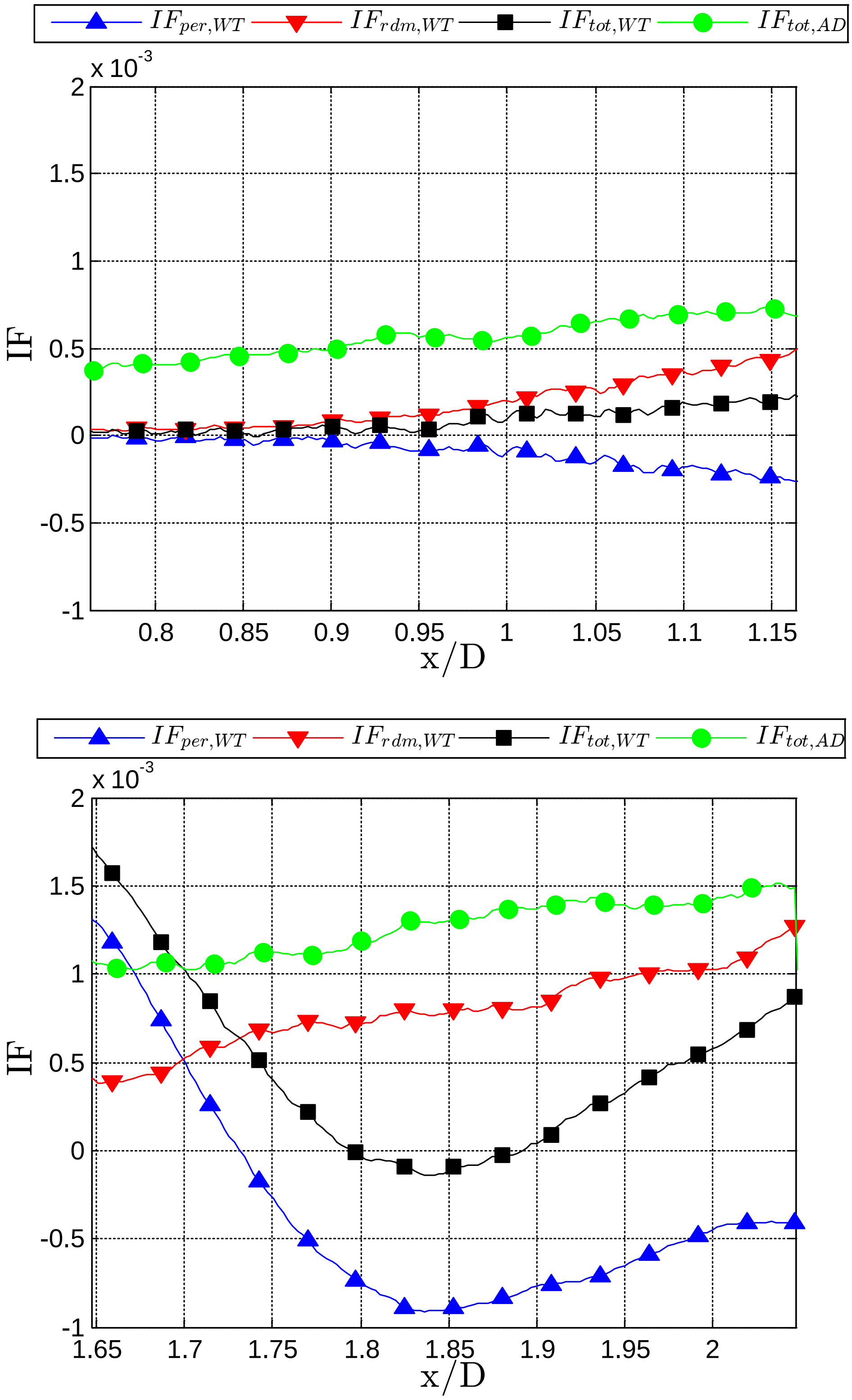

Figure 5-3. Streamwise evolution of the zone averaged mean-flow kinetic-energy flux by the action of periodic and random flow fluctuations in the WT and AD wake, in LOC 1 (top figure) and LOC 2 (bottom figure).

5.4.2 Production Of Turbulence

The time-average total production of turbulence in the WT wake shear layer is composed by two terms (see Chapter 3). The first term, shown in Equation (5-7), represents the extraction of energy from the mean flow by action of the periodic fluctuations $\overline{\tilde{u}_i\tilde{u}_j}$; the second term, in Equation (5-8), represents the decay of the mean-flow kinetic energy into turbulence by action of the random fluctuations $\overline{u_{s,i}u_{s,j}}$. In the wake of the AD, the production is composed by a single term, shown in Equation (5-9) where the Reynolds stresses are calculated with Equation (5-4):

$$\overline{Pe_{m-p,WT}} = -\overline{\tilde{u}^2}\frac{\partial\bar{u}}{\partial x} - \overline{\tilde{v}^2}\frac{\partial\bar{v}}{\partial y} - \overline{\tilde{u}\tilde{v}}\left(\frac{\partial\bar{u}}{\partial y} + \frac{\partial\bar{v}}{\partial x}\right) - \overline{\tilde{u}\tilde{w}}\frac{\partial\bar{w}}{\partial x} - \overline{\tilde{v}\tilde{w}}\frac{\partial\bar{w}}{\partial y} \tag{5-7}$$

$$\overline{Pe_{m-t,WT}} = -\overline{u_s{}^2}\frac{\partial\bar{u}}{\partial x} - \overline{v_s{}^2}\frac{\partial\bar{v}}{\partial y} - \overline{u_s v_s}\left(\frac{\partial\bar{u}}{\partial y} + \frac{\partial\bar{v}}{\partial x}\right) - \overline{u_s w_s}\frac{\partial\bar{w}}{\partial x} - \overline{v_s w_s}\frac{\partial\bar{w}}{\partial y} \tag{5-8}$$

$$\overline{Pe_{tot,AD}} = -\overline{u'^2}\frac{\partial\bar{u}}{\partial x} - \overline{v'^2}\frac{\partial\bar{v}}{\partial y} - \overline{u'v'}\left(\frac{\partial\bar{u}}{\partial y} + \frac{\partial\bar{v}}{\partial x}\right) - \overline{u'w'}\frac{\partial\bar{w}}{\partial x} - \overline{v'w'}\frac{\partial\bar{w}}{\partial y} \tag{5-9}$$

The zone average of these three terms is calculated in cylindrical coordinates as in Equation (3-17) and shown in Figure 5-5. It must be stressed that in this analysis the turbulence production represents the energy extracted from the mean flow by all kind of flow fluctuations, both periodic and random.

$$IP_{m-p,WT} = \frac{D}{dAU_\infty^3}\int_A \overline{Pe_{m-p,WT}(x,y)}\,y\,dy \qquad IP_{m-t,WT} = \frac{D}{dAU_\infty^3}\int_{in}^{out} \overline{Pe_{m-t,WT}(x,y)}\,y\,dy \qquad IP_{tot,AD} = \frac{D}{dAU_\infty^3}\int_{in}^{out} \overline{Pe_{tot,AD}(x,y)}\,y\,d \tag{5-10}$$

Figure 5-4 shows schematically the energy exchange among mean flow, periodic fluctuations and random turbulence motions (see also Hussain (1981)) in the WT (left image) and AD wake (right image). The term $Pe_{p\text{-}t,WT}$, which represents the decay of the periodic fluctuations into turbulence, is treated in Chapter 3 in the phase-locked case, whereas this analysis focuses on the other two terms $Pe_{m\text{-}p,WT}$ and $Pe_{m\text{-}t,WT}$. In both diagrams, the term D is the dissipation of energy into internal thermal energy of the flow and it is not treated in the present analysis. The diagrams represent the most common scenario for the kinetic-energy cascade in a mixing layer with or without coherent periodic structures, in which the direction of the energy flow is from mean flow to large scale structures to small scale structures.

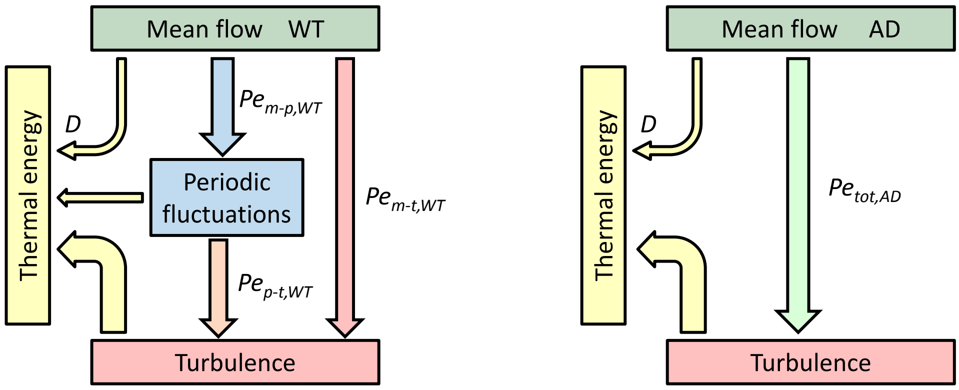

Figure 5-4. Degradation of the mean-flow kinetic energy in the presence of periodic fluctuations in the WT wake (right figure) and without periodic fluctuations in the AD wake (right figure).

Figure 5-5 (top image) visualise the zone averages of the turbulence production in LOC 1. The black curve represents the total production of turbulence in the WT wake $IP_{tot,WT} = IP_{m-t,WT} + IP_{m-p,WT}$, which appears with an average value >0 and several local negative and positive peaks. This term is the summation of the two contribution of $IP_{m-t,WT}$ and $IP_{m-p,WT}$ which have opposite behaviours, similarly to what observed in Figure 5-3 (top image). While the contribution of $IP_{m-t,WT}$ is everywhere positive with an increasing trend, $IP_{m-p,WT}$ has a distinct negative value starting at $x/D = 0.9$, with a decreasing trend. The total turbulence production in the AD wake $IP_{tot,AD}$ is only positive and with fairly high values everywhere. Figure 5-5 (right image) contains the results of LOC 2. Comparing these results with the ones shown in Figure 5-5 (left image), it is possible to appreciate the fluctuations of the quantities $IP_{m-p,WT}$ and $IP_{m-t,WT}$. The former one has positive values for $x/D < 1.7$: this implies a change of sign in the region between LOC 1 and LOC 2, which is not part of the present measurements. A similar behaviour was seen in Figure 5-3. The phenomenon is due to the pairing instability of the tip vortices, which causes a re-orientation of the periodic flow fluctuations (as better explained in Figure 7), affecting the sign of both production of turbulence and flux of mean flow kinetic energy. As far as $IP_{m-t,WT}$ the reason of the oscillation from high positive values in LOC 1 at $x/D > 1.1$ to low positive values in LOC 2 at $x/D < 1.7$ is less clear, but the hypothesis can be made that the magnitude of the random fluctuations is affected by the orientation of the periodic motions, so that during the early stage of the leapfrogging (in the region between LOC 1 and LOC 2) the random fluctuations are also lower. While in Figure 5-3 $IF_{tot,AD}$ had a continuous increasing trend from LOC 1 to LOC 2, $IP_{tot,AD}$ remains constant throughout the whole domain. In this location it is evident how the leapfrogging instability has a major effect on the total production of turbulence $IP_{tot,WT}$, which has a negative value in the region $1.73 < x/D < 2$. The general trend is similar to $IF_{tot,WT}$ in Figure 5-3, but the region characterised by negative values has a much larger extension (almost 3 times as large). The cause of this large area with negative production is the behaviour of the term $IP_{m-t,WT}$, the kinetic energy adsorbed or released by the periodic flow structures, which is negative for most of the extension of LOC 2.

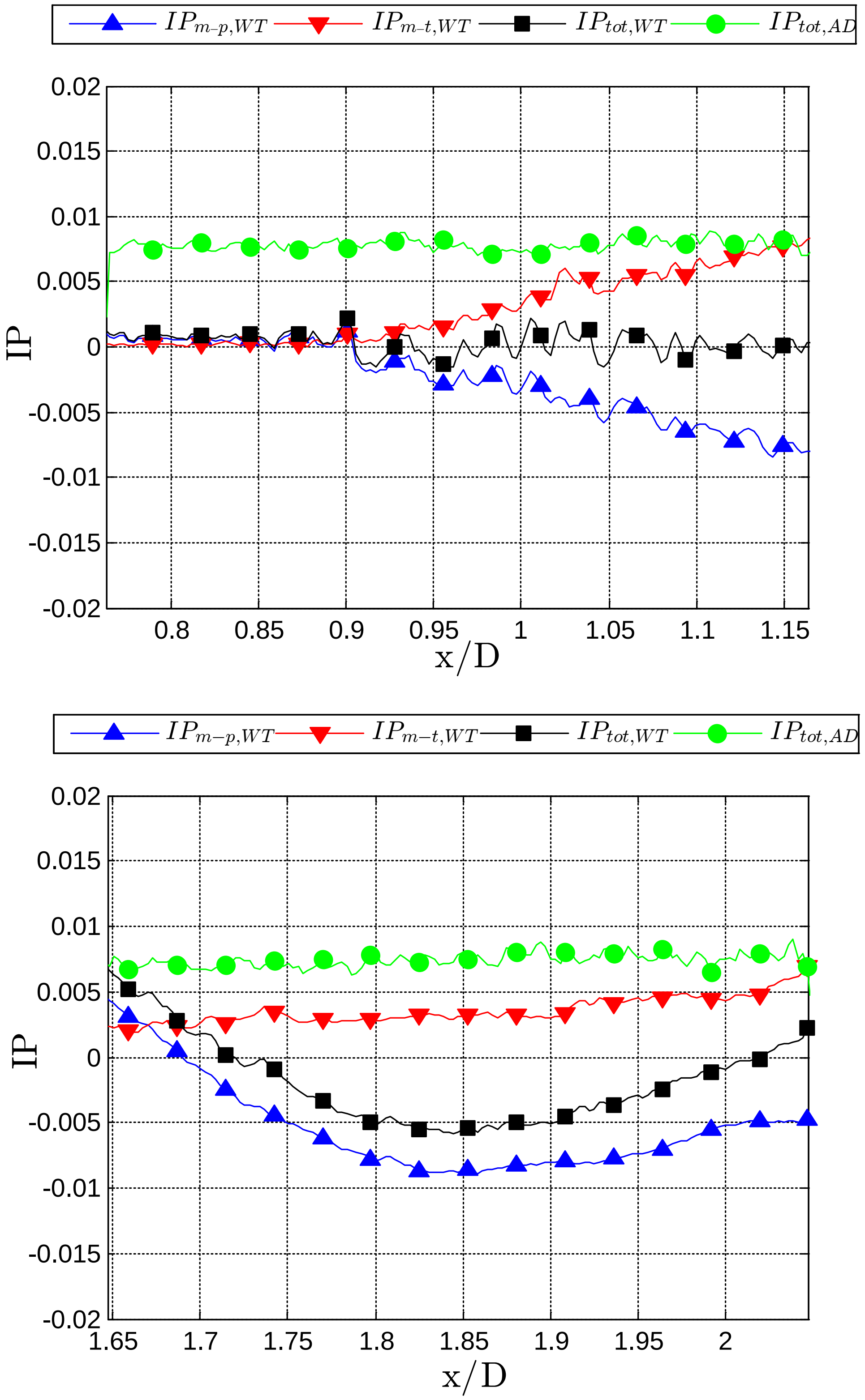

Figure 5-5. Streamwise evolution of the zone averaged turbulence production in the WT and AD wake, in LOC 1 (top figure) and LOC 2 (bottom figure).

As mentioned in section 5.1, Hussain and Zaman (1980), Hussain (1981) and Hussain (1983) made the hypothesis that the regions of negative productions are caused by coherent flow structures, which keep a particular alignment over time in the same location. In the present experiment, the tip-vortex pairing instability is triggered by a constant perturbation and for this reason it occurs at the same position at all instants. This implies that a prevailing direction of the periodic flow fluctuations can be identified in each specific locations. It can be demonstrated that the largest contribution in Equation (3-10) is provided by the term $-\overline{\tilde{u}\tilde{v}}\partial\bar{u}/\partial y$. Since in the shear layer the value of the axial velocity gradient is always positive, the sign of $Pe_{m\text{-}p,WT}$ depends only on the correlation of $\tilde{u}$ and $\tilde{v}$. Figure 5-6 is a schematic impression of a vortex pair during the leapfrogging process within the wake shear layer. The axial velocity gradient is always positive along the radial direction, but the sign of the $\tilde{u}-\tilde{v}$ correlation depends on the inclination of the vortex pair axis. When the inclination is positive, the $\tilde{u}-\tilde{v}$ is also positive and the periodic fluctuations contribute to the acceleration of the external flow and the deceleration of the inner wake flow, with a subsequent decrease of their kinetic energy. This explains the negative value of production.

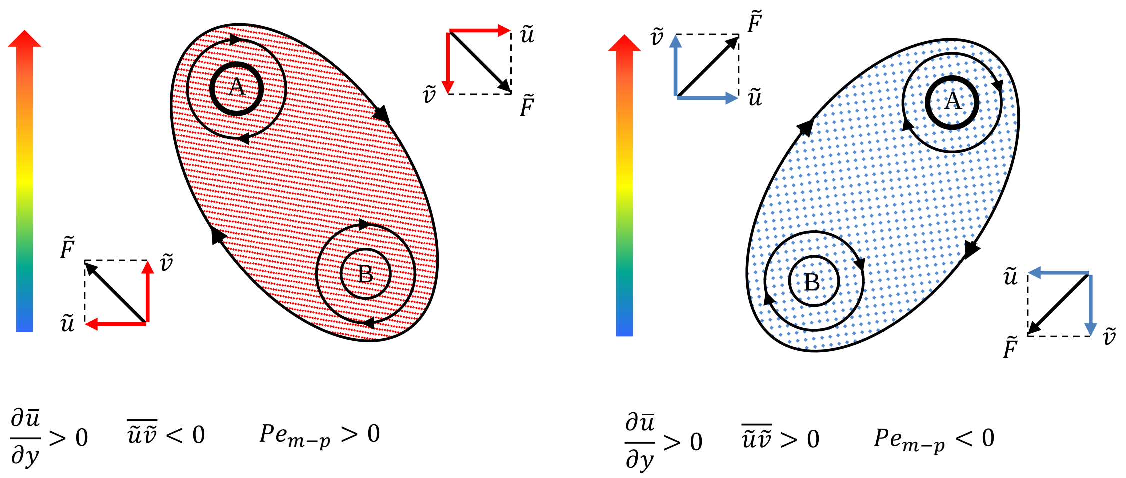

Figure 5-6. Change of orientation of the vortex pairs. On the left, the initial stage of leapfrogging (vortex A leaps over vortex B) causes a negative inclnation of the vortex pair. The red and blue areas indicate positive and negative production respectively. The bolde lines depicts schematically the streamlines and the black arrows indicate the direction of the flow fluctuation $\tilde{F}$. The coloured arrows indicate the direction of the components $\tilde{u}$ and $\tilde{v}$ (red indicates anti-correlation and blue indicates correlation). The gradient arrows on the left of each figure shows the direction of the mean velocity gradient.

5.4.3 Effect On Mean Velocity Field

Figure 5-7 shows the velocity gradient in the streamwise direction of the time averaged velocity magnitude (Eq. (5-11)) at two different radial locations, one in the inner wake flow and the other one in the outer flow, just outside the shear layer in the WT and AD wake at LOC 2, where most of the negative production and negative flux occurs. In standard mixing layers without the presence of instable vortex structures (e.g. as in the

AD wake case) the time average velocity magnitude is expected to decrease steadily in the outer region (high-speed flow) and increase in the inner region (lo-speed flow).

$$G = \frac{\partial |\overline{u}|}{\partial x} \cdot \frac{D}{U_\infty} \tag{5-11}$$

The analysis of the time-average flow reveals the macroscopic effect of the mean-flow kinetic-energy transport and corroborates the findings illustrated in 5.4.1 and 0. In the AD wake, the streamwise gradient is everywhere negative in the outer flow and it is everywhere positive in the inner flow, as expected in a classical mixing layer where the turbulence mixing contributes to the momentum exchange from the high-kinetic-energy flow to the low-kinetic-energy flow, with consecutive deceleration of the former and acceleration of the latter one. In fact, as shown in Figure 5-3 and Figure 5-5, in this region of the AD wake both the mean-flow kinetic-energy flux and turbulence production are positive. A completely opposite scenario occurs in the WT wake flow, where the streamwise gradient of velocity is mainly positive in the outer flow and negative in the inner flow. This demonstrate that in the region affected by the leapfrogging instability, the kinetic energy exchange is in the opposite direction as respect to the natural turbulence mixing, with part of the high-kinetic-energy flow accelerating to the expense of the low-kinetic-energy flow. This is due to the action of the pairing vortices as explained in 5.4.2.

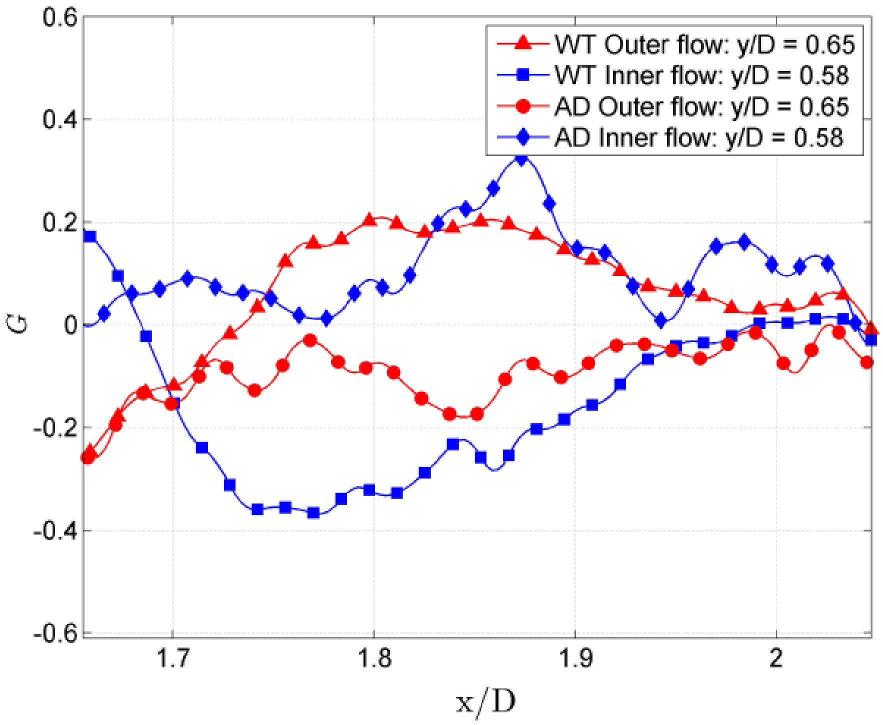

Figure 5-7. Velocity gradient in the streamwise direction of the time averaged velocity magnitude at two different radial locations in LOC 2 WT and LOC 2 AD.

5.5 CONCLUSIONS

An analysis of the turbulent mixing at two streamwise locations in the wake of the near wake of a wind turbine model and of an actuator disc has been performed. Two terms of the mean-flow kinetic-energy equation have been quantified by distinguishing the effect of the periodic and random flow fluctuations through a POD-based triple decomposition of the flow in the WT wake. The analysis of the mean-flow kinetic-energy transport have confirmed the findings of Chapter 3, namely that major contribution to the momentum entrainment in the WT wake is provided by the random flow fluctuations, while the periodic fluctuations have a null or negative contribution (apart from small localised regions). In the AD wake the transport is only positive and of a larger magnitude compared to the one in the WT wake, meaning that the entrainment is general higher. The analysis of the turbulence production have shown a distinct region characterised by large negative values in correspondence of the tip-vortex instability. This phenomenon does not violate any basic principle, but constitutes a clear example of the failure of the gradient transport model in the time-mean field, which normally does not account for the possibility of reverse energy transfer from coherent structures to the mean flow. In Chapter 3, it was explained that the turbulence mixing is influenced both by the magnitude and the direction of the flow fluctuations. In particular, the mean-flow kinetic-energy flux due to random fluctuation can be positive or negative depending on the sign of the u_s-v_s correlation, whereas the production of turbulence is always positive. In the present analysis the previous findings are confirmed and it is shown that the energy exchange between mean flow and periodic fluctuations is also affected by the orientation of the flow fluctuations (namely the $\tilde{u} - \tilde{v}$ correlation) and that it can assume positive or negative value. In this investigation it has been found that the random turbulent fluctuations are generated by velocity gradient and as such their production term can be very well described by the eddy viscosity model, leading to positive values everywhere, independently from the average direction of the fluctuations. Coherent and periodic structures in the shear layer may be generated through a different mechanism (e.g. the force applied by the wind to a rotating blade), which is not related to the direction of the velocity gradient, therefore behaving as sinks or sources of mean-flow kinetic-energy depending on their average direction. The analysis has shown that the negative production has macroscopic effects on the time-average velocity: this corroborates the importance of the present findings for numerical simulations such as Reynolds Average Navier-Stokes simulations combined with the actuator disc model, which only accounts for the time average velocity field in the wake.

6 VALIDATION OF FOUR LES AND A VORTEX MODEL AGAINST STEREO-PIV MEASUREMENTS IN THE NEAR WAKE OF AN ACTUATOR DISC AND A WIND TURBINE

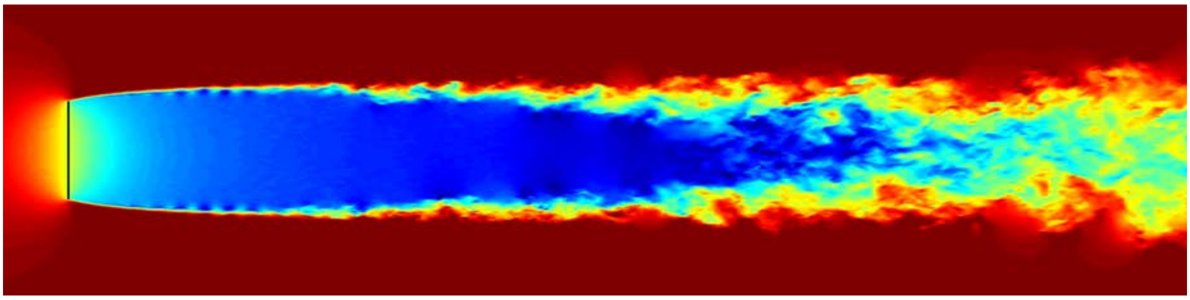

This chapter reports the results of a workshop, in which different state-of-the-art numerical models for the simulation of wind turbine wakes are compared against the experimental data. Researchers have been invited to simulate the experimental case based on the disc drag coefficient and the inflow characteristics. Four large eddy simulation (LES) codes from different institutions and a vortex model are part of the comparison. The purpose of this benchmark is to validate the numerical predictions of flow field in the near wake of an actuator disc, a case that is highly relevant for full wind farm applications. The comparison has shown that, despite its extreme simplicity, the vortex model is capable of reproducing the wake expansion and the centreline velocity with very high accuracy. Also all tested LES models are able to predict the velocity deficit in the very near wake well, contrary to what was expected from previous literature. However, the resolved velocity fluctuations in the LES are below the experimentally measured values.

Cover figure: visualization of a LES of the flow through an actuator disk by Richard Stevens.

This chapter is submitted as:

Lignarolo, L.E.M., Mehta, D., Stevens, R.J.A.M., Yilmaz, A.E., van Kuik, G., Andersen, S.J., Meneveau, C., Simão Ferreira, C.J., Ragni, D., Meyers, J., van Bussel, G.J.W., Holierhoek, J., 2015. Validation of four LES and a vortex model against stereo PIV measurements in the near wake of an actuator disc and a wind turbine. *Renewable Energy* (in review).

6.1 INTRODUCTION

In the last two decades, many new numerical models have been developed with varying degrees of complexity for the simulation of the flow within a wind farm (Pierella et al, 2014). The ultimate challenge in computer modelling of wind farm aerodynamics is to combine an accurate representation of the flow physics and an affordable computational cost, necessary for the implementation of the models in industrial environments. Most of the algorithms used today continue to rely on strong assumptions and parameters, which still need to be calibrated against experimental data or fine-tuned according to the case (Ainslie, 1988, Crespo et al, 1988, Jensen, 1983, Schepers, 2012). One of the main factors influencing the performance and computational effort in a numerical model is the method used for modelling the rotor. Different methods are available, from the most accurate to the very simplified ones, the two extremes are:

- fully-resolved blade geometry with its own boundary layer,
- modelling the rotor as a distributed force field.

The second approach is the actuator disc method (Sørensen et al, 1998), where the turbine is represented as a disc with a constant or variable thrust (and torque) distribution. As far as the flow field simulation is concerned, usually the Navier-Stokes equations are solved using a large eddy simulation (LES) or a steady or unsteady Reynolds average Navier-Stokes (RANS and U-RANS) approach. While simple analytical models are still the standard for industrial applications (Pierella et al, 2014, Schepers, 2012), LES has been receiving more attention in the wind energy community because of its ability to reproduce unsteady and anisotropic turbulent flows characterised by large-scale structures and turbulent mixing, even though its computational cost is considerably higher (Sanderse et al, 2011). Comparisons with wind-tunnel experiments are of great help for validating and implementing more advanced computational models, proving their reliability also for industry. Previous benchmarking workshops have shown that numerically reproducing the behaviour of a single or two wind turbines wakes in uniform flow, despite being the most basic of the test cases, is a complicated task (see the Blind Test 1 workshop in Krogstad and Eriksen (2011), Krogstad and Eriksen (2013) and in the Blind Test 2 workshop in Pierella et al (2014)).

In this chapter, the results of a benchmark test, are reported. The purpose of this benchmark is to evaluate the accuracy and reliability of state-of-the-art numerical models in the near wake of a single actuator disc, a case that is highly relevant for modelling the flow behind wind turbines. In fact, it is known from literature that the actuator disc approach often fails in reproducing the effects of flow turbulence, due to the absence of the blade tip-vortex development and breakdown. In this regard, Schepers (2012) writes about the importance of investigating how to reduce the inaccuracy of the actuator disc (AD) model in the wake region within 5 diameters from the rotor, and he states that including rotational effects can visibly improve the model performances. The experiments in Chapter 4, however, have demonstrated that the actuator disc representation should in principle, be able to reproduce with acceptable accuracy the turbulent flow in the near wake. Comparison between LES and wind tunnel experiments by Wu and Porté-Agel (2013) revealed that the flow profiles behind turbines in a very large wind farm are reasonably well predicted when an actuator disc method is used, especially for turbines from the second row on.

With the increased demands on utilization of available wind-farm space, the limitation to large downstream distances is no longer acceptable for many current engineering applications. For example, in the Lillgrund offshore wind farm turbines are consecutively displaced at approximately 3.3 - 4.3 diameters (Gaumond et al, 2012), and in the Horns Rev offshore wind the spacing is instead within 7 diameters (Barthelmie et al, 2007b). The inability to correctly reproduce the flow in the near wake of the machine in the first-row has already been identified as one of the factors that influences the accuracy of power deficit predictions for the following rows, as the incoming flow develops from an atmospheric boundary layer to a wind farm *canopy* boundary layer (Sanz Rodrigo and Moriarty, 2014). Currently, a high-resolution validation of the performance of CFD codes in the prediction of the turbulent flow in the near wake an actuator disc is not available, in part due to a lack of high-quality experimental data for such a flow. The analysis in this chapter is based on the experimental data documented in Chapter 4. The present benchmark comparison focuses on a series of LES models, which are often considered, despite recent blind test (Pierella et al, 2014) results, to be the most accurate numerical models. The benchmark also includes comparisons with a vortex model, which unlike LES, offers a simpler inviscid, representation of the flow. Researchers with a suitable LES code were invited to simulate the experimental case using as input the known disc drag coefficient, the inflow characteristics, as well as the boundary conditions of the wind tunnel test. Much of the challenge for the participants was to choose the best LES turbulence sub-grid model, setting up the optimum numerical grid, and choosing the best model parameters in order to optimize their results. The high quality and reproducible experimental data were subsequently used to evaluate the performance of the different calculations.

6.2 METHOD

The experiments described in Chapter 4 have been used as test case for benchmarking a series of LES models and a vortex model. Five institutions participated in the workshop including: Technical University of Denmark, Johns Hopkins University, Energy research Centre of the Netherlands and Catholic University of Leuven for the four LES in-house built algorithms. Delft University of Technology participated with an in-house vortex model. The benchmark focusses on the following aspects:

- comparison of the time-average axial velocity field and of the wake expansion;
- comparison of the turbulence intensity;
- grid convergence study.

The wake expansion is theoretically calculated as the width of the stream-tube encompassing the edge of the disc. Due to limitations in the data acquisition system, it was not possible to calculate the stream-tube coordinates in the flow field measured with stereo PIV. For this reason the wake-width is defined as the locus of the points where the flow reaches 99% of the inflow velocity. The turbulence intensity *TI* is calculated as in Equation (2-7). The quantities to be compared are sampled in profiles along the *y*-direction (radial) at five different downstream locations. Each location is chosen on the basis of particular flow features of the WT wake. The first location is at $x/D = 0.1$ right after the model, the second location at $x/D = 0.7$ is in the near wake in a regions where tip-vortices (in the rotating wind turbine case) are stable, the third location at $x/D = 1.1$ is right before the leapfrogging, the fourth location at $x/D = 1.8$ is during the leapfrogging process and the last location at $x/D = 2.2$ can be considered to be in the intermediate wake. The input information to be used by the participants for their simulation was:

- inflow velocity;
- inflow turbulence intensity;
- diameter of the disc;
- drag coefficient of the disc (constantly loaded).

For both the time-average axial velocity and the turbulence intensity, the discrepancy δ between the numerical and experimental results is presented and calculated as in Equation (6-1)

$$\delta_{\overline{u}} = \frac{abs\left(\overline{u}_{i,LES} - \overline{u}_{i,AD}\right)}{\overline{u}_{i,AD}} \qquad \delta_{TI} = \frac{abs\left(\overline{TI}_{LES} - \overline{TI}_{AD}\right)}{\overline{TI}_{AD}} \tag{6-1}$$

It must be acknowledged that in fact, the experiments and numerical simulations represent two different situations: in the experiments, the porous disc introduces small-scale turbulence which quickly dissipates into heat, whereas in the simulation a body force is introduced in the flow, representing the thrust force applied by the rotor to the wind. The small-scale turbulence present in the experiments is not modelled by the numerical simulations, which approach a steady solution irrespective of whether one introduces synthetic turbulence upstream or not.

6.3 NUMERICAL MODELS

6.3.1 VORTEX MODEL (TUD)

The vortex code, developed at TUDelft (van Kuik and Lignarolo, 2015), considers the flow as incompressible and inviscid. The code solves the Euler equation for steady flow and the continuity equation. The AD is modelled as an infinitely thin disc placed normal to the uniform flow U_∞. It carries a uniform pressure jump Δp. The disc generates a cylindrical vortex sheet emanating from the disc edge. This sheet stretches from the disc to downwind infinity, and separates the flow that has passed the disc from the flow outside this stream-tube. The wake vortex sheet is divided in two parts:

- from the disc position x = 0 up to x = $30R_{wake}$ the sheet is discretized using 4650 vortex rings with strength $\Gamma_i(x_i; r_i)$, like in the model of Øye (1990)
- the far wake, starting at x = 30 R_{wake}, is a semi-infinite cylindrical vortex tube with constant strength and radius R_{wake}. An analytical solution has been derived for the axial velocity induced by this semi-infinite tube.

All flow and force properties are axisymmetric. The boundary conditions at the vortex sheet are:

- the sheet is force free;
- the normal velocity v is null.

The code solved for the vortex sheet strength and position with an accuracy of meeting the boundary conditions of 0.5% close to the disc edge, and <0.2% further downstream. In this chapter, the vortex model will be referred to as TUD.

Table 6-1. Computational parameters for the TUD case.

Case	***Number of vortex rings***	**Specials**
A	4650	-

6.3.2 JHU-LES (JHU)

The LES code developed at Johns Hopkins University (JHU) solves the filtered incompressible Navier-Stokes equations without buoyancy, system rotation or other effects. The nonlinear terms are evaluated in rotational form. A pseudo-spectral discretization and thus double periodic boundary conditions are used in the horizontal directions, while a centred second-order finite differencing scheme is used in the vertical direction (Albertson and Parlange, 1999, Moeng, 1984, Porte-Agel et al, 2000). The deviatoric part of the sub-grid scale stress term is modelled using an eddy-viscosity sub-grid scale (SGS) model, employing the scale dependent Lagrangian dynamic approach in conjunction with the Smagorinsky model and a sharp spectral cut-off test-filter (Bou-Zeid et al, 2005) in the pseudo spectral directions. The trace of the SGS stress is combined into the modified pressure, as is common practice in LES of incompressible flow. A second-order accurate Adams-Bashforth scheme is used for the time integration. A conservative time step assuming a CFL number of 0.0625 is used in all simulations in order to assure accurate time integration.

The computational domain in the streamwise, spanwise, and vertical direction is $L_x \times L_y \times L_z = 24 \times 6 \times 6$, where the length is non-dimensional with the disc diameter. The centre of the actuator disc is placed at $(x,y,z) =$ 3D, 3D, 3D, i.e. in the middle of the domain and 3D from the entrance region where the inflow condition is applied. Simulations are performed on different grids (see details in Table 6-2), up to a resolution of $1024 \times 256 \times 1024$ computational nodes in the streamwise, spanwise, and vertical direction. In most cases the inflow is a complete uniform streamwise inflow velocity. As a spectral method is used in the horizontal (streamwise-spanwise) plane, a fringe method is used to impose the inflow profile (Stevens et al, 2014b). The same approach is used in the context of the concurrent-precursor method to impose incoming turbulence, but here a constant inflow velocity is imposed. The long streamwise domain length is used to allow the wake to fully develop and to assure a smooth transition from the wake solution towards the uniform inflow in the fringe region (Stevens et al, 2014b). In the spanwise (spectral) direction periodic boundary conditions are used, while in the vertical (finite difference) direction stress free boundary conditions are applied at the bottom and the top of the domain. An area averaged AD model (Calaf et al, 2010a, Stevens et al, 2014b) is used to compute the disc forces and a Gaussian convolution filter is used to blend out the corresponding forces to prevent oscillations in the flow solution. It was found that the best results were obtained when the resolution in the finite difference direction is approximately 4 times finer than the spectral discretization to assure an equal accuracy of both methods for the mean quantities. This ratio is similar to the 3:1 ratio normally used in other wind-farm simulations at JHU (Stevens et al, 2014a). The presented LES data are averaged in the spanwise (spectral) and vertical (finite difference) direction. In this chapter, the model will be referred to as JHU. In case E the inflow is modulated with and added sinusoidal variation in time with a low frequency of 1.31 Hz to the spanwise velocity component with a magnitude of 2% of the incoming streamwise velocity as this is the easiest way to adjust the inflow condition in this simulation framework. This results in a turbulence intensity of approximately 0.5% in the streamwise velocity component just upstream of the turbine. This only mimics some effect of the turbulence intensity and using for example a Mann spectrum (Mann, 1998) to generate a turbulent inflow condition with given turbulence intensity would be more realistic.

Table 6-2. Computational grid parameters for different cases (JHU)

Case	$L_x \times L_y \times L_z$	$N_x \times N_y \times N_z$	$\Delta = (\Delta x \Delta y \Delta z)^{1/3} / D$	**Specials**
A	24D × 6D × 6D	384 × 96 × 192	0.0496	-
B	24D × 6D × 6D	512 × 128 × 256	0.0372	-
C	24D × 6D × 6D	768 × 192 × 384	0.0248	-
D	24D × 6D × 6D	512 × 128 × 512	0.0295	-
E	24D × 6D × 6D	512 × 128 × 512	0.0295	~0.5%
F	24D × 6D × 6D	768 × 192 × 768	0.0197	-
G	24D × 6D × 6D	1024 × 256 × 1024	0.0148	-
Z	24D × 6D × 6D	192 × 48 × 96	0.0992	-

6.3.3 ECNS (ECN)

The Energy-Conserving Navier-Stokes code (ECNS) uses a Finite Volume approach on a uniform Cartesian grid based on the energy-conserving spatial discretisation and temporal integration proposed by Sanderse (2013). These schemes guarantee the absence of numerical diffusion and ensure stability with all grid sizes and time steps. More in detail, it ensures that while simulating an incompressible flow under the influence of periodic or non-penetrative boundaries, the flow kinetic energy will only reduce through the action of molecular viscosity or in the limit of an inviscid fluid, will remain unchanged. Numerical diffusion on the other hand, would spuriously reduce the energy of the flow. For this simulation, a 2nd order accurate spatial discretisation and a 4th order accurate explicit Runge-Kutta method for time integration have been used. The latter is not energy conserving but conveys negligible numerical diffusion at very small time-steps. The actuator disc is modelled using volume forces introduced using an immersed interface method (Sanderse, 2013).

The computational domain is 14D in axial direction, where D is diameter of the actuator disc. Based on the amount of cells required on the actuator disc, three domains are defined with different widths in the direction along the disc span (y and z). Three grids with different resolutions are obtained by changing the width and the height of the domain, keeping the total number of cells unchanged. In all cases, the length of the domain is kept the unchanged (see Table 6-3). The Smagorinsky sub-grid model is used with $C_S = 0.17$ to model the effect of the sub-grid scales. The time step for all simulations is set conservatively at 0.001s. The disc is placed at 2.8D from the inflow boundary. An advantage that a Finite Volume method offers against the more advanced pseudo-spectral methods for LES is the easier use of non-periodic boundary conditions. Thus, a smaller domain can be adopted with outflow boundaries everywhere, instead of larger domains with a periodic boundaries. Furthermore, the outflow boundaries in the ECNS have been verified to not affect the upstream solution (Sanderse, 2013), which allows to simply reduce the domain size to increase the resolution on the disc, while maintaining the same number of grid points.

Two sets of simulation have been performed, with both laminar and turbulent inflow. The latter is generated with the spectrum obtained by Kang et al (2003) for an isotropic homogeneous flow. With this spectrum and Rogallo's algorithm (Rogallo, 1981), a velocity field is synthesised and manipulated in spectral space to get the correct turbulence intensity and turbulence kinetic energy. The final turbulence field is generated and sampled in a precursor simulation in a long empty domain (14D long). In this chapter, the model will be referred to as ECN.

Table 6-3. Computational grid parameters for different cases (ECN)

Case	$L_x \times L_y \times L_z$	$N_x \times N_y \times N_z$	$\Delta = (\Delta x \Delta y \Delta z)^{1/3} / D$	Specials
A	14D × 10D × 10D	98 × 70 × 70	0.1470	-
B	14D × 5D × 5D	98 × 70 × 70	0.0926	-
C	14D × 3D × 3D	98 × 70 × 70	0.0659	-
D	14D × 10D × 10D	98 × 70 × 70	0.1470	0.5%
E	14D × 5D × 5D	98 × 70 × 70	0.0926	0.5%
F	14D × 3D × 3D	98 × 70 × 70	0.0659	0.5%

6.3.4 ELLIPSYS3D (DTU)

The simulations have been performed using EllipSys3D, which is a three-dimensional flow solver developed in collaboration between Technical University of Denmark (DTU) (Michelsen, 1992) and the former Risø (Sørensen, 1995). EllipSys3D solves the discretized and incompressible Navier-Stokes equations in general curvilinear coordinates, where a block-structured finite volume approach is used. Pressure correction is performed using the PISO algorithm, and pressure decoupling is avoided by utilizing the Rhie-Chow interpolation technique. The convective terms are discretized using a combination of the third order QUICK and the fourth order CDS scheme, which limits any numerical and unphysical wiggles from the fourth order scheme and numerical diffusion from the third order scheme.

Large Eddy Simulations are employed to provide the turbulent closure, and the implemented LES model is based on Ta Phuoc et al (1994) which applies a low-pass filter on the Navier-Stokes equations.

The AD is modelled by imposing body forces (Mikkelsen, 2003), which are applied constantly in both time and space. The body forces are numerically smeared using a Gaussian convolution. Synthetic turbulence has been generated as a so-called Mann turbulence box (Mann, 1994, 1998) and imposed upstream the actuator disc for one of the simulations.

Simulation Setup: Two comparable simulations have been performed with uniform inflow. The only difference between the two simulations is whether the Mann turbulence was imposed or not. The mesh consists of 256 blocks and a total of 28 million grid points. The domain is 4.43D x 4.43D x 22D in the spanwise (*y*), vertical (*z*), and streamwise (*x*) direction, respectively. The spanwise and vertical dimensions corresponds to the full cross-section of the TUDelft wind tunnel. The rotor resolution is 68 cells per diameter, and the grid is stretched towards the boundaries. Symmetry boundary conditions have been applied on the transverse and vertical boundaries. In this chapter, the model will be referred to as DTU.

Table 6-4. Computational grid parameters for different cases (DTU)

Case	$L_x \times L_y \times L_z$	$N_x \times N_y \times N_z$	$\Delta = (\Delta x \Delta y \Delta z)^{1/3} / D$	Turbulence
A	22D × 4.43D × 4.43D	384 × 192 ×192	0.0147	-
B	22D × 4.43D × 4.43D	384 × 192 ×192	0.0147	0.5%

6.3.5 SP-WIND (KULEUVEN)

The numerical simulations are performed with an in-house pseudo-spectral Navier-Stokes solver, SP-Wind. In the current study, the LES framework is used with the standard Smagorinsky sub-grid scale model. In the horizontal directions, the governing equations are discretized with a pseudo-spectral method, while in the third direction a fourth-order energy-conservative finite-difference scheme is used. The time integration is performed with a fourth-order four-stage Runge-Kutta integration method. Further, the finite domain simulations are achieved by the employment of a fringe region in the axial direction.

The AD is modelled by adding body force terms to the momentum equations. Details of the LES framework can be found in (Calaf et al, 2010a). The model constant C_S , is set to 0.14 based on a detailed tuning study carried out by Meyers (2011).

The AD is placed in the middle of the domain on the y-z plane having its centre five rotor diameters away from each of the side boundaries. In the *x*-direction the total domain length is kept 25D and the rotor is placed 6D downstream of the inflow boundary. This setup produces results that are free from the boundary and fringe region effects. In the spectral directions, the boundary conditions are periodic while the symmetry boundary condition is applied to the bottom and the top boundaries. In this chapter, the model will be referred to as LEU.

To be compared with the experimental data, three different grid resolutions with two different inflow conditions are simulated. The reference Coarse grid resolution is typical in the big wind farm simulations. The Medium and the Fine grids are respectively two and four times finer in all three directions compared to the coarse grid. Regarding the inflow conditions, uniform and turbulent cases are simulated. For the latter, an external synthetic turbulence (Mann, 1998) generator, Tugen (Gilling, 2009), is used to produce a turbulent flow field with an integral length scale of turbine diameter and a turbulent intensity of 0.5%.

Table 6-5. Computational grid parameters for different cases (LEU)

Case	$L_x \times L_y \times L_z$	$N_x \times N_y \times N_z$	$\Delta = (\Delta x \Delta y \Delta z)^{1/3} / D$	Turbulence
A	25D × 10D × 10D	72 × 64 × 128	0.1618	-
B	25D × 10D × 10D	144 × 128 × 256	0.0809	-
C	25D × 10D × 10D	288 × 256 × 512	0.0405	-
D	25D × 10D × 10D	72 × 64 × 128	0.1618	0.5%
E	25D × 10D × 10D	144 × 128 × 256	0.0809	0.5%
F	25D × 10D × 10D	288 × 256 × 512	0.0405	0.5%

6.3.6 Comparison Of The LES Codes

Table 6-6 summarises the main information about the sub-grid-scale (SGS) model and the spatial discretisation of each LES code.

Table 6-6. Summary of the mean LES parameters

Code	SGS Model	Spatial Discretisation	CFL number
JHU	Scale Dependent Dynamic model	Horizontal: Pseudo-Spectral Vertical: 2nd order Finite Difference	0.0625
ECN	Smagorinsky model	2nd order Energy Conserving Finite Volume Staggered	0.2
DTU	Mixed Subgrid Scale model	Convective term: Blended 3rd order QUICK and 4th order CDS Other terms: 2nd order CDS	
LEU	Smagorinsky model	Horizontal: Pseudo-Spectral Vertical: 4th order Energy-Conserving Finite Difference	0.4

6.4 Benchmark Of Results

In this section, the results of the comparison are shown. Two series of comparison have been performed: comparison 1 collects the results of the simulations with laminar inflow and comparison 2 the ones of the simulations with turbulent inflow. Table 6-7 contains the names of the different cases, which have been used for each comparison. The compared quantities are sampled in profiles along the *y*-direction (radial) at five different downstream locations. Each location is chosen on the basis of particular flow features of the WT wake, as explained in Section 6.2. The results of the LES cases are compared with the results of the vortex model and the experimental data of the WT and AD wake. Along with each profile, the relative discrepancy between the AD results and the numerical results is provided.

Table 6-7. Cases which are included in the benchmark. The terms in brackets is the grid resolution (Δ) relative to the case expressed in diameters.

Comparison	**Case**				
	DTU	*JHU*	*ECN*	*LEU*	*TUD*
Laminar inflow	A(*0.0147D*)	D(*0.0295D*)	C(*0.0659D*)	C(*0.0405D*)	A
Turbulent inflow	B(*0.0147D*)	E(*0.0295D*)	F(*0.0659D*)	F(*0.0405D*)	A

6.4.1 MEAN VELOCITY FIELD

LAMINAR INFLOW CASE

Figure 6-1 (top) shows the comparison of the time-average axial velocity profiles at five different wake locations along the streamwise direction obtained from the LES simulations and compared to the results of the vortex model and the SPIV measurements. All LES capture the velocity profile in the near wake relatively well. The relative discrepancy, calculated as in Equation (6-1), is plotted in Figure 6-1(bottom). At x/D=0.1 near the centreline at small y/D the experimental data show vanishing velocity due to the wake immediately behind the centre of the model where there is additional blockage. Since none of the models include this additional blockage, neither the reduced centreline velocity nor its downstream development is captured by any of the models. DTU always shows the largest discrepancy in the centreline velocity prediction, with differences larger than 10^{-1} from 1.1D. JHU, ECN and LEU have the best prediction of the centreline velocity discrepancy between 10^{-2} and 10^{-1} up to 1.8D. TUD is characterised by a very good prediction of the centreline velocity both in the near and intermediate wake. In the near wake the VOR is comparable to the other LES models, while it performs better than ECN and LEU in the intermediate wake at x/D > 2. For x/D > 1.1, the discrepancy is consistently lower than that incurred by DTU. The region at 0.2<y/D<0.3 is affected by some inhomogeneity in the flow, caused by the disc mesh: this causes larger localised errors in all the models, which are ascribed to the error in the experiments themselves. In the shear layer regions, the discrepancy decreases slightly for DTU but for JHU increases from 10^{-2} to $5 \cdot 10^{-1}$. ECN decreases slightly, always of the order of 10^{-1}. The discrepancy in LEU stays quite constant and in the last location behaves as JHU. As expected, the largest values are shown by the TUD results: as a matter of fact, in the shear layer region viscosity and, in particular, turbulence play a very important role, while the code is not modelling these aspects and predicts a very sharp velocity gradient.

Figure 6-2 compares the wake width as function of the downstream position for the different LES cases with the vortex model results and the PIV measurements. The most evident features are the large under-prediction of the wake expansion by the DTU model, despite it is the only one able to reproduce correctly the initial expansion at x/D = 0, and the large over-prediction by the ECN model, both by around 7% of the actual AD wake expansion. The JHU and LEU models give the best prediction, among the LES models, although they do not reproduce correctly the initial expansion. In fact, the show respectively a 10% and 14% over-prediction at x/D < 0.1. Further downstream, the minor differences are related to the more advanced LES model used by JHU, which is more accurate at locally varying the Smagorinsky coefficient in the shear layer. It is interesting to notice the striking good prediction by the TUD vortex model: despite its inability to correctly model the shape of the wake shear layer, it predicts the wake expansion in the near wake with a very large accuracy.

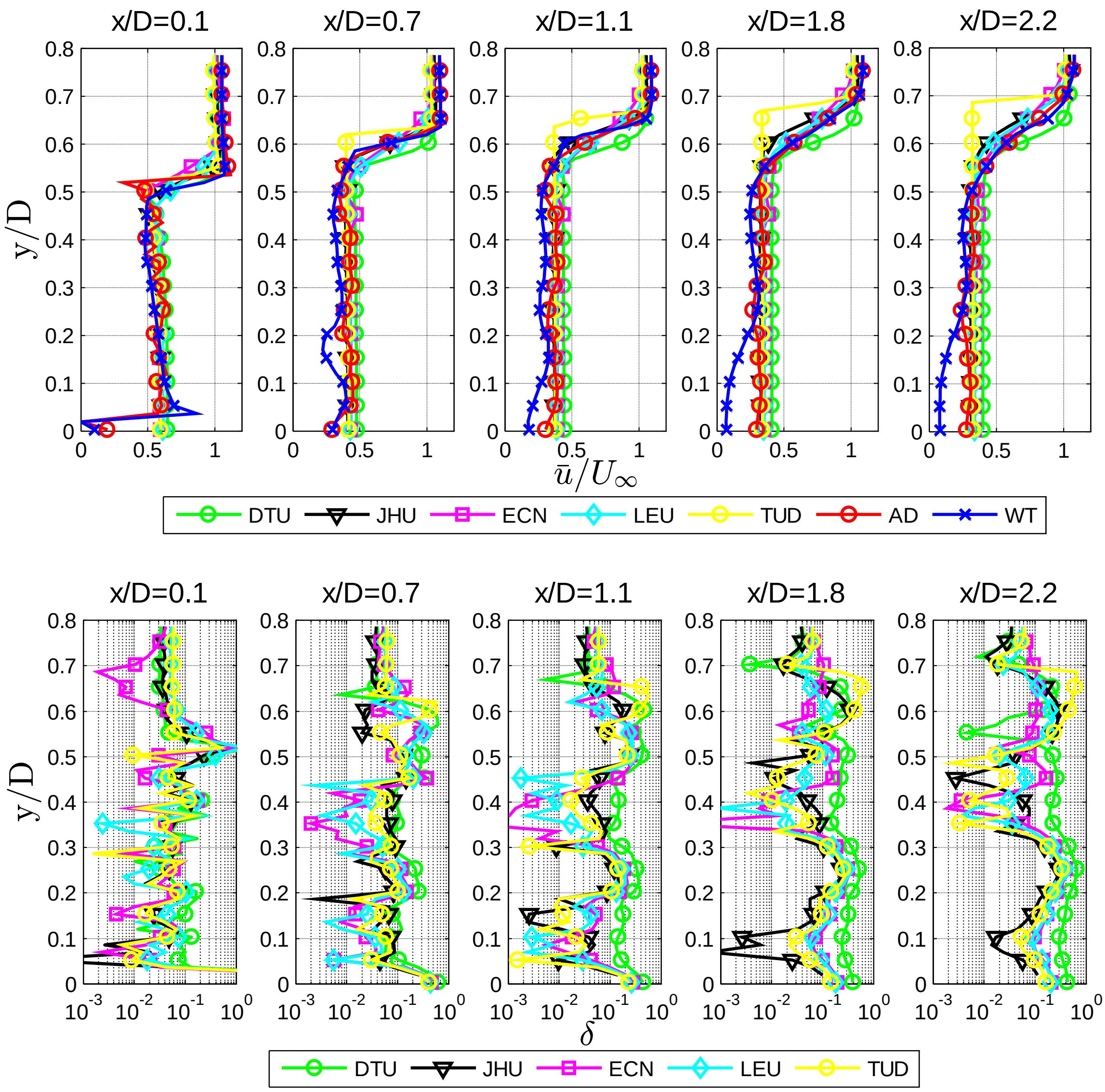

Figure 6-1. Laminar-inflow case. Time averaged axial velocity profiles from the four LES models, the vortex model and the experiments with the WT and AD (top image). Relative discrepancy of the numerical results compared to the AD experimental data (bottom image).

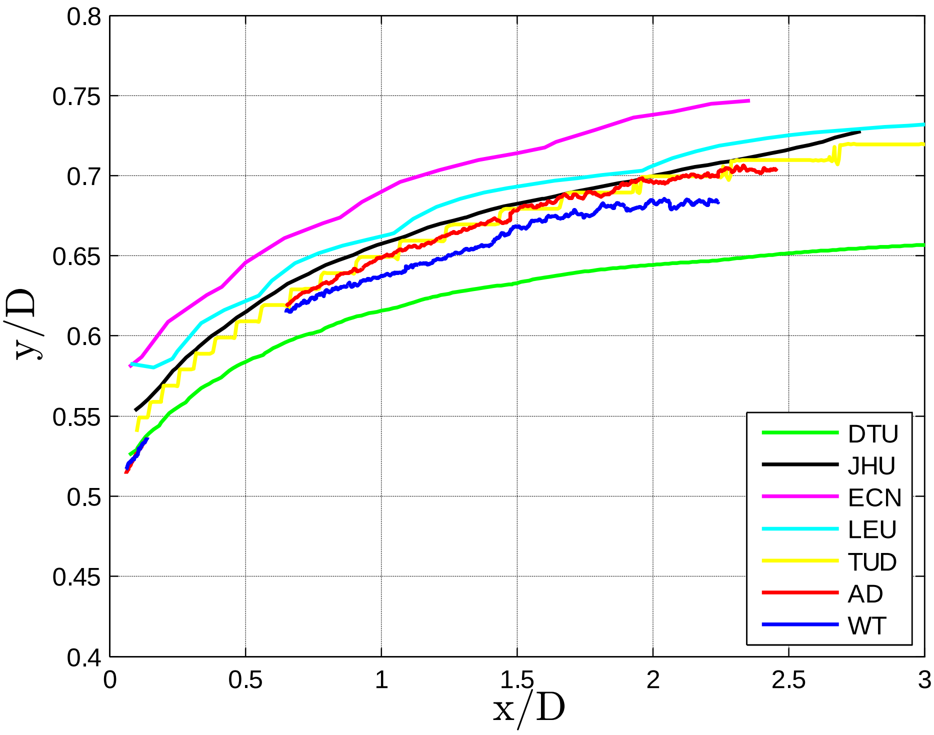

Figure 6-2. Laminar-inflow case. Wake expansion from the four LES models, the vortex model and the experiments with the WT and AD.

TURBULENT INFLOW CASE

In the second set of simulations, the flow is perturbed with a low-intensity (0.5%) turbulent inflow condition to give a faster laminar-to-turbulent transition in the wake of the turbine. This approach results in amplified turbulent intensities in all three directions. By looking at both the actual values and the relative discrepancy in Figure 6-3, two regions can be identified, which are characterised by similar behaviours for nearly all numerical models: in the centreline region the prediction of the axial velocity worsens similarly for all models when moving downstream, whereas in the shear layer region the discrepancy decrease. In the inner region the discrepancy increases while moving downstream in all simulations. In the DTU simulation, the discrepancy increases quickly from the third location becoming 4 times larger in the intermediate wake than in the near wake region. For the JHU case, the discrepancy increases less rapidly, mainly in the intermediate wake from the 4th location. Not much difference with the laminar case is noted. The ECN model follows roughly the same behaviour of JHU, with worse performances in the centreline. The discrepancy in the LEU simulation increases slower than in the ECN's one, but more quickly than in the other cases: the values further downstream is equal to ECN's one and almost two times lower than in the DTU case.

In the shear layer region, the performances of the ECN and LEU models becomes better while moving downstream, it stays constant for the DTU case, but for JHU case the discrepancy increases. The discrepancy in the DTU simulation stays constant at approximately 10^{-2} and diffuses inboard while moving downstream. It visibly predicts a lower wake expansion (see also Figure 6-4) and a sharper shear layer. The JHU simulation follows very well the behaviour of the AD velocity profile in the proximity of the disc within 1D, but then it shows a less diffusive behaviour predicting a sharper shear layer and the discrepancy changes from $3{\cdot}10^{-2}$ to $2{\cdot}10^{-1}$ in the last locations. Not much difference is noted with respect to the laminar case. The discrepancy in the ECN case slightly decreases further downstream, from $3\text{-}5{\cdot}10^{-1}$ to $2{\cdot}10^{-1}$. In the LEU, the discrepancy decreases considerably while moving downstream from $2\text{-}3{\cdot}10^{-1}$ to less than 10^{-1}. In comparison to the laminar-inflow case, the ECN model present poorer performances with over-prediction of the velocity in the shear layer, whereas the DTU, JHU and the LEU models perform better in the turbulent-inflow case. A major change in the prediction of velocity is not noticed primarily because of the low turbulence in the flow. A higher inflow turbulence would have certainly led to a faster wake recovery and different velocity profiles. JHU is able to capture this change in inflow with its very sensitive LES model. Between LEU and ECN, the former has a more accurate numerical scheme and a higher grid resolution, which could lead to the observed differences, despite a similar SGS model. Further, the Smagorinsky model used by ECN, has not yet been tuned correctly, as opposed to that used by LEU, which has been tuned (see section 6.3.5). It is possible that ECN may incur excessive dissipation through the Smagorinsky model than what is required, leading to error in the shear layer characterised by higher turbulence.

Figure 6-4 compares the wake width as function of the downstream position for the different LES cases with the vortex model results and the PIV measurements for the turbulent-inflow case. The most evident features are the large over-prediction of the wake expansion by the ECN model and the large under-prediction by the DTU model, despite the DTU model is the only one able to represent correctly the initial expansion as in the laminar case. Despite the performance of the ECN model improves compared to the laminar-inflow case (the discrepancy goes down to approximately 5%) the DTU model has worse performance in the turbulent-inflow case, with an under-prediction between 7% and 9%. The JHU and LEU models give the best prediction, among the LES models, with a considerable improvement of the LEU performance. Also in the turbulent-inflow case, the TUD vortex model presents the best performance in the prediction of the wake expansion.

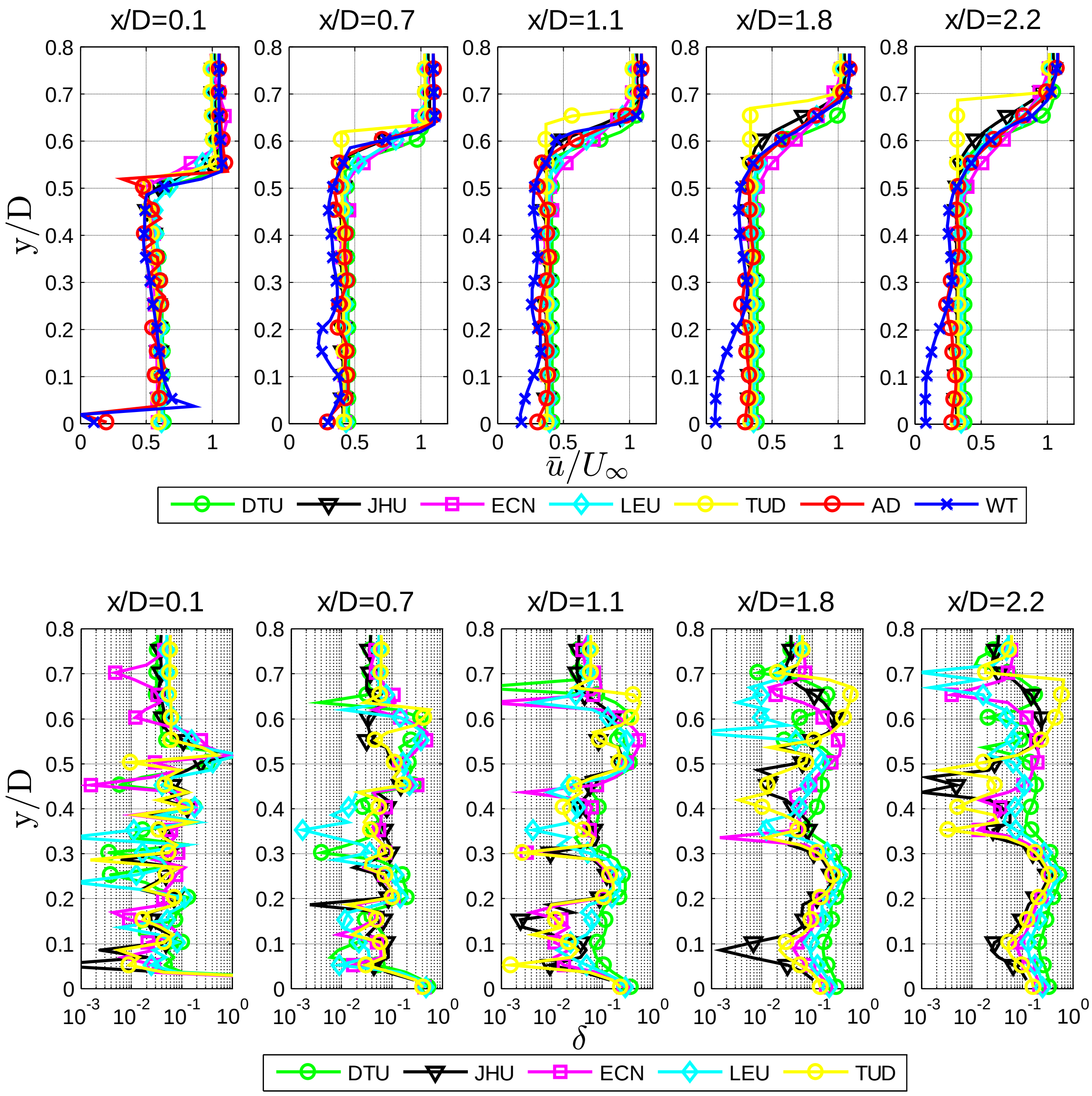

Figure 6-3. Turbulent-inflow case. Time averaged axial velocity profiles from the four LES models, the vortex model and the experiments with the WT and AD (top image). Relative discrepancy of the numerical results compared to the AD experimental data (bottom image).

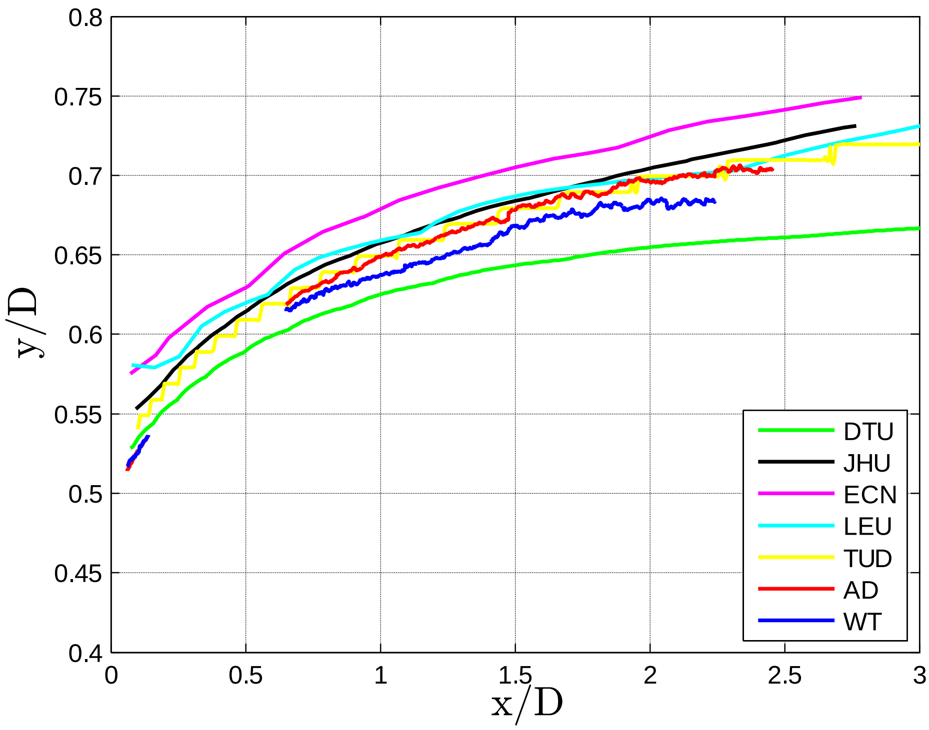

Figure 6-4. Turbulent-inflow case. Wake expansion from the four LES models, the vortex model and the experiments with the WT and AD.

6.4.2 Turbulence Intensity

Laminar Inflow Case

Figure 6-5 (top) shows the comparison of the time-average turbulence intensity profiles at five different wake locations along the streamwise direction obtained from the LES simulations and compared to the results of the SPIV experiments. The relative discrepancy, calculated as in Equation (6-1), is plotted in Figure 6-5 (bottom). In LES, the large-scale flow structures are resolved, while the effect of smaller scale is represented by the sub-grid model. In this section, the *TI* is representative only of the explicitly resolved turbulence scales. For this reason, it is generally observed that very close to the actuator disc, where the shear layer is still very sharp and the relevant length scales are correspondingly small, the resolved stresses in the LES are much lower compared to the experimental observations than further downstream. These effects are revealed in Figure 6-5, which shows that the resolved stresses in the simulations as function of the downstream position develop slower than observed in the experiments. DTU model gives the best prediction in the shear layer region with discrepancy of the order of 10^{-1} from the third location. However, it does not match the peak position very well (mismatch of approximately 0.05D in the radial direction) due to the smaller wake expansion. Moreover, it over-predicts the intensity as one moves from the shear layer towards the centreline, after its peak turbulence intensity has been attained. It is the only model that predicts a $TI \neq 0$ in the centreline region, which is more similar to what is observed in the WT wake. Also the JHU shows a good prediction of the wake turbulence, with discrepancy of the order of 10^{-1} from the fourth location in the shear layer and a good prediction of the *TI* peak in the wake shear layer. In the laminar-inflow case, neither the ECN nor the LEU models are capable to predict any turbulence development in the wake shear layer. This is primarily because of the fact that both the codes use the Smagorinsky model that is more dissipative than the others and may thus prevent early shear layer instabilities to form. As a result, a smaller fraction of the turbulence that originates from the shear layer can be resolved, especially when the inflow is initially laminar.

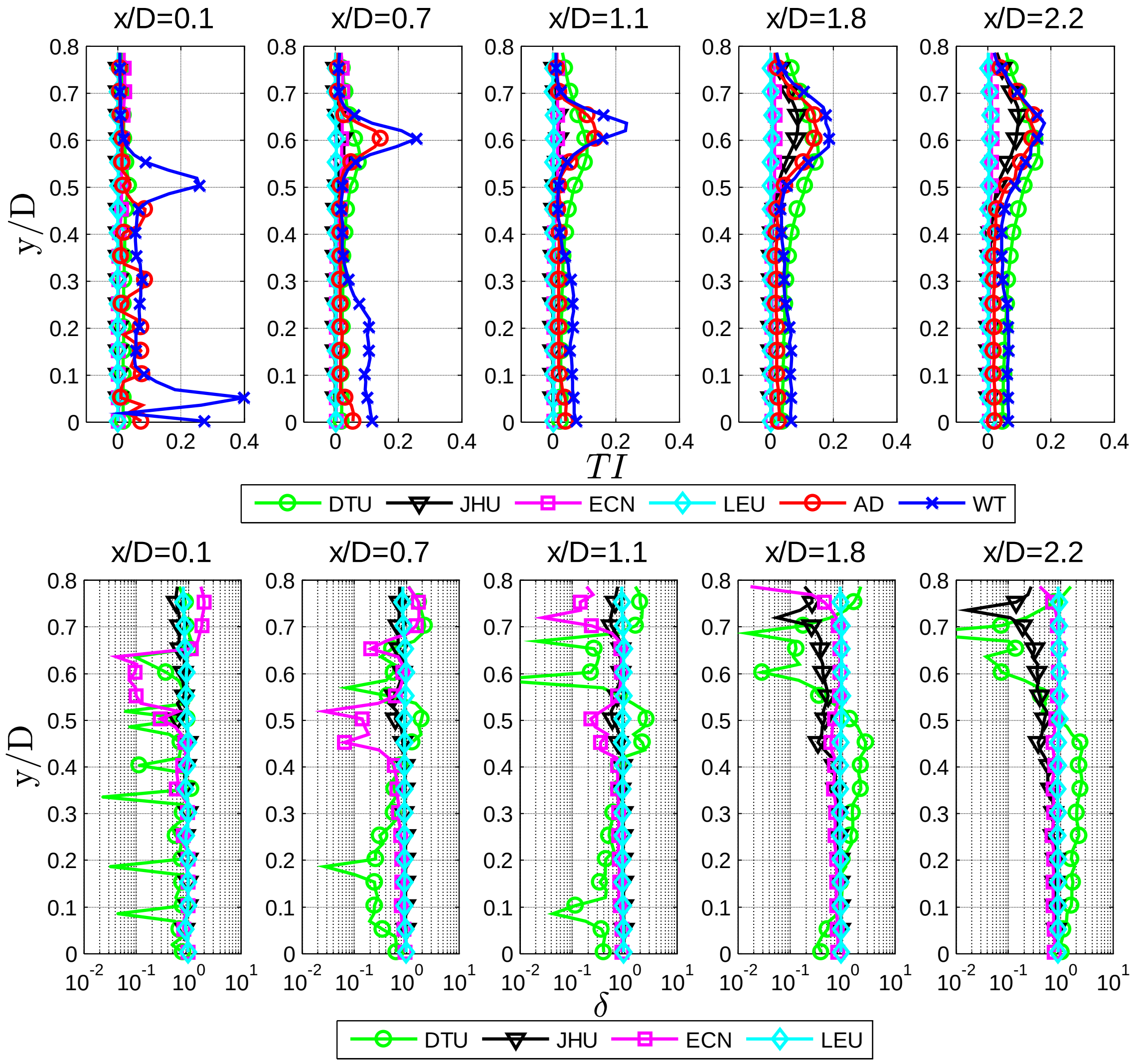

Figure 6-5. Laminar inflow case. Turbulence intensity profiles from the four LES models and the experiments with the WT and AD (top image). Relative discrepancy of the numerical results compared to the AD experimental data (bottom image).

Turbulent Inflow Case

Figure 6-6 shows that among all LES cases only the JHU is able to predict the location of the peaks in the *TI* correctly and the peak value as well after sufficient wake development (2D), which is necessary to predict the wake expansion rate accurately, as seen in Figure 6-4. DTU follows a trend similar to what was noticed with a laminar inflow. The peak turbulence is a little displaced towards the centreline as model reaches the peak value. Moreover, as the wake develops, the intensity increases continuously towards the centreline, leading to an over-prediction. The ECN model is shown to be considerably less capable to correctly predict the position of the TI peak and its magnitude, which is also reflected in the poor performance shown in Figure 6-4, although any spurious amplification of the TI is controlled by the dissipative Smagorinsky model that is used. The LEU model gives rise to a negligible production of turbulence everywhere in the near wake, although the location of its peak is predicted correctly. As numerical dissipation is not a problem with either of the codes, one could surmise that the turbulence model used by JHU, the Scale Dependent Dynamic model, does lead to the differences in accuracy that one observes. These differences have been observed in various comparative studies performed earlier (Porte-Agel et al, 2000). To summarise, it appears that DTU performs similarly for both the laminar and turbulent cases. It allows the turbulence to develop as opposed to ECN and LEU, but leads to its over-prediction in the inner wake. On the other hand, the JHU performs well after adding the turbulence. Even though the intensity of the inflow is low, its comprehensive SGS is able to sense the turbulence and permits it to develop, leading to an agreeable prediction.

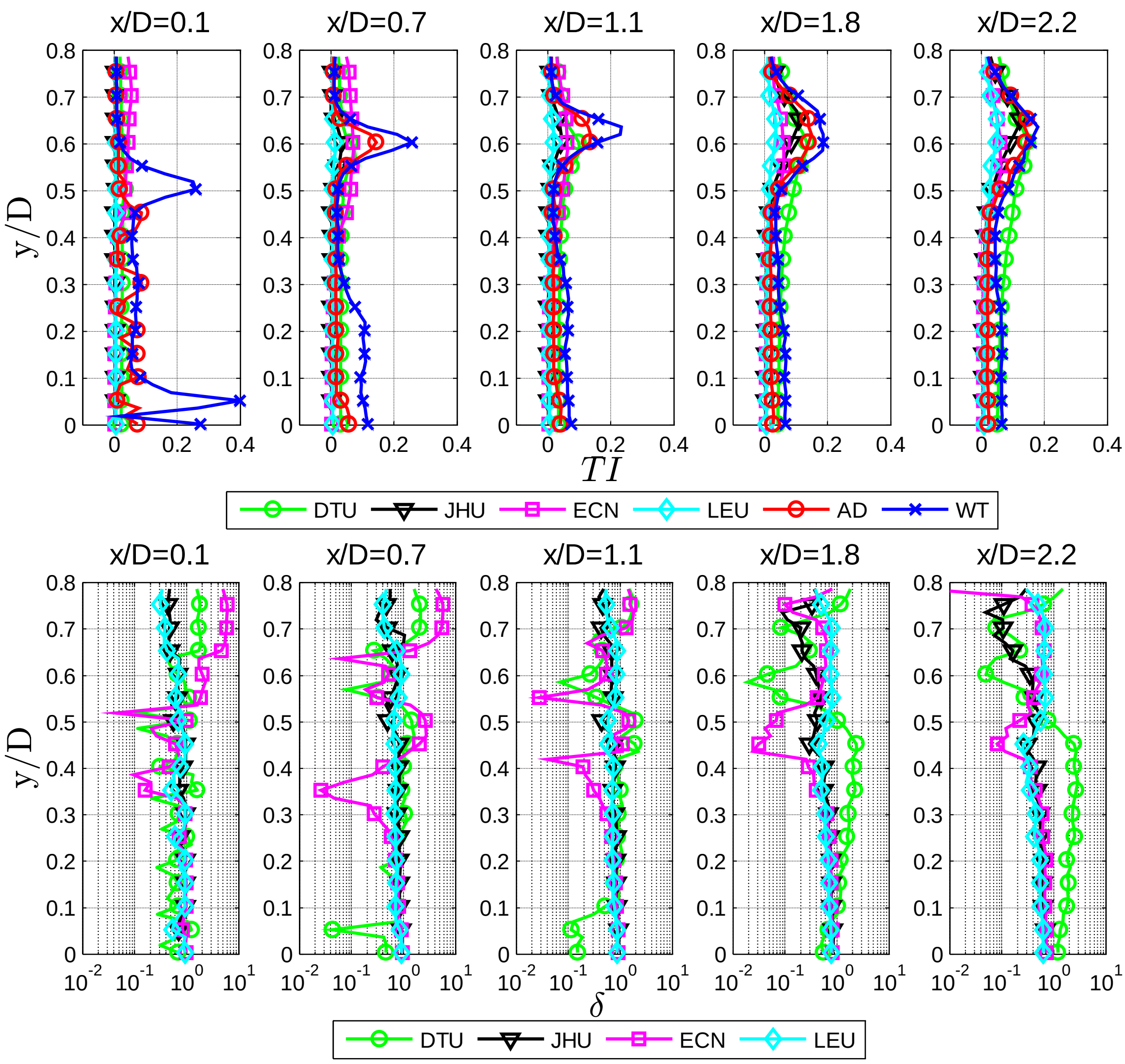

Figure 6-6. Turbulent inflow case. Turbulence intensity profiles from the four LES models, the vortex model and the experiments with the WT and AD (top image). Relative discrepancy of the numerical results compared to the AD experimental data (bottom image).

6.5 GRID CONVERGENCE

Johns Hopkins University, ECN and University of Leuven also provided a grid convergence study, repeating their simulations for difference grid spacing as indicated in Table 6-2, Table 6-3 and Table 6-5. This section reports the results of the 7 cases performed by JHU, the three cases performed by ECN and three by LEU. For sake of simplicity, only the axial velocity and total turbulence intensity profiles in the last location, at $x/D = 2.2$ are reported. Figure 6-7 shows the results of the grid convergence analysis of the axial velocity field. The JHU is performed with a laminar inflow, whereas the other two cases are for a turbulent inflow. The striking observation in the JHU simulation (Figure 6-7, left) is that the best performing case is the one with the coarsest mesh ($\Delta = 0.09902D$) which is able to perfectly reproduce the shape of the wake shear layer up to $y/D = 0.7$. Apart from the highest resolution case, all other cases seem relatively identical and they all overestimate the velocity deficit in the region of the wake shear layer at $0.5 < y/D < 0.7$, predicting a shear layer thickness approximately 25% smaller than the actual one. In the ECN and LEU cases, as expected the prediction of the wake velocity gets better with increasing resolution

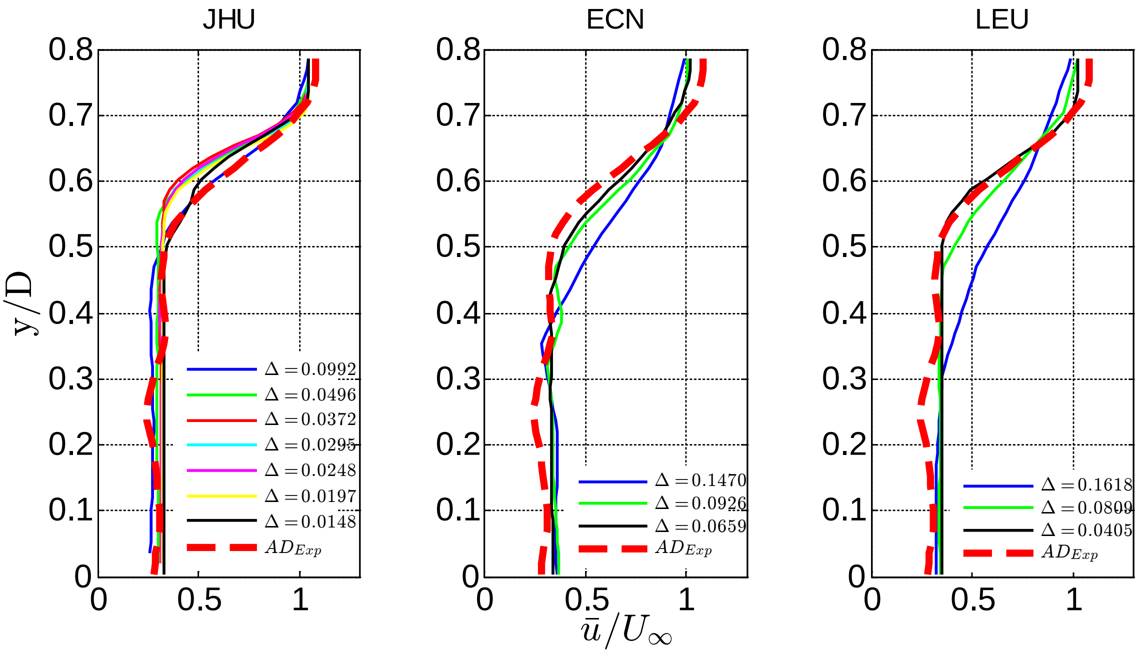

Figure 6-7. Grid convergence analysis: time average axial velocity profiles (the spacing Δ is expressed in rotor diameters).

Figure 6-8 shows the results of the grid convergence analysis of total turbulence intensity. In the JHU simulation, it is evident how the lowest resolution case has the worst performance, despite the fact that it gave the best prediction of the shear layer velocity. Contrary to what may be expected, the prediction of the fluctuations does not improve linearly with increasing resolution, but the best prediction at this location is obtained with the intermediate grid spacing (e.g. $\Delta = 0.0248D$ and $\Delta = 0.0295D$), after which agreement at this location decreases again. However, it is noted that with increasing resolution the location at which the fluctuations set in consistently moves closer towards the disc. Therefore the dissipation, which is controlled by the used sub-grid model, also sets in closer to the disc for higher resolution simulations and this can result in slightly lower fluctuations further downstream when compared to lower resolution simulations. Regarding the ECN and LEU case, as expected the performances improve with increasing resolution, with the two lower resolution cases giving extremely low values of turbulence in the shear layer. It is interesting to observe that the JHU model is able to predict a level of TI ≠ 0 and equal to approximately 30% of the real case also in the laminar inflow case with the coarsest grid (Δ = 0.0992D) whereas for similar resolution the ECN and the LEU cases predicts a turbulence level which is only approximately 10% of the real case, even in the presence of a turbulent inflow.

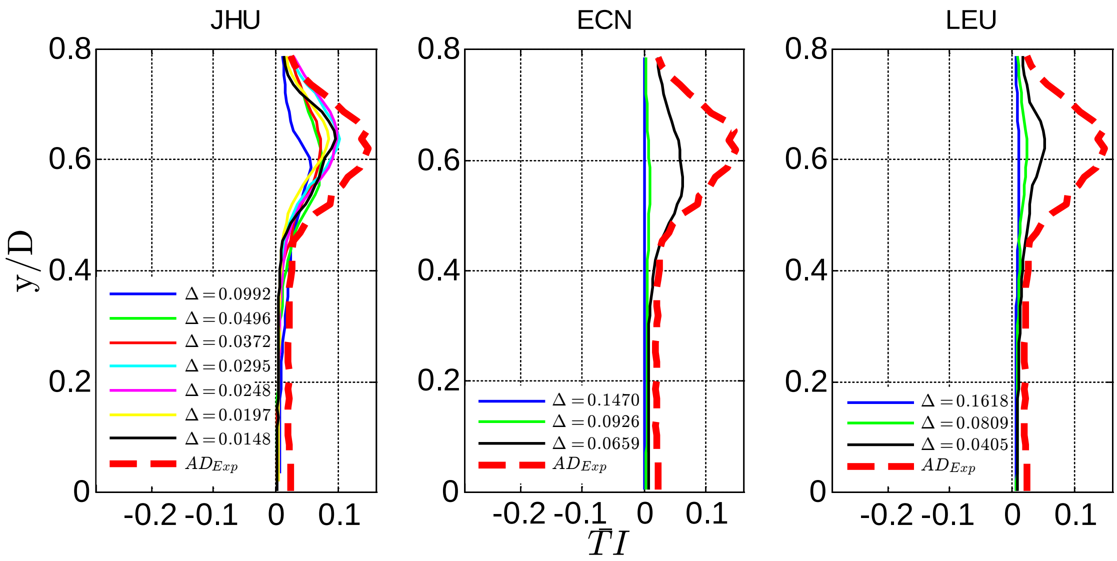

Figure 6-8. Grid convergence analysis: turbulence intensity profiles (the spacing Δ is expressed in rotor diameters).

6.6 CONCLUSIONS

The aim of this study is to validate a series of LES codes, which are developed and used for research purposes in different academic institutions, and a vortex model against high-fidelity data from wind tunnel experiments on the wake of a uniformly loaded actuator disc. When simulating wind farms, it is essential to model the turbines with an accuracy that is enough to generate the correct velocity deficit and turbulence intensity in the wake of the turbines. At the same time, it is also important to ensure that the model is not computationally demanding. Under these circumstances, most of the numerical codes rely on the actuator disc approach. However, many codes used in academia have not yet been directly validated or compared against a common benchmark test case and reported in literature, which was the motivation behind this chapter. A striking observation is the very good performance of the vortex model for predicting certain flow features, e.g. the centreline velocity, both in the near and intermediate wake: in the near wake, the latter is comparable to the other LES models and performs better than ECN and LEU in the downstream region and presents the best performances in the prediction of the wake expansion, both in the laminar and turbulent cases. Also, it predicts the wake expansion in the near wake with a very large accuracy, much better than the other LES models. Conversely, its prediction of the full velocity profile shape is quite poor due to viscosity and turbulence effects that play a very important role in the shear layer region, while the code is not modelling these aspects and predicts a very sharp velocity gradient. Regarding the LES codes, it was noticed that a combination of an accurate pseudo-spectral schemes with an advanced sub-grid scale model leads to favourable results, in terms of both, the velocity deficit and turbulence intensity (JHU). However, with simpler sub-grid scale modelling, one can only predict the velocity deficit correctly, because the growth or decay of turbulence, is to a greater extent, dependent on the sub-grid scale model (LEU). On the other hand, with a finite volume code, it is most important to ensure the absence of numerical dissipation, which is the case with pseudo-spectral schemes. Using an energy-conserving scheme, one predicts the velocity deficit with acceptable accuracy even with relatively coarser grids. However, for prediction of the turbulence intensity one must mainly rely on better sub-grid modelling. Further, should one choose to use a simple model like Smagorinsky’s, the model must be tuned appropriately for high Reynolds number flows, as the comparison between ECN and LEU reveals. This study shows that a suitable combination of numerical schemes and sub-grid modelling, which are not only accurate but simple and computationally efficient, holds the key to industrial applications of LES to wind farm aerodynamics. Future work will include a similar but more comprehensive study with the same inflow conditions, grid resolutions etc. to study the effects of numerical schemes as a whole.

7 CONCLUSIONS AND RECOMMENDATIONS

The work included in this dissertation is a study of the physics of the near and transition wake of horizontal-axis wind turbines and on the limitations and potentials of the actuator disc model.

The analysis in Chapter 2 and Chapter 3 focussed on quantifying the influence of the near wake phenomena on the far wake development. The physical mechanism of the wake re-energising process has been investigated in terms of mean-flow kinetic-kinetic energy transport. The study in Chapter 4 showed the different turbulent mixing mechanisms in the wake of a wind turbine and in the one of a porous disc. Chapter 5 has shown the limitations of the eddy-viscosity based turbulence models and quantified the energy exchange among different flow structures and the energy transport properties of periodic and random flow fluctuations in the near wake. Chapter 6 constitutes an example of a comparative study between experimental data and state-of-the-art numerical models.

In Section 1.5, a series of four main research questions and several sub-questions were presented. After carrying out the study presented in this dissertation, the questions can be answered. In this conclusive section, the answers on each question are reported and some recommendations for future research are provided.

1. How does the tip-vortex instability influence the wake flow and its re-energising process?

1.1. What is the effect on the mean velocity field in the wake?

The tip-vortex pairing instability has an effect on the time-average velocity field, which exhibits a localised enlargement of the wake shear layer in the proximity of the instability location. It is shown that a leapfrogging instability enhances the breakdown and diffusion of the tip-vortex: this entails a direct influence of the large-scale wake behaviour on the tip-vortex flow properties. This finding is corroborated by the observation of the azimuthal velocity field, which shows a clear change of sign of the velocity direction in the vortex region after the leapfrogging location.

1.2. What is the effect on the flow turbulence and on the wake re-energising process?

In the case studies taken into consideration in this research, the re-energising process starts directly after the location where two consecutive tip vortices have completed a 90 degree rotation. After this location, the turbulence intensity due to random fluctuations increases drastically. This supports the hypothesis that the tip-vortex instability leads to a more effective mixing.

The effect of the tip-vortex leapfrogging instability on the wake mixing and re-energising suggests the opportunity to investigate methods for generating unstable wakes and having a partial control on the recovery process. For instance, blade asymmetries and tip devices, such as wing sails or winglets, will help destabilising the tip-vortex spirals and enhancing the mixing in the near wake. The relevance of such strategies may be minor in a very turbulent environment, such as in onshore complex terrains, but could be promising for reducing the wake effect in low-turbulence offshore settings. Future research in this context should also include the experimental demonstration of the hypothesis of Nishino and Willden (2012), who performed a CFD analysis on the near wake of an actuator disc with different turbulence intensity levels, showing the positive effect of the near wake mixing on the performances of the upstream turbine itself. Another valuable step in this research will be the organisation of an experimental campaign with two identical turbines in order to record the performances and the wake characteristics of the downstream turbine as function of the stability properties of the upstream one.

2. What are the key turbulence phenomena in the wake of a wind turbine rotor?

2.1. What is the amount of kinetic energy transported and dissipated by the most relevant flow structures?

The triple decomposition applied to the phase-locked data allowed to distinguish between the mean-flow kinetic energy transport by the action of the periodic and random flow fluctuations across the shear layer at the wake borders. It is shown that, locally, the periodic structures cause a mean-flow kinetic-energy transport which is an order of magnitude larger than the one promoted by the random fluctuations. However, when averaged in space, the former ones have a negligible contribution to the energy exchange, while the latter ones are responsible for most of the transport. The study also quantified the production of turbulence due to the decay of the kinetic energy of the mean flow and of the vortex structures. The two contributions have similar values globally, but in the near wake region the decay of the tip-vortices has a larger contribution in the production of turbulence.

2.2. What is the role of the tip-vortices, their instability and their breakdown in the turbulent mixing?

The near wake region is characterised by strong flow fluctuations, which are generally accounted for as turbulence. However, the actual level of turbulent mixing is very low. In fact, the rotational motion of the tip vortex promotes high transport of mean-flow kinetic energy locally, but with a negligible net value. After the breakdown of the tip vortex after the leapfrogging instability, the random flow fluctuations prevails, promoting a more efficient mixing of the flow.

The present analysis is conducted for a two-blade horizontal axis wind turbine. In future research, the three-blade case should also be addressed. The method used in this study and the knowledge acquired will keep their validity. The expected changes will be a more unstable wake, with an earlier leapfrogging, as shown experimentally by Felli et al (2011); also, the unstable tip vortices will not form pairs, but groups of three, as shown in the visualisation of Bolnot et al (2014).

This study is performed at low turbulence intensity, to be able to separate the flow mixing caused by the external turbulence from that caused by the turbulence induced directly by the wind turbine, and give full control over the tip-vortex instability. To perform a similar analysis with an increased inflow turbulence will allow to investigate the sensitivity of the wake system to the freestream flow fluctuations. The external ambient turbulence would introduce additional perturbations which trigger an earlier tip-vortex spiral instability, causing the leapfrogging to move upstream. The extension of the wake region characterised by stable vortices as function of the ambient turbulence intensity is still an open question, which has been addressed numerically by Ivanell (2009) and needs to be demonstrated experimentally.

3. What are the main differences between the near wake of a wind turbine and an actuator disc?

3.1. What are the key differences in the wind turbine and actuator disc near wake and how do they affect the transport of mean flow kinetic energy?

The analysis showed how the physics governing the turbulent mixing in the two wakes is intrinsically different. The total turbulence intensity peak in the near wake of the WT is two to four times larger than the one in the AD wake, but both wakes exhibit the same peak of mean-flow kinetic-energy transport in the shear layer, which then collapses to 50% of its original value after the breakdown of the WT tip-vortices after the leapfrogging. Major contribution to the momentum entrainment in the WT wake is provided by the random flow fluctuations, while the periodic fluctuations have a null or negative contribution (apart from small localised regions). This corroborates the findings of Chapter 2 and Chapter 3. In the AD wake the transport is only positive and its space integral is of a larger magnitude compared to the one in the WT wake, meaning that the entrainment is generally higher in the AD near wake. The analysis of the turbulence production showed a distinct region characterised by negative values in correspondence of the tip-vortex instability in the WT wake. This phenomenon is absent in the AD wake and it has been shown to have a significant effect on the re-energising process of the wake shear layer in the time-average field. This phenomenon constitutes a clear example of the failure of the gradient transport model in the time-mean field, which normally does not account for the possibility of reverse energy transfer from coherent structures to the mean flow.

3.2. To what extent is the actuator disc assumption valid for the representation of the near wake dynamics?

The experiments have been performed with a very low level of inflow turbulence (0.5%): even in this condition, the velocity fields in the AD and WT wakes compare very well. However, the turbulent mixing in both wakes is very different. This contradicts statements affirming that results from actuator disc simulations are valid only after five diameters downstream the disc (Schepers, 2012).

Also in this case, a valuable recommendation for a follow-up research is to perform the experiments with an increased level of inflow turbulence. Also, the actuator disc model can be modified in order to allow for unsteady loading (e.g. with two movable discs that can switch between two values of porosity). In this way an analysis of the wake unsteadiness can be carried on and several dynamic inflow models can be validated. On this regard, some initial experimental research is already being performed at the Delft University of Technology (Hong, 2015).

4. What is the level of accuracy of the state-of-the-art numerical models in reproducing the near wake features highlighted in the experiments?

The study focussed on the analysis of LES models and of a vortex model. The comparison showed that, despite the lack of a viscosity and turbulence model, the vortex model is capable of reproducing the wake expansion and the centreline velocity with good accuracy, considerably better than the other LES models. All LES models considered are able to predict the velocity deficit in the very near wake accurately within 0.5D from the disc. However, the resolved velocity fluctuations in the LES model are below the experimentally measured values. Chapter 6 constitutes an example of the comparative studies that more and more often should be promoted among different wake-model developers and users.

The present research challenges the classical concept of wake turbulence, which is defined as the ensemble of flow fluctuations caused by the presence of the turbine and which does not distinguish the roles of different flow structures. As of today, the near wake is still treated as a fully turbulent flow region, often disregarding that the tip-vortex has not a specific turbulent character (Gómez-Elvira et al, 2005) . This consideration is also often adopted when developing and validating e.g. actuator-disc based simulations, trying to match the same level of turbulence intensity of the wind turbine near wake. This study showed that only the random turbulent fluctuations are relevant for the kinetic energy transport and as such are most important to be present in a numerical simulation. The conclusion is hence that aiming at a same level of turbulence in the wind turbine and actuator disc near wake will necessarily lead to an overestimated mixing and a too fast re-energising process. The quantity to match is in fact the mean-flow kinetic energy flux. The importance to include the energy exchange among different flow structures and the energy transport properties of periodic and random flow fluctuations in the near wake for the development of more advanced turbulence models, as proposed by Gómez-Elvira et al

(2005) and El Kasmi and Masson (2008) is not evident. The high-resolution stereo particle image velocimetry measurements from the two experimental campaigns constitute a database of information that should be used by developers for validating old and new wake models.

Currently, the use of an actuator disc approach is not recommended in the region between 0 to 5 diameters downstream the rotor, especially in the presence of low ambient turbulence. The present results suggest the possibility to extend the use of the actuator disc model in numerical simulation until the very near wake, provided that the turbulent mixing is correctly represented. As a general recommendation, the stability and re-energising properties of the wake should be considered as one of the design parameters for future wind turbine rotors.

BIBLIOGRAPHY

[1] Ainslie, J.F., 1988. Calculating the flowfield in the wake of wind turbines. Journal of Wind Engineering and Industrial Aerodynamics 27, 213-224

[2] Akay, B., Ferreira, C.S., Van Bussel, G.J.W., Herraez, I., 2012. Experimental and Numerical Quantification of Radial Flow in the Root Region of a HAWT, 50th AIAA Aerospace Sciences Meeting. American Institute of Aeronautics and Astronautics (AIAA), Nashville, USA.

[3] Albertson, J.D., Parlange, M.B., 1999. Surface length scales and shear stress: Implications for land-atmosphere interaction over complex terrain. Water Resources Research 35, 2121-2132

[4] Antonia, R.A., Browne, L.W.B., 1987a. Quadrant analysis in the turbulent far-wake of a cylinder. Fluid Dynamics Research 2, 3-14

[5] Antonia, R.A., Browne, L.W.B., 1987b. Quadrant analysis in the turbulent far-wake of a cylinder. Fluid Dynamics Research 2, 3

[6] Antonia, R.A., Browne, L.W.B., Bisset, D.K., Fulachier, L., 1987. A description of the organized motion in the turbulent far wake of a cylinder at low Reynolds number. Journal of Fluid Mechanics 184, 423-444

[7] Antonia, R.A., Chambers, A.J., Britz, D., Browne, L.W.B., 1986. Organized structures in a turbulent plane jet: topology and contribution to momentum and heat transport. Journal of Fluid Mechanics 172, 211-229

[8] Aubrun, S., Devinant, P., Espana, G., 2007. Physical modelling of the far wake from wind turbines. Application to wind turbine interactions, European Wind Energy Conference EWEC 2007.

[9] Aubrun, S., Loyer, S., Hancock, P.E., Hayden, P., 2013. Wind turbine wake properties: Comparison between a non-rotating simplified wind turbine model and a rotating model. Journal of Wind Engineering and Industrial Aerodynamics 120, 1-8

[10] Barthelmie, R.J., Frandsen, S.T., Nielsen, M.N., Pryor, S.C., Rethore, P.E., Jørgensen, H.E., 2007a. Modelling and measurements of power losses and turbulence intensity in wind turbine wakes at Middelgrunden offshore wind farm. Wind Energy 10, 517-528

[11] Barthelmie, R.J., Pryor, S.C., Frandsen, S.T., Hansen, K.S., Schepers, J.G., Rados, K., Schlez, W., Neubert, A., Jensen, L.E., Neckelmann, S., 2010. Quantifying the impact of wind turbine wakes on power output at offshore wind farms. Journal of Atmospheric and Oceanic Technology 27, 1302-1317

[12] Barthelmie, R.J., Rathmann, O., Frandsen, S.T., Hansen, K.S., Politis, E., Prospathopoulos, J., Rados, K., Cabezón, D., Schlez, W., Phillips, J., Neubert, A.,

Schepers, J.G., van der Pijl, S.P., 2007b. Modelling and measurements of wakes in large wind farms. Journal of Physics: Conference Series 75, 012049

[13] Batchelor, G.K., 2000. An Introduction to Fluid Dynamics. Cambridge University Press.

[14] Batchelor, G.K., Townsend, A.A., 1947. Decay of Vorticity in Isotropic Turbulence. Proceedings of the Royal Society of London. Series A, Mathematical and Physical Sciences 190, 534-550

[15] Batchelor, G.K., Townsend, A.A., 1948a. Decay of Isotropic Turbulence in the Initial Period. Proceedings of the Royal Society of London. Series A, Mathematical and Physical Sciences 193, 539-558

[16] Batchelor, G.K., Townsend, A.A., 1948b. Decay of Turbulence in the Final Period. Proceedings of the Royal Society of London. Series A, Mathematical and Physical Sciences 194, 527-543

[17] Benedict, L.H., Gould, R.D., 1996. Towards better uncertainty estimates for turbulence statistics. Exp Fluids 22, 129-136

[18] Betz, A., 1919. Schraubenpropeller mit geringstem Energieverlust. Mit einem Zusatz von l. Prandtl. Nachrichten von der Gesellschaft der Wissenschaften zu Göttingen, Mathematisch-Physikalische Klasse 1919, 193-217

[19] Bingöl, F., Mann, J., Larsen, G.C., 2010. Light detection and ranging measurements of wake dynamics part I: one-dimensional scanning. Wind Energy 13, 51-61

[20] Bolnot, H., Le Dizès, S., Leweke, T., 2014. Pairing Instability in Helical Vortices, Wind Energy - Impact of Turbulence. Springer Berlin Heidelberg, pp. 23-28.

[21] Bolnot, H., Leweke, T., Le Dizes, S., 2011. Spatio-temporal development of the pairing instability in helical vortices, 6th AIAA Theoretical Fluid Mechanics Conference. American Institute of Aeronautics and Astronautics, Inc.,

[22] Bou-Zeid, E., Meneveau, C., Parlange, M., 2005. A scale-dependent Lagrangian dynamic model for large eddy simulation of complex turbulent flows. Physics of Fluids (1994-present) 17, 025105

[23] Browand, F.K., Weidman, P.D., 1976. Large scales in the developing mixing layer. Journal of Fluid Mechanics 76, 127-144

[24] Burton, T., Sharpe, D., Jenkins, N., Bossanyi, E., 2001. Wind Energy Handbook. John Wiley & Sons.

[25] Cal, R.B., Lebrón, J., Castillo, L., Kang , H.S., Meneveau, C., 2010. Experimental study of the horizontally averaged flow structure in a model wind-turbine array boundary layer. Journal of Renewable and Sustainable Energy 2

[26] Calaf, M., Meneveau, C., Meyers, J., 2010a. Large eddy simulation study of fully developed wind-turbine array boundary layers. Physics of Fluids 22, 015110-015116

[27] Calaf, M., Meneveau, C., Meyers, J., 2010b. Large eddy simulation study of fully developed wind-turbine array boundary layers. Physics of Fluids (1994-present) 22, -

[28] Cantwell, B., Coles, D., 1983. An experimental study of entrainment and transport in the turbulent near wake of a circular cylinder. Journal of Fluid Mechanics 136, 321-374

[29] Chamorro, L., Porté-Agel, F., 2009. A Wind-Tunnel Investigation of Wind-Turbine Wakes: Boundary-Layer Turbulence Effects. Boundary-Layer Meteorology 132, 129-149

[30] Chamorro, L.P., Arndt, R.E.A., Sotiropoulos, F., 2012. Reynolds number dependence of turbulence statistics in the wake of wind turbines. Wind Energy 15, 733-742

[31] Chatterjee, A., 2000. An introduction to the proper orthogonal decomposition.

[32] Chen, T.Y., Liou, L.R., 2011. Blockage corrections in wind tunnel tests of small horizontal-axis wind turbines. Experimental Thermal and Fluid Science 35, 565-569

[33] Corten, G.P., Schaak, P., 2004. More power and less loads in wind farms: “heat and flux”, EWEC.

[34] Cotroni, A., Di Felice, F., Romano, G.P., Elefante, M., 2000. Investigation of the near wake of a propeller using particle image velocimetry. Exp Fluids 29, S227-S236

[35] Crespo, A., Hernandez, J., 1996. Turbulence characteristics in wind-turbine wakes. Journal of Wind Engineering and Industrial Aerodynamics 61, 71-85

[36] Crespo, A., Hernandez, J., Fraga, E., Andreu, C., 1988. Experimental validation of the UPM computer code to calculate wind turbine wakes and comparison with other models. Journal of Wind Engineering and Industrial Aerodynamics 27, 77-88

[37] Crespo, A., Hernández, J., Frandsen, S., 1999. Survey of modelling methods for wind turbine wakes and wind farms. Wind Energy 2, 1-24

[38] Dobrev, I., Maalouf, B., Troldborg, N., Massouh, F., 2008. Investigation of the Wind Turbine Vortex Structure, 14th International Symposium on Applications of Laser Techniques to Fluid Mechanics.

[39] Eitelberg, G., 2016. TU Delft Lecture notes AE4115, Rotor corrections., Delft

[40] El Kasmi, A., Masson, C., 2008. An extended model for turbulent flow through horizontal-axis wind turbines. Journal of Wind Engineering and Industrial Aerodynamics 96, 103-122

[41] Elsinga, G.E., van Oudheusden, B.W., Scarano, F., 2005. Evaluation of aero-optical distortion effects in PIV. Exp Fluids 39, 246-256

[42] Escudié, R., Liné, A., 2003. Experimental analysis of hydrodynamics in a radially agitated tank. AIChE Journal 49, 585-603

[43] Fabris, G., 1979. Conditional sampling study of the turbulent wake of a cylinder. Part 1. Journal of Fluid Mechanics 94, 673-709

[44] Felli, M., Camussi, R., Di Felice, F., 2011. Mechanisms of evolution of the propeller wake in the transition and far fields. Journal of Fluid Mechanics 682, 5-53

[45] Ferreira, C.S., 2009. The near wake of the VAWT: 2D and 3D views of the VAWT aerodynamics. Delft University of Technology.

[46] Fourier, J., 1808. Mémoire sur la propagation de la chaleur dans les corps solides. Nouveau Bulletin des sciences par la Société philomatique de Paris 1, 112-116

[47] Frandsen, S., Barthelmie, R., Pryor, S., Rathmann, O., Larsen, S., Højstrup, J., Thøgersen, M., 2006. Analytical modelling of wind speed deficit in large offshore wind farms. Wind Energy 9, 39-53

[48] Froude, R.E., 1889. On the part played in propulsion by difference of fluid pressure. Trans Roy Inst Naval Arch.

[49] Gaumond, M., Rethore, P.E., Bechmann, A., Ott, S., Larsen, G.C., Peña, A., Hansen, K.S., 2012. Benchmarking of Wind Turbine Wake Models in Large Offshore Windfarms, Science of Making Torque from Wind.

[50] Ghaemi, S., Scarano, F., 2011. Counter-hairpin vortices in the turbulent wake of a sharp trailing edge. Journal of Fluid Mechanics 689, 317-356

[51] Gilling, L., 2009. TuGen: Synthetic Turbulence Generator Manual and User's Guide,

[52] Glauert, H., 1935. Aerodynamic theory. Julius Springer, Berlin, Germany.

[53] Gómez-Elvira, R., Crespo, A., Migoya, E., Manuel, F., Hernández, J., 2005. Anisotropy of turbulence in wind turbine wakes. Journal of Wind Engineering and Industrial Aerodynamics 93, 797-814

[54] Hamilton, N., Kang, H.S., Meneveau, C., Cal, R.B., 2012. Statistical analysis of kinetic energy entrainment in a model wind turbine array boundary layer. Journal of Renewable and Sustainable Energy 4, 063105-063119

[55] Hattori, Y., Moeng, C.-H., Suto, H., Tanaka, N., Hirakuchi, H., 2010. Wind-Tunnel Experiment on Logarithmic-Layer Turbulence under the Influence of Overlying Detached Eddies. Boundary-Layer Meteorology 134, 269-283

[56] Herpin, S., Wong, C.Y., Stanislas, M., Soria, J., 2008. Stereoscopic PIV measurements of a turbulent boundary layer with a large spatial dynamic range. Exp Fluids 45, 745-763

[57] Hong, V.W., 2015. Analysis of an actuator disc under unsteady loading - Validation of engineering models using experimental and numerical methods, Aerospace Engineering. Delft University of Technology, Delft.

[58] Humble, R.A., 2008. Unsteady flow frganisation of a shock wave/boundary layer interaction, Aerospace Engineering. Delft University of Technology.

[59] Hussain, A.K.M.F., 1981. Role of coherent structures in turbulent shear flows. Proc. Indian Acad. Sci. (Engg. Sci.) 4, 129-175

[60] Hussain, A.K.M.F., 1983. Coherent structures-reality and myth. Physics of Fluids 26, 2816-2850

[61] Hussain, A.K.M.F., Zaman, K.B.M.Q., 1980. Vortex pairing in a circular jet under controlled excitation. Part 2. Coherent structure dynamics. Journal of Fluid Mechanics 101, 493-544

[62] Hütter, U., 1977. Optimum Wind-Energy Conversion Systems. Annual Review of Fluid Mechanics 9, 399-419

[63] Ivanell, S., 2009. Numerical Computations of Wind Turbine Wakes, Linne Flow Centre, Department of Mechanics. Royal Institute of Technology KTH - Gotland University, SE-100 44 Stockholm, Sweden.

[64] Ivanell, S., Mikkelsen, R., Sørensen, J.N., Henningson, D., 2010. Stability analysis of the tip vortices of a wind turbine. Wind Energy 13, 705-715

[65] Jensen, N.O., 1983. A note on wind generator interaction, Risø National Laboratory, Roskilde

[66] Joukowsky, N.E., 1912. Vortex Theory of Screw Propeller. Gauthier-Villars, Paris.

[67] Kang, H.S., Chester, S., Meneveau, C., 2003. Decaying turbulence in an active-grid-generated flow and comparisons with large-eddy simulation. Journal of Fluid Mechanics 480, 129-160

[68] Katul, G., Kuhn, G., Schieldge, J., Hsieh, C.-I., 1997. The ejection-sweep character of scalar fluxes in the unstable surface layer. Boundary-Layer Meteorology 83, 1-26

[69] Katul, G., Poggi, D., Cava, D., Finnigan, J., 2006. The relative importance of ejections and sweeps to momentum transfer in the atmospheric boundary layer. Boundary-Layer Meteorology 120, 367-375

[70] Krogstad, P.-Å., Eriksen, P., 2011. “Blind Test” Workshop., NTNU,

[71] Krogstad, P.-Å., Eriksen, P.E., 2013. “Blind test” calculations of the performance and wake development for a model wind turbine. Renewable Energy 50, 325-333

[72] Larsen, G.C., Højstrup, J., Madsen, H.A., 1996. Wind field in wakes, European Wind Energy Conference and Exhibition, 764–768. H.S. Stephens & Associates,

[73] Leishman, J.G., 1998. Measurements of the aperiodic wake of a hovering rotor. Exp Fluids 25, 352-361

[74] Leweke, T., Bolnot, H., Quaranta, U., Le Dizes, S., 2013. Local and global pairing in helical vortex systems, International Conference on Aerodynamics of Offshore Wind Energy Systems and Wakes

[75] Lignarolo, L.E.M., Ragni, D., Krishnaswami, C., Chen, Q., Simão Ferreira, C.J., van Bussel, G.J.W., 2014. Experimental analysis of the wake of a horizontal-axis wind-turbine model. Renewable Energy 70, 31-46

[76] Lignarolo, L.E.M., Ragni, D., Scarano, F., Simao Ferreira, C.J., van Bussel, G.J.W., 2015. Tip vortex instability and turbulent mixing in wind turbine wakes. Journal of Fluid Mechanics 781, 467-493

[77] Liu, X., Katz, J., 2006. Instantaneous pressure and material acceleration measurements using a four-exposure PIV system. Exp Fluids 41, 227 - 240

[78] Lugt, H.J., 1996. Introduction to Vortex Theory. Vortex Flow Press.

[79] Mann, J., 1998. Wind field simulation. Probabilistic Engineering Mechanics 13, 269-282

[80] Medici, D., 2005. Experimental Studies of Wind Turbine Wakes – Power Optimisation and Meandering, Mechanics. Royal Institute of Technology (KTH), Stockholm.

[81] Meyers, J., 2011. Error-Landscape Assessment of Large-Eddy Simulations: A Review of the Methodology. J Sci Comput 49, 65-77

[82] Meyers, J., Meneveau, C., 2012. Optimal turbine spacing in fully developed wind farm boundary layers. Wind Energy 15, 305-317

[83] Mikkelsen, R., 2003. Actuator Disc Methods Applied to Wind Turbines, Department of Mechanical Engineering. Technical University of Denmark, Denmark.

[84] Moeng, C.-H., 1984. A Large-Eddy-Simulation Model for the Study of Planetary Boundary-Layer Turbulence. Journal of the Atmospheric Sciences 41, 2052-2062

[85] Naumov, I.V., Rahmanov, V.V., Okulov, V.L., Velte, C.M., Meyer, K.E., Mikkelsen, R.F., 2012. Flow diagnostics downstream of a tribladed rotor model. Thermophys. Aeromech. 19, 171-181

[86] Nishino, T., Willden, R.H.J., 2012. Effects of 3-D channel blockage and turbulent wake mixing on the limit of power extraction by tidal turbines. International Journal of Heat and Fluid Flow 37, 123-135

[87] Odemark, Y., Fransson, J.H.M., 2013. The stability and development of tip and root vortices behind a model wind turbine. Exp Fluids 54, 1-16

[88] Okulov, V., Sorensen, J., 2004. Instability of a vortex wake behind wind turbines. Doklady Physics 49, 772-777

[89] Okulov, V.L., 2004. On the stability of multiple helical vortices. Journal of Fluid Mechanics 521, 319-342

[90] Okulov, V.L., Sorensen, J.N., 2007. Stability of helical tip vortices in a rotor far wake. Journal of Fluid Mechanics 576, 1–25

[91] Øye, S., 1990. A simple vortex model of a turbine rotor, 3rd IEA Symposium on the aerodynamics of wind turbines, p4.1-4.15. IEA Aero Expert Meeting,

[92] Pentek, A., Tel, T., Toroczkai, T., 1995. Chaotic advection in the velocity field of leapfrogging vortex pairs. Journal of Physics A: Mathematical and General 28, 2191

[93] Perrin, R., Braza, M., Cid, E., Cazin, S., Barthet, A., Sevrain, A., Mockett, C., Thiele, F., 2007. Obtaining phase averaged turbulence properties in the near wake of a circular cylinder at high Reynolds number using POD. Exp Fluids 43, 341-355

[94] Pierella, F., Krogstad, P.-Å., Sætran, L., 2014. Blind Test 2 calculations for two in-line model wind turbines where the downstream turbine operates at various rotational speeds. Renewable Energy 70, 62-77

[95] Pierella, F., Sætran, L.R., 2010. Effect of initial conditions on flow past grids of finite extension, 17th Australasian Fluid Mechanics Conference.

[96] Poggi, D., Katul, G., 2008. The effect of canopy roughness density on the constitutive components of the dispersive stresses. Exp Fluids 45, 111-121

[97] Porte-Agel, F., Meneveau, C., Parlange, M.B., 2000. A scale-dependent dynamic model for large-eddy simulation: application to a neutral atmospheric boundary layer. Journal of Fluid Mechanics 415, 261-284

[98] Raffel, M., Willert, C.E., Kompenhans, J., 1998. Particle Image Velocimetry: A Practical Guide ; with 24 Tables. Springer-Verlag GmbH.

[99] Ragni, D., Ashok, A., van Oudheusden, B.W., Scarano, F., 2009. Surface pressure and aerodynamic loads determination of a transonic airfoil based on particle image velocimetry. Measurement Science and Technology 20, 074005

[100] Ragni, D., Oudheusden, B.W., Scarano, F., 2011. Non-intrusive aerodynamic loads analysis of an aircraft propeller blade. Exp Fluids 51, 361-371

[101] Ragni, D., Oudheusden, B.W., Scarano, F., 2012. 3D pressure imaging of an aircraft propeller blade-tip flow by phase-locked stereoscopic PIV. Exp Fluids 52, 463-477

[102] Ragni, D., Simao Ferreira, C.J., Correale, G., 2014. Experimental investigation of an optimized airfoil for vertical-axis wind turbines. Wind Energy, n/a-n/a

[103] Raupach, M.R., 1981. Conditional statistics of Reynolds stress in rough-wall and smooth-wall turbulent boundary layers. Journal of Fluid Mechanics 108, 363-382

[104] Réthoré, P.E., 2009. Wind Turbine Wake in Atmospheric Turbulence, Department of Civil Engineering. Aalborg University - Risø DTU.

[105] Réthoré, P.E., Sørensen, N.N., Bechmann, A., 2010. Modelling Issues with Wind Turbine Wake and Atmospheric Turbulence, TORQUE, 349-357.

[106] Reynolds, W.C., Hussain, A.K.M.F., 1972. The mechanics of an organized wave in turbulent shear flow. Part 3. Theoretical models and comparisons with experiments. Journal of Fluid Mechanics 54, 263-288

[107] Riley, N., Stevens, D.P., 1993. A note on leapfrogging vortex rings. Fluid Dynamics Research 11, 235-244

[108] Rogallo, R.S., 1981. Numerical experiments in homogeneous turbulence, NASA Ames Research Center, Moffett Field, CA, United States

[109] Saffman, P.G., 1970 The velocity of viscous vortex rings. Studies in Applied Mathematics 49, 371–380

[110] Sanderse, B., 2013. Energy-Conserving discretization methods for the incompressible Navier-Stokes equations, Department of Mathematics and Computer Science. Eindhoven University of Technology., Eindhoven

[111] Sanderse, B., van der Pijl, S.P., Koren, B., 2011. Review of computational fluid dynamics for wind turbine wake aerodynamics. Wind Energy 14, 799-811

[112] Sanz Rodrigo, J., Moriarty, P., 2014. TASK 31 - Benchmarking of wind farm flow models. Final Report to ExCo 74 Prince Eduard Island, Canada

[113] Schepers, J.G., 2012. Engineering models in wind energy aerodynamics, Aerospace Engineering. Delft University of Technology.

[114] Schreck, S., Lundquist, J., Shaw, W., 2008. U.S. Department of Energy workshop report research needs for wind resource characterization. National Renewable Energy Laboratory, Golden, CO.

[115] Schreck, S.J., Sørensen, N.N., Robinson, M.C., 2007. Aerodynamic structures and processes in rotationally augmented flow fields. Wind Energy 10, 159-178

[116] Schümann, H., Pierella, F., Sætran, L., 2013. Experimental Investigation of Wind Turbine Wakes in the Wind Tunnel. Energy Procedia 35, 285-296

[117] Selig, M.S., Guglielmo, J.J., Broeren, A.P., Giguère, P., 1995. Summary of Low-Speed Airfoil Data. SoarTech Publications, Virginia Beach, VA.

[118] Sforza, P.M., Sheerin, P., Smorto, M., 1981. Three-Dimensional Wakes of Simulated Wind Turbines. AIAA Journal 19, 1101-1107

[119] Sherry, M., Sheridan, J., Lo Jacono, D., 2010. Horizontal axis wind turbine tip and root vortex measurements, 15th International Symposium on Applications of Laser Techniques to Fluid Mechanics.

[120] Sørensen, J.N., 2011. Instability of helical tip vortices in rotor wakes. Journal of Fluid Mechanics 682, 1-4

[121] Sørensen, J.N., Shen, W.Z., Munduate, X., 1998. Analysis of wake states by a full-field actuator disc model. Wind Energy 1, 73-88

[122] Stanislas, M., Perret, L., Foucaut, J.M., 2008. Vortical structures in the turbulent boundary layer: a possible route to a universal representation. Journal of Fluid Mechanics 602, 327-382

[123] Stevens, R.J.A.M., Gayme, D.F., Meneveau, C., 2013. Effect of turbine alignment on the average power output of wind-farms, ICOWES2013 Conference.

[124] Stevens, R.J.A.M., Gayme, D.F., Meneveau, C., 2014a. Large eddy simulation studies of the effects of alignment and wind farm length. Journal of Renewable and Sustainable Energy 6, 023105

[125] Stevens, R.J.A.M., Graham, J., Meneveau, C., 2014b. A concurrent precursor inflow method for Large Eddy Simulations and applications to finite length wind farms. Renewable Energy 68, 46-50

[126] Taylor, J.R., 1997. An Introduction to Error Analysis: The Study of Uncertainties in Physical Measurements. University Science Books.

[127] Tophøj, L., Aref, H., 2013. Instability of vortex pair leapfrogging. Physics of Fluids 25, 014107

[128] van Kuik, G.A.M., Lignarolo, L.E.M., 2015. Potential flow solutions for energy extracting actuator disc flows. Wind Energy (accepted pending a minor revision)

[129] van Oudheusden, B.W., 2013. PIV-based pressure measurement. Measurement Science and Technology 24, 032001

[130] van Rooij, R.P.J.O.M., 1996. Modification of the boundary layer calculation in RFOIL for improved airfoil stall prediction,IW-96087R, Delft University of Technology, Delft

[131] Vandernoot, F.-X., Barricau, P., Bézard, H., Boisson, H.-C., 2008. Mean and turbulence measurements of wake vortices. Wandering effects. , 14th Int Symp on Applications of Laser Techniques to Fluid Mechanics

[132] Vermeer, L.J., Sørensen, J.N., Crespo, A., 2003. Wind turbine wake aerodynamics. Progress in Aerospace Sciences 39, 467-510

[133] Vermeulen, P.E.J., 1979. Mixing of Simulated Wind Turbine Wakes in Turbulent Shear Flow: Report. Hoofdgroep Maatschappelijke Technologie TNO.

[134] Violato, D., Scarano, F., 2011. Three-dimensional evolution of flow structures in transitional circular and chevron jets. Physics of Fluids 23, 124104

[135] Wallace, J.M., Eckelmann, H., Brodkey, R.S., 1972. The wall region in turbulent shear flow. Journal of Fluid Mechanics 54, 39-48

[136] Westerweel, J., 1993. Digital Particle Image Velocimetry, Mechanical Maritime and Materials Engineering. Delft University of Technology, Delft.

[137] Westerweel, J., 1997 Fundamentals of digital particle image velocimetry. Measurement Science and Technology 8, 1379–1392

[138] Whale, J., Anderson, C.G., Bareiss, R., Wagner, S., 2000. An experimental and numerical study of the vortex structure in the wake of a wind turbine. Journal of Wind Engineering and Industrial Aerodynamics 84, 1-21

[139] White, F.M., 1991. Viscous fluid flow. McGraw-Hill Professional Publishing.

[140] Widnall, S.E., 1972. The stability of a helical vortex filament. Journal of Fluid Mechanics 54, 641-663

[141] Widnall, S.E., Sullivan, J.P., 1973. On the Stability of Vortex Rings.

[142] Wieneke, B., 2015. PIV uncertainty quantification from correlation statistics. Measurement Science and Technology 26, 074002

[143] Willmarth, W.W., Lu, S.S., 1972. Structure of the Reynolds stress near the wall. Journal of Fluid Mechanics 55, 65-92

[144] Winant, C.D., Browand, F.K., 1974. Vortex pairing : the mechanism of turbulent mixing-layer growth at moderate Reynolds number. Journal of Fluid Mechanics 63, 237-255

[145] Wu, Y.T., Porté-Agel, F., 2011. Large-Eddy Simulation of Wind-Turbine Wakes: Evaluation of Turbine Parametrisations. Boundary-Layer Meteorology 138, 345-366

[146] Wu, Y.T., Porté-Agel, F., 2013. Simulation of Turbulent Flow Inside and Above Wind Farms: Model Validation and Layout Effects. Boundary-Layer Meteorology 146, 181-205

[147] Yule, A.J., 1978. Large-scale structure in the mixing layer of a round jet. Journal of Fluid Mechanics 89, 413-432

CURRICULUM VITAE

Lorenzo Edoardo Maria Lignarolo was born in Turin, in the northern part of Italy. Since an early age, he showed a strong interest in both science and art, but he picked the first one as a career choice. He studied Energy and Nuclear Engineering at Polytechnic University of Turin, where he developed a genuine love for sustainability, especially concerning the built environment. He obtained his BSc degree with a final project on building energy simulation. After enrolling in the Erasmus programme in 2008, he spent the last two semesters of his Masters in an exchange programme at the Royal Institute of Technology (KTH) in Stockholm, where he focussed on theoretical and numerical fluid dynamics and obtained his MSc degree with a thesis on the design of gas turbine blades. He decided to deepen his knowledge on fluid dynamics by enrolling in a postgraduate Masters at the Von Karman Institute for Fluid Dynamics in Brussels in 2009. His research project was about the numerical simulation of the atmospheric boundary layer, an important topic for wind engineering with application in the energy field as well as in architecture. This experience gave him the opportunity to discover a passion for scientific research. For this reason, he moved to the Delft University of Technology's Faculty of Architecture in 2010 as a guest researcher in Architectural Engineering, where he studied the interaction between wind and high-rise buildings in collaboration with the Stuttgart-based office Teuffel Engineering Consultants. In 2011, Lorenzo started a PhD project at the Delft University of Technology's Faculty of Aerospace Engineering in the chair of Wind Energy under the supervision of Professor Gerard van Bussel. During his PhD, Lorenzo studied the process of turbulent mixing in horizontal axis wind turbine wakes, in the framework of the Dutch research program FLOW (Far and Large Offshore Wind). He collaborated with several other institutions, such as ECN, Johns Hopkins University, Katholieke Universiteit Leuven and Technical University of Denmark. In his private life, Lorenzo is a connoisseur of art, architecture and music and is an amateur art collector. He holds a diploma in music theory and plays piano since age five. He enjoys travelling, looking for great architecture, emerging artists and learning about different cultures.

PUBLICATIONS

Published Articles

Lignarolo, L.E.M., Ragni, D., Krishnaswami, C., Chen, Q., Simão Ferreira, C.J., van Bussel, G.J.W., **2014**. Experimental analysis of the wake of a horizontal-axis wind-turbine model. *Renewable Energy* 70, 31-46

van Kuik, G.A.M., **Lignarolo, L.E.M.**, **2015**. Potential flow solution for energy extracting actuator disc flows. *Wind Energy*, 1-17.

Lignarolo, L.E.M., Ragni, D., Scarano, F., Simao Ferreira, C.J., van Bussel, G.J.W., **2015**. Tip vortex instability and turbulent mixing in wind turbine wakes. *Journal of Fluid Mechanics* 781, 467-493.

Lignarolo, L.E.M., Ragni, D., Simao Ferreira, C.J., van Bussel, G.J.W., **2015**. Experimental comparison of a wind turbine and of an actuator disc wake. *Journal of Renewable and Sustainable Energy* (In press)

Submitted Articles

Lignarolo, L.E.M., Mehta, D., Stevens, R.J.A.M., Yilmaz, A.E., van Kuik, G., Andersen, S.J., Meneveau, C., Simão Ferreira, C.J., Ragni, D., Meyers, J., van Bussel, G.J.W., Holierhoek, J., **2015**. Validation of four LES and a vortex model against stereo PIV measurements in the near wake of an actuator disc and a wind turbine. *Renewable Energy* (in review).

Lignarolo, L.E.M., Ragni, D., Simão Ferreira, C.J., van Bussel, G.J.W., **2015**. Turbulence production and kinetic energy transport in the wake of a wind turbine and of an actuator disc. *Physics of Fluids* (in review).

Articles published in conference proceedings

Lignarolo, L.E.M., Ragni, D., Chen, Q., Simão Ferreira, C.J., van Bussel, G.J.W., **2013**. Experimental analysis of the kinetic energy transport and turbulence production in the wake of a model wind turbine. *In Proceedings of the ICOWES2013* (pp. 1-11). Copenhagen, Denmark: Technical University of Denmark.

Lignarolo, L.E.M., Ragni, D., Simão Ferreira, C.J., van Bussel, G.J.W., **2014**. Kinetic energy entrainment in wind turbine and actuator disc wakes: an experimental analysis, *Journal of Physics: Conference Series. The Science of Making Torque from Wind 2014.*

Andersen, S.J., **Lignarolo, L.E.M.**, Ragni, D., Simão Ferreira, C.J., Sørensen, J.N., Mikkelsen, R.F., van Bussel, G.J.W., **2014**. Comparison between PIV measurements and computations of the near-wake of an actuator disc. *Journal of Physics: Conference Series. The Science of Making Torque from Wind 2014.*

Lignarolo, L.E.M., Ragni, D., Simão Ferreira, C.J., van Bussel, G.J.W., **2014**. Experimental quantification of the entrainment of kinetic energy and production of turbulence in the wake of a wind turbine with Particle Image Velocimetry. *32nd ASME Wind Energy Symposium. American Institute of Aeronautics and Astronautics.*

Lignarolo, L.E.M., Ragni, D., Simao Ferreira, C.J., van Bussel, G.J.W., **2015**. Turbulent mixing in wind turbine and actuator disc wakes: experiments and POD analysis. *33rd ASME Wind Energy Symposium. American Institute of Aeronautics and Astronautics.*

Lignarolo, L.E.M., Ragni, D., Simao Ferreira, C.J., van Bussel, G.J.W., **2015**. Wind turbine and actuator disc wake: two experimental campaigns. In s.n. (Ed.), 14th International Conference on Wind Engineering – Porto Alegre, Brazil – June 21-26, 2015.

Oral Presentation only

Experimental analysis of wind turbine wakes for validation and improvement of numerical models. Windkracht14, Rotterdam 22nd – 23rd January 2014